

Origin of Low Lattice Thermal Conductivity in Metal Chalcogenides and its Implication in Thermoelectrics

A Thesis

Submitted for the Degree of

Doctor of Philosophy

by

Moinak Dutta



**New Chemistry Unit
Jawaharlal Nehru Centre for Advanced Scientific Research
(A Deemed University)
Bangalore - 560 064, India**


August 2021

Dedicated to my parents.

DECLARATION

I hereby declare that this thesis entitled “Origin of Low Lattice Thermal Conductivity in Metal Chalcogenides and its Implication in Thermoelectrics” is a result of studies carried out by me at the New Chemistry Unit, Jawaharlal Nehru Centre for Advanced Scientific Research, Bangalore, India, under the supervision of **Prof. Kanishka Biswas**. This work has not been submitted elsewhere for the award of any degree or diploma.

In keeping with the general practices of reporting scientific observations, due acknowledgements have been made wherever the work described is based on the findings of other investigators in a collaborative pursuit. Any omission which might have occurred by oversight or error in judgement is regretted.

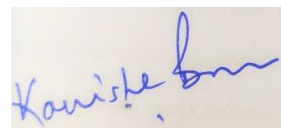


Bangalore, India
02 August 2021

Moinak Dutta

CERTIFICATE

I hereby certify that the work described in this thesis titled "Origin of Low Lattice Thermal Conductivity in Metal Chalcogenides and its Implication in Thermoelectrics" has been carried out by Mr. Moinak Dutta at New Chemistry Unit, Jawaharlal Nehru Centre for Advanced Scientific Research, Bangalore, India under my supervision and that it has not been submitted elsewhere for the award of any degree or diploma.



Bangalore, India
02 August 2021

Prof. Kanishka Biswas
(Research Supervisor)

ACKNOWLEDGEMENTS

Completion of my Ph.D. thesis necessitated a lot of guidance and supports from many people. I take this opportunity to mention a few of them. However, my sincere thanks extend to everyone who has played a role in making this dream a reality.

Firstly, my research supervisor, Prof. Kanishka Biswas for constant guidance throughout my PhD career and giving me the freedom to carry out and express my scientific thoughts. His inputs in both scientific and non-scientific problems (like how to make better presentations, how to write grant proposals etc.) has led to me become a much well prepared researcher.

My beloved labmates: Dr. Satya, Dr. Manoj, Dr. Ananya, Dr. Subhajit, Dr. Manisha, Dr. Provas, Dr. Tanmoy, Dr. Suresh, Dr. Shidaling, Dr. Kaushik, Dr. Prabir, Dr. Archana, Dr. R. K. Gopal, Dr. Jayita, Dr. Ekashmi, Dr. Subarna, Dr. Manjunatha Arka, Sushmita, Paribesh, Krishnendu, Debattam, Riddhimoy, Animesh Bhui, Anustoop, Animesh Das, Subhajit, Aditya, Ivy, Chahat and Pavan for their cheerful company and keeping a healthy competitive spirit in the lab.

I would like to thank Bharat Ratna Prof. C. N. R. Rao, FRS for his words of encouragements. I also thank him for providing the infrastructure and facilities to carry out my research work.

I would like to thank Prof. Umesh V. Waghmare, Prof. Swapan K. Pati, Dr. Koushik Pal, Prof. Ajay Soni, Prof. Goutam Sheet, Prof. Dirtha Sanyal, Prof. Pankaj Mandal, Dr. David J. Voneshen, Prof. Wolfgang G. Zeier, Dr. Martin Etter, Dr. M.V.D. Prasad, Dr. Juhi, Dr. Raju, Mr. Avinash for the fruitful scientific collaborations and all the insightful discussions. I have learnt a lot whenever we had meeting or discussion with them.

I would like to thank all the funding agencies like UGC and Synchrotron facilities at DESY-Germany due to DST-DESY collaboration and neutron facilities at UK due to DST-RAL collaboration. Without their support, it would have never been possible to conduct research.

I am thankful to all my course instructors: Prof. Kanishka Biswas, Prof. Sebastian C. Peter, Prof. Sarit S. Agasti and Prof. A. Sundaresan, whose courses have been extremely helpful.

Constant assistance and a friendly nature of the technical staff helped me doing my experiments smoothly. Here, I would like to acknowledge Mrs. Usha, Mr. Vasu, Mr. Anil, Mr. Rahul, Dr. Jay Ghatak, Mr. Mahesh, Mr. Shiva, Mr. Kanan, Mr. N. Kishore, Mr. M. Gowda, Mr. Dileep, Mr. Peer, Mr. Srinivas and others.

I thank all the staff members associated with Academic, Admin, NCU, ICMS, Library, Hostel, Mess, Security, Utility, Gardening, Cleaning, Dhanvantari and other depts.

I would like to thank UGC for the research fellowship.

I thank Prof. Rajeev Ranjan and Arnab De (IISc.) for helping us with temperature dependent powder X-ray diffraction measurements.

I thank all my seniors, friends, and juniors in JNCASR. I have been benefited a lot from my JNC friends. Their help and advice made my academic and non-academic life a memorable and comfortable one here at JNC.

I would like to acknowledge my childhood, school, college, and university friends who left an everlasting impression on me.

The various sports groups I have been associated with in JNCASR.

Lastly, I would like to acknowledge my parents and family. Without their unconditional love and support, all my efforts would have gone to vain.

PREFACE

Metal chalcogenides constitute one of the most important classes of materials with a rich structural diversity on par with oxides and a plethora of significant properties and applications. This PhD thesis investigates the origin of low lattice thermal conductivity in crystalline metal chalcogenides and their potential in the field of thermoelectrics. I have divided my thesis into five parts.

Part 1 introduces the chemistry of metal chalcogenides, covering a brief summary of low lattice thermal conductivity, thermoelectrics, synthesis, detailed characterizations and measurement techniques.

Part 2 is divided into 2 chapters. **Chapter 1** deals with the investigation of low lattice thermal conductivity (κ_{lat}) in Zintl compound TlSe, which exhibit almost glass like κ_{lat} of 0.62 – 0.4 W/mK in the temperature range of 300 – 573 K. Through various experimental and theoretical measurements, we have established that Tl⁺ intrinsically rattles in a covalent $(\text{TlSe}_2)_n^{-n}$ Thompson cage. This intrinsic Tl⁺ rattling enhances the phonon scattering and aids in lowering the lattice thermal conductivity of TlSe. In **chapter 2** we have discussed about the anisotropic nature of heat transport in simple binary compound InSe. InSe which forms a 2D layered structure along the crystallographic c-direction shows ultralow κ_{lat} of < 0.7 W/mK at 610 K while perpendicular to c-direction it shows a high κ_{lat} of 4.4 W/mK at the same temperature. The κ_{lat} parallel to c-direction is almost 8.25 times higher than the κ_{lat} perpendicular to c-direction at room temperature. This chapter brings out the role of bonding in determining the κ_{lat} of a compound.

Part 3 is divided into 2 chapters. **Chapter 1** provides experimental evidence in to the origin of low κ_{lat} (~ 0.5 W/mK at 300 K) in 1-D Zintl compound TlInTe₂ using synchrotron X-ray pair distribution function (PDF) and inelastic neutron scattering (INS). PDF analysis shown direct evidence of bonding hierarchy in the compound as well as the rattling nature of Tl⁺, while INS provided conclusive proof of the low phonon density of states. All these factors are found to be responsible in hindering the phonon propagation in TlInTe₂. **Chapter 2** deals with the investigation of low lattice thermal conductivity in positionally disordered metal selenide AgSbSe₂. Here through PDF, we have established that the although the global structure of AgSbSe₂ is rock-salt like, the local structure

deviates from the global symmetry. Our analysis of the local structure revealed that the cations (Ag/Sb) are off-centered along the crystallographic $\langle 100 \rangle$ direction a factor of $\sim 0.2 \text{ \AA}$. Further theoretical calculations revealed that the local off-centering of the cations are catalysed by the stereochemically active $5s^2$ lone pair of Sb. Such local off-centering is the root cause behind low lattice thermal conductivity in AgSbSe_2 .

Part 4 is divided into 3 chapters. In **Chapter 1** we have investigated the origin of low κ_{lat} ($0.5\text{--}0.4 \text{ W/mK}$ in $290\text{--}820 \text{ K}$) in rock-salt AgPbBiSe_3 using low temperature heat capacity, temperature dependent PDF and phonon calculations. We revealed the presence of low energy optical phonons through low temperature heat capacity. First-principles calculations augmented with low temperature heat capacity measurements and the experimentally determined synchrotron PDF revealed bonding heterogeneity within the lattice and lone pair induced local off-centering of Pb and Bi. All these factors enhance the phonon–phonon scattering and are thereby responsible for the suppressed κ_{lat} . Since low κ_{lat} is useful for thermoelectrics, we have studied its properties and found a respectable n-type figure of merit (zT) of 0.8 at 814 K for $\text{AgPbBiSe}_{2.97}\text{I}_{0.03}$. **Chapter 2** deals with investigation of low κ_{lat} and thermoelectric properties of rock-salt $(\text{SnSe})_{0.5}(\text{AgSbSe}_2)_{0.5}$. Through PDF analysis we have revealed that the local structure deviates from the overall average cubic rock-salt structure of the compound with warming, a rare phenomenon which is termed as *emphanisis*. This disrupts the periodicity of the lattice which hinders phonon flow, thus resulting in low κ_{lat} of 0.50 W/mK at 295 K in $(\text{SnSe})_{0.5}(\text{AgSbSe}_2)_{0.5}$. Thermoelectric studies shown a high p-type zT of ~ 1 at 706 K for 6 mol% Ge doped $(\text{SnSe})_{0.5}(\text{AgSbSe}_2)_{0.5}$. **Chapter 3** deals with the role of off-stoichiometric cations in vanishing of p-n-p type conduction switching in superionic compound AgCuS . AgCuS which is a polymorphic compound, undergo p-n-p type conduction switching with large change in thermopower. We have observed that the removal of Cu is much more efficient in arresting conduction switching, whereas in the case of Ag vacancy, p-n-p type conduction switching vanishes at higher vacant concentrations. The $\text{Ag}_{1-x}\text{CuS}$ and $\text{AgCu}_{1-x}\text{S}$ samples exhibit ultralow thermal conductivity ($\sim 0.3\text{--}0.5 \text{ W/mK}$) in the $290\text{--}623 \text{ K}$ temperature range because of the low-energy cationic sublattice vibration that arises as a result of the movement of loosely bound Ag/Cu within the stiff S sublattice.

Part 5 is divided into 2 chapters. In **chapter 1** we have investigated the reason behind high thermoelectric figure of merit of n-type PbTe via Gd doping. Gd doping in PbTe enhances the electron effective mass via flattening of the conduction band which improves the electrical transport but at the same time induces a flat low energy optical phonon which lowers the thermal conductivity. Such synergistic optimization of both electrical and phonon transport led to high n-type zT of ~ 1.2 for $\text{Pb}_{1-x}\text{Gd}_x\text{Te}$ ($x = 0.33\%$), at 783 K and with further optimization with iodine doping zT reaches a remarkable value of 1.65 at 678 K for 1 mol% I doped $\text{Pb}_{1-x}\text{Gd}_x\text{Te}$ ($x = 0.33\%$). **Chapter 2** discusses about the origin of low κ_{lat} in $\text{Sn}_{0.7}\text{Ge}_{0.3}\text{Te}$ which led to an extraordinary zT of 1.6 at 721 K. GeTe alloying in SnTe increases the ferroelectric transition to near room temperature, *i.e.*, around the thermoelectric operating temperature. GeTe which favours a rhombohedral structure at room temperature is found to remain in an off-centred position in rock-salt SnTe which enhances the phonon scattering thus resulting in the lowering of κ_{lat} , and ultimately aids in improving the thermoelectric performance of the material.

In **Part 6**, the whole thesis has been summarized along with a brief glimpse into the future pathway for achieving low κ_{lat} for high thermoelectric performance.

TABLE OF CONTENTS

DECLARATION	III
CERTIFICATE	V
ACKNOWLEDGEMENTS	VII
PREFACE	IX

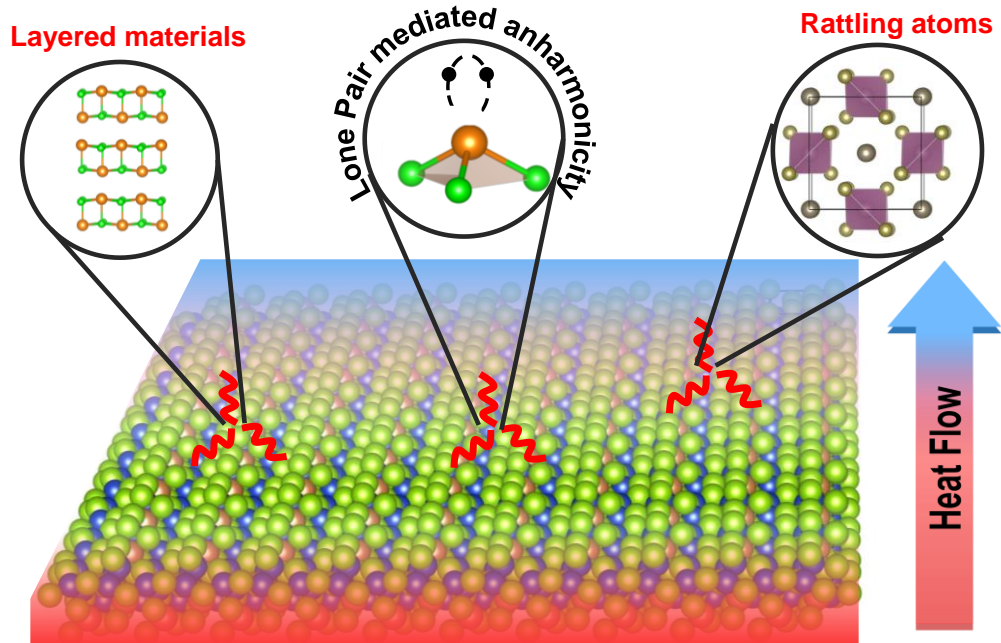
Part 1: A Brief Introduction to Origin of Low Lattice Thermal Conductivity in Metal Chalcogenides and its Implication in Thermoelectrics	1
Summary	3
1.1. Introduction to Metal Chalcogenides	5
1.2. Structural Diversity of Metal Chalcogenides and Their Role in Phonon Transport	8
1.2.1. Presence of Stereochemically Active Lone Pair of Electrons	11
1.2.2. Two-Dimensional Layered Stacking	12
1.2.3. Intrinsic Rattling of Cations.....	13
1.2.4. Bonding Heterogeneity	15
1.2.5. Local Off-centering and Emphasis	16
1.2.6. Part-Crystalline Part-Liquid States	18
1.3. Application of Low Lattice Thermal Conductive Metal Chalcogenides in Thermoelectric Energy Conversion	19
1.3.1. Brief Introduction into Thermoelectrics	19
1.3.2. Relation Between Low Lattice Thermal Conductivity and Thermoelectric Figure of Merit.....	21
1.3.3. Additional Factors to Improve Thermoelectric Figure of Merit.....	23
1.3.3.1. Carrier Concentration Optimization	23
1.3.3.2. Resonance Level	24
1.3.3.3. Band Convergence	25
1.4. Experimental Methods	27
1.4.1. Synthesis	27
1.4.2. Characterizations	30
1.4.2.1. Powder X-ray diffraction (PXRD)	30
1.4.2.2. X-ray pair distribution function (PDF)	31
1.4.2.3. Inelastic Neutron Scattering (INS)	32
1.4.2.4. Raman Spectroscopy.....	33
1.4.2.5. Transmission Electron Microscope (TEM)	34
1.4.2.6. Field Emission Scanning Electron Microscope (FESEM)	34
1.4.2.7. Energy dispersive X-ray analysis (EDAX).....	35
1.4.2.8. Positron Annihilation Spectroscopy (PAS)	35
1.4.2.9. Optical Bandgap	37

1.4.2.10. Differential Scanning Calorimetry (DSC).....	37
1.4.2.11. Hall Effect	38
1.4.3. Thermoelectric Measurements	39
1.4.3.1. Electronic Transport.....	39
1.4.3.2. Thermal Conductivity	40
1.5. Scope of the Thesis.....	42
1.6. References.....	47
Part 2: Origin of Low Lattice Thermal Conductivity in Binary IIIA - VIA Compounds	59
Chapter 2.1: Ultralow Thermal Conductivity in Chain-like TlSe Due to Inherent Tl⁺ Rattling.....	61
Summary	63
2.1.1. Introduction	65
2.1.2. Methods	66
2.1.3. Results and Discussion.....	70
2.1.4. Conclusion.....	82
2.1.5. References	84
Chapter 2.2: Giant anisotropy in Layered InSe: Coexistence of high and low lattice thermal conductivity	87
Summary	89
2.2.1. Introduction	91
2.2.2. Methods	92
2.2.3. Results and Discussion.....	95
2.2.4. Conclusion.....	102
2.2.5. References	104
Part 3: Elucidating the Origin of Low Lattice Thermal Conductivity through Synchrotron X-ray Pair Distribution Function (PDF) and Inelastic Neutron Scattering (INS).....	107
Chapter 3.1: Evidence of Highly Anharmonic Soft Lattice Vibrations in a Zintl Rattler.....	109
Summary	111
3.1.1. Introduction	113
3.1.2. Methods	115
3.1.3. Results and Discussion.....	117
3.1.4. Conclusion.....	129

3.1.5. References	130
Chapter 3.2: Local Cation Off-centering Induces Glass-like Thermal Conduction in AgSbSe₂	135
Summary	137
3.2.1. Introduction	139
3.2.2. Methods.....	141
3.2.3. Results and Discussion.....	143
3.2.4. Conclusion	156
3.2.5. References	157
Part 4: Potential Use of Intrinsically Low Lattice Thermal Conductive Compound as Thermoelectric Materials	163
Chapter 4.1: Bonding Heterogeneity and Lone Pair Induced Anharmonicity Resulted in Ultralow Thermal Conductivity and Promising Thermoelectric Properties in n-type AgPbBiSe₃	165
Summary	167
4.1.1. Introduction	169
4.1.2. Methods.....	170
4.1.3. Results and Discussion.....	174
4.1.4. Conclusion	195
4.1.5. References	196
Chapter 4.2: Emphasis in Cubic (SnSe)_{0.5}(AgSbSe₂)_{0.5}: Dynamical off-centering of Anion Leads to Low Thermal Conductivity and High Thermoelectric Performance	199
Summary	201
4.2.1. Introduction	203
4.2.2. Methods.....	205
4.2.3. Results and Discussion.....	208
4.2.4. Conclusion	223
4.2.5. References	224
Chapter 4.3: Tuning of <i>p-n-p</i>-Type Conduction in AgCuS through Cation Vacancy: Thermopower and Positron Annihilation Spectroscopy Investigations	229
Summary	231
4.3.1. Introduction	233
4.3.2. Methods.....	236
4.3.3. Results and Discussion.....	238
4.3.4. Conclusion	250
4.3.5. References	252

Part 5: High Performance Thermoelectrics of IV-VI Chalcogenides Driven by Low Lattice Thermal Conductivity	255
Chapter 5.1: Discordant Gd and Electronic Band Flattening Synergistically Induce High Thermoelectric Performance in n-type PbTe	257
Summary	259
5.1.1. Introduction	261
5.1.2. Methods	263
5.1.3. Results and Discussion	265
5.1.4. Conclusion	283
5.1.5. References	284
Chapter 5.2: Local Ge Off-centering in Sn_{1-x}Ge_xTe Induces Ferroelectric Instability and Softens Polar Phonons: Pair Distribution Function (PDF) Analysis	289
Summary	291
5.2.1. Introduction	293
5.2.2. Methods	294
5.2.3. Results and Discussion	296
5.2.4. Conclusion	301
5.2.5. References	302
Part 6: Summary and Future Outlook	305
6.1. Summary	307
6.2. Future Outlook	310
6.3. References	313
List of Publications	315
Biography	317

Part 1



A Brief Introduction to Origin of Low Lattice Thermal Conductivity in Metal Chalcogenides and its Implication in Thermoelectrics

A Brief Introduction to Origin of Low Lattice Thermal Conductivity in Metal Chalcogenides and its Implication in Thermoelectrics[†]

Summary

Thermoelectric materials which can convert heat energy to electricity rely on crystalline inorganic solid state compounds exhibiting low phonon transport (i.e. low thermal conductivity) without much inhibiting the electrical transport. Suppression of phonons traditionally has been carried out via extrinsic pathways, involving formation of point defects, foreign nanostructures, and meso-scale grains, but the incorporation of extrinsic substituents also influences the electrical properties. Crystalline materials with intrinsically low lattice thermal conductivity (κ_{lat}) provide an attractive paradigm as it helps in simplifying the complex interrelated thermoelectric parameters and allows us to focus largely on improving the electronic properties. Several heavy metal chalcogenides by virtue of their diverse chemical and structural ingenuities provides several novel intrinsic phonon suppressing pathways, which lowers their κ_{lat} . This chapter highlights a brief introduction to heavy metal chalcogenides followed by their unique chemistry and bonding which intrinsically lowers the κ_{lat} and their potential application in the field of thermoelectrics. Last part of this chapter is focused on a general methods for chalcogenide synthesis, characterizations and thermoelectric measurements.

[†]A part of this chapter is published in M. Dutta, D. Sarkar and K. Biswas. *Chem. Commun.*, 2021, **57**, 4751-4767 (Perspective).

1.1. Introduction to Metal Chalcogenides

Chalcogenides constitute one of the most important classes in the field of chemistry, exhibiting rich compositional and structural diversity on par with oxides and organic compounds. Chalcogenides are compounds that contain at least one chalcogen Q atom ($Q = S/ Se/ Te$) in a chemically reduced state compared to its elemental form. Chalcogenides bear few chemical resemblances to oxides, but there are also big dissimilarities in chemical character and physical properties among them which are significant enough to warrant a separate treatment of the chalcogenides as a distinct class of materials. These differences must, of course, originate from the differences between the oxygen atom on the one hand and the atoms of S, Se, Te on the other. Some important differences in the atomic properties of oxygen and the chalcogen are:¹

- (a) The chalcogen atoms are larger (and also heavier) than oxygen atoms.
- (b) The chalcogens are less electronegative than oxygen.
- (c) The chalcogens have d orbitals of accessible energy (3d for S, 4d for Se and 5d for Te), while oxygen has not.

These differences in the atomic properties cause differences among metal – S/Se/Te bond with respect to metal – oxygen bond. Some of these differences are:

- (d) The metal-to-chalcogen bonds are more covalent than metal-to-oxygen bonds (consequence of (b)).
- (e) The metal-to-chalcogen bonds often involve the d orbitals of the chalcogen, while this is not possible for the bonding to oxygen (consequence of (c)).
- (f) The chalcogenides are more polarizable than oxide ions (consequence of (a) and (c)).

One of the most striking differences between oxides and chalcogenides is the facile ability of the chalcogen to form stable Q–Q bonds: catenation. For instance, there are many allotropes of sulfur, owing to the ability of sulfur to form chains of singly bonded atoms. This catenation is also observed in metal chalcogenides, for example, in pyrite where S–S (S_2^{2-}) units are found. Similarly, selenides and tellurides also exhibit Q–Q bonding as in Se_2^{2-} and Te_2^{2-} units of pyrite-type structures but in contrast with sulfides, they can form solid-state structures that contain Q_n rings or chains with $n > 2$ as exemplified by Se_5 moiety in Nb_2Se_9 ² and Te_6 group in $Re_6Te_{16}C_{16}$ ³. In general, as we move from sulfides to

selenides to tellurides, the degree of covalent bonding, delocalization of electrons and metallic behaviour increase, and the importance of long range Q-Q interactions (*i.e.*, less than single bond) increases.⁴ Te-Te single bonds are ca. 275 pm in length, but in a large number of telluride compounds, Te-Te bonds with distances intermediate between single bonds and van der Waals interactions (ca. 420 pm) exist. These bonds are energetically weak but are structurally important; they also manifest as Te...Te interlayer interactions that essentially stabilize the structures of layered tellurides such as TaIrTe₄ and NbIrTe₄.⁵

Besides, catenation can produce stable complex polychalcogenide anions (Q_x^{2-} , where x is up to 7 or 8). These anions serve as reactive building blocks for molecules and solid-state materials. Chalcogenides are similar to oxides in that there are as many chalcocanions, particularly with the main-group and early-transition metal atoms (e.g. $[PS_4]^{3-}$, $[P_2S_7]^{4-}$, $[SiS_4]^{4-}$, $[GeS_4]^{4-}$, $[MoS_4]^{2-}$, $[VS_4]^{3-}$ etc.), as there are oxyanions (e.g. $[PO_4]^{3-}$, $[P_2O_7]^{4-}$, $[SiO_4]^{4-}$, $[Si_2O_7]^{6-}$, $[MoO_4]^{2-}$, $[VO_4]^{3-}$ etc.). In fact, chalcogens can form many other chalcocanions which do not have analogous oxyanions, few examples being $[P_2Se_6]^{4-}$, $[P_3Se_7]^{3-}$, $[P_2Se_8]^{2-}$, $[P_8Se_{18}]^{6-}$, $[GeS_4]^{4-}$, $[GeSe_5]^{4-}$, $[Ge_2Se_6]^{6-}$ etc.⁶⁻⁸ Metal oxides are usually ionic in character, and they resemble fluorides more than they do chalcogenides. For instance, dioxides such as VO₂, CrO₂, and MnO₂ crystallize in a rutile-type (TiO₂) structure similar to the corresponding fluorides *viz.* VF₂, CrF₂ and MnF₂. On the other hand, while VS₂ and CrS₂ are not known, MnS₂ has a pyrite-type structure characterized by S₂²⁻ units, which is rarely found in oxides. Similarly, MnSe₂ and MnTe₂ also crystallize in pyrite-type structures. It is noteworthy that although Mn metal atoms have octahedral coordination in both MnO₂ and MnQ₂, the overall structures are significantly different. Besides, layered structures are very common among metal dichalcogenides but seldom found among oxides. The structures of most oxides are well represented by models that treat atoms as hard, charged spheres with ionic radii specific to a given element. The constant-radius approximation is, however, not accurate for metal chalcogenides because of their more covalent character.⁴ Some of the important distinctions between metal oxides and metal chalcogenides are summarized in table 1.1.

Metal chalcogenides are central to many important technologies. They exhibit a broad range of chemical and physical properties associated with diverse scientific phenomena and enable a plethora of applications.⁹⁻¹⁶ For example, CdTe and CuInSe₂ are

high-performing materials for thin-film solar photovoltaics; PbTe, GeTe and Bi₂Te_{3-x}Se_x are the champion thermoelectric materials; Co(Ni)/Mo/S composites are the best available catalysts for hydro-desulphurization of crude oil; Ge₂Sb₂Te₅ is a high density memory material; CdHgTe is the key infrared detector material in night-vision cameras etc.

Table 1.1. *Some important distinctions between metal oxides and metal chalcogenides.*

Feature	Oxides	Chalcogenides
Close packing	Usually	Sometimes
Octahedral/tetrahedral metal-coordination	Yes	Usually
Trigonal prismatic metal-coordination	Very rarely	Groups 5 and 6
Layered structures	Rarely	Usually
Q-Q bonds	Peroxides	Common
Bonding	Ionic	Covalent

Metal chalcogenides are at the cutting edge of many research areas. Some examples include nonlinear optics,¹⁷ optical information storage,¹⁸ photovoltaic energy conversion,¹⁹ thermoelectric energy conversion,^{14, 20, 21} radiation detectors,²² thin-film electronics,²³ spintronics,²⁴ fast-ion conductivity,²⁵ rechargeable batteries,²⁶ catalysis,²⁷ novel magnetism,²⁸ unconventional superconductivity²⁹ and science in two dimensions.^{15, 30} In the recent times, the scientific community has witnessed sensational discoveries pertinent to metal chalcogenides such as quantum spin Hall Effect,³¹ topological insulators,³²⁻³⁵ topological crystalline insulators,^{36, 37} non-saturating magnetoresistance³⁸ and many others which will have huge implications, especially in the fields of spintronics and (opto) electronics. We are currently in the midst of an impressive expansion in solid-state chalcogenide chemistry with emphasis on the synthesis of materials with new compositions and structures on the one hand, and exploration of their novel properties on the other. Most of the aforementioned applications and phenomena are associated with chalcogenides of transition metals and main group p-block metals. The following sections will brief structural aspects and novel properties pertinent to these metal chalcogenides

along with its relevance for phonon transport, which provide a background to my thesis work.

1.2. Structural Diversity of Metal Chalcogenides and Their Role in Phonon Transport

The p-block metal chalcogenides exhibit rich structural diversity.³⁹ Wurtzite and zinc blende structures are prevalent in quasi-binary III₂-VI₃ metal chalcogenides. Anisotropic layered structures are also found in III-VI compounds with covalently bonded layers stacked via weak van der Waals interactions. For instance, GaQ (Q = S, Se, Te) and InSe are all found in layered structures stabilized by cation-cation bonds.⁴⁰ TlSe, TlS and InTe crystallize in a tetragonal TlSe-type structure [i.e., Tl¹⁺Tl³⁺(Se²⁻)₂] with monovalent and trivalent cations, characterized by anionic and cationic substructures similar to Zintl compounds.⁴⁰

Among IV-VI metal chalcogenides, GeQ and SnQ (Q = S, Se) exhibit orthorhombic puckered layered structure similar to black phosphorous, which can be derived from three-dimensional distortion of the rock salt (NaCl) structures. GeTe and SnTe have rock-salt (NaCl) structures with slight deformations due to phase transitions. The high-temperature phase shows the perfect NaCl-structure, stable above 670 K and 100 K for GeTe and SnTe, respectively. SnQ₂ (Q = S and Se) crystallizes in layered CdI₂ – type structure. PbQ (Q = S, Se, Te) crystallizes in cubic rock-salt structure.^{41, 42}

Among group V-VI chalcogenides, Sb₂S₃, Sb₂Se₃ and Bi₂S₃ have orthorhombic Sb₂S₃-type stibnite structure with one-dimensional connectivity. Sb₂Te₃, Bi₂Se₃ and Bi₂Te₃ are found in rhombohedral layered structures comprised of covalently bonded Q-M-Q-M-Q (M = Sb/Bi; Q = Se/Te) quintuple layers stacked via weak van der Waals interactions along the c-axis. It is interesting to note the effect of cation lone pair on the structural stability of group 13-15 metal chalcogenides. The valence ns² lone pairs on the cations in these compounds play a key role in their structural, chemical, thermal and electronic properties.³⁹

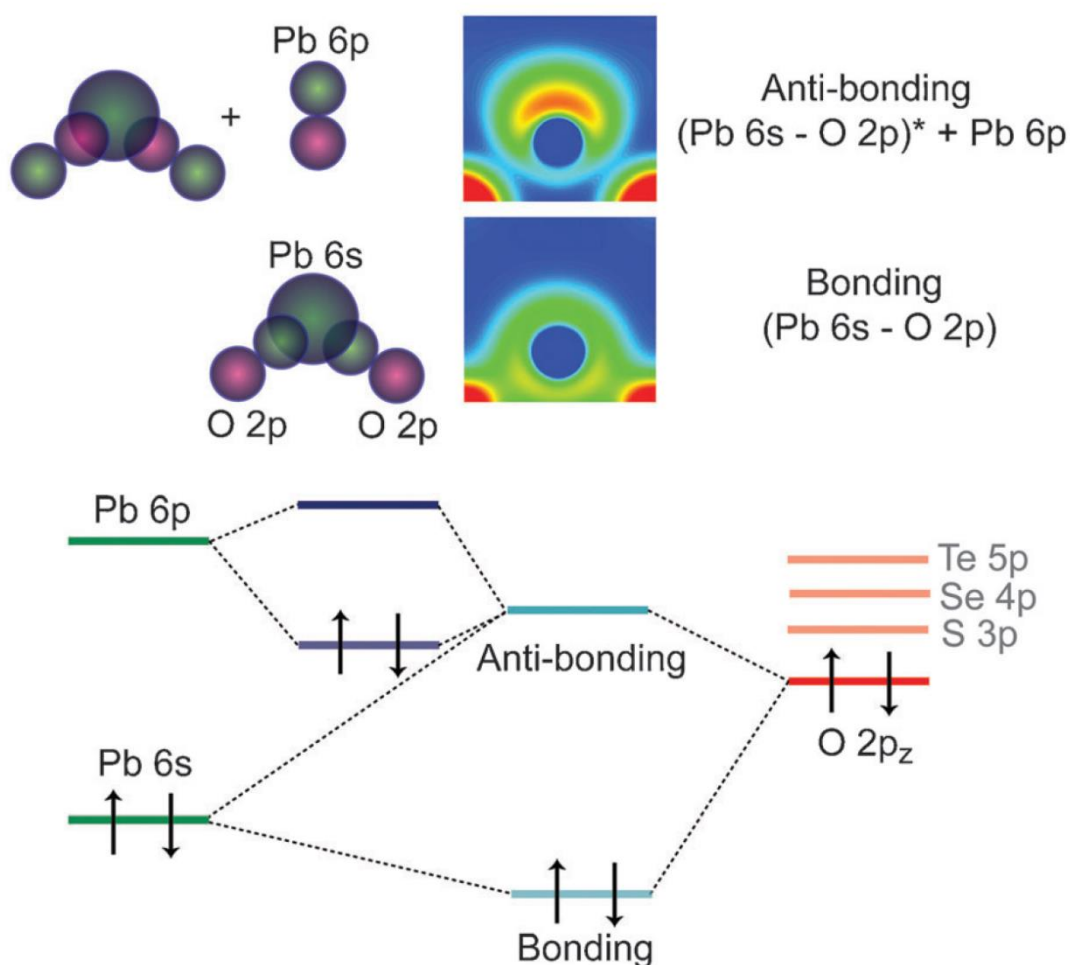


Figure 1.1. Illustration of orbital interactions leading to stereochemical active lone pair in PbO (upper panel) and the corresponding energy level diagram (lower panel). The cation s and anion p orbital-interaction lead to formation of bonding and antibonding states which appear at the bottom and top of the upper valence band, respectively. The empty cation p states then interact with the filled antibonding state, resulting in stabilization of the cation ns^2 electrons. This interaction becomes symmetry-allowed by lattice distortion accompanied by an asymmetric electron density that is projected into the structural void. Reproduced with permission from ref. 39 © 2011 Royal Society of Chemistry.

For example, as the metal becomes heavier on going down the group 13, the lone pair becomes increasingly stable in the order: $\text{Ga}^+ < \text{In}^+ < \text{Tl}^+$ and the same applies to groups 14 and 15 where the Pb^{2+} and Bi^{3+} cations possess stable lone pairs. The large stability of ns^2 lone pairs in the heavier elements of the main group is ascribed to

relativistic effects that contract the s-orbital and bring it closer to the nucleus thereby lowering its energy level.³⁹

The cation ns^2 lone pair behaves in different ways depending on the local coordination environment as well as the metal and chalcogen atoms involved.^{39, 43} It can either express stereochemically by occupying a distinct space around the metal atom or effectively remain ‘quenched’. When expressed stereochemically, the ns^2 lone pair can cause lattice distortion accompanied by lowering of ns^2 energy level. The formation of a stereochemically active lone pair (distortion) depends on the strength of interaction between cation s-states and the anion p-states; the stronger the interaction, the more contribution of cation s-states to the upper valence band (Figure 1.1). Down the group 16, the p-orbital energies increase on going from O to Te. As mentioned above, cation ns^2 energy decreases down the groups 13-15. Therefore, PbO exhibits low symmetry litharge structure (distorted rock-salt structure) with stereochemically active ns^2 lone pairs whereas PbQ (Q = S, Se, Te) occurs in the symmetric rock-salt structure.³⁹ Similar arguments hold true for orthorhombic Sb_2S_3 , Sb_2Se_3 and Bi_2S_3 vs. rhombohedral Bi_2Se_3 and Bi_2Te_3 , orthorhombic $SnSe$ vs. cubic $SnTe$, and rhombohedral $GeTe$ versus cubic $SnTe$ and $PbTe$. As the stereochemical expression stabilizes the ns^2 pair which lies above or near the highest occupied state, the energy band gaps are usually higher in the low-symmetry structures relative to symmetric structures.⁴⁴ In the latter, the ‘quenched’ cationic lone pair may experience repulsion from the surrounding anions unlike the former where the structural distortion relieves this repulsion. The structural strain associated with the lone pair repulsion can result in highly anharmonic phonons as in the case of $PbTe$, Bi_2Se_3 causing low lattice thermal conductivity.⁴³ It is also worth noting that in $PbTe$, the stereochemical expression of ns^2 lone pair increases with temperature, a phenomenon dubbed ‘emphanisis’.⁴⁵ As a consequence, off-centering of Pb atoms occurs from their ideal octahedral sites at high temperatures.

I-V-VI₂ (where I = Cu, Ag, Au or alkali metal; V = As, Sb, Bi; and VI = S, Se, Te) type of compounds are a special class of semiconductors which are renowned for their intrinsically low lattice thermal conductivity due to the strong anharmonicity of their bonding arrangements.^{43, 46} Some of the members of this class crystallize in cation disordered high symmetry cubic rock salt structure at room temperature (eg. $AgSbSe_2$,

AgSbTe₂, NaBiTe₂, NaBiSe₂, NaSbSe₂, NaSbTe₂ etc).^{43,47} However, few of the members show structural phase transitions as a function of temperature (AgBiS₂, AgBiSe₂, AgBiTe₂, etc) and finally transform to cation disordered rock salt cubic structure at high temperatures.⁴⁷ Below I have outlined several case studies where lowering of lattice thermal conductivity is attributed to the unique structural and bonding environment of various metal chalcogenides.

1.2.1. Presence of Stereochemically Active Lone Pair of Electrons

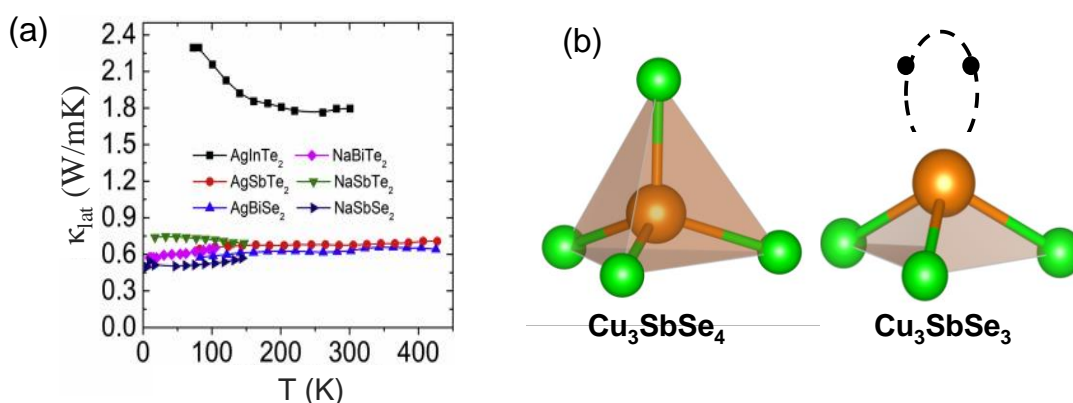


Figure 1.2. (a) Temperature dependent lattice thermal conductivity (κ_{lat}) of I-VA-VIA₂ compounds. AgInTe₂ with no lone pair of electrons (LPE) shows a much higher κ_{lat} compared to the other compounds possessing LPE. (b) Polyhedron around Sb atoms in Cu₃SbSe₄ (left) and Cu₃SbSe₃ (right). Cu₃SbSe₃ contains an active 4s² LPE which decreases its κ_{lat} . Reproduced with permission from ref. 49 © 2021 Royal Society of Chemistry.

Presence of stereochemically active lone pair of electrons (LPE) is found typically in compounds containing post-transition elements. Such elements exhibit an oxidation state of (n-2), where n is the main group number as in case of Sb³⁺ (Group VA) or Pb²⁺ (Group VIA). It infers that the outer most s-electrons remains available as lone pair and if expressed significantly in a particular direction will lead to a possible asymmetric coordination.^{48, 49} The ability of outermost s-electrons to stereochemically express itself is dependent on the relative energy of the cation s and anion p-states^{39, 50} and can be understood by comparing the thermal conductivity of AgInTe₂ and AgSbTe₂. Indium in AgInTe₂ contains 5s² 5p¹ valence electrons with little energy offset between the 5p and

5s orbitals. This results in a complete sp hybridization of all three valence electrons of In with Te, thus eliminating any possible formation of lone pair. However, Sb which contains $5s^2 5p^3$ valence electrons have larger offset between them. This makes the $5s^2$ electrons unable to participate in the hybridization with Te and consequently resides as a lone pair. This lone pair exerts a repulsive force on the Sb-Te bond thus, imparts a significant lattice anharmonicity. Lone pair induced lattice anharmonicity lowers the lattice thermal conductivity of AgSbTe_2 to ~ 0.6 W/mK at 300 K compared to 1.8 W/mK for AgInTe_2 (Figure 1.2a).^{43, 51} However, the presence of such lone pair is not atom specific. Cu_3SbSe_4 and Cu_3SbSe_3 despite of possessing similar average atomic mass and stoichiometry, show stark contrast in their κ_{lat} . Sb in Cu_3SbSe_4 has a nominal charge of +5, indicating all its valence electrons participates in the bonding, while Sb for Cu_3SbSe_3 is trivalent (Sb^{3+}) indicating the presence of $5s^2$ LPE (Figure 1.2b). This LPE enhances the intrinsic phonon-phonon interaction and thereby lowering the κ_{lat} to almost glasslike (~ 0.49 W/mK at 300 K) for Cu_3SbSe_3 while Cu_3SbSe_4 exhibits a high κ_{lat} of ~ 2.9 W/mK at 300 K.⁵² Similarly, In although devoid of LPE in AgInTe_2 , forms LPE in InTe and thus shows low κ_{lat} of $0.76 - 0.5$ W/mK in the temperature range of $300 - 673$ K.⁵³ I have studied the role of LPE in determining the κ_{lat} in **chapter 3.2 of part 3** and **chapters 4.1 of part 4** of my thesis.

1.2.2. Two-Dimensional Layered Stacking

Two dimensional (2D) layered materials by virtue of their very weak interaction along the direction of layer stacking, disrupts the phonon flow between the layers, lowers its group velocity (v_g) which eventually limits their κ_{lat} .⁵⁴⁻⁵⁶ The weak interlayer bonding gives rise to soft optical modes which in turn couples with the heat carrying acoustic phonons and thereby reducing the κ_{lat} . A case in point, charge layered heterostructure compounds, such as $\text{Bi}_2\text{O}_2\text{Se}$ and BiCuSeO , where charged layers are held together by weak coulombic interactions, several low frequency flat optical modes with frequency less than 100 cm^{-1} were observed.^{57, 58} The optical-acoustic phonon coupling is also observable in natural van der Waals (vdWs) heterostructured compounds which exhibit intrinsically ultralow κ_{lat} .⁵⁹⁻⁶¹ Furthermore, these layered materials exhibit considerable lattice anharmonicity due to the anisotropic bonding nature in different crystallographic

direction as strong covalent bonds exist in in-plane where out-of-plane weak bonds are mainly governed by either van der Waals or Coulombic interactions.⁵⁴ SnSe for example, have layers stacked along the crystallographic a-direction (Figure 1.3a), exhibits low κ_{lat} along the layers stacking direction as compared to other directions (Figure 1.3b). SnSe further exhibits large average Grüneisen parameter (γ) of ~ 3.13 which is almost twice that of PbTe ($\gamma \sim 1.69$) and PbSe ($\gamma \sim 1.65$) respectively.⁵⁶ Therefore, layered materials possessing anisotropic bonding are beneficial for obstructing the phonon transport for potential thermoelectric applications.⁶² In my thesis, I have discussed the role of 2D materials in lowering κ_{lat} in **chapter 2.2 of part 2**.

1.2.3. Intrinsic Rattling of Cations

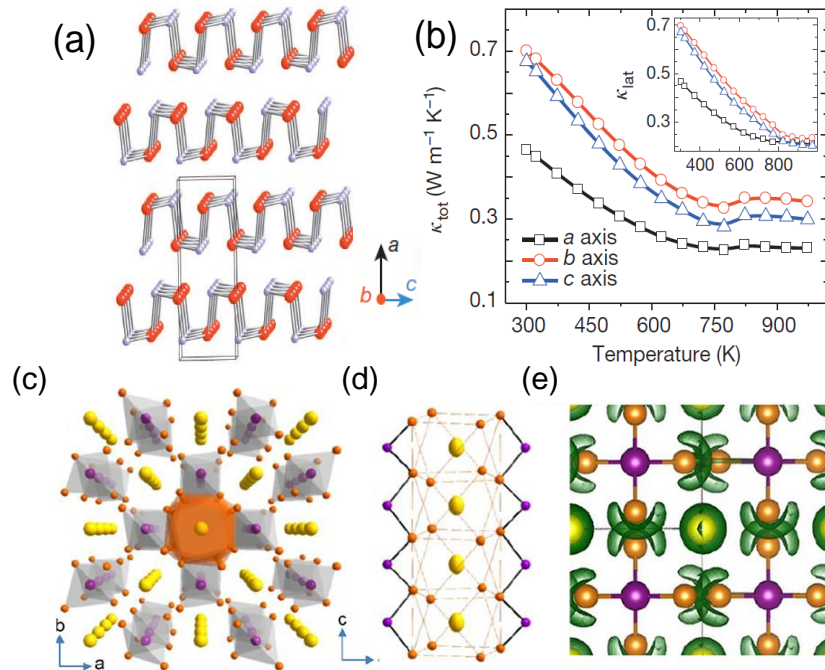


Figure 1.3. (a) Layered and corrugated crystal structure of SnSe at room temperature. (b) Temperature variation of total thermal conductivity (κ_{tot}) along the crystallographic a, b and c-axis. Inset shows the lattice thermal conductivity (κ_{lat}). (c) Tetragonal crystal structure of $AlnTe_2$ ($A = Tl^+/In^+$) Zintl compounds showing the chains of anionic (violet polyhedra) and cationic (orange polyhedron) substructures along the crystallographic c-axis. Purple, orange, and yellow spheres represent In^{3+} , Te^{2-} , and Tl^+/In^+ ions, respectively. (d) Atomic displacement parameters of Tl, In, and Te atoms in $TlInTe_2$ plotted as 80% probability ellipsoids. (e) Electron localization function diagram of $TlInTe_2$. The Yellow spheres represent Tl and show no strong bonding interactions while

violet and orange represent In and Se atoms respectively, shows strong covalent interaction. (a and b) Reproduced with permission from ref. 133 © 2014 Springer Nature. (c - e) Reproduced with permission from ref. 72 © 2017 American Chemical Society.

If an atom is weakly bonded in an oversized covalently bonded cage and vibrates with a much greater amplitude compared to the caged atoms with temperature perturbation, the atom is termed as a rattler atom. Commonly observed for guest atoms in oversized cages like that of skutterudites and clathrates, these guest atoms rattle within the large cages.⁶³⁻⁷⁰ These guest rattler atoms vibrate independently similar to Einstein modes and manifest several low frequency optical modes. These low energy Einstein modes are highly efficient in scattering the heat carrying acoustic phonons and thus lowering their κ_{lat} . However, these rattlers are extrinsically incorporated. Moreover, the rattling nature of these guest atoms are debated.⁷¹

Zintl compounds presents an intriguing case where an atom is weakly attached to a covalently bonded polyanionic substructure. This atom due to its weak bonding to the covalent sub-lattice can show enhanced vibration with temperature characteristic of its rattling behavior. TlInTe₂ belongs to this class of compounds and crystallizes in tetragonal I4/mcm lattice shows such weak and strong sub-structures.⁷² The polyanionic chain here is comprised of covalently bonded 1D chain of [InTe₂]_n⁻ⁿ tetrahedra propagating along the crystallographic c-axis. [InTe₂]_n⁻ⁿ is comprised of four In – Te bonds sharing 3 electrons and hence remains electron deficit. Tl which is the electropositive atom donates its valence electron to the polyanionic framework, thus maintaining the charge balance (Figure 1.3c). This electrostatic interaction between Tl⁺ and [InTe₂]_n⁻ⁿ is evident from their bond lengths. The room temperature In -Te bond distance of ~ 2.82 Å is close to summation of covalent radii of In³⁺ (1.42 Å) and Te²⁻ (1.38 Å) indicating a strong covalent framework, however, Tl-Te has much larger distance of 3.59 Å which can only be accounted for if we consider their corresponding ionic radii (r_{ion}) (r_{ion} of Tl⁺ is 1.64 Å; r_{ion} of Te²⁻ is 2.07 Å). The presence of such heterogeneous bonding means the phonons are devoid of a uniform conduit to flow through the system and will invariably scatter, resulting in the lowering of lattice thermal conductivity. Furthermore, from Atomic Displacement Parameter (U) analysis it is evident that Tl vibrates at a greater magnitude as compared to In and Te indicative of its

rattling behavior (Figure 1.3d). These Tl vibrations, are rather independent analogous to Einstein rattlers, disrupt the acoustic vibrations and further induce low energy optical modes. These low energy optical modes are detrimental to heat flow and reduces the phonon lifetime of the compound. It resulted in an ultralow κ_{lat} of 0.46 – 0.31 W/mK in the temperature range of 300 – 673 K (Fig. 7b).⁷² InTe which have similar structure to that of TlInTe₂, also exhibit ultralow κ_{lat} owing to the intrinsic rattling vibration of the electropositive In⁺.⁵³ Several other compounds with low room temperature κ_{lat} like CsAg₅Te₃ (0.18 W/mK), AgBi₃S₅ (0.5 W/mK), Tl₃VSe₄ (0.3 W/mK), Y₁₄MnSb₁₁ (0.7 W/mK) etc. attributes their ability to restrict heat flow to the intrinsic rattling dynamics of atoms.⁷³⁻⁷⁸ In my thesis, I have investigated the role or intrinsic rattler atoms in lowering of κ_{lat} in **chapter 2.1 of part 2** and **chapter 3.1 of part 3**.

1.2.4. Bonding Heterogeneity

Presence of heterogeneous bonds in a solid incurs a negative effect on the phonon propagation pathway. A weak bonding indicates that the atoms will vibrate with greater frequency on thermal agitation and will act as phonon scattering centers while a strong bonding will provide a smooth conduit for phonon propagation. Multiple type of bonding in a solid hence will disrupt the uniformity required for phonon propagation and hence is highly effective in lowering the κ_{lat} of a material. AgBiS₂ which belongs to the family of I-V-VI₂ compounds ideally crystallizes as hexagonal $P\bar{3}m1$ at room temperature and undergoes an order-disorder transition at 475 K to cubic $Fm\bar{3}m$ crystal structure. Rathore *et. al.*, have observed that kinetically stabilized cubic AgBiS₂ at room temperature shows ultralow κ_{lat} of 0.68 W/mK.⁷⁹ This ultralow value mainly arises due to the presence of soft Ag vibrations and locally distorted Bi atoms. A shallow potential well for Ag as compared to Bi and S, indicated that Ag can be easily perturbed from its equilibrium position with thermal excitations and is a consequence of weaker bonding of Ag - S in the lattice as compared to Bi - S bond (Figure 1.4a). This non-uniformity in the local bonding will generate addition phonon-phonon scattering and will aid in the lowering of thermal conductivity in AgBiS₂. This simultaneous presence of weak Ag - S bonds and strong Bi - S bonds in the crystal lattice lowers the κ_{lat} in AgBiS₂. The presence of such bonding heterogeneity is also observed in several other compounds like BaAgYTe₃,

BaAuP₄, Cu_{17.6}Fe_{17.6}S₃₂ Zintl phases etc. which exhibit intrinsically ultra-low κ_{lat} .^{76, 80-83} I have discussed about the role of bonding heterogeneity in reducing κ_{lat} in **chapter 4.1 of part 4**, of my thesis.

1.2.5. Local Off-centering and Emphasis

The term “*emphasis*” signifies a structural phenomenon in which a material system transforms from high symmetry structure to a low symmetry structure on heating. Generally observed for simple binary systems like PbQ (Q = S, Se, Te) and SnTe, these systems near room temperature remain as undistorted rock-salt type, however undergo a local distortion on heating to high temperatures.^{45, 84, 85}

PbTe a champion thermoelectric material possesses low lattice thermal conductivity of ~ 2.4 W/mK at room temperature.⁸⁶ The main contributing factor for such low lattice thermal conductivity is the large anharmonicity as observed from the Inelastic Neutron Scattering (INS) measurements.⁸⁷ The INS measurements further revealed a new phonon mode at high temperatures, indicating dynamic symmetry breaking.⁸⁸ Božin *et al.*, while investigating the emergence of local structural dipoles in PbTe on heating, observed a local symmetry breaking in the high temperature region through X-ray Pair Distribution Function (PDF) measurements. Temperature dependent X-ray PDF measurements from 15 K to 500 K revealed a drastic drop in the intensity of the nearest neighbour peak (*i.e.*, the closest Pb-Te bond distance) with warming and cannot be accounted for using only Debye-Waller effects. This decrease in the intensity is also accompanied by peak asymmetry (Figure 1.4b), which increases from 15 K to ~ 250 K, above which it saturates (Figure 1.4c). The non-Gaussian peak asymmetry is indicative of several, incompletely resolved local short and long bonds within an average high symmetric PbTe. Local structural analysis using PDF exhibits that although PbTe at high temperatures is globally cubic, but locally it remains in an off-centered position along $\langle 100 \rangle$ crystallographic direction. This locally off-centered Pb²⁺ cation explains the high lattice anharmonicity and its consequent low κ_{lat} in PbTe.⁴⁵ The magnitude of this local off-centering increases with increase in temperature reaching a peak value of 0.24 Å (Figure 1.4d). The transition from high symmetric structure to low symmetric structure

on warming termed as *emphanisis* explains in part the origin of lattice anharmonicity in PbTe. Similar experiments indicate that this lowering of thermal conductivity due to local off-centering of an atom (or atoms) is not an exception for PbTe but is much wider spread as seen for other promising thermoelectric materials like PbS, PbSe, SnTe, α -MgAgSb etc.^{45, 84, 85, 89, 90} In my thesis, I have investigated several materials which show local distortion, thus impeding the thermal flow in materials. The role of local distortion and emphanisis are discussed in **chapter 3.2 of part 3, chapter 4.1 and 4.2 of part 4, chapter 5.1 and 5.2 of part 5**, of my thesis.

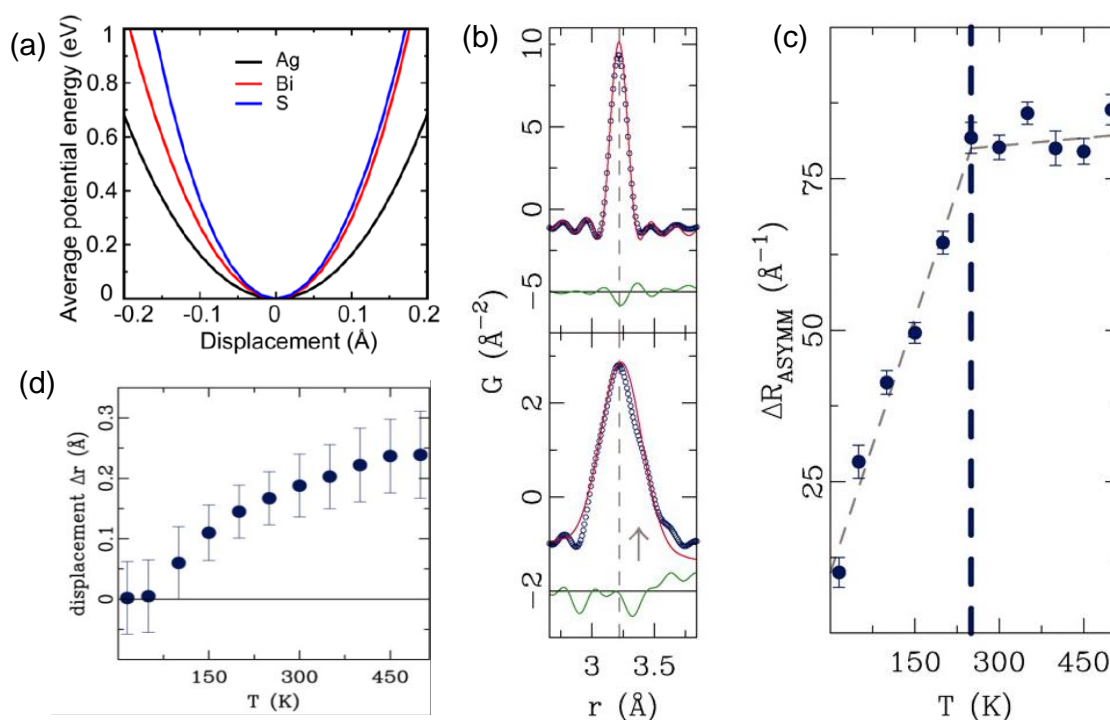


Figure 1.4. (a) Potential energy versus displacement of Ag, Bi and S in AgBiS₂. Nearest neighbour peak of PbTe at 15 K (top) and 500 K (bottom). Clear non-Gaussian peak asymmetry is observed for the 500 K PDF data. (b) Temperature dependent variation in the peak asymmetry of the nearest neighbour peak. (c) Temperature dependent local displacement of Pb along the $\langle 100 \rangle$ direction. (d) Anomalous phonon hardening of the new optical mode in PbTe. (a) Reproduced with permission from ref. 79 © 2019 American Chemical Society. (b - d) Reproduced with permission from ref. 49 © 2021 Royal Society of Chemistry, which copyrighted from ref. 45 American Association for the Advancement of Science.

1.2.6 Part-Crystalline Part-Liquid States

A perfect thermoelectric material system is the one which can provide a facile conduction of electrons (or holes) while simultaneously blocking out the thermal propagation; commonly termed as “Phonon Glass Electron Crystal (PGEC)” as envisaged by Slack.⁹¹ For PGEC to be implemented, a material must embody seemingly two distinct sub-lattices (one glass like and one metal like sublattice) into one. Materials with significant bonding hierarchy like those of clathrates and Zintl compounds can be visualized to be PGEC type of compounds.⁹² Another class of compounds which can be termed as PGEC are those which comprises of liquid like mobile superionic cations held inside a rigid anionic framework.⁹³ These mobile cations flow unhindered throughout the lattice causing extensive phonon damping, while the stiff anionic sub-lattice provides a conduit for electron flow. $\text{Cu}_{2-\delta}\text{X}$ (S, Se, Te)⁹⁴⁻⁹⁸ and their derivatives AgCuX (S, Se, Te)⁹⁹⁻¹⁰¹ which undergo a low symmetric – ordered to high symmetric – disorder transition exhibits such part liquid and part crystalline state in their high temperature superionic phase. A case in point, AgCuTe which undergoes phase transition from hexagonal ($P3m1$) to cubic ($Fm\bar{3}m$) around 460 K show ultra-low κ_{lat} value of 0.2 W/mK at the high temperature superionic phase.¹⁰¹ At room temperature hexagonal phase, the compound comprises of significant chemical bonding inhomogeneity which lowers its room temperature κ_{lat} to ~ 0.35 W/mK. This bonding heterogeneity is accompanied by the soft vibrations of Ag and Te atoms as seen from theoretical phonon calculations. However, on phase transition above 460 K, the structure shifts to cubic $Fm\bar{3}m$ where the Ag^+/Cu^+ are weakly bonded and flows seamlessly through the lattice. These mobile liquid-like Ag^+/Cu^+ ions subdue the phonon mean free path and dampens the heat flow, which is evident from their temperature independent low κ_{lat} of ~ 0.2 W/mK in the temperature range of 450 – 723 K. However, cubic AgCuTe despite of possessing partly liquid state comprising of the cations, it also contains a rigid anionic framework of Te. This rigid Te framework provides a conducive platform for the carriers to flow unhindered which is evident from their relatively superior electrical conductivity, thus approaching a PGEC system. **Chapter 4.3 of part 4** of my thesis involves discussion regarding the low κ_{lat} in part crystalline part liquid AgCuS .

1.3. Application of Low Lattice Thermal Conductive Metal Chalcogenides in Thermoelectric Energy Conversion

In this part we will delve into the practical aspects of having low thermal conductive materials in thermoelectrics. First, we will briefly discuss about what do we mean by thermoelectrics and its relevance in the present scenario, followed by why low lattice thermal conductivity is pivotal to high performing thermoelectrics and finally the other important parameters to optimize to obtain high thermoelectric performance.

1.3.1. Brief Introduction into Thermoelectrics

The advent of technological modernization and improvement in the standard of living has coincided with the burgeoning increase in energy consumption, bulk of which are fulfilled using rapidly dwindling non-renewable energy resources. Overcoming such energy dilemma led to exploration of alternative sustainable energy sources, and thermoelectricity is being increasingly viewed as an essential piece to this energy puzzle.^{20, 21, 62, 102, 103} Thermoelectric material which can generate electricity through a temperature gradient directly (Figure 1.5a), is a clean energy conversion process, whose performance is guided by its figure of merit zT , defined as:¹⁰⁴

$$zT = \frac{\sigma S^2}{\kappa} T \quad (1.1)$$

where, σ , S and T denotes electrical conductivity, Seebeck co-efficient, and absolute temperature respectively, while κ denotes the thermal conductivity of the material. Quest for high performing thermoelectric materials have traditionally relied on either improving the power factor (σS^2) or decreasing the thermal conductivity (κ).

While the phenomenon of thermoelectricity is already 200 years old, as Seebeck first observed it in 1821, the figure of merit equation was defined much later in 1911, with first generation thermoelectric devices having $zT \sim 1.0$ being furnished only in 1950s and 1960s.^{105, 106} This followed by a period of relatively stagnant improvement in this field until 1990s, after which following the new ideas brought forward by Hicks and Dresselhaus, significant breakthroughs have been achieved in this field. The last couple of decades oversaw second and third generation of thermoelectric materials with

efficiency exceeding 15% and is largely due to our improved understanding of the electrical and phonon transport properties.¹⁰⁶

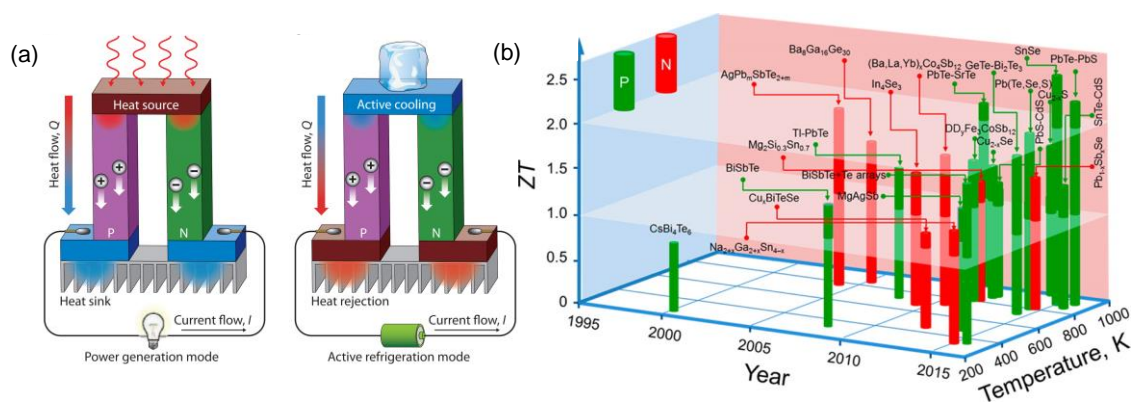


Figure 1.5. (a) Schematic illustrations of a thermoelectric (TE) module for active power generation-Seebeck effect (left) and refrigeration-Peltier effect (right). (b) TE figure-of-merit (zT) as a function of temperature and year illustrating important milestones. (b) Reproduced with permission from ref. 20 © 2016 American Chemical Society.

Band engineering approaches such as band flattening,¹⁰⁷ band convergence,^{108, 109} introduction of resonant levels,^{110, 111} mobility and carrier concentration engineering,^{112, 113} quantum confinement¹¹⁴ etc. has been successfully applied to improve the power factor of a thermoelectric material. While on the other hand, phonon suppressing techniques like point defect/alloy scattering,^{115, 116} introduction of nano-precipitates,^{117, 118} all-scale hierarchical architectures^{119, 120} and intrinsic phonon scattering techniques¹²¹ etc. are also being employed efficiently. The present approaches to engineer high performance thermoelectric material revolve around the simultaneous optimization of both electronic and phonon transport.^{103, 122} With the help of the advanced approaches, rational designing of several state-of-the-art thermoelectric materials have been possible which includes $\text{Bi}_{2-x}\text{Sb}_x\text{Te}_3$,^{118, 123, 124} PbTe ,^{111, 119, 125} SnTe ,^{108, 115, 126} GeTe ,^{41, 127-129} SnSe ,¹³⁰⁻¹³⁴ Clathrates and skutterudites,^{63, 67, 135} half-Heuslers,^{136, 137} Cu_{2-x}Se ^{138, 139} etc., most of which has peak zT values > 2 at high temperatures (Figure 1.5b).

Despite of having made such progress in achieving high thermoelectric figure of merit, the potential application of these materials in thermoelectric energy generators

(TEGs) have somewhat been restricted due to their poor energy conversion efficiency. The power generation efficiency, η , of TEGs is given by:²¹

$$\eta = \frac{T_h - T_c}{T_h} \frac{\sqrt{1 + Z\bar{T}} - 1}{\sqrt{1 + Z\bar{T}} + \frac{T_c}{T_h}} = \varepsilon \frac{\sqrt{1 + Z\bar{T}} - 1}{\sqrt{1 + Z\bar{T}} + \frac{T_c}{T_h}} \quad (1.2)$$

where, T_h , T_c and \bar{T} denotes temperatures of the hot-side, cold-side and average temperature of T_h and T_c respectively. $Z\bar{T}$ of a material is defined as:²¹

$$Z\bar{T} = \frac{\int_{T_c}^{T_h} ZT \, dT}{T_h - T_c} \quad (1.3)$$

The above equation indicates that if a high zT value is achieved over a wide range of temperature, a high average zT ($Z\bar{T}$) can be obtained, and as a consequence an efficient thermoelectric material can be furnished.

1.3.2. Relation Between Low Lattice Thermal Conductivity and Thermoelectric Figure of Merit

One of the customary approaches to high performance thermoelectrics is by reducing the thermal conductivity of the solids.¹⁴⁰ In general, for solids, total thermal conductivity (κ_{tot}) mainly constitutes of three parts, *viz.*, the electronic thermal conductivity (κ_{el}), the lattice thermal conductivity (κ_{lat}), and the bipolar thermal conductivity (κ_{b}). With the aid of Wiedemann–Franz–Lorenz law, $\kappa_{\text{el}} = L\sigma T$, for the electronic thermal conductivity, zT can be re-written as $zT = \frac{S^2}{L} \left[\frac{1}{1 + \frac{\kappa_{\text{lat}} + \kappa_{\text{b}}}{\kappa_{\text{el}}}} \right]$. Here, L is

the Lorenz number, and the values mostly lie in the range of 1.6 to $2.5 \times 10^{-8} \text{ V}^2 \text{ K}^{-2}$. Materials exhibiting low κ_{lat} , and low κ_{b} is paramount in order to achieve high TE performance, while a high κ_{el} augurs well as it corresponds to high power factor.¹⁴ Contributions from κ_{b} comes only at elevated temperatures and in very narrow-gap semiconductors, being almost negligible in room temperature conditions. Thus, exploring new strategies to maximize the suppression of κ_{lat} is crucial for a better TE performance. For bulk materials, $\kappa_{\text{lat}} = \frac{1}{3} C_V v_g^2 \tau$, provides proper description to the lattice thermal conductivity. Thus, to minimize the κ_{lat} , one has to engineer materials which decrease the specific heat (C_V), the group velocity (v_g) or the phonon relaxation time (τ). Typically, in thermoelectrics, the phonon relaxation time is the most focused variable to tweak and

achieve desirable κ_{lat} via extrinsically introducing 0D point defects, 1D dislocations or 2D grain boundaries or fine precipitates (Figure 1.6). Each of these defects enhances the phonon-scattering process and decreases the relaxation time (τ) and thereby decreasing the κ_{lat} .¹⁴¹ Each of the aforementioned processes has their own frequency (ω) dependence. For example, the 0D point defects scatters the high frequency phonons ($\tau_{PD} \sim \omega^{-4}$); 1D dislocation scatters the mid frequency phonons ($\tau_{DC} \sim \omega^{-3}$ for dislocation cores and $\tau_{DS} \sim \omega^{-1}$ for dislocation strains); 2D interface scattering originating from grain boundaries or precipitates are effective for the low frequency phonons ($\tau_{inter} \sim \omega^0$).¹⁴¹ The Umklapp process¹⁴² which is ubiquitous has a relaxation time, $\tau_U \sim \omega^{-2}$, thus being effective in scattering the phonons of all frequencies. Callaway devised a phenomenological model considering all the contributions arising from the microstructural effects on phonon scattering at various length scales.¹⁴³ The model which is given as,^{143, 144}

$$\kappa_{lat} = \frac{k_B}{2\pi^2 v_g} \left(\frac{k_B T}{\hbar} \right)^3 \int_0^{\theta_D/T} \tau_C(x) \frac{x^4 e^4}{(e^x - 1)^2} dx \quad (1.4)$$

acts as a guide to quantitatively access the contributions arising from each microstructural effect. k_B in equation (1.4) corresponds to Boltzmann's constant; \hbar , T and τ_C denotes Plank's constant, absolute temperature and total relaxation time respectively. τ_C corresponds to the individual relaxation time via the relation $\tau_C^{-1} = \tau_U^{-1} + \tau_{PD}^{-1} + \tau_{DS}^{-1} + \tau_{DC}^{-1} + \tau_{inter}^{-1} + \dots$, where τ_U , τ_{PD} , τ_{DS} , τ_{DC} and τ_{inter} corresponds to relaxation times arising from the contributions of Umklapp scattering, point defects, dislocation strain, dislocation cores and interface scattering respectively.

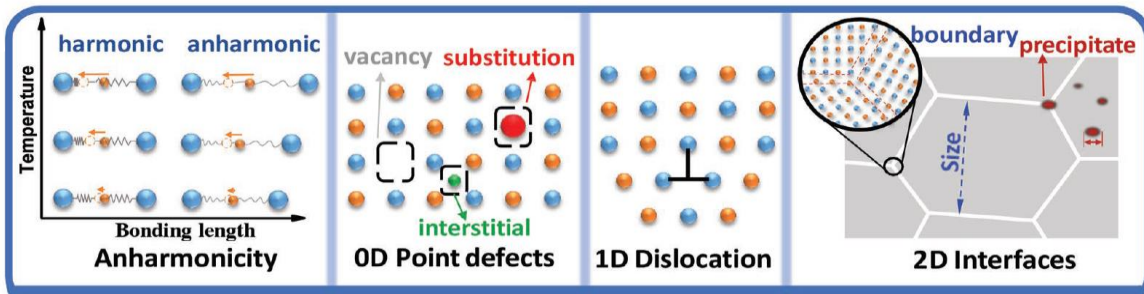


Figure 1.6. A simple schematic to explain the various routes to suppress κ_{lat} in the crystal system. Reproduced with permission from ref. 141 © 2018 John Wiley and Sons.

Apart from the extrinsic approaches to reduce the thermal conductivity, rational unearthing of materials with intrinsically low lattice thermal conductivity is an intriguing

and efficient prospect. Since electrons and phonons propagate within the same sublattice, suppressing the phonon transport also handicaps the electron mobility. Thus materials with innate κ_{lat} offer an independent control to achieve high TE performances without having to compromise on the electrical mobility which is beneficial in maintaining high power factor.¹²¹ The factors which influences intrinsic lowering of κ_{lat} are explained in section 1.2.

1.3.3. Additional Factors to Improve Thermoelectric Figure of Merit

From equation (1.1) it is clear that improving zT can also be achieved by improving the power factor (σS^2) of a material. Power factor (σS^2) is a purely electronic property, governed by materials' electronic structure and scattering mechanism. Strategies to enhance power factor include: a) engineering of carrier-concentration (n_H) through chemical doping,¹⁴⁵ b) enhancement of the effective carrier mass (m^*) and Seebeck coefficient (S) via the convergence of multiple valence/conduction band extrema,^{109, 110, 146} or distortion of the density of states near Fermi level by resonance impurity levels,^{111, 126, 147, 148} and c) enhancement of carrier mobility (μ) by modulation-doping.^{149, 150} Here, I will summarize the most recent approaches of designing high-performance Thermoelectric materials.

1.3.3.1. Carrier Concentration Optimization

The fundamental challenge of designing high zT thermoelectric materials is strong interdependence of σ , S and κ through carrier concentration, n (Figure 1.7) which can be optimized by controlling the doping level. The maximum zT value arises in the carrier concentration range of 10^{19} - 10^{21} cm^{-3} , which falls in between metals and semiconductors - that is concentration typically found in heavily doped semiconductors (i.e. degenerate semiconductor).¹⁵¹ However, carrier concentration (n_H) increases rapidly with rising temperature, following the power law of $T^{3/2}$. Although conventional doping is effective to tune room temperature carrier optimization, it is difficult to achieve optimum carrier concentration at high temperature. Thus, the maximum theoretical zT cannot be fully realized at every working temperature. An effective solution to this issue is the use of

functionally graded doping, by integrating two or multiple segments with dissimilar n_H . The modifications to the conventional doping method to include temperature-dependent doping behaviour are helpful to acquire larger average zT values which are especially important for technological applications.

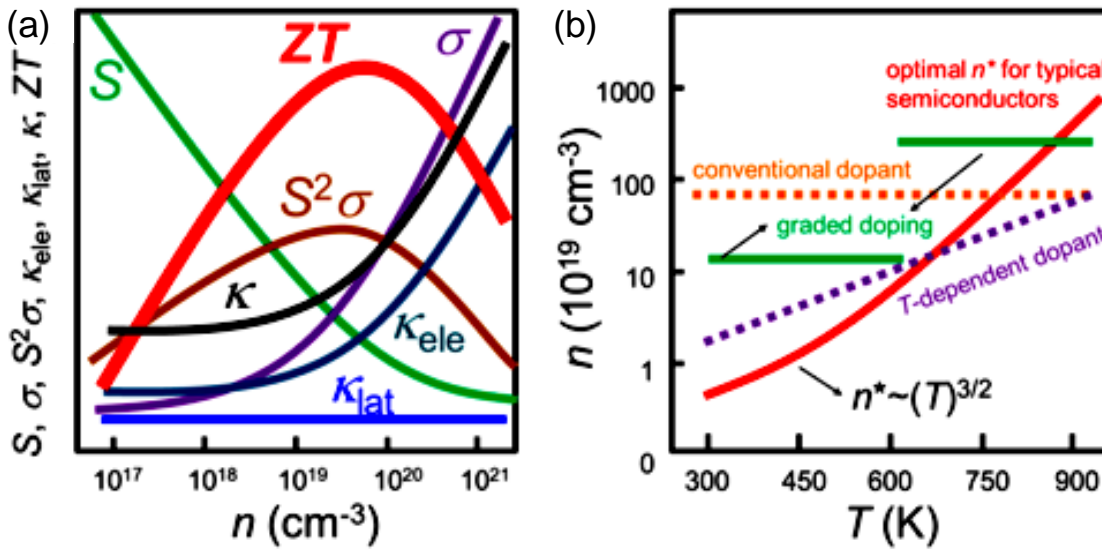


Figure 1.7. (a) Schematic diagram showing the dependence of ZT ($\sim zT$) and its parameters (electrical conductivity σ , Seebeck coefficient S , power factor $S^2\sigma$, electronic thermal conductivity κ_{el} , lattice thermal conductivity κ_{lat} and total thermal conductivity, κ) on carrier concentration n . (b) Strategies for stabilizing the optimal carrier concentration. Reproduced with permission from ref. 20 © 2016 American Chemical Society.

1.3.3.2. Resonance Level

The concept of resonance level was first proposed in 1950.¹⁵² Resonance level originates from the coupling between electrons of a dilute impurity with those of the valence or conduction band of the host solid near its Fermi level.¹⁵³ Thus, resonance dopant creates an excess density of states near the valence or the conduction band edge of the host compound (Figure 1.8a) and results in higher effective mass, m^* and thereby enhances Seebeck coefficient, according to Mott expression (Equation 1.15).¹⁴

$$\begin{aligned}
 S &= \frac{\pi^2}{3} \frac{k_B}{q} k_B T \left\{ \frac{d[\ln(\sigma(E))]}{dE} \right\}_{E=E_F} \\
 &= \frac{\pi^2}{3} \frac{k_B}{q} k_B T \left\{ \frac{1}{n_H} \frac{dn_H(E)}{dE} + \frac{1}{\mu} \frac{d\mu(E)}{dE} \right\}_{E=E_F} \quad (1.5)
 \end{aligned}$$

Here, $\sigma(E)$ is the electrical conductivity determined as a function of the band filling or Fermi energy, E_F ($\sigma(E) = n_H(E)q\mu(E)$) and $n_H(E)$ ($n_H(E) = g(E)f(E)$), the carrier density at the energy level, E (here q is the carrier charge, and $\mu(E)$ is the mobility as a function of energy, $f(E)$ is the Fermi function, $g(E)$ is density of state).

When electronic scattering is independent of energy, $\sigma(E)$ is just proportional to the density of states (DOS) at E . Based on the above expression it is clear that the system with rapid change in DOS near E_F is expected to have large Seebeck. Pisarenko plot represents the dependence of Seebeck on carrier concentration. A significantly higher S value than what a Pisarenko plot gives the indication of resonance level formation (Figure 1.8b).¹¹¹ Group-III (mainly Al, In and Tl) dopants form resonance level in PbTe.¹⁵³ Heremans, *et. al.*, demonstrated experimentally that Tl doping improves S of PbTe by resonance level formation and thereby achieved the double value of zT , as seen in Figure 1.8c.¹¹¹

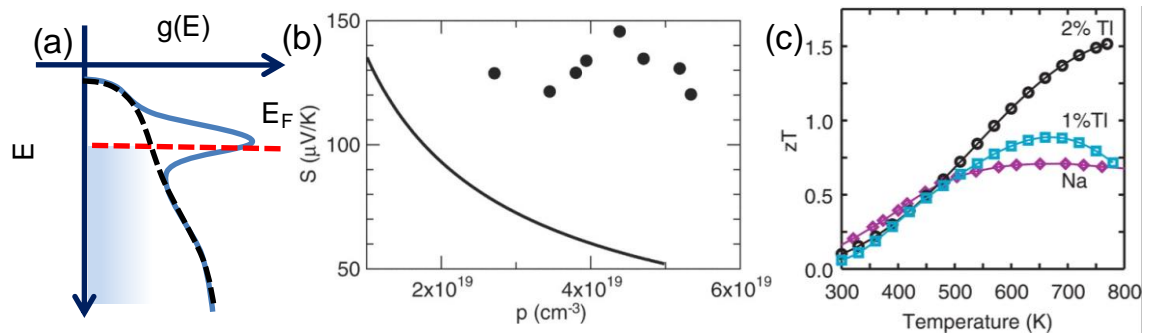


Figure 1.8. (a) Schematic diagram of resonance level in the valence band. Schematic diagram of density of state (DOS) of the valence band of pristine sample (dotted black line). Tl-doped PbTe shows asymmetric distortion of DOS (blue line) near Fermi level. (b) Pisarenko relation of Seebeck coefficient vs hole concentration, p for PbTe (solid line) at 300 K compared to the results on Tl-PbTe sample. Significantly large S value in Tl-doped PbTe confirmed the presence of resonance level. (c) The temperature dependent zT values for $Tl_{0.02}Pb_{0.98}Te$ (black circles) and $Tl_{0.01}Pb_{0.99}Te$ (blue squares) compared to that of a reference sample of Na-PbTe (purple diamonds). Figure 1.8 is taken from ref. 150 which obtained copyrights from ref. 111.

1.3.3.3. Band Convergence

Multiple pockets in valence or conduction band extreme give rise to high Seebeck coefficient because these valleys (separate pockets of Fermi surface with the same

energy) have the effect of producing large effective mass (m^*) without explicitly reducing μ , as seen in equation 1.6.^{109, 110, 146}

$$m^* = N_V^{2/3} m_b^* \quad (1.6)$$

Where N_V represents orbital degeneracy and m_b^* represents single valley density of state effective mass of degenerate valleys. Thus, effective doping to energetically align the electronic bands for a higher degree of band degeneracy lies at the core of the band-convergence scheme. The aim is to enhance the Seebeck coefficient without substantially degrading the σ . When the system is heavily doped, overall effective mass can be enhanced through carrier redistribution to multiple valleys, thus results in high Seebeck coefficient. Since carrier mobility will be unaffected in this process, valence band convergence gives rise to significantly high σS^2 and zT in carrier optimized system.

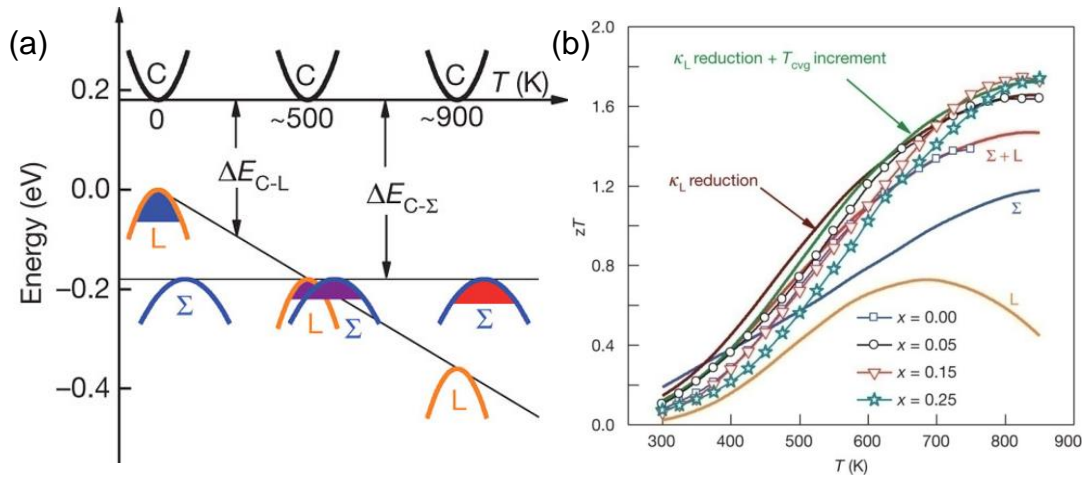


Figure 1.9. (a) Relative energy of the valence bands in $PbTe_{0.85}Se_{0.15}$. At, 500 K the two valence bands converge, resulting in contributions from both the L and Σ bands in the transport properties. (b) Temperature dependent zT of $p-PbTe_{1-x}Se_x$ materials doped with 2 atom % Na. Reproduced with permission from ref. 109 © 2011 Nature Publishing Group.

Pei *et al.* have demonstrated the band convergence of at least 12 valleys in doped $PbTe_{1-x}Se_x$ alloys, leading to an extraordinarily high zT value of 1.8 at about 850 K, as seen in Figure 1.9.¹⁰⁹ Alloying Se reduces the energy difference between the L and Σ bands of the PbTe making the two bands effectively converged. Hence enhancement in N_V from 4 (for L band) to 12 (for Σ band) results in an increase in m^* and Seebeck. A

similar result was observed in PbTe, after it was alloyed with wide band gap chalcogenides (MgTe, CaTe, BaTe).

Recently, an innovative strategy of slight-symmetry reduction has been adopted to realize band convergence in GeTe. Detailed electronic structure analysis of GeTe demonstrate that rhombohedral distortion of GeTe along the [111] crystallographic direction (along the L point of BZ) splits up the 4 L pockets of cubic GeTe ($Fm\bar{3}m$) into 3 L + 1 Z pockets in rhombohedral GeTe ($R3m$) and 12 Σ pockets of cubic GeTe into 6 Σ + 6 η pockets in rhombohedral GeTe.^{129, 154} Thus manipulation of the degree of the rhombohedral distortion (also referred as slight symmetry reduction) can result in band convergence of L and Σ bands. In a recent report by Li *et al.*, it has been shown that slight symmetry reduction of cubic GeTe towards rhombohedral symmetry by Pb and Bi doping causes an effective valence band (L and Σ bands) convergence, resulting in a high zT of ~ 2.4 in rhombohedral phase of Pb and Bi codoped GeTe at 600 K.^{129, 154}

1.4. Experimental Methods

1.4.1. Synthesis

The successful utilization of thermoelectric devices depends critically on the synthesis techniques. A great majority of chalcogenides known to date have been synthesized by sealed-tube reactions in vacuum (10^{-3} - 10^{-5} Torr) either by employing high-temperature melt cooling or alkali metal polychalcogenide fluxes A_2Q_n ($Q = S/Se/Te$) at low temperatures. In high temperature vacuum sealed tube melting reaction, appropriate quantities of starting materials (mostly in their elemental form) are heated above the melting point of the desired product in absence of air, followed by cooling of the subsequent reaction mixture at a specific cooling speed depending upon material's nature (congruent/incongruent). Products of the reactions are generally thermodynamically stable polycrystalline or single-crystalline ingots.

For single and highly oriented crystals, one of the common approaches is to use the vertical Bridgman technique. The core principle behind the Bridgman method is the directional solidifying of the compounds by translating the compound from a hot zone where it has been kept above the melting temperature to a cold zone of the furnace which is below the melting temperature of the compound. Initially the polycrystalline material

in a tapered shaped high vacuum sealed ampoule is melted fully in the hot zone and then slowly translated towards the cold zone with a speed of ~ 1 mm/hr. Single crystal generally starts to grow along a certain direction once it starts to solidify from the pointed portion of the tapered ampoule. Sometimes a seed of the single crystal with specific orientation is kept at the bottom of the crucible from where the crystal growth starts. My thesis involves use of both furnace melting and Bridgman technique for material synthesis.

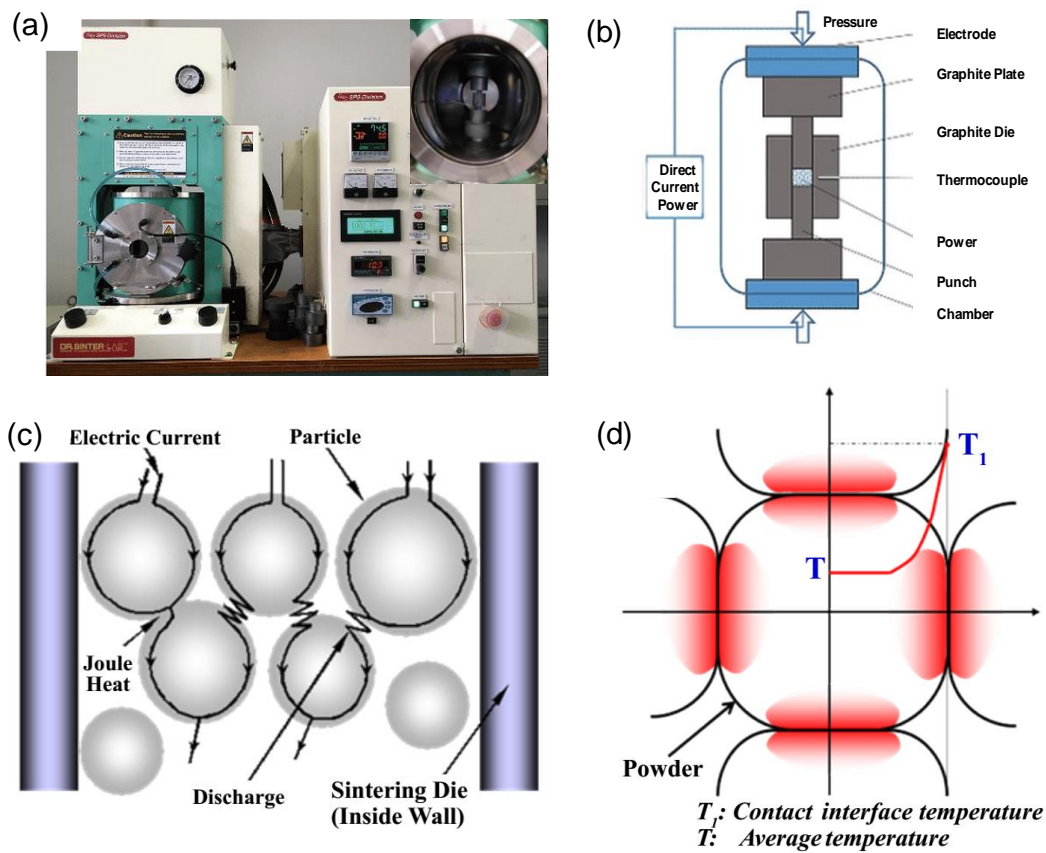


Figure 1.10. (a) Photograph of SPS-211Lx instrument. The inset image shows sintering chamber. (b) Schematic illustration of a spark plasma sintering equipment. (c) Possible electric current path through powder particles inside the die. (d) The temperature image on powder particles surface. Contact surface temperature (T_1) differs significantly from average temperature (T).¹⁵⁷

The Spark plasma sintering (SPS) is newly developed technique for the syntheses and processing of thermoelectric materials employing ON-OFF pulse DC voltage / current (Figure 1.10).¹⁵⁵⁻¹⁵⁷ This is considered as an energy-saving sintering technology

due to its short processing time and a small number of processing steps. The SPS process is based on the electrical spark discharge phenomenon. Application of a high energy, low voltage spark pulse (spark discharge) momentarily produces a local high temperature state (several to ten thousand degree) in the gap between the particles of a material *via* joule heating (Figure 1.10c, d). This results in vaporization and melting of the powder particles' surfaces and formation of constricted shapes or "necks" around the contact area between the particles. These constricted shapes gradually develop and plastic transformation progresses during sintering, resulting in a sintered material with density of $\geq 97\%$. By application of voltage and current repeatedly with this ON-OFF, the discharge point and the Joule heating point (locally high-temperature generation field) move throughout the sample, resulting in less power consumption and efficient sintering. Since only the surface temperature of the particles rises rapidly by self-heating, particle growth of the starting powder materials is controlled. Therefore, a precision sintered compact is manufactured in a shorter time. At the same time, bulk fabrication of particles with an amorphous structure and crystalline nanostructure formation are now possible without changing their characteristics. Vaporization, melting and sintering are completed in short periods of approximately 5-20 minutes, including temperature rise and holding times. SPS sintering temperatures range from low to over 2000 °C which are 200-500 °C lower than with conventional sintering.

In order to prepare high performance thermoelectric materials, we have done spark plasma sintering (SPS) of the melt grown ingots in SPS-211Lx, Fuji Electronic Industrial Co., Ltd (Figure 1.10a). The SPS process and geometrical configuration of the punches, mould and powder are illustrated in Figure 1.10. Powders to be consolidated, are placed in a die and heated by applying the electric current. The melt grown ingots were first ground into fine powders using a mortar and pestle to reduce the grains size in an inert glove box. This powder was then pressed into cylindrical shape by SPS method (SPS-211Lx, Fuji Electronic Industrial Co., Ltd.) at specific temperature and pressure under vacuum (Figure 1.10a). Highly dense ($\sim \geq 98\%$ of theoretical density) disk-shaped pellets with ~ 10 mm diameter and ~ 10 mm thickness were obtained.

1.4.2. Characterizations

I have used the following characterization techniques for my thesis works.

1.4.2.1. Powder X-ray Diffraction (PXRD)

Powder X-ray diffraction is the most commonly used technique in solid state inorganic chemistry and has many uses from analysis and assessing phase purity to determining the structure. In this thesis, lab source X-ray have been used for structural characterization. In the laboratory, X-rays are generated in a cathode tube. In this technique, a tungsten filament was heated to produce electrons and electron beam was then accelerated towards an anode by applying a voltage ($\sim 30 - 40$ kV). When electrons have sufficient energy to dislodge inner shell electrons of the target material, characteristic X-ray spectra are produced. These spectra consist of several components, the most common being $K\alpha$ and $K\beta$. $K\alpha$ consists, in part, of $K\alpha_1$ and $K\alpha_2$. $K\alpha_1$ has a slightly shorter wavelength and twice intensity than $K\alpha_2$. The specific wavelengths are characteristic of the target material (Cu, Fe, Mo, Cr). Cu is the most common target material use for laboratory X-ray. To produce monochromatic X-rays, it is required filtering out $K\beta$ radiation by foils or crystal monochromators. For Cu radiation, a sheet of Ni foil is a very effective filter, but it is difficult to remove $K\alpha_2$ from $K\alpha_1$ because of close wavelength. The filtering process in laboratory X-ray leads to a reduction in intensity and hence it is difficult to detect low-intensity peaks in laboratory X-ray diffraction. In addition, it is difficult to distinguish peak splitting when peaks appear closely.

X-ray diffraction obeys Bragg's law, which states that constructive interference would occur if the path difference between the X-rays scattered from parallel planes were an integer number of the wavelength of radiation. If the planes of atoms, separated by a distance d , make an angle θ with the incident beam, then the path difference would be $2d\sin\theta$. So, for constructive interference, the Braggs law must be satisfied

$$\text{i.e. } n\lambda = 2d\sin\theta, n = 1, 2, 3, \quad (1.7)$$

λ = wavelength of the X-ray radiation

In this thesis, room-temperature PXRD experiments on the samples are carried out using Bruker D8 diffractometer and Rigaku SmartLab SE. High temperature PXRD experiments were done Rigaku using Smart-lab X-ray diffractometer using Cu- $K\alpha$

radiation having wavelength 1.5406 Å. Samples were placed on a glass plate sample holder during measurement.

1.4.2.2. X-ray Pair Distribution Function (PDF)

Pair distribution function (PDF) analysis is a powerful technique for probing atomic-scale disorder that cannot be detected using traditional diffraction methods.¹⁵⁸ Unlike other crystallographic methods, PDF analysis is a total scattering technique, which means that both Bragg and diffuse scattering are included. The PDF reveals both the long-range periodic structure (Bragg reflections) and the local structure imperfections (diffuse component of the diffraction pattern).¹⁵⁸

Temperature dependent X-ray PDF data was collected using finely ground powder in beamline P02.1, PETRA III, DESY, Hamburg. Synchrotron beam of fixed energy (energies are given at respective chapters) and spot size 0.5 X 0.5 mm² was used to collect data.¹⁵⁹ From the coherent part $I^{coh}(Q)$ of the measured total diffracted intensity of the material, the total scattering structure function, $S(Q)$, is obtained as

$$S(Q) = \frac{I^{coh}(Q) - \sum c_i |f_i(Q)|^2}{|\sum c_i f_i(Q)|^2} + 1 \quad (1.8)$$

where the coherent intensity is corrected for background and other experimental effects and normalized by the flux and number of atoms in the sample. Here c_i and f_i are the atomic concentration and X-ray atomic form factor, respectively, for the atomic species of type i . The momentum transfer, Q , is given by:

$$Q = 4\pi \sin\theta/\lambda \quad (1.9)$$

Via Fourier-transforming the expression $Q[S(Q)-1]$, we obtain:

$$G(r) = \frac{2}{\pi} \int_0^\infty Q[S(Q) - 1] \sin Q(r) dQ \quad (1.10)$$

Where $G(r)$ is the atomic pair distribution function, which is also defined as:

$$G(r) = 4\pi r[\rho(r) - \rho_0] \quad (1.11)$$

Where ρ_0 is the average atomic number density, $\rho(r)$ is the atomic pair density, and r is a radial distance. The function $G(r)$ gives information about the number of atoms in a spherical shell of unit thickness at a distance r from a reference atom. Finally, the experimental $G(r)$ can be compared and refined against the theoretical $G(r)$ from a structural model, given by:

$$G(r) = 4\pi r \rho_0 = \frac{1}{r} \sum_v \sum_\mu \frac{f^{(0)}_v f^{(0)}_\mu}{\langle f^{(0)} \rangle^2} \delta(r - r_{v\mu}) \quad (1.12)$$

2D image plate data was collected using a Perkin-Elmer detector which was processed using Fit2D or DAWNSci¹⁶⁰ software to obtain the scattering intensities $S(Q)$ in the Q-space. The pair distribution $G(r)$ was then obtained by Fourier transformation of the scattering structure function $F(Q) = Q[S(Q) - 1]$ using PDFgetX2¹⁶¹ or PDFgetX3¹⁶² software. Finally, the modelling and refinement of $G(r)$ was done using the software PDFgui.¹⁶³

1.4.2.3. Inelastic Neutron Scattering (INS)

Inelastic neutron scattering (INS) is a spectroscopic technique, widely used in solid state chemistry and condensed matter physics and is primarily based on analysing the energy of neutrons before and after they have been scattered by a material. The main measurable quantity is the energy change of the incident radiation, reflecting an excitation of the material under investigation. Typically, energy transfer of several meV takes place, which arises due to the atomic vibrations. Thus, INS gives an amplitude-of-motion and neutron incoherent cross section weighted phonon density of states. INS is used to characterize chemical bonds in both bulk as well as on the surface of a material.

In solid state chemistry and condensed matter physics, using neutron as a probe as a significant advantage as it can be used to measure the nature of atomic and molecular motions through INS, in which the neutron exchanges energy with the atoms in a material. When an incident neutron is scattered by a crystalline solid, it can either absorb or release an amount of energy equal to a quantum of phonon energy, $h\nu$. This gives rise to inelastic coherent scattering in which the neutron energy before and after the scattering differ by an amount, $h\nu$ (*i.e.*, energy transfer). In most solids ν is a few meV. Because neutrons used for INS also have energies in the meV range, scattering by a phonon causes an appreciable fractional change in the neutron energy, allowing accurate measurement of phonon frequencies. For INS, the neutron has different velocities, and thus different wavevectors, before and after it interacts with the sample. To determine the phonon energy and the scattering vector, Q , one need to determine the neutron wavevector before (k_i , i = initial) and after (k_f , f = final) the scattering event. Several different methods are

available but for our measurement we have used Time-Of-Flight neutron spectrometer at the ISIS pulsed neutron source (Figure 1.11).

The advantage of INS compared to the related Raman scattering (*i.e.*, inelastic photon scattering) and infrared spectroscopies (IR absorption and reflectivity) is its independence on optical selection rules.¹⁶⁴ Moreover, phonons (lattice vibrations) in metals cannot readily be detected by IR techniques,¹⁶⁵ and Raman scattering from metals is weak due to the screening of electromagnetic radiation by quasi-free electrons.¹⁶⁴ In contrast, neutrons do not interact with electrons and sample the entire Brillouin zone (different k -vector and momentum transfer), while Raman and IR are restricted to the zone center (Γ -point). INS is particularly sensitive at low energy transfers, which is difficult for infrared spectroscopy.

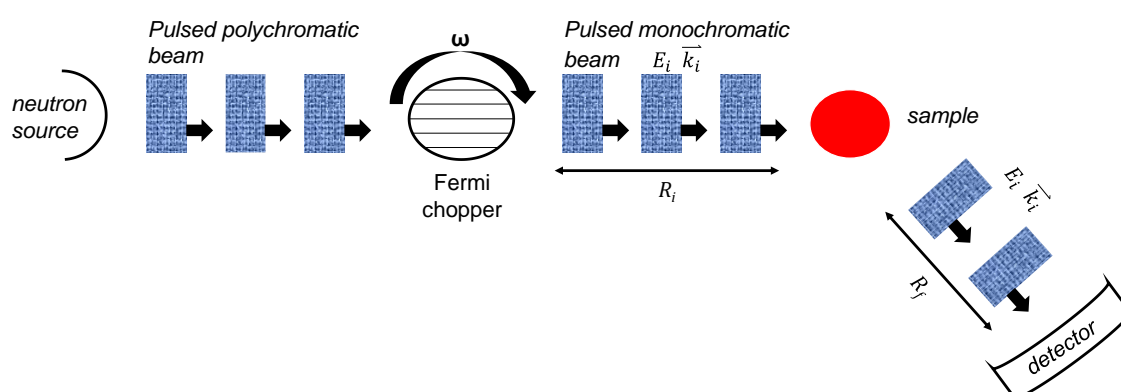


Figure 1.11. Schematic of the Time-of-Flight neutron spectrometer. Here the incident neutron energy is selected by the rotation frequency ω of the Fermi chopper (which consists of curved neutron-absorbing blades) and its phase delay relative to the source emission. The final energy can be computed from the time of arrival of the scattered neutron pulse at the detector.

1.4.2.4. Raman Spectroscopy

Raman spectroscopy is one of the vibrational spectroscopic techniques used to provide information on molecular vibrations and crystal structures. This technique is based on inelastic scattering of monochromatic light. A change in the molecular polarizability with respect to the vibronic coordinate is required for a molecule to exhibit Raman effect. Normally, a laser source Nd-YAG with a fixed wavelength of 532 nm, an Argon ion laser source at 514 nm or He-Ne laser at 633 nm is used as light source. The

laser light interacts with molecular vibrations, phonons or other excitations in the system, resulting in the energy of the laser photons being shifted up or down. The shift in energy gives information about the vibrational modes in the system. Low temperature Raman spectroscopic measurements were carried out on pellet shaped samples using Horiba Jobin-Yvon LabRAM HR evolution Raman spectrometer with 1800 gr/mm and Peltier cooled CCD detector.

1.4.2.5. Transmission Electron Microscope (TEM)

TEM is one of the important tools in material science for characterization of the microscopic structure of materials. A TEM image represents a two-dimensional projection of a three-dimensional object. TEM operates on the same basic principles as the light microscope, however, uses electrons as “light source” that makes it possible to get a resolution of about thousand times better than a visible light microscope. Instead of glass lenses focusing the light in the light microscope, the TEM uses electromagnetic lenses to focus the electrons into a very thin beam. The electron beam then travels through the specimen you want to study. When the electron beam passes through an ultra-thin specimen, it gets absorbed or diffracted through the specimen. Some of the electrons are scattered and disappear from the beam depending on the density of the material present on the focused region. A “shadow image” is formed by the interaction of the electrons transmitted through the specimen focused onto a fluorescent screen or a photographic film or by a sensor such as a charge-coupled device (CCD). TEM study allows to focus electron beam to any part of specimen and electron diffraction data from a different area of the specimen can give us more details about the accurate local structure of the sample. The details of TEM instrument where used are given in the respective chapter.

1.4.2.6. Field Emission Scanning Electron Microscope (FESEM)

A FESEM is used to visualize topographic details of the sample surface. Similar to TEM, FESEM microscope also uses electrons as a light source. Electrons are ejected from a field emission source and accelerated in a high electrical field gradient. These electrons (termed as primary electrons) produce a narrow scan beam within the high vacuum column, which bombards the sample material. The incident electrons cause

emission of electrons from the sample due to elastic and inelastic scattering. The angle and velocity of these secondary electrons produced by inelastic collision of accelerated electrons with sample atoms relate to the surface structure of the object. High-energy electrons those are produced by an elastic collision of a primary electrons with atom's nucleus of the sample are termed as backscattered electrons (BSE). Larger atoms (with a high atomic number, Z) have a higher chance of producing elastic collisions because of their greater cross-sectional area. Thus, a "brighter" BSE intensity correlates with higher average Z in the sample, and "dark" areas have lower average Z . BSE images are very helpful for obtaining high-resolution compositional maps of a sample. The details of FESEM instrument where used are given in the respective chapter.

1.4.2.7. Energy Dispersive X-ray Analysis (EDAX)

EDAX is an analytical technique used for elemental composition analysis of the sample. EDAX makes use of the X-ray spectrum emitted by a solid sample bombarded with a focused beam of electrons. For EDAX analysis, an X-ray detector is generally integrated with FESEM instrument. Its characterization capabilities are due in large part to the fundamental principle that each element has a unique atomic structure allowing a unique set of peaks on its electromagnetic emission spectrum. In my Ph.D., FESEM images in back scattered electron (BSE) mode and normal mode were taken using ZEISS Gemini attached to JEOL (JEM2100PLUS) FESEM instrument.

1.4.2.8. Positron Annihilation Spectroscopy (PAS)

PAS is a nondestructive nuclear solid state technique commonly used for defects and voids study in materials. It is a powerful technique to study open volume defects like dislocation, agglomerates, and vacancies at ppm concentration. Positrons (e^+) is an antiparticle of the electron (e^-) having exactly equal rest-mass of the electron (511 keV) but with a positive charge. One can obtain positrons from the β^+ decay of radioactive isotopes such as ^{22}Na , ^{64}Cu , and ^{58}Co . In my work, $^{22}\text{NaCl}$ has been used as positron source. Positrons injected from a radioactive source get thermalized within 1-10 ps and annihilate with a nearby electron inside the material, normally (379 out of 380 cases) emitting two exactly opposite 511 keV gamma rays, in the center of mass frame.

The positron lifetime is inversely proportional to the electron density at the annihilation site. Hence by measuring the positron lifetime (sub nano-second) one can study the electron density distribution in the studied material. Naturally, the lifetime of positrons annihilated at defects is larger compared to the annihilation of positron in the bulk of the material, since the electron density is lower at such defects and positrons survive relatively longer time before annihilation. Therefore, the measured positron lifetime at defects indicates the nature and type of the open volume and the corresponding intensity (weight of that particular lifetime in the overall spectrum) represents the relative abundance of such defect sites in the studied material.

The other PAS technique is to measure the Doppler broadening of the electron-positron annihilated γ -ray (511 keV) line shape (DBEPARL) with a high purity germanium (HPGe) detectors. The basic concept is that although before annihilation positrons are thermalized but the electron has some energy and the corresponding momentum is p_{el} . Thus, the electron-positron pair has some momentum which is translated as a Doppler shift to the 511 keV γ -rays by an amount ($\pm \Delta E = p_L c/2$) in the laboratory frame, where p_L is the component of p_{el} along the direction of measurement. Contributions from all possible p_{el} s are convoluted in the DBEPARL spectrum which looks like an inverted parabola with the centroid at 511 keV ($p_{el} = 0$). The region close to the centroid is formed due to positron annihilation with very low momentum electrons. In the open volume defects, it is more probable for a positron to find a nearly free electron ($p_{el} \sim 0$), the wave function of which are spatially extended. The core electron wave functions are localized and do not span inside the open volumes. Therefore, a more sharpened DBEPARL spectrum represents sample with high concentration of open volume defects. The wing region of DBEPARL spectrum (away from centroid with a higher value of p_L) carries the information about the annihilation of positrons with the core electrons (which are element specific). De-convolution of DBEPARL spectrum is not straightforward thus ambiguous and in general, a simple methodology is adopted to understand the element specific changes in the wing region of the spectrum. Area-normalized DBEPARL spectrum of a high purity material, either Al, Si single crystal or a single crystal of the respective material is recorded in the same detector assembly. The ratio of counts at each energy is taken and the so-called “ratio curve” is formed. The peak

and dip positions in this ratio curve represent more or less annihilation (respectively) with the electrons of nearby momentum region. The Compton continuum of 1276 keV gamma ray, simultaneously emitted with a positron from the ^{22}Na radioactive source, enhances the background counts in the wing region of the spectrum and thereby blurred the peak or dip shapes as well as positions. Two HPGe detector in coincidence successfully suppresses this Compton continuum and the chemical sensitivity of ratio curves with high precision can be achieved. In general, defects modify the local electronic configuration and hence, an intimate relationship is found between PAS parameters (PAL and DBEPARL) and electronic properties of a material.^{166, 167} The experimental details about the positron annihilation spectroscopy have been given in the relevant chapter.

1.4.2.9. Optical Bandgap

In my thesis work, the diffuse reflectance method has been used for the determination of band gap of the solid powdered materials. Diffuse reflectance is an excellent sampling tool for powdered crystalline materials. When light shines onto a powder sample, two types of reflections can occur. Some of the light undergoes specular reflection at the powder surface. Diffuse reflection happens when radiation penetrates into the sample and then emerges at all the angles after suffering multiple reflections and refractions by sample particles. A diffuse reflection accessory is designed to minimize the specular component. To estimate optical energy difference between the valence band and conduction band, optical diffuse reflectance measurements have been done with finely ground powder at room temperature using FT-IR Bruker IFS 66V/S spectrometer and Perkin-Elmer Lambda 900, UV/Vis/NIR spectrometer. Absorption (α/Λ) data were estimated from reflectance data using Kubelka–Munk equation:

$$\alpha/\Lambda = (1-R)^2 / (2R) \quad (1.13)$$

where R is the reflectance, α and Λ are the absorption and scattering coefficients, respectively. The energy band gaps were derived from α/Λ vs E (eV) plots.

1.4.2.10. Differential Scanning Calorimetry (DSC)

DSC is a thermo-analytical technique in which the difference in the amount of heat required to increase the temperature of a sample and reference is measured as a

function of temperature. Both the sample and reference are maintained at nearly the same temperature throughout the experiment. The basic principle underlying this technique is that when the sample undergoes any physical transformation such as phase transition, melting etc, amount of heat flow required to maintain both of them at the same temperature will be different. When the amount of heat required for the sample is lesser than the reference, the process is termed as exothermic. Endothermic process requires a higher amount of heat flow to maintain the temperature. By observing the difference in heat flow between the sample and reference, differential scanning calorimeters are able to measure the amount of heat absorbed or released during such transitions.

DSC data were collected using TA INSTRUMENT Differential Scanning Calorimeter (DSC Q2000) in N₂ atmosphere. The temperature range has been given in the relevant chapter.

1.4.2.11. Hall Effect

The Hall effect describes the behavior of the free carriers in a semiconductor when applying an electric as well as a magnetic field along the perpendicular direction.¹⁶⁸ Thus, measurement of the Hall voltage is used to determine the type of charge carrier present in the system, the free carrier density and the carrier mobility. When a current-carrying semiconductor is kept in a magnetic field, the charge carriers of the semiconductor experience a force in a direction perpendicular to both the magnetic field and the current. At equilibrium, a voltage appears at the semiconductor edges. The ratio of the induced voltage to the product of the current density (I/t , where I is applied current and t is sample thickness) and the applied magnetic field (B) is defined as Hall coefficient (R_H) (Equation 1.14 and 1.15).

$$R_H = \frac{Vt}{IB} \quad (1.14)$$

$$n_H = \frac{1}{R_H e} \quad (1.15)$$

where, e is the charge of an electron (1.602×10^{-19} C). In this thesis Hall measurement has been done in an inhouse equipment developed by Excel instrument. We have used a four-contact Hall-bar geometry and a varying magnetic field up for the measurements.

1.4.3. Thermoelectric Measurements

1.4.3.1. Electronic Transport

The power factor of the zT expression depends on the product of the Seebeck coefficient and the electrical conductivity. The Seebeck coefficient is the ratio of a resulting electric field gradient to an applied temperature gradient. In a typical measurement, the temperature is varied around a constant average temperature and the slope of the voltage (V) vs. temperature difference (ΔT) curve gives the Seebeck coefficient (the slope method) or just $V/\Delta T$ is measured (single point measurement). Either a specific temperature difference is stabilized before each measurement (steady-state), which takes longer, or measurements are conducted continuously while the temperature difference is varied slowly (quasi-steady-state). Little difference was found between steady-state and quasi-steady-state measurements when good thermal and electrical contact is ensured. The employed temperature difference should be kept small, but too small will lead to decreased accuracy. Usually, 4 - 20 K (or 2 - 10 K) is appropriate for the full temperature span.

In the present thesis, temperature dependent Seebeck coefficient measurement has been done using the most popular commercial instruments ULVAC ZEM 3 RIKO using off-axis 4-point geometry under low-pressure helium (He) atmosphere (Figure 1.12a) and Linseis LSR-3. In the off-axis, 4-point geometry, the thermocouples, and voltage leads are pressed against the sides of the sample (Figure 1.12b). The instrument uses slope method to extract the Seebeck coefficient from steady-state measurements. In the slope method, the measured raw data is corrected for constant offset voltages by using the slope of several (ΔT , V) points for extracting the Seebeck coefficient. The typical sample for measurement has a rectangular shape with the dimensions of $\sim 2 \text{ mm} \times 2 \text{ mm} \times 8 \text{ mm}$ and ΔT values 5, 10, 15 K have been used in the measurement. The error in the measurement is $\sim 5\%$. In a typical measurement, the sample is set in a vertical position between the upper and lower electrode blocks in the heating furnace. For temperature dependent measurement, the sample was first heated to a specified temperature using an infrared (IR) furnace. Thereafter a temperature gradient across the sample was created by heating the lower part of it by a heater. Seebeck coefficient is measured by measuring the

upper and lower temperatures T_1 and T_2 with the thermocouples pressed against the side of the sample, followed by measurement of voltage (ΔV) between the same wires on one side of the thermocouple.¹⁶⁹

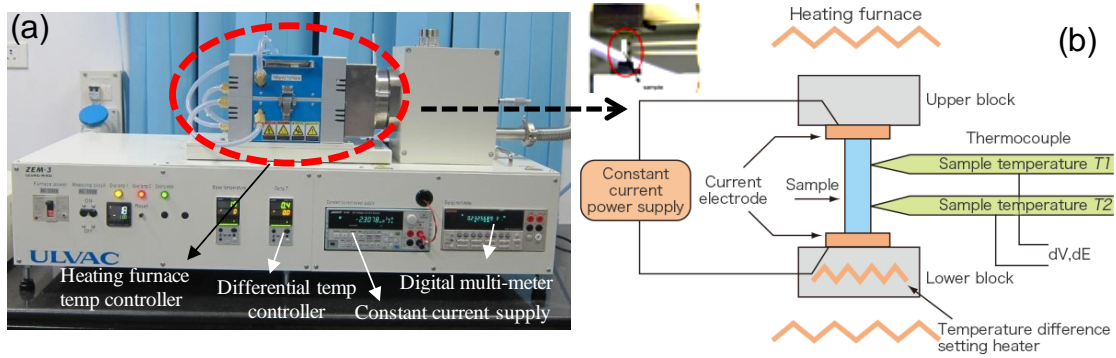


Figure 1.12. (a) Photograph of sample-chamber in ULVAC-ZEM3 apparatus. (b) Schematic of ULVAC-ZEM 3 four-probe measurement system.

The electrical conductivity, σ is measured using the four-probe method. Temperature dependent σ has been measured concurrently during Seebeck measurement in ULVAC ZEM 3 RIKO. For the measurement, a constant current I is applied to both ends of the sample to measure the voltage V between the thermocouples. By knowing resistance of sample, R ($R = V/I$), we can calculate σ from resistivity (ρ) of the sample using following equations:

$$\rho = R \times \frac{A}{l} \quad (1.16)$$

$$\sigma = \frac{1}{\rho} \quad (1.17)$$

where A is sample cross section and l is the distance between probes.

1.4.3.2. Thermal Conductivity

The flash diffusivity method most frequently is used for the determination of thermal conductivity (κ) of material. Non-contact, non-destructive, easy sample preparation, applicability for a wide range of diffusivity values with excellent accuracy and reproducibility makes this method more advantageous than direct method. In the flash diffusivity method, the thermal conductivity is calculated as $\kappa = DC_p\rho$, where D is thermal diffusivity, ρ is density, and C_p is the constant pressure heat capacity. In this method, the

sample is mounted on a carrier system, which is located in a furnace. After the sample reaches a predetermined temperature, a short heat pulse from a pulsed laser is applied to one side of a thin sample, resulting in homogeneous heating. The relative temperature increase on the rear face of the sample is then measured as a function of time by an IR detector. The temperature will rise to a maximum, after which it will decay. The time for the temperature to increase to half-maximum, $t_{1/2}$, is used to calculate the thermal diffusivity using equation 1.18

$$D = 0.1388 \times \frac{l^2}{t_{1/2}} \quad (1.18)$$

where D is thermal diffusivity in cm^2/sec , l is the thickness.¹⁷⁰

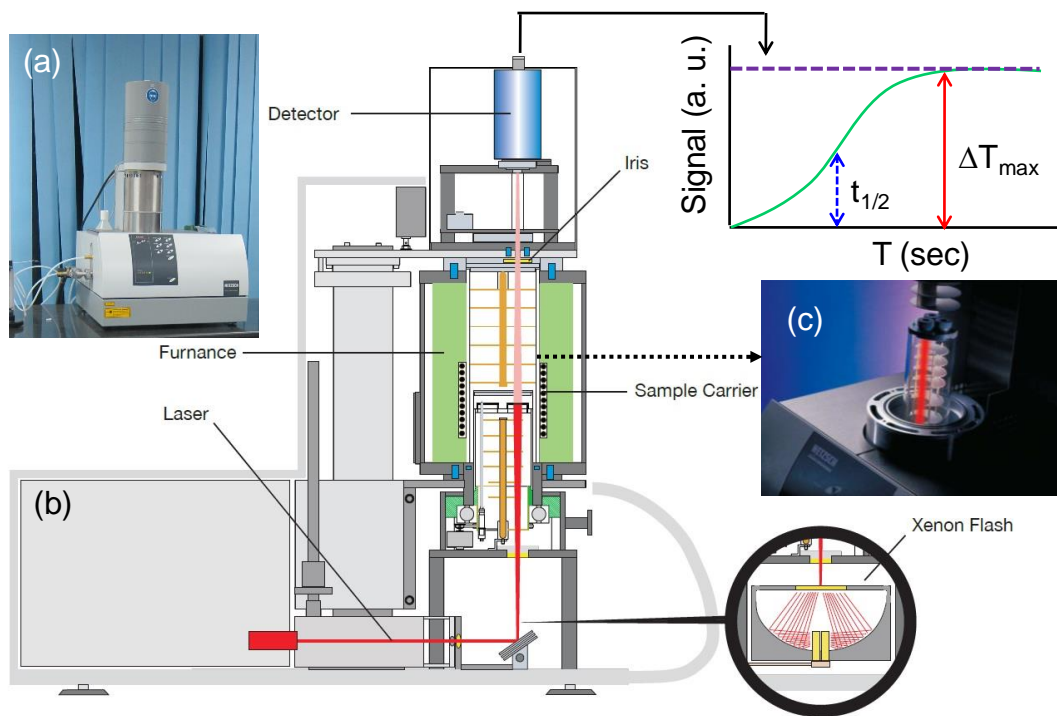


Figure 1.13. (a) Photograph of NETZSCH LFA-457 instrument. (b) and (c) Schematic of LFA- 457 diffusivity measurement apparatus.

In this thesis, temperature dependent thermal transport measurement has been done using the most popular NETZSCH LFA-457 instrument in N_2 atmosphere (Figure 1.13). The samples were coated with a thin layer of graphite ($\sim 5 \mu\text{m}$) in order to enhance the absorption of laser energy and emission of IR radiation to the detector. It also increases the signal to noise ratio. The error for the κ measurement is $\sim 5\%$. The samples

were placed inside SiC sample holder to mount on carrier system (Figure 1.13c). A Nd-Glass pulsed laser source of wavelength 1054 nm has been used for all the measurement. To measure the increased temperature on the rear face of the sample a liquid N₂ cooled InSb IR detector has been used. The density (ρ) was determined using the dimensions and mass of the sample and C_p , was derived indirectly using a standard sample (pyroceram). The thermal diffusivity data were analyzed using a Cowan model with pulse correction to account for heat losses on the sample faces.¹⁷¹

1.5. Scope of the Thesis

Metal chalcogenides constitute one of the most important classes of materials with a rich structural diversity and plethora of diverse transport properties. In my Ph.D. work, I have synthesized and investigated the phonon transport properties of various metal chalcogenides, gained an in-depth understanding of their diverse structure (on both local and global scales) and their structure-property relationships. Finally, I have probed their applicability in thermoelectrics. Apart from the present introductory part (**part 1**), my thesis work is divided into four parts (2-5), containing two chapters each for part 2, 3 and 5, while part 4 contains 3 chapters.

Thermoelectric materials which can convert heat energy to electricity rely on crystalline inorganic solid state compounds exhibiting low phonon transport (i.e. low thermal conductivity) without much inhibiting the electrical transport. Suppression of phonons traditionally has been carried out via extrinsic pathways, involving formation of point defects, foreign nanostructures, and meso-scale grains, but the incorporation of extrinsic substituents also influences the electrical properties. Crystalline materials with intrinsically low lattice thermal conductivity (κ_{lat}) provide an attractive paradigm as it helps in simplifying the complex interrelated thermoelectric parameters and allows us to focus largely on improving the electronic properties. In **Part 2** of my thesis, I have investigated the origin of intrinsically low κ_{lat} in binary IIIA-VIA Selenides TlSe and InSe. Although Tl and In are from the same group of the periodic table, where In lies just above Tl, the crystal structure and chemical bonding characteristics of TlSe and InSe are vastly different. TlSe resides in a 1-D Zintl type structure (space group $I4/mcm$) with Tl showing a mixed oxidation state of +1 and +3. Tl⁺ remains weakly bonded in a slightly

distorted Thomson cubes formed by a covalently bonded tetrahedra of formed by trivalent Tl (Tl^{3+}) and Se, *i.e.*, $(\text{TlSe}_2)_n^{n-}$. This Tl^+ due to its weak bonding interaction with the covalent moiety vibrates with a much larger amplitude, reminiscent of the guest rattlers in clathrates and skutterudites. This intrinsic rattling dampens the phonon flow through the material and as a result low κ_{lat} of 0.43 W/mK at 523 K is observed for TlSe. InSe interestingly crystallizes as a 2-D layered hexagonal structure having space group $P6_3/mmc$ (β -InSe). The layers in β -InSe are stacked along the crystallographic *c*-direction having two sub-layers of Se-In-In-Se sequence and the sub-layers are separated by a van der Waals (vdW) gap. Perpendicular to *c*-direction, InSe are covalently bonded. The vdW gap between two layers attenuates the phonon flow along the crystallographic *c*-direction while phonon flows unimpeded perpendicular to the *c*-direction. As a result, low κ_{lat} of 1.26 W/mK is achieved along the layer stacking direction (\parallel to *c* axis) while a high κ_{lat} of 10.43 W/mK is achieved perpendicular to the layer stacking direction at room temperature and having an anisotropic thermal ratio of ~ 8.25 at 298 K.

Part 3 of my thesis involve gathering experimental evidences to elucidate the origin of intrinsically ultralow κ_{lat} in ternary chalcogenides. In this chapter we have used state-of-the-art techniques like pair distribution function (PDF) and inelastic neutron scattering (INS) to explain the cause for low κ_{lat} in TlInTe_2 and AgSbSe_2 . TlInTe_2 is a TlSe type Zintl compound and shows low κ_{lat} of ~ 0.5 W/mK at 300 K. Similar to the TlSe structure here Tl^+ resides in a slightly skewed Thomson cage formed by $(\text{InTe}_2)_n^{n-}$ tetrahedra. Through PDF analysis we have revealed the presence of bonding heterogeneity with Tl-Te is weakly bonded while In-Te forms a strong covalent bonding. Absence of uniform bonding in the structure hinders the phonon flow through the material. Furthermore, atomic displacement parameter (*U*) reveals an enhanced thermal vibration for Tl despite it being a much heavier element. This indicated the presence of intrinsic rattling nature of Tl atoms in this material. Such rattlers induce very low energy optical modes, and through INS we have visualized the presence of several low energy optical phonon density of states ($< 100 \text{ cm}^{-1}$). These low energy optical modes are known to scatter the heat carrying acoustic phonons and this results in dampening the phonon flow through the material; ultimately resulting in low κ_{lat} . AgSbSe_2 which resides in fairly simple rock-salt type structure also show low κ_{lat} of 0.36 W/mK at 711 K. The reason

behind such low κ_{lat} is attributed to the presence of $5s^2$ lone pair of electrons of Sb which stereochemically expresses itself along a certain crystallographic direction, thus Sb residing in a distorted environment and inducing significant lattice anharmonicity. We have directly evidenced the presence of locally distorted cation environment in AgSbSe_2 from PDF analysis, which arises due to the stereochemically active lone pair of Sb. Our analysis revealed that the globally rock-salt AgSbSe_2 is off-centered locally along the crystallographic $\langle 100 \rangle$ direction a factor of $\sim 0.2 \text{ \AA}$. Such local off-centering is known to dampen the phonon flow and is the primary reason for low κ_{lat} in AgSbSe_2 .

Part 4 involves the potential application of metal selenides with low κ_{lat} for potential thermoelectric applications. Here we have studied the origin of low thermal conductivity and the thermoelectric properties of quaternary chalcogenides. Two of the studied compounds, *i.e.*, AgPbBiSe_3 and $(\text{SnSe})_{0.5}(\text{AgSbSe}_2)_{0.5}$ resides in a rock-salt lattice with all three cations sharing the Na position. The κ_{lat} of both the material is found to be ultra-low $\sim 0.5 \text{ W/mK}$ at 300 K. First-principles calculations augmented with low temperature heat capacity measurements and the experimentally determined synchrotron X-ray pair distribution function (PDF) reveal bonding heterogeneity within the lattice and lone pair induced lattice anharmonicity in AgPbBiSe_3 . Both of these factors enhance the phonon–phonon scattering, and are thereby responsible for the suppressed κ_{lat} . As material with low κ_{lat} is beneficial for thermoelectrics, optimization of the electrical properties was performed by aliovalent halide doping, and a promising thermoelectric figure of merit (zT) of 0.8 at 814 K was achieved for $\text{AgPbBiSe}_{2.97}\text{I}_{0.03}$. In the case of $(\text{SnSe})_{0.5}(\text{AgSbSe}_2)_{0.5}$, PDF analysis revealed that the local structure deviates from the overall average cubic rock-salt structure of the compound with warming, a rare phenomenon which is termed as *emphanisis*. This *emphanisis* is due to the local off-centering of Se along $[111]$ crystallographic direction. This disrupts the periodicity of the lattice which hinders phonon flow, thus resulting in low κ_{lat} . This low κ_{lat} is highly favourable for thermoelectrics and a p-type zT of 0.77 at 725 K is achieved which on optimization of the electrical conductivity via Ge doping increases to >1 at 706 K for $(\text{SnSe})_{0.5}(\text{AgSb}_{1-x}\text{Ge}_x\text{Se}_2)_{0.5}$ ($x = 0.06$). Extrinsic stoichiometric modifications via dopant/alloying etc. not only influences the κ_{lat} but influences the electronic transport also as seen in the above compounds. In AgCuS , we have modulated the electronic transport

via extrinsically removing a fraction of Ag or Cu from AgCuS. AgCuS which at high temperature behaves as part-crystalline part-liquid materials shows intrinsically low κ_{lat} due to the mobile movement of the cations. However, it shows a change in the conduction switching from p-type to n-type near the vicinity of orthorhombic (β) to rhombohedral (α) phase transition. This transition is accompanied by a colossal change in the Seebeck co-efficient. Here through creating off-stoichiometric ratio of Ag and Cu in AgCuS, we were able to manipulate the p-n-p transition in AgCuS. We have observed that Cu is much efficient in arresting the conduction switching than Ag. This work establishes the role of externally created vacancy in modulating the electronic transport in a material. All the off-stoichiometric compounds show ultralow κ_{lat} due to the presence of mobile cations which are known to impede phonon transport.

While part 4 gave an indication that materials with low κ_{lat} can be used in thermoelectrics, in **part 5** we have synthesized high performing IVA-VIA based thermoelectric materials though lowering their κ_{lat} . PbTe is a front runner as a high performing thermoelectric material, but most of their development has been in p-type materials. The development in high performing n-type PbTe thermoelectric is lacking behind due to its simple conduction bands as compared to its rich valence bands. Also given the complex interrelation ship among in the zT equation (1.1), simultaneous enhancement of power factor and lowering of κ_{lat} is extremely difficult. We have been able to address this issue to a certain extent via Gd doping in PbTe. Gd doping in PbTe enhances the electron effective mass via flattening of the conduction band, which significantly improves the Seebeck coefficient. Gd is found to remain in an off-centered position inside the rock-salt PbTe lattice, which increased the lattice anharmonicity and induces a low energy nearly flat optical phonon mode that drastically increases the phonon scattering rate and lowers lattice thermal conductivity to 0.78 W/mK. As a result, we achieved a high zT of 1.65 at 678 K for $\text{Pb}_{1-x}\text{Gd}_x\text{Te}_{1-y}\text{I}_y$ ($x = 0.33\%$, $y = 1\%$). In case of SnTe, we have observed that with 30 mol% Ge alloying, the zT reaches an impressive value of 1.6 at 721 K. Here, the high zT is the resultant of engineering the ferroelectric transition to near room temperature. GeTe which favours a rhombohedral structure at room temperature is found to remain in an off-centred position in rock-salt SnTe. Here, we have performed temperature dependent (250 – 603 K) PDF analysis and found that

below the ferroelectric transition temperature, Ge remains off-centered by $\sim 0.25 \text{ \AA}$, while after the transition such local distortion decreases with temperature but remains intact up to higher temperatures. This local off-centering is found to be the driving force in lowering the κ_{lat} to an ultralow value. This low κ_{lat} induces the high thermoelectric performance in $\text{Sn}_{0.70}\text{Ge}_{0.30}\text{Te}$.

In **part 6** we have summarized all the chapters and provided a brief outlook into the looked into the future directions in optimizing thermoelectric performance via tuning the κ_{lat} .

To summarize, the initial part of my thesis involved understanding the origins of low thermal conductivity in simple binary compounds through theoretical calculations and indirect experimental methods (**part 2**). Being an experimental chemist, I then worked in the pursuit of obtaining direct evidence, which induces low κ_{lat} in material (**part 3**). I have then investigated the potential of having low κ_{lat} solids in thermoelectrics (**part 4**). Finally, I have demonstrated how low κ_{lat} can be instrumental in realizing high thermoelectric performance in IVA – VIA compounds (**part 5**). The whole work is then summarized briefly along with future outlook (**part 6**).

1.6. References

- [1] F. Jellinek, *React. Solids*, 1988, **5**, 323-339.
- [2] A. Meerschaut, L. Guemas, R. Berger and J. Rouxel, *Acta Crystallogr., Sect. B: Struct. Sci.*, 1979, **35**, 1747-1750.
- [3] Y. V. Mironov, M. A. Pell and J. A. Ibers, *Angew. Chem. Int. Ed. Engl.*, 1996, **35**, 2854-2856.
- [4] T. Weber, R. Prins and R. A. van Santen, *Transition metal sulphides: chemistry and catalysis*, Springer Science & Business Media, 1998.
- [5] A. Mar, S. Jovic and J. A. Ibers, *J. Am. Chem. Soc.*, 1992, **114**, 8963-8971.
- [6] S. Dehnen and M. Melullis, *Coord. Chem. Rev.*, 2007, **251**, 1259-1280.
- [7] M. G. Kanatzidis, *Curr. Opin. Solid State Mater. Sci.*, 1997, **2**, 139-149.
- [8] M. G. Kanatzidis, *Inorg. Chem.*, 2017, **56**, 3158-3173.
- [9] M. K. Jana and C. N. R. Rao, *Phil. Trans. R. Soc. A*, 2016, **374**, 20150318.
- [10] M. Chhowalla, H. S. Shin, G. Eda, L.-J. Li, K. P. Loh and H. Zhang, *Nat. Chem.*, 2013, **5**, 263-275.
- [11] C. N. R. Rao, U. Maitra and U. V. Waghmare, *Chem. Phys. Lett.*, 2014, **609**, 172-183.
- [12] C. N. R. Rao, H. S. S. Ramakrishna Matte and U. Maitra, *Angew. Chem. Int. Ed.*, 2013, **52**, 13162-13185.
- [13] Q. Si, R. Yu and E. Abrahams, *Nat. Rev. Mater.*, 2016, **1**, 16017.
- [14] J. R. Sootsman, D. Y. Chung and M. G. Kanatzidis, *Angew. Chem. Int. Ed.*, 2009, **48**, 8616-8639.
- [15] Q. H. Wang, K. Kalantar-Zadeh, A. Kis, J. N. Coleman and M. S. Strano, *Nat. Nanotechnol.*, 2012, **7**, 699-712.
- [16] G. Eda, T. Fujita, H. Yamaguchi, D. Voiry, M. Chen and M. Chhowalla, *ACS Nano*, 2012, **6**, 7311-7317.

-
- [17] H. Lin, L. Chen, L.-J. Zhou and L.-M. Wu, *J. Am. Chem. Soc.*, 2013, **135**, 12914-12921.
- [18] S. Hudgens and B. Johnson, *MRS Bull.*, 2004, **29**, 829-832.
- [19] S. C. Riha, B. A. Parkinson and A. L. Prieto, *J. Am. Chem. Soc.*, 2009, **131**, 12054-12055.
- [20] G. Tan, L.-D. Zhao and M. G. Kanatzidis, *Chem. Rev.*, 2016, **116**, 12123-12149.
- [21] X.-L. Shi, J. Zou and Z.-G. Chen, *Chem. Rev.*, 2020, **120**, 7399-7515.
- [22] A. Rogalski, *Rep. Prog. Phys.*, 2005, **68**, 2267-2336.
- [23] B. Radisavljevic, A. Radenovic, J. Brivio, V. Giacometti and A. Kis, *Nat. Nanotechnol.*, 2011, **6**, 147-150.
- [24] J. J. Cha, J. R. Williams, D. Kong, S. Meister, H. Peng, A. J. Bestwick, P. Gallagher, D. Goldhaber-Gordon and Y. Cui, *Nano Lett.*, 2010, **10**, 1076-1081.
- [25] N. Kamaya, K. Homma, Y. Yamakawa, M. Hirayama, R. Kanno, M. Yonemura, T. Kamiyama, Y. Kato, S. Hama, K. Kawamoto and A. Mitsui, *Nat. Mater.*, 2011, **10**, 682-686.
- [26] F. Cheng, J. Liang, Z. Tao and J. Chen, *Adv. Mater.*, 2011, **23**, 1695-1715.
- [27] D. Merki and X. Hu, *Energy Environ. Sci.*, 2011, **4**, 3878-3888.
- [28] J. M. Caron, J. R. Neilson, D. C. Miller, K. Arpino, A. Llobet and T. M. McQueen, *Phys. Rev. B*, 2012, **85**, 180405.
- [29] S. Medvedev, T. M. McQueen, I. A. Troyan, T. Palasyuk, M. I. Eremets, R. J. Cava, S. Naghavi, F. Casper, V. Ksenofontov, G. Wortmann and C. Felser, *Nat. Mater.*, 2009, **8**, 630-633.
- [30] H. S. S. Ramakrishna Matte, A. Gomathi, A. K. Manna, D. J. Late, R. Datta, S. K. Pati and C. N. R. Rao, *Angew. Chem. Int. Ed.*, 2010, **49**, 4059-4062.
- [31] M. König, S. Wiedmann, C. Brüne, A. Roth, H. Buhmann, L. W. Molenkamp, X.-L. Qi and S.-C. Zhang, *Science*, 2007, **318**, 766.
- [32] D. Hsieh, Y. Xia, D. Qian, L. Wray, J. H. Dil, F. Meier, J. Osterwalder, L. Patthey, J. G. Checkelsky, N. P. Ong, A. V. Fedorov, H. Lin, A. Bansil, D. Grauer, Y. S. Hor, R. J. Cava and M. Z. Hasan, *Nature*, 2009, **460**, 1101-1105.

-
- [33] D. Kong and Y. Cui, *Nat. Chem.*, 2011, **3**, 845-849.
- [34] L. MÜchler, F. Casper, B. Yan, S. Chadov and C. Felser, *Phys. Status Solidi RRL*, 2013, **7**, 91-100.
- [35] Y. Xia, D. Qian, D. Hsieh, L. Wray, A. Pal, H. Lin, A. Bansil, D. Grauer, Y. S. Hor, R. J. Cava and M. Z. Hasan, *Nat. Phys.*, 2009, **5**, 398-402.
- [36] L. Fu, *Phys. Rev. Lett.*, 2011, **106**, 106802.
- [37] T. H. Hsieh, H. Lin, J. Liu, W. Duan, A. Bansil and L. Fu, *Nat. Commun.*, 2012, **3**, 982.
- [38] M. N. Ali, J. Xiong, S. Flynn, J. Tao, Q. D. Gibson, L. M. Schoop, T. Liang, N. Haldolaarachchige, M. Hirschberger, N. P. Ong and R. J. Cava, *Nature*, 2014, **514**, 205-208.
- [39] A. Walsh, D. J. Payne, R. G. Egdell and G. W. Watson, *Chem. Soc. Rev.*, 2011, **40**, 4455-4463.
- [40] P. Fielding, G. Fischer and E. Mooser, *J. Phys. Chem. Solids*, 1959, **8**, 434-437.
- [41] S. Roychowdhury, M. Samanta, S. Perumal and K. Biswas, *Chem. Mater.*, 2018, **30**, 5799-5813.
- [42] A. Banik, S. Roychowdhury and K. Biswas, *Chem. Commun.*, 2018, **54**, 6573-6590.
- [43] M. D. Nielsen, V. Ozolins and J. P. Heremans, *Energy Environ. Sci.*, 2013, **6**, 570-578.
- [44] W. G. Zeier, A. Zevalkink, Z. M. Gibbs, G. Hautier, M. G. Kanatzidis and G. J. Snyder, *Angew. Chem., Int. Ed.*, 2016, **55**, 6826.
- [45] E. S. Božin, C. D. Malliakas, P. Souvatzis, T. Proffen, N. A. Spaldin, M. G. Kanatzidis and S. J. L. Billinge, *Science*, 2010, **330**, 1660.
- [46] S. N. Guin, A. Chatterjee, D. S. Negi, R. Datta and K. Biswas, *Energy Environ. Sci.*, 2013, **6**, 2603-2608.
- [47] S. Geller and J. H. Wernick, *Acta Cryst.*, 1959, **12**, 46-54.
- [48] K. Tolborg, C. Gatti and B. B. Iversen, *IUCrJ*, 2020, **7**, 480-489.
- [49] M. Dutta, D. Sarkar and K. Biswas, *Chem. Commun.*, 2021, **57**, 4751-4767.

-
- [50] E. Rathore, M. Dutta and K. Biswas, *J. Chem. Sci.*, 2019, **131**, 116.
- [51] D. T. Morelli, V. Jovovic and J. P. Heremans, *Phys. Rev. Lett.*, 2008, **101**, 035901.
- [52] E. J. Skoug and D. T. Morelli, *Phys. Rev. Lett.*, 2011, **107**, 235901.
- [53] M. K. Jana, K. Pal, U. V. Waghmare and K. Biswas, *Angew. Chem. Int. Ed.*, 2016, **55**, 7792-7796.
- [54] M. Samanta, T. Ghosh, S. Chandra and K. Biswas, *J. Mater. Chem. A*, 2020, **8**, 12226-12261.
- [55] D. Bessas, I. Sergueev, H. C. Wille, J. Perbon, D. Ebling and R. P. Hermann, *Phys. Rev. B*, 2012, **86**, 224301.
- [56] Y. Xiao, C. Chang, Y. Pei, D. Wu, K. Peng, X. Zhou, S. Gong, J. He, Y. Zhang, Z. Zeng and L.-D. Zhao, *Phys. Rev. B*, 2016, **94**, 125203.
- [57] C. Wang, G. Ding, X. Wu, S. Wei and G. Gao, *New J. Phys.*, 2018, **20**, 123014.
- [58] S. Kumar and U. Schwingenschlögl, *Phys. Chem. Chem. Phys.*, 2016, **18**, 19158-19164.
- [59] M. Samanta, K. Pal, P. Pal, U. V. Waghmare and K. Biswas, *J. Am. Chem. Soc.*, 2018, **140**, 5866-5872.
- [60] A. Banik and K. Biswas, *Angew. Chem. Int. Ed.*, 2017, **56**, 14561-14566.
- [61] A. Chatterjee and K. Biswas, *Angew. Chem. Int. Ed.*, 2015, **54**, 5623-5627.
- [62] Y. Xiao and L.-D. Zhao, *Science*, 2020, **367**, 1196.
- [63] X. Shi, J. Yang, J. R. Salvador, M. Chi, J. Y. Cho, H. Wang, S. Bai, J. Yang, W. Zhang and L. Chen, *J. Am. Chem. Soc.*, 2011, **133**, 7837-7846.
- [64] Y. Qiu, L. Xi, X. Shi, P. Qiu, W. Zhang, L. Chen, J. R. Salvador, J. Y. Cho, J. Yang, Y.-c. Chien, S.-w. Chen, Y. Tang and G. J. Snyder, *Adv. Funct. Mater.*, 2013, **23**, 3194-3203.
- [65] X. Shi, J. Yang, L. Wu, J. R. Salvador, C. Zhang, W. L. Villaire, D. Haddad, J. Yang, Y. Zhu and Q. Li, *Sci. Rep.*, 2015, **5**, 14641.
- [66] T. Takabatake, K. Suekuni, T. Nakayama and E. Kaneshita, *Rev. Mod. Phys.*, 2014, **86**, 669-716.

- [67] M. S. Ikeda, H. Euchner, X. Yan, P. Tomeš, A. Prokofiev, L. Prochaska, G. Lientschnig, R. Svagera, S. Hartmann, E. Gati, M. Lang and S. Paschen, *Nat. Commun.*, 2019, **10**, 887.
- [68] P.-F. Lory, S. Pailhès, V. M. Giordano, H. Euchner, H. D. Nguyen, R. Ramlau, H. Borrmann, M. Schmidt, M. Baitinger, M. Ikeda, P. Tomeš, M. Mihalkovič, C. Allio, M. R. Johnson, H. Schober, Y. Sidis, F. Bourdarot, L. P. Regnault, J. Ollivier, S. Paschen, Y. Grin and M. de Boissieu, *Nat. Commun.*, 2017, **8**, 491.
- [69] M. Christensen, A. B. Abrahamsen, N. B. Christensen, F. Juranyi, N. H. Andersen, K. Lefmann, J. Andreasson, C. R. H. Bahl and B. B. Iversen, *Nat. Mater.*, 2008, **7**, 811-815.
- [70] W. Li and N. Mingo, *Phys. Rev. B*, 2015, **91**, 144304.
- [71] M. Koza, M. Johnson, R. Viennois, H. Mutka, L. Girard and D. Ravot, *Nat. Mater.*, 2008, **7**, 805-810.
- [72] M. K. Jana, K. Pal, A. Warankar, P. Mandal, U. V. Waghmare and K. Biswas, *J. Am. Chem. Soc.*, 2017, **139**, 4350-4353.
- [73] H. Lin, G. Tan, J.-N. Shen, S. Hao, L.-M. Wu, N. Calta, C. Malliakas, S. Wang, C. Uher, C. Wolverton and M. G. Kanatzidis, *Angew. Chem. Int. Ed.*, 2016, **55**, 11431-11436.
- [74] G. Tan, S. Hao, J. Zhao, C. Wolverton and M. G. Kanatzidis, *J. Am. Chem. Soc.*, 2017, **139**, 6467-6473.
- [75] S. Mukhopadhyay, D. S. Parker, B. C. Sales, A. A. Puretzky, M. A. McGuire and L. Lindsay, *Science*, 2018, **360**, 1455.
- [76] S. R. Brown, S. M. Kauzlarich, F. Gascoin and G. J. Snyder, *Chem. Mater.*, 2006, **18**, 1873-1877.
- [77] D. J. Voneshen, K. Refson, E. Borissenko, M. Krisch, A. Bosak, A. Piovano, E. Cemal, M. Enderle, M. J. Gutmann, M. Hoesch, M. Roger, L. Gannon, A. T. Boothroyd, S. Uthayakumar, D. G. Porter and J. P. Goff, *Nat. Mater.*, 2013, **12**, 1028.
- [78] J. Qi, B. Dong, Z. Zhang, Z. Zhang, Y. Chen, Q. Zhang, S. Danilkin, X. Chen, J. He, L. Fu, X. Jiang, G. Chai, S. Hiroi, K. Ohara, Z. Zhang, W. Ren, T. Yang, J. Zhou, S. Osami, J. He, D. Yu, B. Li and Z. Zhang, *Nat. Commun.*, 2020, **11**, 5197.
- [79] E. Rathore, R. Juneja, S. P. Culver, N. Minafra, A. K. Singh, W. G. Zeier and K. Biswas, *Chem. Mater.*, 2019, **31**, 2106-2113.

-
- [80] K. Pal, Y. Xia, J. He and C. Wolverton, *Phys. Rev. Mater.*, 2019, **3**, 085402.
- [81] K. Pal, J. He and C. Wolverton, *Chem. Mater.*, 2018, **30**, 7760-7768.
- [82] K. Pal, Y. Xia, J. He and C. Wolverton, *Chem. Mater.*, 2019, **31**, 8734-8741.
- [83] H. Xie, X. Su, X. Zhang, S. Hao, T. P. Bailey, C. C. Stoumpos, A. P. Douvalis, X. Hu, C. Wolverton, V. P. Dravid, C. Uher, X. Tang and M. G. Kanatzidis, *J. Am. Chem. Soc.*, 2019, **141**, 10905-10914.
- [84] K. R. Knox, E. S. Bozin, C. D. Malliakas, M. G. Kanatzidis and S. J. L. Billinge, *Phys. Rev. B*, 2014, **89**, 014102.
- [85] R. Yu, E. S. Bozin, M. Abeykoon, B. Sangiorgio, N. A. Spaldin, C. D. Malliakas, M. G. Kanatzidis and S. J. L. Billinge, *Phys. Rev. B*, 2018, **98**, 144108.
- [86] Y. Xiao and L.-D. Zhao, *npj Quantum Mater.*, 2018, **3**, 55.
- [87] O. Delaire, J. Ma, K. Marty, A. F. May, M. A. McGuire, M. H. Du, D. J. Singh, A. Podlesnyak, G. Ehlers, M. D. Lumsden and B. C. Sales, *Nat. Mater.*, 2011, **10**, 614-619.
- [88] K. M. Ø. Jensen, E. S. Božin, C. D. Malliakas, M. B. Stone, M. D. Lumsden, M. G. Kanatzidis, S. M. Shapiro and S. J. L. Billinge, *Phys. Rev. B*, 2012, **86**, 085313.
- [89] X. Li, P.-F. Liu, E. Zhao, Z. Zhang, T. Guidi, M. D. Le, M. Avdeev, K. Ikeda, T. Otomo, M. Kofu, K. Nakajima, J. Chen, L. He, Y. Ren, X.-L. Wang, B.-T. Wang, Z. Ren, H. Zhao and F. Wang, *Nat. Commun.*, 2020, **11**, 942.
- [90] Y. Wang, Y. Sui, P. Ren, L. Wang, X. Wang, W. Su and H. J. Fan, *Inorg. Chem.*, 2010, **49**, 3216-3223.
- [91] G. A. Slack and D. Rowe, *CRC handbook of thermoelectrics*, CRC press Boca Raton, FL, 1995.
- [92] W. Qiu, L. Xi, P. Wei, X. Ke, J. Yang and W. Zhang, *Proc. Natl. Acad. Sci. U. S. A.*, 2014, **111**, 15031.
- [93] G. J. Snyder, M. Christensen, E. Nishibori, T. Caillat and B. B. Iversen, *Nat. Mater.*, 2004, **3**, 458-463.
- [94] Y. He, T. Day, T. Zhang, H. Liu, X. Shi, L. Chen and G. J. Snyder, *Adv. Mater.*, 2014, **26**, 3974-3978.

- [95] Z.-H. Ge, B.-P. Zhang, Y.-X. Chen, Z.-X. Yu, Y. Liu and J.-F. Li, *Chem. Commun.*, 2011, **47**, 12697-12699.
- [96] H. Liu, X. Shi, F. Xu, L. Zhang, W. Zhang, L. Chen, Q. Li, C. Uher, T. Day and G. J. Snyder, *Nat. Mater.*, 2012, **11**, 422.
- [97] X. Su, F. Fu, Y. Yan, G. Zheng, T. Liang, Q. Zhang, X. Cheng, D. Yang, H. Chi, X. Tang, Q. Zhang and C. Uher, *Nat. Commun.*, 2014, **5**, 4908.
- [98] Y. He, T. Zhang, X. Shi, S.-H. Wei and L. Chen, *NPG Asia Mater.*, 2015, **7**, e210-e210.
- [99] S. N. Guin, J. Pan, A. Bhowmik, D. Sanyal, U. V. Waghmare and K. Biswas, *J. Am. Chem. Soc.*, 2014, **136**, 12712-12720.
- [100] S. Ishiwata, Y. Shiomi, J. S. Lee, M. S. Bahramy, T. Suzuki, M. Uchida, R. Arita, Y. Taguchi and Y. Tokura, *Nat. Mater.*, 2013, **12**, 512.
- [101] S. Roychowdhury, M. K. Jana, J. Pan, S. N. Guin, D. Sanyal, U. V. Waghmare and K. Biswas, *Angew. Chem. Int. Ed.*, 2018, **57**, 4043-4047.
- [102] B. Jiang, Y. Yu, J. Cui, X. Liu, L. Xie, J. Liao, Q. Zhang, Y. Huang, S. Ning, B. Jia, B. Zhu, S. Bai, L. Chen, S. J. Pennycook and J. He, *Science*, 2021, **371**, 830.
- [103] S. Roychowdhury, T. Ghosh, R. Arora, M. Samanta, L. Xie, N. K. Singh, A. Soni, J. He, U. V. Waghmare and K. Biswas, *Science*, 2021, **371**, 722.
- [104] M. Dutta, T. Ghosh and K. Biswas, *APL Mater.*, 2020, **8**, 040910.
- [105] C. Goupil, H. Ouerdane, K. Zabrocki, W. Seifert, N. F. Hinsche and E. Müller, *Thermodynamics and thermoelectricity*, 2016, 1-74.
- [106] L.-D. Zhao, V. P. Dravid and M. G. Kanatzidis, *Energy Environ. Sci.*, 2014, **7**, 251-268.
- [107] Y. Xiao, H. Wu, J. Cui, D. Wang, L. Fu, Y. Zhang, Y. Chen, J. He, S. J. Pennycook and L.-D. Zhao, *Energy Environ. Sci.*, 2018, **11**, 2486-2495.
- [108] D. Sarkar, T. Ghosh, A. Banik, S. Roychowdhury, D. Sanyal and K. Biswas, *Angew. Chem. Int. Ed.*, 2020, **59**, 11115-11122.
- [109] Y. Pei, X. Shi, A. LaLonde, H. Wang, L. Chen and G. J. Snyder, *Nature*, 2011, **473**, 66-69.

- [110] A. Banik, U. S. Shenoy, S. Saha, U. V. Waghmare and K. Biswas, *J. Am. Chem. Soc.*, 2016, **138**, 13068-13075.
- [111] J. P. Heremans, V. Jovovic, E. S. Toberer, A. Saramat, K. Kurosaki, A. Charoenphakdee, S. Yamanaka and G. J. Snyder, *Science*, 2008, **321**, 554.
- [112] J. M. Hodges, S. Hao, J. A. Grovogui, X. Zhang, T. P. Bailey, X. Li, Z. Gan, Y.-Y. Hu, C. Uher, V. P. Dravid, C. Wolverton and M. G. Kanatzidis, *J. Am. Chem. Soc.*, 2018, **140**, 18115-18123.
- [113] Y. Qin, Y. Xiao and L.-D. Zhao, *APL Mater.*, 2020, **8**, 010901.
- [114] T. C. Harman, P. J. Taylor, M. P. Walsh and B. E. LaForge, *Science*, 2002, **297**, 2229.
- [115] S. Roychowdhury, R. K. Biswas, M. Dutta, S. K. Pati and K. Biswas, *ACS Energy Lett.*, 2019, **4**, 1658-1662.
- [116] L. Fu, M. Yin, D. Wu, W. Li, D. Feng, L. Huang and J. He, *Energy Environ. Sci.*, 2017, **10**, 2030-2040.
- [117] K. Biswas, J. He, Q. Zhang, G. Wang, C. Uher, V. P. Dravid and M. G. Kanatzidis, *Nat. Chem.*, 2011, **3**, 160.
- [118] B. Poudel, Q. Hao, Y. Ma, Y. Lan, A. Minnich, B. Yu, X. Yan, D. Wang, A. Muto, D. Vashaee, X. Chen, J. Liu, M. S. Dresselhaus, G. Chen and Z. Ren, *Science*, 2008, **320**, 634.
- [119] K. Biswas, J. He, I. D. Blum, C.-I. Wu, T. P. Hogan, D. N. Seidman, V. P. Dravid and M. G. Kanatzidis, *Nature*, 2012, **489**, 414.
- [120] L. D. Zhao, H. J. Wu, S. Q. Hao, C. I. Wu, X. Y. Zhou, K. Biswas, J. Q. He, T. P. Hogan, C. Uher, C. Wolverton, V. P. Dravid and M. G. Kanatzidis, *Energy Environ. Sci.*, 2013, **6**, 3346-3355.
- [121] M. K. Jana and K. Biswas, *ACS Energy Lett.*, 2018, **3**, 1315-1324.
- [122] Y. Xiao, H. Wu, W. Li, M. Yin, Y. Pei, Y. Zhang, L. Fu, Y. Chen, S. J. Pennycook, L. Huang, J. He and L.-D. Zhao, *J. Am. Chem. Soc.*, 2017, **139**, 18732-18738.
- [123] S. I. Kim, K. H. Lee, H. A. Mun, H. S. Kim, S. W. Hwang, J. W. Roh, D. J. Yang, W. H. Shin, X. S. Li, Y. H. Lee, G. J. Snyder and S. W. Kim, *Science*, 2015, **348**, 109.

- [124] Z. Xu, H. Wu, T. Zhu, C. Fu, X. Liu, L. Hu, J. He, J. He and X. Zhao, *NPG Asia Mater.*, 2016, **8**, e302-e302.
- [125] Y. Xiao and L.-D. Zhao, *npj Quantum Mater.*, 2018, **3**, 55.
- [126] Q. Zhang, B. Liao, Y. Lan, K. Lukas, W. Liu, K. Esfarjani, C. Opeil, D. Broido, G. Chen and Z. Ren, *Proc. Natl. Acad. Sci. U. S. A.*, 2013, **110**, 13261.
- [127] P. Acharyya, S. Roychowdhury, M. Samanta and K. Biswas, *J. Am. Chem. Soc.*, 2020, **142**, 20502-20508.
- [128] M. Samanta and K. Biswas, *J. Am. Chem. Soc.*, 2017, **139**, 9382-9391.
- [129] J. Li, X. Zhang, Z. Chen, S. Lin, W. Li, J. Shen, I. T. Witting, A. Faghaninia, Y. Chen, A. Jain, L. Chen, G. J. Snyder and Y. Pei, *Joule*, 2018, **2**, 976-987.
- [130] S. Chandra and K. Biswas, *J. Am. Chem. Soc.*, 2019, **141**, 6141-6145.
- [131] C. Chang, M. Wu, D. He, Y. Pei, C.-F. Wu, X. Wu, H. Yu, F. Zhu, K. Wang, Y. Chen, L. Huang, J.-F. Li, J. He and L.-D. Zhao, *Science*, 2018, **360**, 778.
- [132] L.-D. Zhao, G. Tan, S. Hao, J. He, Y. Pei, H. Chi, H. Wang, S. Gong, H. Xu, V. P. Dravid, C. Uher, G. J. Snyder, C. Wolverton and M. G. Kanatzidis, *Science*, 2016, **351**, 141.
- [133] L.-D. Zhao, S.-H. Lo, Y. Zhang, H. Sun, G. Tan, C. Uher, C. Wolverton, V. P. Dravid and M. G. Kanatzidis, *Nature*, 2014, **508**, 373.
- [134] S. Chandra, A. Banik and K. Biswas, *ACS Energy Lett.*, 2018, **3**, 1153-1158.
- [135] Y. Tang, Z. M. Gibbs, L. A. Agapito, G. Li, H. S. Kim, M. B. Nardelli, S. Curtarolo and G. J. Snyder, *Nat. Mater.*, 2015, **14**, 1223.
- [136] C. Fu, T. Zhu, Y. Liu, H. Xie and X. Zhao, *Energy Environ. Sci.*, 2015, **8**, 216-220.
- [137] C. Fu, S. Bai, Y. Liu, Y. Tang, L. Chen, X. Zhao and T. Zhu, *Nat. Commun.*, 2015, **6**, 8144.
- [138] H. Liu, X. Yuan, P. Lu, X. Shi, F. Xu, Y. He, Y. Tang, S. Bai, W. Zhang, L. Chen, Y. Lin, L. Shi, H. Lin, X. Gao, X. Zhang, H. Chi and C. Uher, *Adv. Mater.*, 2013, **25**, 6607.
- [139] A. A. Olvera, N. A. Moroz, P. Sahoo, P. Ren, T. P. Bailey, A. A. Page, C. Uher and P. F. P. Poudeu, *Energy Environ. Sci.*, 2017, **10**, 1668-1676.

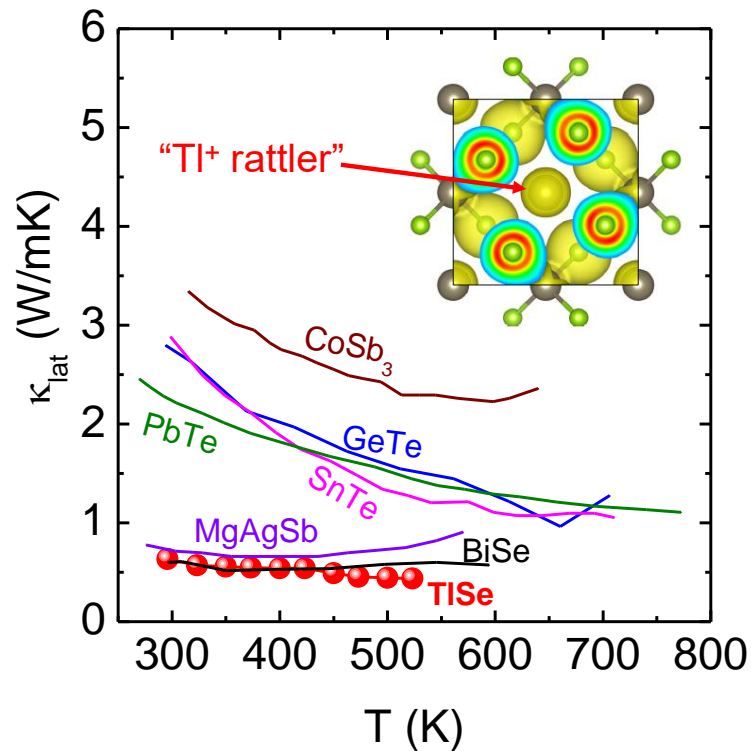
-
- [140] T. Zhu, Y. Liu, C. Fu, J. P. Heremans, J. G. Snyder and X. Zhao, *Adv. Mater.*, 2017, **29**, 1605884.
- [141] Z. Chen, X. Zhang and Y. Pei, *Adv. Mater.*, 2018, **30**, 1705617.
- [142] J. P. Heremans, *Nat. Phys.*, 2015, **11**, 990-991.
- [143] J. Callaway, *Phys. Rev.*, 1959, **113**, 1046-1051.
- [144] J. He, S. N. Girard, M. G. Kanatzidis and V. P. Dravid, *Adv. Funct. Mater.*, 2010, **20**, 764-772.
- [145] Y. Pei, A. D. LaLonde, N. A. Heinz, X. Shi, S. Iwanaga, H. Wang, L. Chen and G. J. Snyder, *Adv. Mater.*, 2011, **23**, 5674.
- [146] Z. Zheng, X. Su, R. Deng, C. Stoumpos, H. Xie, W. Liu, Y. Yan, S. Hao, C. Uher, C. Wolverton, M. G. Kanatzidis and X. Tang, *J. Am. Chem. Soc.*, 2018, **140**, 2673-2686.
- [147] C. M. Jaworski, V. Kulbachinskii and J. P. Heremans, *Phys. Rev. B*, 2009, **80**, 233201.
- [148] L. Wu, X. Li, S. Wang, T. Zhang, J. Yang, W. Zhang, L. Chen and J. Yang, *NPG Asia Mater.*, 2017, **9**, e343.
- [149] T. Berry, C. Fu, G. Auffermann, G. H. Fecher, W. Schnelle, F. Serrano-Sanchez, Y. Yue, H. Liang and C. Felser, *Chem. Mater.*, 2017, **29**, 7042-7048.
- [150] M. Samanta, M. Dutta and K. Biswas, in *Advances in the Chemistry and Physics of Materials*, WORLD SCIENTIFIC, 2019, pp. 350-375.
- [151] G. J. Snyder and E. S. Toberer, *Nat. Mater.*, 2008, **7**, 105.
- [152] J. Koringa and A. N. Gerritsen, *Physica*, 1953, **19**, 457-507.
- [153] Y. I. Ravich and S. A. Némov, *Semiconductors*, 2002, **36**, 1-20.
- [154] S. Roychowdhury and K. Biswas, *Chem*, 2018, **4**, 939-942.
- [155] Z. A. Munir, U. Anselmi-Tamburini and M. Ohyanagi, *J. Mater. Sci.*, 2006, **41**, 763-777.
- [156] O. Guillon, J. Gonzalez-Julian, B. Dargatz, T. Kessel, G. Schierning, J. Räthel and M. Herrmann, *Adv. Eng. Mater.*, 2014, **16**, 830-849.

-
- [157] G. J. Xie, *Powder Metall. Min.*, 2013, **2**, e109.
- [158] T. Egami and S. J. Billinge, *Underneath the Bragg peaks: structural analysis of complex materials*, Elsevier, 2003.
- [159] A.-C. Dippel, H.-P. Liermann, J. T. Delitz, P. Walter, H. Schulte-Schrepping, O. H. Seeck and H. Franz, *J. Synchrotron Rad.*, 2015, **22**, 675-687.
- [160] M. Basham, J. Filik, M. T. Wharmby, P. C. Y. Chang, B. El Kassaby, M. Gerring, J. Aishima, K. Levik, B. C. A. Pulford, I. Sikharulidze, D. Sneddon, M. Webber, S. S. Dhesi, F. Maccherozzi, O. Svensson, S. Brockhauser, G. Naray and A. W. Ashton, *J. Synchrotron Rad.*, 2015, **22**, 853-858.
- [161] X. Qiu, J. W. Thompson and S. J. L. Billinge, *J. Appl. Crystallogr.*, 2004, **37**, 678.
- [162] P. Juhas, T. Davis, C. L. Farrow and S. J. L. Billinge, *J. Appl. Crystallogr.*, 2013, **46**, 560-566.
- [163] C. L. Farrow, P. Juhas, J. W. Liu, D. Bryndin, E. S. Božin, J. Bloch, P. Th and S. J. L. Billinge, *J. Phys: Condens. Matter*, 2007, **19**, 335219.
- [164] P. Brüesch, *Phonons: Theory and Experiments II: Experiments and Interpretation of Experimental Results*, Springer Science & Business Media, 2012.
- [165] M. Rode, A. Borgschulte, A. Jacob, C. Stellmach, U. Barkow and J. Schoenes, *Phys. Rev. Lett.*, 2001, **87**, 235502.
- [166] A. N. Singh, *Appl. Spectrosc. Rev.*, 2016, **51**, 359-378.
- [167] P. Hautojärvi and C. Corbel, in *Positron spectroscopy of solids*, IOS press, 1995, pp. 491-532.
- [168] E. H. Hall, *Am. J. Math.*, 1879, **2**, 287-292.
- [169] ULVACZEM3RIKO, *Seebeck-Coefficient and Eleectric-Resistance-Measuring-System Manual*, 2012.
- [170] W. J. Parker, R. J. Jenkins, C. P. Butler and G. L. Abbott, *J. Appl. Phys.*, 1961, **32**, 1679-1684.
- [171] R. D. Cowan, *J. Appl. Phys.*, 1963, **34**, 926-927.

PART 2

Origin of Low Lattice Thermal Conductivity in Binary IIIA - VIA Compounds

Chapter 2.1



**Ultralow Thermal Conductivity in
Chain-like TlSe Due to Inherent Tl⁺
Rattling**

Ultralow Thermal Conductivity in Chain-like TlSe Due to Inherent Tl⁺ Rattling[†]

Summary

Understanding the mechanism that correlates phonon transport with chemical bonding and solid-state structure is the key to envisage and develop materials with ultralow thermal conductivity, which are essential for efficient thermoelectrics and thermal barrier coatings. We synthesised thallium selenide (TlSe), which comprised of intertwined stiff and weakly bonded substructures, exhibits intrinsically ultralow lattice thermal conductivity (κ_{lat}) of 0.62 - 0.4 W/mK in the range 300 to 525 K. Ultralow κ_{lat} of TlSe is a result of its low energy optical phonon modes which strongly interacts with the heat carrying acoustic phonons. Low energy optical phonons of TlSe are associated with the intrinsic ratter-like vibration of Tl⁺ cations in the cage constructed by the chains of (TlSe₂)_n⁻, as evident in low temperature heat capacity, terahertz (THz) time-domain spectroscopy and temperature dependent Raman spectroscopy. Density functional theoretical (DFT) analysis reveals the bonding hierarchy in TlSe which involves ionic interaction between Tl⁺-Se while Tl³⁺-Se bonds are covalent, which causes significant lattice anharmonicity and intrinsic rattler like low energy vibrations of Tl⁺, resulting in ultralow κ_{lat} .

[†]M. Dutta, S. Matteppanavar, M. V. D. Prasad, J. Pandey, A. Warankar, P. Mandal, A. Soni, U. V. Waghmare and K. Biswas. *J. Am. Chem. Soc.*, 2019, **141**, 20293–20299.

2.1.1. Introduction

Heat is the primary channel for drainage of unutilized energy, thus, its effective management through thermoelectrics,¹⁻³ thermal barrier coatings and refractories⁴ relies on the solid-state materials that obstruct the heat transport efficiently, by virtue of their ultralow thermal conductivity (κ). Thus, understanding the mechanism of thermal transport and the ability to tune its transport by tailoring the chemical bonding and solid-state structures stand crucial to develop energy efficient materials.⁵ Within the kinetic theory, the lattice thermal conductivity (κ_{lat}) is described as $\kappa_{\text{lat}} = 1/3 C_v \nu l$, where C_v is the specific heat at constant volume, ν is the group velocity of phonon and l represents the phonon mean free path. Most common studies to reduce the κ_{lat} of a material have largely focussed on deploying features that are “*extrinsic*” to the material, for example through solid solution point defects, nano and meso-scale structuring of the lattice, all of which reduce the phonon relaxation time and impede the heat flow.⁶⁻⁸ Although the aforementioned strategies lower the κ_{lat} of a material, they often adversely affect the electrical mobility. It is thus desirable to uncover “*intrinsic*” lattice dynamical features of a material to cause ultralow κ_{lat} without compromising its efficiency of the electrical conduction.

Rigorous probes into the lattice dynamics and phonon-transport mechanisms have unearthed various avenues to lower the κ_{lat} of a material.³ Accommodation of guest atoms into the cage-like structural voids of compounds like clathrates⁹ and skutterudites¹⁰ leads to low frequency rattling-like motion of the guest atoms, thus lowering the κ_{lat} . Likewise, Zintl compounds like InTe,¹¹ TlInTe₂¹², Tl₃VSe₄¹³ and NaCoO₂¹⁴ also contain intrinsic rattling cations within a rigid anionic framework. Fluid-like movement of cations in a stiff crystalline matrix also causes lowering of κ_{lat} as seen in the cases of “Phonon Glass-Electron Crystal (PGEC)” compounds such as Cu₂Se,¹⁵ Cu₃SbSe₃,¹⁶ AgCrSe₂¹⁷ and AgCuX (X = S, Se and Te)^{18, 19}. Large lattice anharmonicity, which often arises from participation of ns^2 lone pairs of an atom also shown to induce phonon obstruction and hence lowering the κ_{lat} of a compound.^{20, 21} Compounds with two dimensional (2D) layered structure such as SnSe,^{3, 22} BiSe,²³ and GeSe²⁴ contain different bonding environments in between the layers and intra layers, coupled with lone pair led anharmonicity display innate ultralow κ_{lat} . Thus, exploring new compounds with

intrinsically low κ_{lat} and understanding of their chemical bonding and lattice dynamics which influence the phonon transport are essential to develop new thermoelectrics and thermal barrier coatings.

Herein, we have synthesized a simple binary Zintl compound TlSe, which shows intrinsically ultralow κ_{lat} of 0.62-0.4 W/mK in the range 300 to 525 K. To comprehend the cause for the ensuing ultralow κ_{lat} and its relationship with the lattice dynamics and chemical bonding, we have carried out low temperature heat capacity measurements, THz time-domain spectroscopy (THz-TDS), temperature dependent Raman spectroscopy and augmented our observations with density functional theoretical (DFT) analysis. Low temperature heat capacity, THz-TDS and Raman spectroscopy revealed the presence of low frequency optical phonon modes which hinder the acoustic phonon transport and lowers the κ_{lat} . TlSe exhibits fascinating hierarchical bonding environments. Presence of distinct Tl^+ and Tl^{3+} cations in different crystallographic positions and their interactions with the neighbouring Se atoms reveal a great deal of bonding heterogeneity (weak and strong bonded substructures) in the lattice. Weakly bonded Tl^+ resides in the cage-like channel constructed by the chains of $(\text{TlSe}_2)_n^{n-}$, which exhibits intrinsic anharmonic rattling dynamics that provides significant phonon damping. First-principles DFT calculations reveal bonding heterogeneity in the system arising from different bonding interactions between Tl^+ -Se (ionic) and Tl^{3+} -Se (covalent) as well as high degree of anharmonicity within the lattice. Phonon density of states (PhDOS) further reveals the presence of low frequency optical modes mainly constituted of “rattler-like” Tl^+ cation which corroborates our experimental findings. We believe that our findings and conclusions are not system specific and are inclusive of a wide range of materials with significant bonding hierarchy that show such impressive intrinsically ultralow κ_{lat} .

2.1.2. Methods

Synthesis. High quality crystalline TlSe prepared by modified Bridgman technique. Used stoichiometric quantities of high-purity Tl (99.999 %) and Se (99.999 %) (total weight of 5 g) in a quartz ampoule, sealed during high vacuum of 10^{-5} torr. The contents were heated up to 773 K in 6 hr, soaked at this temperature for 6 hr and cooled to crystallization temperature 673 K in 3 hr and soaked for 20 hr and further cooled to room temperature

in 6 hr. The obtained product was then finely ground and then Spark Plasma Sintering (SPS) was performed. The Sample was taken in a graphite die of 10 mm diameter. The die was then heated to 523 K in 5 mins; kept at that temperature for 5 mins and then cooled to room temperature in 10 mins. The pressure was maintained at 3.9 kN throughout the sintering process.

Powder X-ray diffraction (PXRD). PXRD measurements were recorded on Bruker D8 diffractometer using Cu K α ($\lambda = 1.5406 \text{ \AA}$) radiation. Rietveld refinement was carried out using Full prof program.

Thermal conductivity. The thermal diffusivity, D, was measured between 300 K and 525 K using laser flash diffusivity technique in Netzsch LFA-457 instrument. The thermal diffusivity was measured along the parallel and perpendicular to the spark plasma sintering pressed direction. Disc-shaped pellets with *ca.* 10 mm x 2 mm dimensions were used for thermal transport measurement. Total thermal conductivity (κ) was estimated using the relation, $\kappa = D \times C_P \times \rho$, where ρ is the density (99%) of the sample and C_P is the specific heat capacity at constant pressure measured with respect to Pyroceram reference-standard in Netzsch LFA-457 instrument. Lattice thermal conductivity (κ_{lat}) is extracted by subtracting electronic thermal conductivity (κ_{el}) from total thermal conductivity. κ_{el} is calculated using the Wiedemann Franz law, $\kappa_{el} = L\sigma T$, where σ is the electrical conductivity and L is the temperature dependent Lorentz number. L is calculated using Single Parabolic Band (SPB) model²⁵. Assuming SPB model Lorenz number (L) is given as:

$$L = \left(\frac{k_B}{e}\right)^2 \frac{3F_0(\eta)F_2(\eta) - 4F_1(\eta)^2}{F_0(\eta)^2} \quad (2.1.1)$$

Where, η is the reduced chemical potential and can be obtained by fitting the experimental Seebeck coefficients. k_B represents Boltzmann constant and $F_n(\eta)$ is the n^{th} order Fermi Integral.

Electronic properties. Electrical conductivity (σ) and Seebeck coefficient (S) were simultaneously measured along the SPS pressing direction under He-atmosphere from 300 K up to 525 K using ULVAC-RIKO ZEM-3 instrument. Rectangular bar shaped

samples (*ca.* $2 \times 2 \times 8$ mm³) cut from cylindrical samples were used for the electrical measurements.

Band gap measurement. Finely ground sample was used to obtain the optical band gap of the synthesized samples. The optical band gap was estimated in a FT-IR Bruker IFS 66V/S spectrometer within the range of 6000 – 400 cm⁻¹. Absorption (α/S) data were derived using Kubelka-Munk equation: $\alpha/S = (1-R)^2/(2R)$, where R is the reflectance, α and S corresponds to absorption and scattering coefficient, respectively. The energy band gaps were deduced from α/S vs E_g (eV) plot.

Raman spectroscopy. Raman measurement was conducted in back scattering geometry using Horiba Jobin-Yvon LabRAM HR evolution Raman spectrometer with 1800 gr/mm and Peltier cooled CCD detector. Temperature dependent Raman measurements were performed using Montana cryostat in the range of 4 - 300 K, using 532 nm Unpolarized excitation laser. Raman spectroscopy measurements have been done with the collaboration of Prof. A. Soni of Indian Institute of Technology (IIT), Mandi.

THz time-domain spectroscopy (THz-TDS). We have used home-built THz time-domain spectrometer of Prof. P. Mandal of IISER, Pune, India to record the THz spectrum of TlSe in reflection geometry. The spectrometer is based on a 4 mJ ultrafast (50 fs) amplified laser system. The details of our THz set-up are described elsewhere.^{26, 27} The use of air-plasma as the THz generation source and employing air-biased coherent detection (ABCD) scheme enables us to extend the spectral function of the sample.²⁸ In the present experiment, time-domain range from 0.5 THz to 15 THz. An enclosure continuously purged with dry nitrogen gas avoids THz absorption by water vapour present in ambient air.

In reflection geometry, the reflected THz waveforms are collected and analyzed to determine the dielectric THz waveforms reflected from a Reference (high resistivity silicon) and the sample (TlSe pallet) are collected in normal incidence. Fourier transformations of the reference and sample THz waveforms and use of Fresnel equation (Eq. 2.1.2) for reflection yield the complex refractive index of the sample.

$$\frac{\tilde{E}_{Sample}(\omega)}{\tilde{E}_{Si}(\omega)} = \frac{\frac{\tilde{n}_{sample}-n_{air}}{\tilde{n}_{sample}+n_{air}}}{\frac{n_{si}-n_{air}}{n_{si}+n_{air}}} \quad (2.1.2)$$

Here, $\tilde{E}_{sample}(\omega)$ and $\tilde{E}_{si}(\omega)$ are the reflected THz electric fields in frequency domain from sample and reference (silicon), respectively. \tilde{n}_{sample} , n_{si} and n_{air} are complex/real refractive indices of sample, reference, and dry air, respectively. High resistivity silicon and dry air are nearly non-absorbing media with their refractive indices ($n_{si} = 3.45$ and $n_{air} = 1$) constant over the frequency range of this study. Complex refractive index is written as, $\tilde{n}_{sample} = n + ik$, where n is the real part of the refractive index and k is the extinction coefficient of the sample. Absorption coefficient (α) is obtained from the relation, $\alpha = 2 \cdot \omega \cdot k/c$, where ω is the angular frequency and c is the speed of light. THz-TDS measurements have been done with the collaboration of Prof. P. Mandal of IISER, Pune.

Computational methods. Electronic and phonon properties are calculated based on the first-principles pseudo potentials within density functional theory (DFT) as implemented in Quantum Espresso code.²⁹ In DFT calculations, we employed generalized gradient approximation (GGA) to the exchange correlation energy functional and used norm-conserving pseudopotentials to treat the interactions between ionic cores and valence electrons, and a plane wave basis with an energy cutoff of 60 Ry (240 Ry) in the representation of the Kohn-Sham wave functions (density). Brillouin zone of the tetragonal unit cell is sampled with a uniform 12x12x12 k-point mesh which is in accordance with Monkhorst-Pack³⁰ scheme. The discontinuity in the occupations number of electronic states near the gap was smeared with Fermi-Dirac distribution functions with a broadening of $k_B T = 0.003$ Ry. Optimized lattice parameters are in agreement with the experimental values. Theoretical calculations have been done with the collaboration of Prof. U. V. Waghmare of JNCASR, Bangalore.

Calculation of minimum thermal conductivity (κ_{min}). Minimum thermal conductivity was calculated using Cahill's model³¹ which is given by:

$$\kappa_{min} = \frac{1}{2} \left(\frac{\pi}{6} \right)^{1/3} k_B V^{-2/3} (2v_t + v_l) \quad (2.1.3)$$

where k_B denotes Boltzmann constant, V being the average volume per atom, and v_t (1486 m/s and 2101 m/s) and v_l (3471 m/s) denotes mean speed of sound in transverse and longitudinal directions obtained from theoretical calculations by deducing the slope of longitudinal and transverse acoustic phonons in the Γ -X direction. For Γ -X direction, κ_{min} value is found to be 0.41 W/mK. For Γ -Z direction the v_t (568 m/s and 568 m/s) and v_l (4378 m/s) values lead to κ_{min} value of 0.32 W/mK.

2.1.3. Results and Discussion

TlSe is a low-dimensional semiconductor with a band gap (E_g) of 0.67 eV (Figure 2.1.1a) belongs to the TIQ (Q = S, Se, Te) family of compounds and possesses chain-like Zintl structure.³² This semiconducting compound^{33, 34} has been earlier studied for γ -ray detectors.³⁵ Highly oriented polycrystals of TlSe were synthesized using a modified Bridgman technique, then dense pellet (~99 %) was further prepared by spark plasma sintering (SPS). Figure 2.1.1b shows the Rietveld refinement of the PXRD pattern at room temperature. TlSe procures tetragonal symmetry having space group $I4/mcm$ and the obtained lattice parameters $a = b = 8.01171$ (3) Å; $c = 6.96665$ (2) Å; unit cell volume = 447.172 (2) Å³.³² The refinement parameters are given in Table 2.1.1.

TlSe is a mixed valent compound, *i.e.*, $Tl^+ Tl^{3+} (Se^{2-})_2$, the univalent and trivalent thallium ions occupy two crystallographically inequivalent sites (Figure 2.1.1c, d). The Tl^{3+} cations form covalent (sp^3) Tl – Se bonds and are located at the center of $(TlSe_2)_n^{n-}$ tetrahedra, which are linked by joint horizontal edges and form linear chains along the c -axis (Figure 2.1.1c, d). Tl^{3+} can only donate 3 electrons per tetrahedra; and as a result, the tetrahedra remains in the form of anionic chains of $(TlSe_2)_n^{n-}$. The Tl^{3+} –Se distance of 2.69 Å nearly matches the sum of the covalent radii of Tl^{3+} (1.49 Å) and Se (1.17 Å) with the Se – Tl – Se angle being 115° thus imparting a high degree of covalency in the Tl^{3+} -Se bond. However, the Tl^+ with a $6s^2$ lone pair in 4a Wyckoff position is surrounded by eight Se atoms, which form slightly deformed cage like Thomson cubes and are skewed by a small angle. To maintain the charge balance, this Tl atom donates one electron and remains in +1 oxidation states. Tl^+ – Se distance is 3.43 Å that is close to the sum of the

ionic radii of Tl^+ (1.59 Å for CN = 8) and Se^{2-} (1.98 Å), which indicates towards a weaker electrostatic interaction between Tl^+ and $(TlSe_2)^-$ tetrahedra. The presence of bonding hierarchy (strong and weak bonding) within a lattice can be an excellent motivation to obtain low κ_{lat} in TlSe.

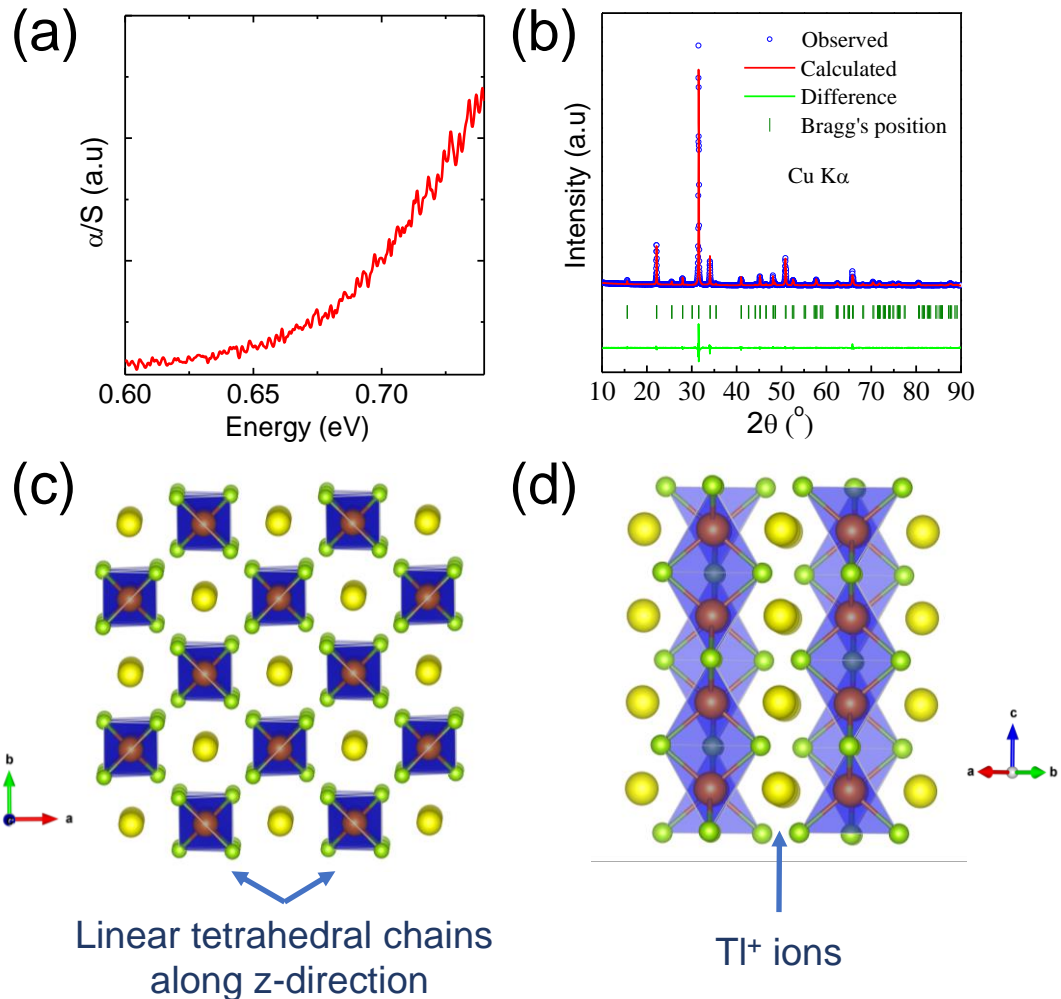


Figure 2.1.1. (a) Band gap of TlSe. (b) Rietveld refinement of the PXRD of TlSe. (c) Structure of TlSe viewed down the c-axis. (d) Tl⁺ rattles in the channel. Yellow, orange and green balls represent Tl⁺, Tl³⁺ and Se atoms respectively.

Figure 2.1.2a shows the κ_{lat} of TlSe for both the directions, *i.e.*, parallel (\parallel) and perpendicular (\perp) to spark plasma sintering (SPS) pressing direction. Total thermal conductivity κ (Figure 2.1.2b) is similar to κ_{lat} (Figure 2.1.2a) as the thermal transport is dominated by phonons rather than charge carrier in TlSe. The heat capacity estimated using a reference Pyroceram is given in Figure 2.1.2c. Measurement in both directions

show intrinsically low κ_{lat} within the temperature range of 300 – 525 K and is found to be ultralow compared to other state of the art low κ_{lat} materials (Figure 2.1.2d).^{1, 2, 23, 36-38} κ_{lat} of TlSe varies slightly from 0.63 W/mK at 300 K to 0.43 W/mK at 523 K for || direction, whereas for \perp direction it varies from 0.67 W/mK at 300 K to 0.59 W/mK at 525 K, lying close to the theoretical minimum thermal conductivity (κ_{min}) of 0.41 W/mK obtained using Cahill's formulation as given in equation 2.1.3.³¹ Small κ_{lat} difference between the || and \perp direction is due to anisotropy arising from 1D chain like structure of TlSe.

Table 2.1.1. Rietveld refined structural parameters.

Space group: I4/mcm; a = b = 8.01171 (3) Å; c = 6.96665 (2) Å; unit cell volume = 447.172 (2) Å ³ R _{wp} = 10.1 and $\chi^2 = 6.88$						
Atom	x	y	z	Occupancy	Wyck.	U _{iso} (Å ²)
Se	0.18063	0.68063	0.00000	1.053	8h	0.015
Tl (1)	0.0	0.0	0.25	1.000	4a	0.026
Tl (2)	0.0	0.5	0.25	0.991	4b	0.023

In order to determine the underlying cause of the low κ_{lat} , we have investigated the nature of chemical bonding in TlSe through visualization of charge density and electron localization function (ELF) (Figure 2.1.3a, b respectively). These real-space functions within DFT can provide a lucid understanding of the nature of bonding. In Figure 2.1.3a, two features are evident: firstly, the overlapping charge density of Tl³⁺ and Se²⁻ indicates covalent bonding that builds the edge sharing tetrahedra. Secondly, Tl⁺, having spherical charge density (due to 6s² lone pair), electrostatically (ionic) interacting with the surrounding chains of (TlSe₂)_n⁻. The ELF (Figure 2.1.3b), which accounts for the degree of electron localization due to Pauli repulsion, shows a symmetrically localized state of lone pair around Tl⁺ in the channel, resulting in a weak electrostatic interaction with the (TlSe₂)_n⁻ tetrahedra. The asymmetric lobe-shaped electron clouds near the Se

atoms resulted from the hybridization with Tl^{3+} indicating a covalent interaction between Tl^{3+} and Se^{2-} .

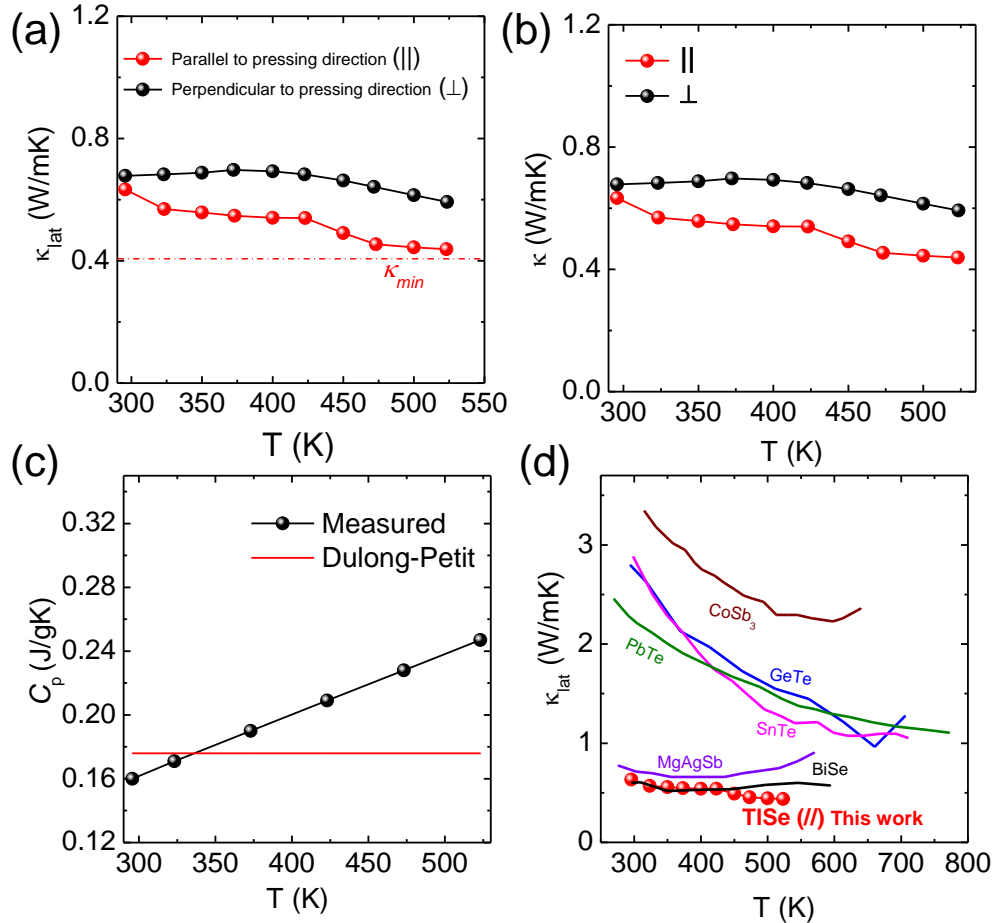


Figure 2.1.2. (a) Lattice thermal conductivity (κ_{lat}) and (b) total thermal conductivity (κ) of TlSe measured (\parallel) and (\perp) to SPS pressing directions. (c) T dependent C_p measured using Pyroceram standard and Dulong-Petit calculated C_p . (d) Comparative plot of κ_{lat} vs. Temperature with some well-known ultralow thermal conductive compounds. References imported for the plot are SnTe ,¹ PbTe ,² BiSe ,²³ GeTe ,³⁶ CoSb_3 ,³⁷ and MgAgSb .³⁸

The Rietveld refinement of the PXRD pattern revealed higher atomic displacement parameters (ADPs) of Tl atom (Table 2.1.1) as compared to Se. ADPs give a qualitative idea of the mean displacement of atoms from its mean Wyckoff position. The potential energy vs. displacement plot for each atom (Figure 2.1.3c) reveals that Tl^+ by virtue of their weak electrostatic interaction with the $(\text{TlSe}_2)_n^{n-}$ tetrahedra, shows a shallow potential in both x and z-directions. Tl^{3+} and Se^{2-} which are covalently bonded to

each other shows much deeper potentials which resonates with the charge density function and ELF (Figure 2.1.3a, b respectively). The flat potential vs. displacement indicates “rattler-like” motion of the Tl^+ in the cage.

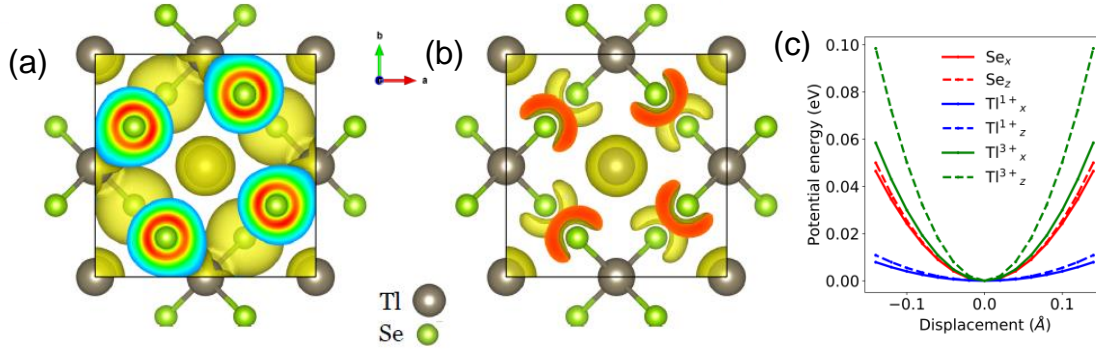


Figure 2.1.3. Isosurface of (a) electronic charge density plotted at isovalue of 0.0225 and of (b) electron localization function (ELF) of TlSe at isovalue of 0.85. Grey balls signify Tl atoms while green balls represent Se atoms. (c) Plot of total energy governing the dynamics of atomic displacements along x and z -directions.

To investigate into the mechanism for ultralow κ_{lat} in TlSe , we have performed low temperature (2-120 K) heat capacity (C_p) measurements. As the temperature decreases, C_p of TlSe decreases gradually and no anomalies associated with any structural transitions are observed (Figure 2.1.4a). Figure 2.1.4b presents the C_p/T vs. T^2 plot within the temperature range of 2-22 K. Debye model, which accounts largely for acoustic phonon modes with longer wavelength, is found to be a poor descriptor for the obtained data. Hence Einstein oscillators were incorporated to get a proper fitting. A combined Debye-Einstein^{12, 23} model is given as:

$$\frac{C_p}{T} = \gamma + \beta T^2 + \sum_n \left(A_n (\theta_{E_n})^2 \cdot (T^2)^{-\frac{3}{2}} \cdot \frac{e^{\frac{\theta_{E_n}}{T}}}{\left(e^{\frac{\theta_{E_n}}{T}} - 1 \right)^2} \right) \quad (2.1.4)$$

Eq. 2.1.4 provides contributions arising from the electronic and phonon regions quantitatively where the first and second term of above equation denotes the electronic and Debye lattice contribution with $\beta = C \cdot (12\pi^4 N_A k_B / 5) \cdot (\Theta_D)^{-3}$, where N_A is Avogadro Number, k_B is Boltzmann constant and Θ_D is Debye temperature, respectively. The parameter C is assigned as $C = 1 - \sum_n A_n / 3NR$, where N being number of atoms per

formula unit and R is the gas constant (8.314 J/mol. K). The last summation term signifies the Einstein oscillator modes where A_n being the pre-factor of n^{th} Einstein mode. A total of 3 distinct oscillators having characteristic temperatures of $\Theta_{E1} = 43.46$ K, $\Theta_{E2} = 22.74$ K and $\Theta_{E3} = 73.41$ K were required for a proper description of the data. These Einstein modes (Θ_{E1} , Θ_{E2} and Θ_{E3}) are attributed to the low-energy optical modes originating from feebly TI^+ -rattlers. These Einstein oscillators couple with heat-carrying acoustic phonon modes decreasing the group velocities of the latter and thereby suppressing κ_{lat} . All the obtained fitting parameters are given in Table 2.1.2. Inset of figure 2.1.4b shows the C_p/T^3 vs. T plot. A broad boson like peak around 9K that can be fitted only with combined Debye – Einstein model corroborates the existence of Einstein oscillators in the sample. This Boson like peak is indicative towards the presence of excess optical phonon density of states (PhDOS).⁹ The Debye temperature (Θ_D) derived from the lattice contribution is found to be 217 K.

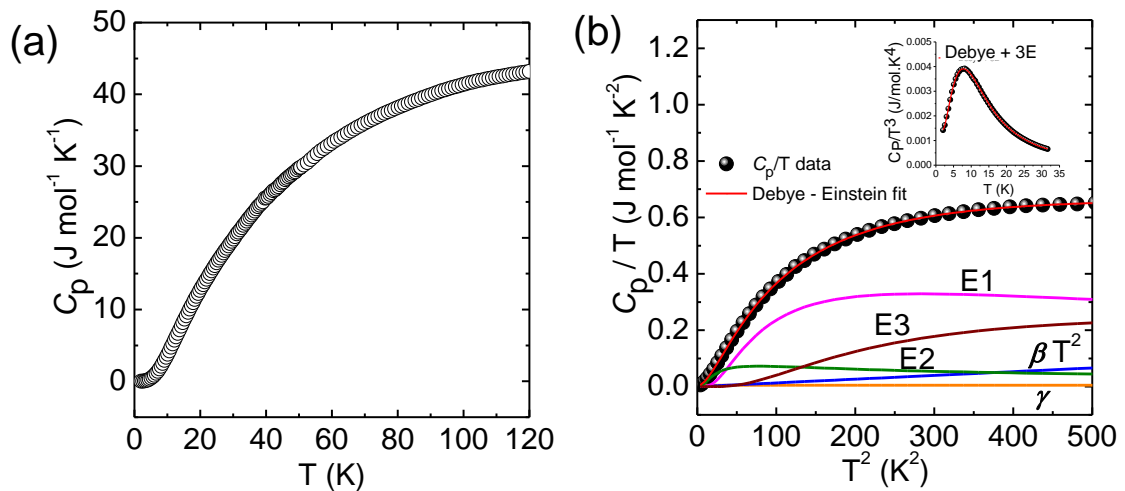


Figure 2.1.4. (a) Temperature dependent heat capacity (C_p). (b) Debye-Einstein fit of C_p/T vs T^2 along with individual contributions of low energy Einstein modes. Inset of Figure b shows Boson like peak and can only be fitted using a combination of Debye and Einstein model.

We have complimented our experimental observations with first-principles DFT calculations to gain insight into the relevant phonon scattering mechanisms. An important indicator of rattler atoms is the presence of a non-dispersive (flat) band(s) in phonon dispersion along high symmetry directions in the Brillouin Zone (BZ). TISe exhibits such

non-dispersive bands at fairly low frequencies (Figure 2.1.5a) indicating the presence of rattling atom in the system. In full relaxed structure of TlSe (atomic positions and lattice constants, black lines), this rattler band is weakly unstable having imaginary frequency of $\sim i0.2$ THz (Figure 2.1.5a), which gets stabilized in the optimized structure at 1 GPa (red lines). This imaginary frequency indicates that ambient TlSe structure is at the brink of lattice instability (Figure 2.1.5a, b), and the rattler modes must have large Gruneisen parameter. From the frequencies of phonons (see Table 2.1.3), we find that low energy optical phonons at 0.51 THz (~ 17 cm^{-1}) and 0.65 THz (26 cm^{-1}) at $P = 1$ GPa constitutes of flat bands. These values are in reasonable agreement with their values estimated from model fit to the measured heat capacity. Highest frequencies of vibrations of TlSe at $P = 0$ GPa and $P = 1$ GPa are 6.12 THz and 6.21 THz respectively. Partial phonon density of states (Figure 2.1.5c) reveal the dominance of Tl⁺ vibrations at low frequencies, whereas, in the moderate to high frequency range, vibrational activity of Se atoms is prominent.

Table 2.1.2. Parameters obtained after C_p fitting using 3 Einstein Oscillators.

Parameters	Values
$\gamma / \text{J mol}^{-1} \text{K}^{-2}$	$0.00483 \pm 9.91\text{E-}4$
$\beta / 10^{-4} \text{J mol}^{-1} \text{K}^{-4}$	$1.32 \pm 2.95\text{E-}3$
Θ_{E1}/K	43.46 ± 2.32
Θ_{E2}/K	22.74 ± 1.46
Θ_{E3}/K	73.41 ± 4.72
A_1	9.38 ± 1.32
A_2	1.08 ± 0.29
A_3	11.57 ± 0.82
$\Theta_D (\text{K})$	217 K
R^2	0.99999
χ^2	7.25E-7

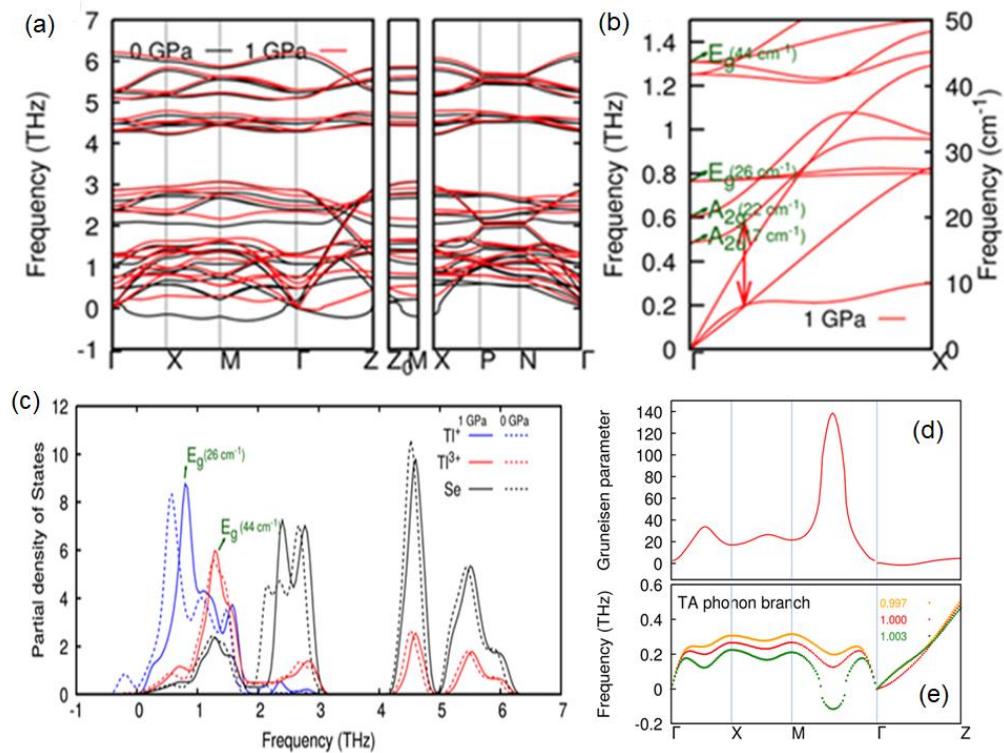


Figure 2.1.5. (a) Phonon dispersion of TlSe at $P = 0$ GPa and $P = 1$ GPa. (b) Avoided-crossing between branches of TA and TO phonons highlighted in the low frequency phonon dispersion along Γ to X, marking symmetry labels of phonons at Γ , (c) Partial phonon DOS of TlSe, showing dominance of Tl⁺ (blue) displacements in the low frequency vibrations. (d) Gruneisen parameters corresponding to the TA phonon branch ($P = 1$ GPa) of TlSe. (e) Sensitivity of dispersions of TA branch to the change in volume.

It is important to note that the two E_g modes marked at 26 cm^{-1} and 44 cm^{-1} in Figure 2.1.5b correspond to the peaks in the PDOS of Tl⁺ and Tl³⁺ ions (Figure 2.1.5c) respectively for $P = 1$ GPa. Interestingly, their frequencies match closely with the measured E_g modes in Raman spectrum at room temperature (Figure 2.1.7a). Visualization of their eigen vectors (in Figure 2.1.6f, j) shows displacements of Tl⁺ and Tl³⁺ atoms in the a-b plane, which may cause significant anharmonic phonon scattering of acoustic modes.

A_{2u} mode marked at 17 cm^{-1} involves dominant z-displacements of Tl⁺ atoms along with collective anti-parallel displacements of chains of $(\text{TlSe}_2)_n^-$ tetrahedra. In contrast, A_{2g} mode at 22 cm^{-1} involves axial rotations of tetrahedral chains and displacements of Tl⁺ in z-direction. Vibrations in the low frequency range, up to $\omega(E_g) = 26\text{ cm}^{-1}$ involve displacements of Tl⁺ atoms are along z-direction. Thus, flat bands containing z-polarized

A_{2u} and A_g as well as those containing ab-polarized E_g modes are responsible to low κ_{lat} of TlSe. A strong acoustic-optic hybridization is observed here which manifests as avoided-crossing and are responsible for low κ_{lat} in TlSe which is akin to some known clathrate compounds^{39, 40}.

Table 2.1.3. Calculated zone centre phonon frequencies of TlSe.

0 GPa			1 GPa	
S. No.	Mode	Freq. (THz)	Mode	Freq. (THz)
1	A_{2u}	-0.0656	A_{2u}	0.1854
2	E_u	0.1898	E_u	0.2108
3	A_{2u}	0.3085	A_{2u}	0.5152
4	E_g	0.4866	A_{2g}	0.6547
5	A_{2g}	0.7735	E_g	0.7702
6	E_u	1.0804	E_u	1.2607
7	E_g	1.3273	E_g	1.3144
8	A_{2g}	2.0915	A_{2g}	2.3686
9	E_u	2.4182	E_u	2.5184

10	B _{1g}	2.6219	B _{1g}	2.7618
11	B _{2g}	2.8815	B _{2g}	2.8737
12	A _{2u}	4.2950	A _{2u}	4.3368
13	B _{1u}	4.3106	B _{1u}	4.3442
14	E _g	4.4984	E _g	4.5926
15	A _{1g}	5.1316	A _{1g}	5.1186
16	E _u	5.2448	E _u	5.3162
17	B _{2g}	6.1214	B _{2g}	6.2193

To assess anharmonic contributions of phonons in the flat band to thermal transport, we calculated mode Gruneisen parameters using phonon dispersions of TlSe determined at three different crystal cell volumes. Gruneisen parameter, γ , of each phonon mode [q; p] (\mathbf{q} is the wave vector and p is the phonon polarization index) is a measure of its volume dependence, which is calculated using finite difference formula:

$$\gamma_p(\mathbf{q}) = - \frac{V}{\omega_p(\mathbf{q})} \frac{\partial \omega_p(\mathbf{q})}{\partial V} \cong - \frac{V}{2[\omega_p(\mathbf{q})]^2} \langle e_p(\mathbf{q}) \left| \frac{\Delta D(\mathbf{q})}{\Delta V} \right| e_p(\mathbf{q}) \rangle \quad (2.1.5)$$

where V is the unit cell volume, ω is the phonon frequency, D is the dynamical matrix, and e is the eigen vector. The calculated γ of phonons in the flat band are shown in Figure 2.1.5d along with the phonon branches corresponding to three unit cell volumes used in the calculation. Throughout Γ -X-M- Γ line, mode γ is significantly high and it shows anomalously high values in M- Γ line ($\gamma \sim 140$). The striking sensitivity of this particular flat band to the change of unit cell volume (Figure 2.1.5e) explains the unusually high values of the mode γ which originated from the weak electrostatic interaction of Tl⁺ in

TlSe. Mention must be made that mode γ for other phonon branches are calculated to be less than 5. Such large values of γ mean the acoustic modes couple strongly with TO phonons in the flat band, which affect the acoustic phonon propagation, thereby lowering the thermal conductivity of TlSe.

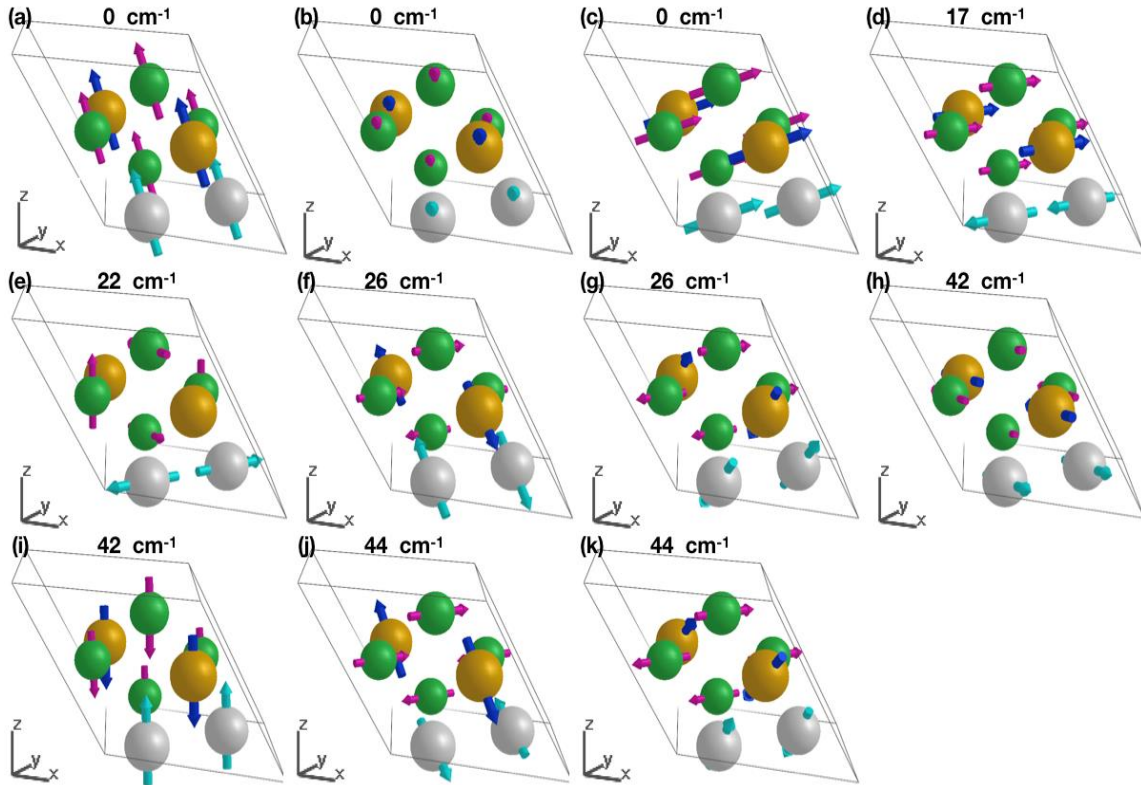


Figure 2.1.6. Eigen vector visualizations for the phonon modes at Γ point for 1 GPa case calculated using optimized lattice constant. Grey balls signify Tl^+ , Gold balls represent Tl^{3+} whereas Green balls signify Se atoms.

Finally, we have visualized these low energy optical modes using THz-TDS and Raman spectroscopy. To understand the phonon dynamics and possibly the role of Tl^+ rattler at atomic level, we have performed the THz-TDS at room temperature and Raman spectroscopic measurements at varied temperatures (4-300 K). The group theoretical analysis for TlSe (space group $I4/mcm$ (D_{4h}^{18})) reveals seventeen normal modes of vibrations active at Brillouin zone center which have been classified by following irreducible representation:

$$\Gamma = A_{1g} + 2A_{2g} + B_{1g} + 2B_{2g} + 3E_g + B_{1u} + 3A_{2u} + 4E_u$$

among these modes, only seven modes, namely, A_{1g} , B_{1g} , $2B_{2g}$ and $3E_g$ are Raman active. On the other hand, seven modes ($3A_{2u}$ and $4E_u$) are THz active. The centrosymmetric TISe should have mutually exclusive Raman and THz (IR) active vibrational normal modes. Hence, the Raman and THz spectral analysis are complementary to each other, enabling us to observe all low frequency optical phonons.

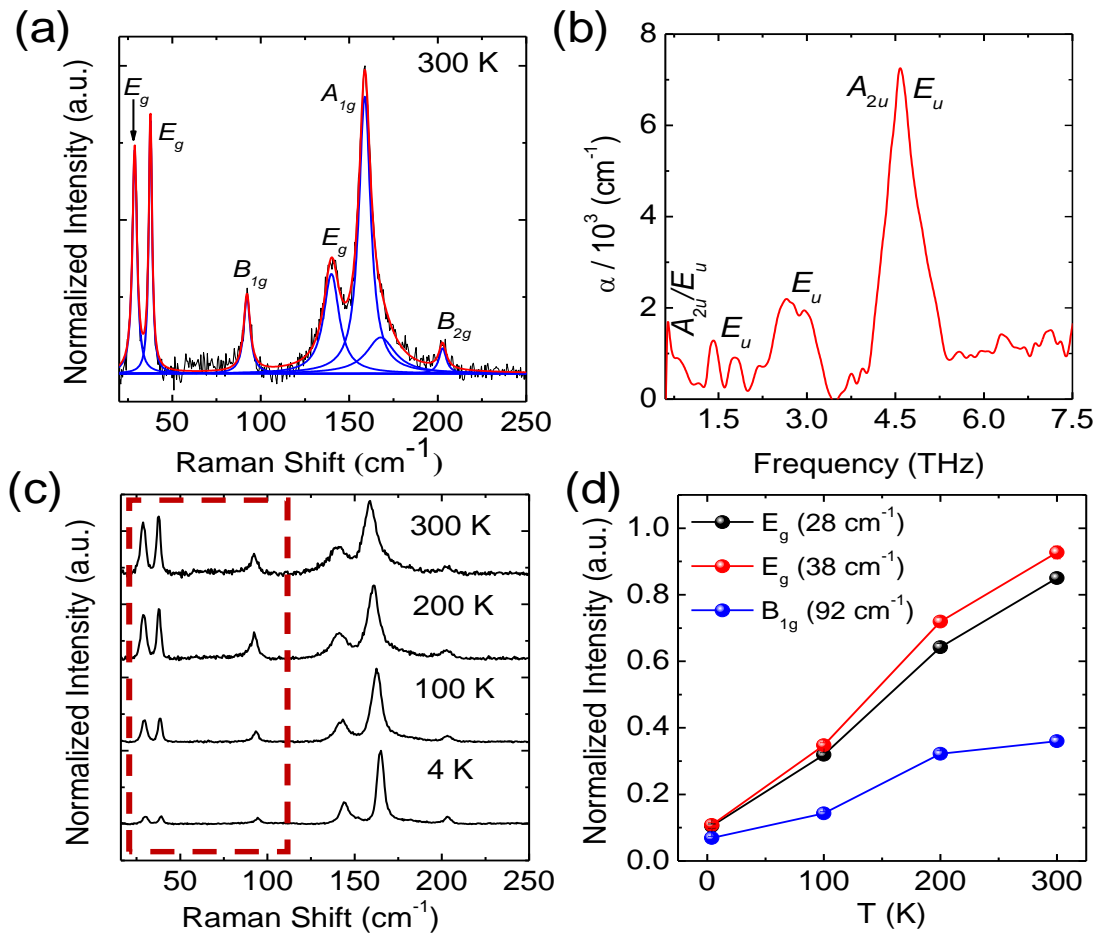


Figure 2.1.7. (a) Raman spectrum at 300 K with their corresponding peaks assigned. (b) THz-TDS spectrum of TISe at room temperature in reflection geometry. (c) Temperature dependent Raman spectra and (d) Normalized intensity of the first 3 low energy Raman peaks.

Room temperature Raman spectra for TISe is shown in Figure 2.1.7a, where these seven modes have been presented at ~ 28 cm⁻¹ (E_g), ~ 38 cm⁻¹ (E_g), ~ 92 cm⁻¹ (B_{1g}), ~ 140 cm⁻¹ (E_g), ~ 158 cm⁻¹ (A_{1g}), ~ 168 cm⁻¹ and ~ 203 cm⁻¹ (B_{2g}). The Raman data is taken at

an excitation of 532 nm. Figure 2.1.7b shows the broadband (0.6 to 7.5 THz) THz-TDS spectrum of TlSe collected at room temperature in reflection geometry. We observe several broad peaks below 4 THz (133 cm^{-1}) and a strong peak at 4.6 THz (153 cm^{-1}). The frequencies of the observed optical modes (possible assignments are in Figure 2.1.7b) are in reasonable agreement with the DFT prediction. THz spectrum shows additional peaks ($\sim 2.2 \text{ THz}$ and $\sim 3.7 \text{ THz}$) than the number of allowed transitions within the frequency range, which is attributed to the large anharmonicity of the lattice that may lead to the violation of the transition selection rules.

Temperature dependent Raman spectra from 4 K to 300 K are shown in Figure 2.1.7c. Peak intensities of the Raman modes are normalized with the intensity of A_{1g} modes. The low frequency modes i.e., $E_g \sim 28 \text{ cm}^{-1}$ and $E_g \sim 38 \text{ cm}^{-1}$ are in good agreement with our DFT calculations and heat capacity data, which also complements the THz-TDS findings. The normalized intensity (area under the curve) of both these low energy phonon modes are shown to increase with increasing the temperature (Figure 2.1.7d). The increase in relative intensities of the low frequency modes confirms the enhancement in the phonon population which in turn gives higher scattering of the acoustic phonons and thereby reducing κ_{lat} of TlSe, significantly.

2.1.4. Conclusion

Simple binary Zintl-type TlSe is a mixed valent compound, i.e., $\text{Tl}^+ \text{Tl}^{3+} (\text{Se}^{2-})_2$, possessing noticeable bonding hierarchy in structural sublattices, exhibits ultralow lattice thermal conductivity (κ_{lat}) of 0.62 - 0.4 W/mK in the range 300 to 525 K. Low lying optical phonon modes generated by intrinsic Tl^+ rattling within the one-dimensional channel formed between the chains of $(\text{TlSe}_2)_n^-$ significantly hinders the movement of the heat carrying acoustic phonons and thereby obstruct the heat conduction. Anomalously high lattice anharmonic interaction between acoustic modes and the rattler TO modes is evident in high Gruneisen parameter arising from the freely vibrating Tl^+ rattler. Eigen displacements analysis of TA and TO phonons indicated avoided crossing between themselves, which indicates rattling dynamics. Finally, to shed light on inherent Tl^+ rattling, room temperature THz-TDS measurement and temperature dependent Raman spectroscopic measurements have been performed, which demonstrate the

presence of several low energy optical modes. The lowest frequency optical modes correspond to the caged intrinsic TI^+ rattler and their intensity increases with the increase in temperature which provides additional channels for phonon scattering. Our findings provide a strong viewpoint to unearth and design materials with bonding hierarchy and lattice anharmonicity which can exhibit intrinsically ultralow κ_{lat} .

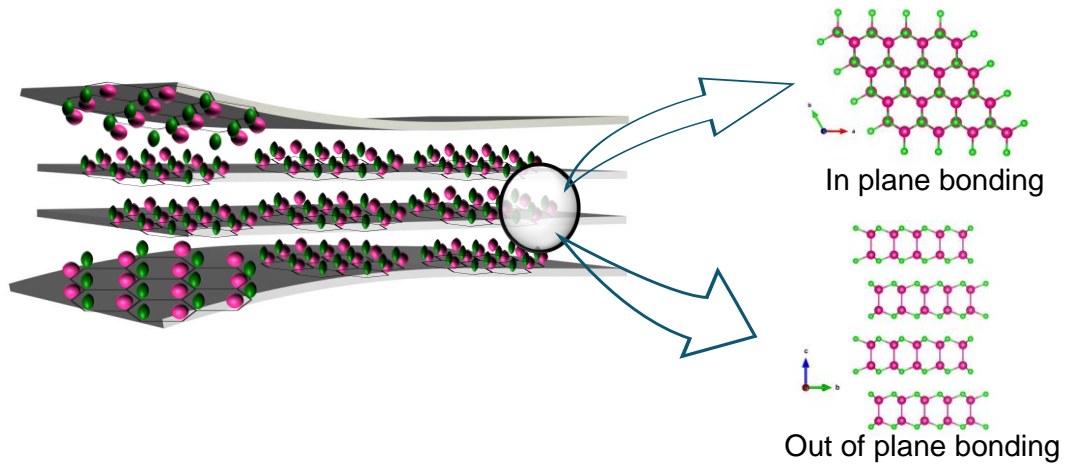
2.1.5. References

- [1] G. Tan, L.-D. Zhao and M. G. Kanatzidis, *Chem. Rev.*, 2016, **116**, 12123-12149.
- [2] L.-D. Zhao, V. P. Dravid and M. G. Kanatzidis, *Energy Environ. Sci.*, 2014, **7**, 251-268.
- [3] C. Chang, M. Wu, D. He, Y. Pei, C.-F. Wu, X. Wu, H. Yu, F. Zhu, K. Wang, Y. Chen, L. Huang, J.-F. Li, J. He and L.-D. Zhao, *Science*, 2018, **360**, 778.
- [4] N. P. Padture, M. Gell and E. H. Jordan, *Science*, 2002, **296**, 280.
- [5] M. K. Jana and K. Biswas, *ACS Energy Lett.*, 2018, **3**, 1315-1324.
- [6] K. Biswas, J. He, I. D. Blum, C.-I. Wu, T. P. Hogan, D. N. Seidman, V. P. Dravid and M. G. Kanatzidis, *Nature*, 2012, **489**, 414.
- [7] B. Poudel, Q. Hao, Y. Ma, Y. Lan, A. Minnich, B. Yu, X. Yan, D. Wang, A. Muto, D. Vashaee, X. Chen, J. Liu, M. S. Dresselhaus, G. Chen and Z. Ren, *Science*, 2008, **320**, 634.
- [8] M. Samanta and K. Biswas, *J. Am. Chem. Soc.*, 2017, **139**, 9382-9391.
- [9] T. Takabatake, K. Suekuni, T. Nakayama and E. Kaneshita, *Rev. Mod. Phys.*, 2014, **86**, 669-716.
- [10] X. Shi, J. Yang, J. R. Salvador, M. Chi, J. Y. Cho, H. Wang, S. Bai, J. Yang, W. Zhang and L. Chen, *J. Am. Chem. Soc.*, 2011, **133**, 7837-7846.
- [11] M. K. Jana, K. Pal, U. V. Waghmare and K. Biswas, *Angew. Chem. Int. Ed.*, 2016, **55**, 7792-7796.
- [12] M. K. Jana, K. Pal, A. Warankar, P. Mandal, U. V. Waghmare and K. Biswas, *J. Am. Chem. Soc.*, 2017, **139**, 4350-4353.
- [13] S. Mukhopadhyay, D. S. Parker, B. C. Sales, A. A. Puretzky, M. A. McGuire and L. Lindsay, *Science*, 2018, **360**, 1455.
- [14] D. J. Voneshen, K. Refson, E. Borissenko, M. Krisch, A. Bosak, A. Piovano, E. Cemal, M. Enderle, M. J. Gutmann, M. Hoesch, M. Roger, L. Gannon, A. T. Boothroyd, S. Uthayakumar, D. G. Porter and J. P. Goff, *Nat. Mater.*, 2013, **12**, 1028.

- [15] H. Liu, X. Shi, F. Xu, L. Zhang, W. Zhang, L. Chen, Q. Li, C. Uher, T. Day and G. J. Snyder, *Nat. Mater.*, 2012, **11**, 422.
- [16] W. Qiu, L. Xi, P. Wei, X. Ke, J. Yang and W. Zhang, *Proc. Natl. Acad. Sci. U. S. A.*, 2014, **111**, 15031.
- [17] B. Li, H. Wang, Y. Kawakita, Q. Zhang, M. Feygenson, H. L. Yu, D. Wu, K. Ohara, T. Kikuchi, K. Shibata, T. Yamada, X. K. Ning, Y. Chen, J. Q. He, D. Vaknin, R. Q. Wu, K. Nakajima and M. G. Kanatzidis, *Nat. Mater.*, 2018, **17**, 226-230.
- [18] S. Ishiwata, Y. Shiomi, J. S. Lee, M. S. Bahramy, T. Suzuki, M. Uchida, R. Arita, Y. Taguchi and Y. Tokura, *Nat. Mater.*, 2013, **12**, 512.
- [19] S. Roychowdhury, M. K. Jana, J. Pan, S. N. Guin, D. Sanyal, U. V. Waghmare and K. Biswas, *Angew. Chem. Int. Ed.*, 2018, **57**, 4043-4047.
- [20] D. T. Morelli, V. Jovovic and J. P. Heremans, *Phys. Rev. Lett.*, 2008, **101**, 035901.
- [21] M. Dutta, K. Pal, U. V. Waghmare and K. Biswas, *Chem. Sci.*, 2019, **10**, 4905-4913.
- [22] L.-D. Zhao, S.-H. Lo, Y. Zhang, H. Sun, G. Tan, C. Uher, C. Wolverton, V. P. Dravid and M. G. Kanatzidis, *Nature*, 2014, **508**, 373.
- [23] M. Samanta, K. Pal, P. Pal, U. V. Waghmare and K. Biswas, *J. Am. Chem. Soc.*, 2018, **140**, 5866-5872.
- [24] S. Roychowdhury, T. Ghosh, R. Arora, U. V. Waghmare and K. Biswas, *Angew. Chem. Int. Ed.*, 2018, **57**, 15167-15171.
- [25] L.-D. Zhao, S.-H. Lo, J. He, H. Li, K. Biswas, J. Androulakis, C.-I. Wu, T. P. Hogan, D.-Y. Chung, V. P. Dravid and M. G. Kanatzidis, *J. Am. Chem. Soc.*, 2011, **133**, 20476-20487.
- [26] G. R. Yettapu, D. Talukdar, S. Sarkar, A. Swarnkar, A. Nag, P. Ghosh and P. Mandal, *Nano Letters*, 2016, **16**, 4838-4848.
- [27] S. Sarkar, D. Saha, S. Banerjee, A. Mukherjee and P. Mandal, *Chem. Phys. Lett.*, 2017, **678**, 65-71.
- [28] P. U. Jepsen, D. G. Cooke and M. Koch, *Laser Photonics Rev.*, 2011, **5**, 124-166.
- [29] P. Giannozzi, S. Baroni, N. Bonini, M. Calandra, R. Car, C. Cavazzoni, D. Ceresoli, G. L. Chiarotti, M. Cococcioni, I. Dabo, A. Dal Corso, S. de Gironcoli,

- S. Fabris, G. Fratesi, R. Gebauer, U. Gerstmann, C. Gougoussis, A. Kokalj, M. Lazzeri, L. Martin-Samos, N. Marzari, F. Mauri, R. Mazzarello, S. Paolini, A. Pasquarello, L. Paulatto, C. Sbraccia, S. Scandolo, G. Scლაუzero, A. P. Seitsonen, A. Smogunov, P. Umari and R. M. Wentzcovitch, *J. Phys.: Condens. Matter*, 2009, **21**, 395502.
- [30] H. J. Monkhorst and J. D. Pack, *Phys. Rev. B*, 1976, **13**, 5188-5192.
- [31] D. G. Cahill, S. K. Watson and R. O. Pohl, *Phys. Rev. B*, 1992, **46**, 6131-6140.
- [32] J. A. A. Ketelaar, W. H. t'Hart, M. Moerel and D. Polder, *zkri*, 1939, **101**, 396.
- [33] Ş. Ellialtıođlu, E. Mete, R. Shaltaf, K. Allakhverdiev, F. Gashimzade, M. Nizametdinova and G. Orudzhev, *Phys. Rev. B*, 2004, **70**, 195118.
- [34] P. S. Nayar, J. K. D. Verma and B. D. Nag, *J. Phys. Soc. Jpn.*, 1967, **23**, 144-144.
- [35] S. G. Abdinova and I. V. Alekseev, *Nucl. Instrum. Methods Phys. Res.*, 1998, **411**, 365-368.
- [36] S. Roychowdhury, M. Samanta, S. Perumal and K. Biswas, *Chem. Mater.*, 2018, **30**, 5799-5813.
- [37] Y. Qiu, L. Xi, X. Shi, P. Qiu, W. Zhang, L. Chen, J. R. Salvador, J. Y. Cho, J. Yang, Y.-c. Chien, S.-w. Chen, Y. Tang and G. J. Snyder, *Adv. Funct. Mater.*, 2013, **23**, 3194-3203.
- [38] H. Zhao, J. Sui, Z. Tang, Y. Lan, Q. Jie, D. Kraemer, K. McEnaney, A. Guloy, G. Chen and Z. Ren, *Nano Energy*, 2014, **7**, 97-103.
- [39] M. Christensen, A. B. Abrahamsen, N. B. Christensen, F. Juranyi, N. H. Andersen, K. Lefmann, J. Andreasson, C. R. H. Bahl and B. B. Iversen, *Nat. Mater.*, 2008, **7**, 811-815.
- [40] T. Tadano, Y. Gohda and S. Tsuneyuki, *Phys. Rev. Lett.*, 2015, **114**, 095501.

Chapter 2.2



Giant Anisotropy in Layered InSe: Coexistence of High and Low Lattice Thermal Conductivity

Giant Anisotropy in Layered InSe: Coexistence of High and Low Lattice Thermal Conductivity[†]

Summary

Heat conduction through a material is subjected to decades of research, mostly due to their vast applicability in both ends of the spectrum. High thermal conductive compounds are useful for heat sinks, heat radiators, while the low thermal conductive compounds are useful for thermoelectrics and thermal insulators. In crystalline insulators, the heat conduction is mainly carried out via quantized lattice vibrations (phonons), and thus understanding the nature of their propagation is imperative to formulate useful thermal management modules. Herein, we have investigated the nature of lattice thermal conductivity (κ_{lat}) in a highly oriented β -InSe. β -InSe which is a layered material, shows very anisotropic κ_{lat} when measured in the layer (10.43 W/mK at 295 K) and across the layer directions (1.26 W/mK at 295 K) with an anisotropic ratio of 8.25 at 295 K. Theoretical calculations revealed the presence of weak inter-layer bonding and low cut-off frequency of the acoustic modes for such low κ_{lat} in the cross-plane direction. Sound velocity measurements corroborated the theoretical findings with high average sound velocity (3181 m/s) in the in-plane direction as opposed to 2037 m/s in the cross-plane directions. Phonon mean free path calculation revealed that most of the phonons gets scattered when traversing the interlayer vdW barrier of β -InSe, while in the in-plane direction, the phonon conducts seamlessly. All these factors collectively lower the κ_{lat} in the cross-plane direction as compared to the in-plane direction of β -InSe, and causes such anisotropy in the lattice thermal conductivity.

[†]M. Dutta, K. Pal, S. Matteppanavar, A. Warankar, P. Mandal and K. Biswas. [Manuscript under preparation.](#)

2.2.1. Introduction

Layered materials are subjected to rigorous investigation due to their unique bonding environment which brings up intriguing electronic, optical, mechanical and thermal properties.¹ Moreover, these 2D materials offer great flexibility which can be used in wearable electronics.² These materials are generally held up by weak van der Waals (vdW) interaction, which can be exfoliated and can be studied as single 2-dimensional (2D) materials. Recently, the layered materials like BiSbTe,³ Bi₂Te₃,⁴ SnSe,⁵ SnS,⁶ In₄Se₃⁷ etc. shown superior thermoelectric performance owing to their distinctive electronic and thermal transport properties. Particularly these materials have shown anisotropic lattice thermal conductivity (κ_{lat}) with particularly very low thermal transport in the cross-plane direction.^{8, 9} These low κ_{lat} materials are subjected to rigorous investigation owing to their vast applicability ranging from refractories, thermal insulators¹⁰ to thermoelectrics¹¹⁻¹³. Hence, the atomic insights into the lattice thermal transport of these 2D materials warrants thorough examination.

Indium selenide (InSe), a IIIA – VIA based mono-chalcogenide have been under comprehensive scrutiny for nearly 50 years due to their outstanding optoelectronic properties,^{14, 15} exceptionally high plasticity,¹⁶ bendable photodetectors,¹⁷ 2D ferromagnets,¹⁸ photovoltaics,¹⁹ magneto-optical effects or field effect transistors²⁰. InSe has also been investigated in energy management application like thermoelectrics, mainly due to its potential as a flexible and wearable thermoelectric material.²¹⁻²⁴ Recent theoretical investigations on monolayer InSe indicated that the thermoelectric figure of merit (zT) of InSe can reach up to 1.6 with optimum carrier concentration.²⁵ However, the low room temperature carrier concentration ($\sim 3.2 \times 10^{13} \text{ cm}^{-3}$) of pristine bulk InSe, limits its zT performance.^{21, 23, 24} Several works on InSe focussed on improving the carrier concentration of InSe via external doping, but with only limited success.^{21-24, 26-29} Recently, it has been shown the presence of dynamic carrier transport property in bulk β -InSe where the carrier concentration increases with increase in temperature.²³ This is due to the presence of amphoteric In atom, residing as In⁺ and In³⁺. With thermal activation the In⁺ converts into In³⁺ and releases two electrons in the matrix, thus increasing the carrier concentration from $3.2 \times 10^{13} \text{ cm}^{-3}$ to $6.2 \times 10^{16} \text{ cm}^{-3}$ in 300 – 723 K temperature range.²³ Although thorough investigation into the electronic properties of InSe has been done via

both experimental and theoretical means,^{30, 31} similar insights into the phonon transport properties of bulk InSe are missing and to achieve superior thermoelectric properties in InSe it is imperative to understand its structure-thermal property relationship.

Herein, we have investigated the phonon transport property of highly oriented β -InSe crystals in the in-plane (\perp to c-axis) and cross-plane (\parallel to c-axis) directions. β -InSe is a layered hexagonal compound comprised of quadruple layers (QL) of Se-In-In-Se separated by a vdW gap growing along the crystallographic c-direction. The κ_{lat} of InSe along the in-plane direction is found to be high ~ 10.43 W/mK at 295 K while in the cross-plane direction, the κ_{lat} is almost 8.25 times less, having a value of ~ 1.26 W/mK at 295 K. Theoretical investigations revealed the strong charge overlap between the intralayer In-Se and In-In bonding while the interlayer bonding is found to be very weak. Furthermore, from the phonon dispersion, the cut off frequency for the acoustic mode along the cross-plane direction is very low at 18 cm^{-1} while along the in-plane direction the cut off frequency is found to be 62 cm^{-1} . Both these calculations indicate the role of anisotropic phonon propagation in InSe. These theoretical calculations are backed up by experimental sound velocity calculations where very low average sound velocity of 2037 m/s is obtained in the cross-plane direction compared to almost twice the value in the in-plane direction. The calculated phonon mean free path (MFP) is found to be much lower ($\sim 12.90 \text{ \AA}$) in the cross-plane direction as compared to the in-plane direction (68.35), indicating that most of the phonons gets scattered while crossing the interlayer vdW barrier. Finally, we observed the presence of very low frequency vibrational modes below 4 THz which scatters the heat carrying acoustic phonons and results in low κ_{lat} in InSe.

2.2.2. Methods

Synthesis. Highly oriented InSe single crystals were prepared by dual zone vertical Bridgman technique. Used stoichiometric quantities of high purity In (99.99%, Alfa Aesar) and Se (99.9999%, Alfa Aesar) (total weight of 10 g) in a tapered quartz ampoule, sealed during high vacuum of 10^{-5} torr. The contents were heated up to 773 K in 12 hours, kept at this temperature for 20 hours, ramped to then ramped to 1223 K in 8 hours, followed by dwelling at this temperature for 44 hours, and then cooled to 998 K in 24 hours. The melt was then passed through a temperature gradient from 998 K to 848 K at

a speed of 1.5 mm/hr. Finally, the sample was slowly cooled to room temperature in 43 h.

X-ray diffraction (XRD). Room temperature XRD measurements of InSe are Rigaku SmartLab SE diffractometer using Cu K α ($\lambda= 1.54059 \text{ \AA}$) radiation.

Optical Band gap measurements. To estimate the optical band gap, diffuse reflectance measurements were carried out using a PerkinElmer Lambda 900 UV/Vis/near-IR spectrometer in reflectance mode. Absorption (α/S) data were calculated from the reflectance data by using the Kubelka–Munk equation: $\alpha/S = (1 - R)^2/(2R)$, in which R is the reflectance, and α and S are the absorption and scattering coefficients, respectively. The energy band gaps were derived from α/S vs. E (nm) plots.

Thermal conductivity. The thermal diffusivity, D , was measured between 290 K and 615 K using laser flash diffusivity technique in Netzsch LFA-457 instrument. Disc-shaped and square pellets were used for thermal transport measurement for cross-plane and in-plane directions respectively. Total thermal conductivity (κ_{tot}) was estimated using the relation, $\kappa = D \times C_p \times \rho$, where ρ is the density (> 97%) of the sample and C_p is the heat capacity ($C_p = 0.257 \text{ J/gK}$) estimated using Dulong-Petit limit.

Electronic properties. Electrical conductivity (σ) and Seebeck coefficient (S) were simultaneously measured under He-atmosphere from 290 K up to 615 K using ULVAC-RIKO ZEM-3 instrument.

Sound Velocity Measurements. The longitudinal (v_l) and shear (v_s) sound velocities were measured using Epoch 650 Ultrasonic Flaw Detector (Olympus) instrument with the transducer frequency of 5 MHz.

Computational details. All density functional theory (DFT) calculations were performed using the Vienna Ab-initio Simulation Package (VASP).^{32,33} We used the VASP supplied potentials for In ($4d^{10} 5s^2 5p^1$), and Se ($4s^2 4p^4$) which were constructed using the

projector augmented wave (PAW) method.^{34, 35} We utilized the PBEsol³⁶ generalized gradient approximation (GGA)³⁷ to the exchange-correlation energy functional. All calculations were done using a kinetic energy cut-off of 520 eV. We used a k-point mesh of $16 \times 16 \times 4$ for the relaxation of the cell parameters using the primitive unit cell of the beta phase (Space group: $P6_3/mmc$, No. 194) of InSe. The optimized lattice parameters ($a=4.01 \text{ \AA}$, $c=16.98 \text{ \AA}$) agree very well with the experimentally reported values ($a=4.05 \text{ \AA}$, $c=16.93 \text{ \AA}$) with the changes being smaller than 1%. We calculated the phonon dispersion of InSe within a finite-displacement method using the Phonopy³⁸ code, where the atom-displaced supercell configurations were generated using $4 \times 4 \times 1$ supercell (containing 128 atoms) of the primitive unit cell (with 8 atoms). We have used $4 \times 4 \times 4$ k-point grid for the calculations of interatomic force constants (IFCs) before determining the phonon dispersion. We calculated the bulk (B) and shear (G) moduli using Voigt's formula³⁹ utilizing the elastic tensor obtained from VASP. Theoretical calculations are done in collaboration with Dr. Koushik Pal, JNCASR, India.

THz Time-Domain Spectroscopy. We have performed THz-Time Domain Spectroscopy (THz-TDS) of InSe in reflection geometry at room temperature. This technique is based on the ultrafast laser system which consists of Ti:Sapphire oscillator (Tsunami) and regenerative amplifier (Spitfire Pro), both from Spectra Physics, Newport. In our home-built setup, amplified laser pulses have peak wavelength around 800 nm with pulse repetition rate of 1 KHz, average pulse energy of ~4 mJ (equivalent to total power of 4 W) and pulse width of ~50 fs. Nearly half of the power, ~2 W has been used to generate and detect THz pulses.⁴⁰

THz pulses are produced in air plasma by focusing fundamental wavelength of 800 nm and its BBO crystal generated second harmonics (400 nm). THz radiations along with many other parts of electromagnetic radiations are produced in air plasma. High resistivity (HR) silicon wafer (resistivity $> 10^4 \text{ \Omega m}$) is used to separate THz frequencies from rest of the other electromagnetic frequencies. Detection of THz pulses is done by Air Biased Coherent Detection (ABCD) technique. In our setup, we could detect broadband THz spectrum ranging from 0.5 to 15 THz by this method. THz generation

and detection path has been continuously purged with dry nitrogen gas to avoid THz absorption in water vapour present in ambient air.

To find complex refractive index of InSe in THz frequency range, THz Time-domain spectroscopy (THz-TDS) in reflection geometry with normal incidence mode was carried out. THz pulses, reflected from HR silicon (used as reference) and sample (InSe) are collected in time domain. Fresnel equation for reflection in normal incidence is used to find complex refractive index of InSe. It is given by following equation,^{41, 42}

$$\frac{\tilde{E}_{Sample}(\omega)}{\tilde{E}_{Si}(\omega)} = \frac{\frac{\tilde{n}_{sample}-n_{air}}{\tilde{n}_{sample}+n_{air}}}{\frac{n_{si}-n_{air}}{n_{si}+n_{air}}} \quad (2.2.1)$$

where, $\tilde{E}_{sample}(\omega)$ and $\tilde{E}_{si}(\omega)$ are Fourier transforms of time-domain THz electric fields, collected in normal reflection from sample and silicon (reference), respectively. \tilde{n}_{sample} , n_{si} and n_{air} are complex/real refractive indices of sample, reference and dry air, respectively. Refractive indices of HR silicon and dry air (mainly containing N₂ gas) remain constant over studied THz frequency range ($n_{si} = 3.45$ and $n_{air} = 1$). Complex refractive index is written as, $\tilde{n}_{sample} = n + ik$, n is the actual refractive index and k is extinction coefficient of sample. Absorption coefficient (α) is obtained by the relation, $\alpha = 2 \cdot \omega \cdot k/c$, where ω is the angular frequency and c is the speed of light. THz-TDS measurement is done in collaboration with Prof. P. Mandal, IISER, Pune.

2.2.3. Results and Discussion

Highly oriented crystals of InSe are grown via vertical Bridgman technique. Figure 1a shows the X-ray Diffraction (XRD) data of InSe measured along the in-plane direction layer direction and cross-plane direction and can be indexed for the β -InSe phase. The compound when measured along the cross-plane direction (\parallel to c-axis) shows highly intensified (0, 0, l) peaks, while the intensity of the same peaks gets subsided when measured along the in-plane direction (\perp to c-axis) (Figure 1a). This indicates the formation of highly oriented β -InSe, with layers stacked along the crystallographic c-axis.

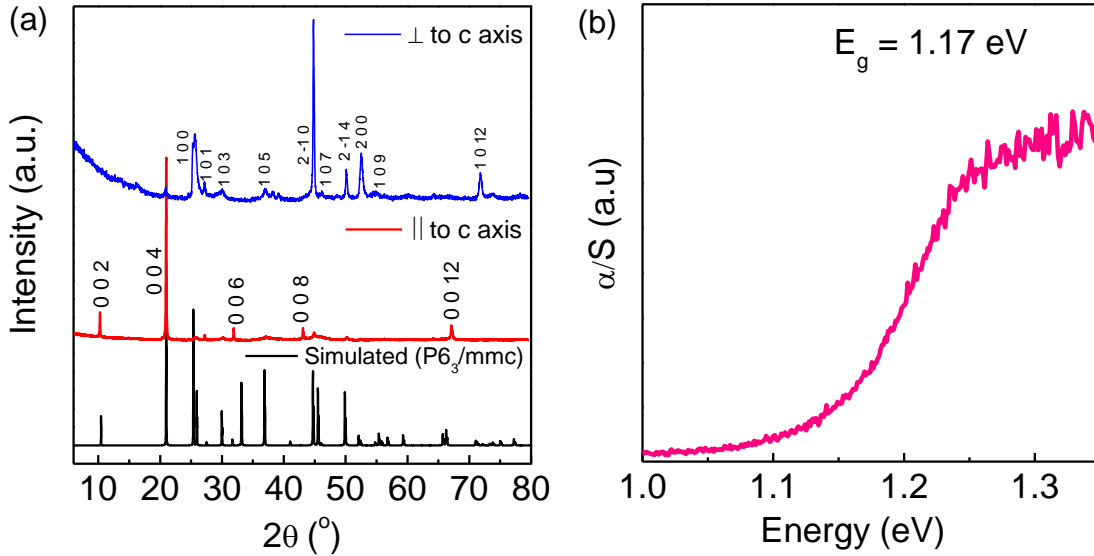


Figure 2.2.1. (a) XRD of β -InSe measured along parallel (//) and perpendicular (\perp) direction to the crystallographic c -axis. (b) Optical band gap of β -InSe.

β -InSe is a layered compound and crystallises in a hexagonal crystal lattice having the space group $P6_3/mmc$ with an optical band gap of ~ 1.17 eV (Figure 1b). Here each layer is made up of quadruple Se-In-In-Se bonds and are separated from each other by a vdW gap of ~ 0.8 nm (Figure 2a).¹⁶ The layers are stacked parallel to each other in a honeycomb lattice, with the subsequent layers are rotated by 60° (Figure 2b). The thermal conductivity of β -InSe when measured in the in-plane and cross-plane direction are found to show highly anisotropic transport (Figure 3a). The κ_{lat} is then derived using the relation $\kappa_{\text{lat}} = \kappa - \kappa_{\text{el}}$, where electrical thermal conductivity, κ_{el} (Figure 3b) can be extracted using the Wiedemann-Franz law $\kappa_{\text{el}} = L\sigma T$ (L being the temperature dependent Lorenz number obtained by fitting the Seebeck coefficient to the reduced chemical potential, σ is the electrical conductivity and T is the absolute temperature). Very low value of κ_{el} indicate that κ_{lat} is the primary carrier of heat across the material. The κ_{lat} of β -InSe is found to be high having a value of ~ 10.43 W/mK at 295 K when measured \perp to the c -axis (i.e., in-plane direction) and decreases with increase in temperature to ~ 4.36 W/mK at 610 K (Figure 3c). However, the κ_{lat} when measured \parallel to the c -axis shows very low value of 1.26 W/mK at 295 K, which decreases to ~ 0.68 W/mK at 610 K, lying very close to the theoretical minimum thermal conductivity (κ_{min}) of 0.573 W/mK (derivation of κ_{min} is

discussed later) and are consistent with previous report (Figure 3c).⁴³ The anisotropic ratio between the two measured direction is found to be very high around 8.25 at room temperature (Figure 3d). To investigate the nature of lattice thermal conductivity in β -InSe, we have looked into the temperature dependence of κ_{lat} . The κ_{lat} is found it to be linear when plotted against $1/T$, indicating that Umklapp scattering is the dominant mechanism⁴⁴ and there are no significant other phonon-scattering mechanisms present along both the directions (Figure 4).

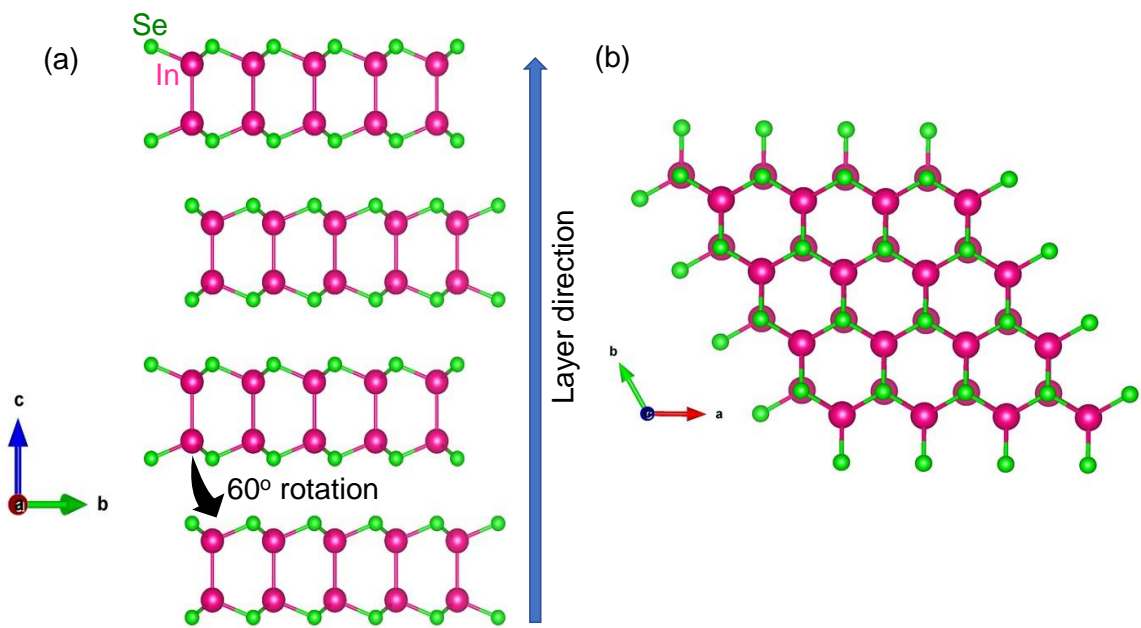


Figure 2. Crystal structure of β -InSe (space group: $P6_3/mmc$) (a) along the cross-plane layer stacking direction and (b) along in-plane direction.

To understand the nature of the chemical bonding in this compound, we performed the analysis of (i) interatomic force-constants (IFCs) which we obtained from our harmonic phonon calculations and (ii) electronic charge density distributions obtained from static DFT calculations. From iso-surfaces of the charge density (Figure 5a), we see that In and Se atoms have strong overlap of charge clouds along the direction of their bonding, indicating covalent bonding between them. Surprisingly on the other hand, we found similar charge overlapping and directional covalent bonding between the two In atoms within a layer. Our bonding analysis is consistent with a previous electronic structure study of InSe.³¹ Due to the presence of vdW gap between two quadruple layers,

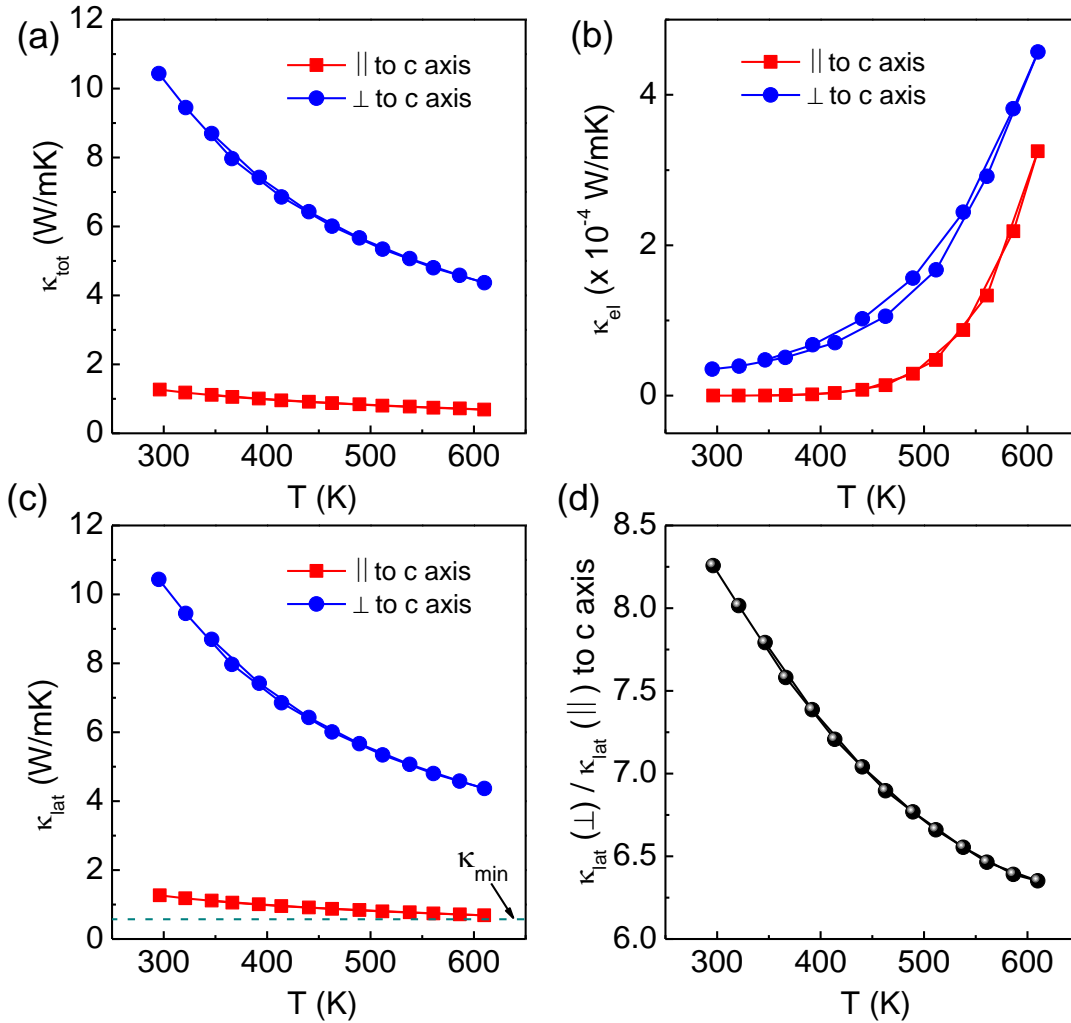


Figure 2.2.3. Temperature dependent (a) total thermal conductivity (κ_{tot}), (b) electrical thermal conductivity (κ_{el}), (c) lattice thermal conductivity (κ_{lat}) and (d) anisotropy of thermal conductivity between two directions of β -InSe.

no charge density appears between them as expected. To quantify the strength of the chemical bonds within a quadruple layer, we plot the IFCs between nearest neighbor atoms in Figure 5b, which shows that In-In bond has the highest value of the IFCs (-5.8 eV/\AA^2), indicating very strong bonding between them. On the other hand, the IFCs between In and Se are marginally smaller (-5.4 eV/\AA^2), indicating the relatively weaker bond strength between In-Se. As practically there is no bonding between the quadruple layers, the IFC for intralayer Se atoms are very small (-0.5 eV/\AA^2). Such a large difference of interlayer and interlayer bonding strengths and a very strong In-In bonding within a layer strongly influence the thermal transport properties of the compound. The absence

of strong connectivity between the quadruple layers makes the crystal structure elastically soft as revealed by our calculations of bulk (24 GPa) and shear modulus ($G = 14$ GPa), which are quite low.

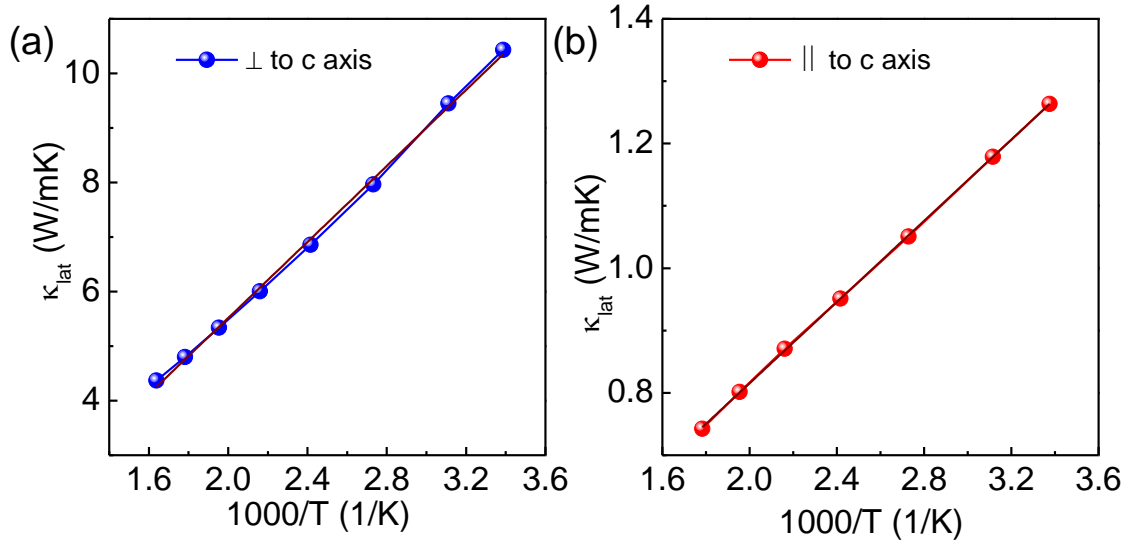


Figure 2.2.4. $1/T$ dependence of κ_{lat} in the (a) in-plane direction (\perp to c -axis), and (b) cross-plane direction (\parallel to c -axis).

To understand how the disparate bond-strengths and soft elasticity of InSe affect its vibrational properties, we have calculated and analyzed its phonon dispersion and density of states. The calculated phonon dispersion (Figure 5c) exhibits soft acoustic phonon branches with frequency below 20 cm^{-1} along Γ -A direction in the Brillouin zone, which in real space correspond to parallel the layer direction in the crystal structure. Such low frequencies of the acoustic phonons originate from the weak bonding between the quadruple layers. On the other hand, along the Γ -M direction that corresponds to in-plane layer direction in the crystal, the frequencies of the acoustic phonon branches become much higher ($> 60 \text{ cm}^{-1}$) due to relatively much stronger intralayer bonding which is dominated by In-In bonds. Due to this strong hybridization, there is a strong overlap of phonon contributions originating from In and Se in the low-frequency range up to 100 cm^{-1} (Figure 5d). As a result, the lattice heat propagates quite well within the quadruple layer and parallel to the layer direction in InSe, resulting in a high lattice thermal conductivity (κ_{lat}). On the other hand, due to very weak bonding between the quadruple

layers, the transport of heat is severely impeded by the vdW gap, resulting in a much lower κ_{lat} along the layer direction.

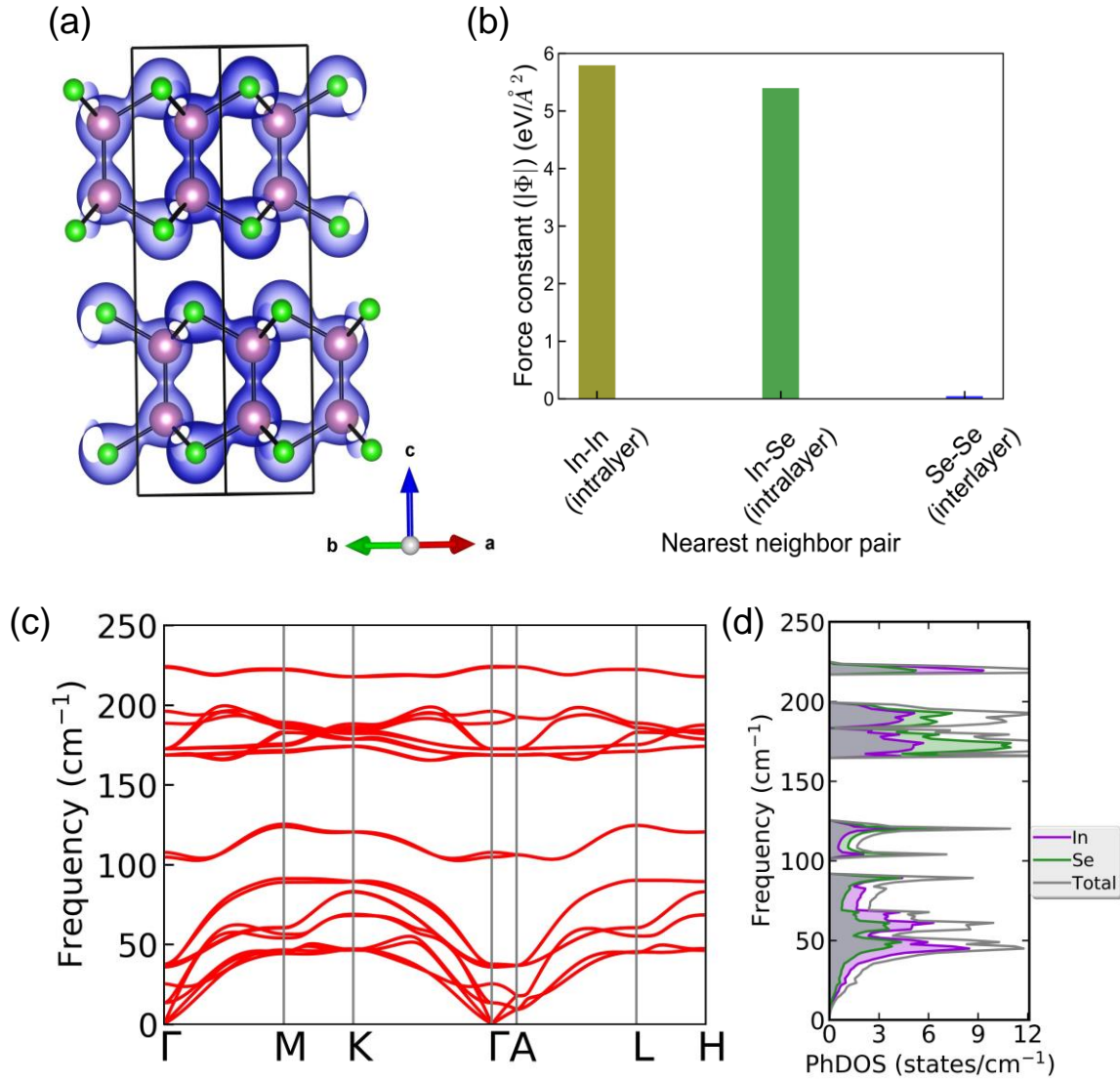


Figure 2.2.5. (a) Iso-surfaces of electronic charge density (colored in blue) shown in the unit cell of β -InSe. (b) Second order interatomic force constants for the nearest neighbour atom pair in the crystal structure of β -InSe. (c) Phonon dispersion and (d) atom-resolved phonon density of states β -InSe. In and Se atoms are denoted by the pink and green spheres, respectively.

This large anisotropy in κ_{lat} can also be rationalized by the different values of sound velocities when measured along the different direction. Since the acoustic phonons determine the sound velocities, there is a large difference of sound velocities along the

in-plane and cross-plane directions which corroborate to the high cut-off frequencies in the acoustic phonon branches. The experimental sound velocity along the in-plane direction is measured to be ~ 4473 m/s and 2900 m/s along the longitudinal (v_l) and shear (v_s) directions. While the cross-plane direction, the v_l and v_s is found to be very low ~ 3028 m/s and 1844 m/s respectively. The average sound velocity (v_{ave}) calculated using the equation,⁴⁵

$$v_{ave} = \frac{3}{v_l^{-3} + 2v_s^{-3}} \quad (2.2.2)$$

is found to be ~ 3181 m/s along the in-plane direction, while along the cross-plane direction it is almost halved to ~ 2037 m/s, thus corroborating the theoretical cut-off frequencies. The minimum thermal conductivity calculated using the formula,⁴⁶

$$\kappa_{min} = \frac{3}{2} \left(\frac{\pi}{6} \right)^{1/3} k_B n^{2/3} v_{ave} \quad (2.2.3)$$

is found to be 0.573 W/mK and 0.895 W/mK in the in-plane and cross-plane directions, respectively. Here k_B is the Boltzmann constant and n is the number density of the compound. The phonon mean free path (l) calculated using the equation,⁴⁷

$$\kappa_{lat} = \frac{1}{3} C_v v_{ave} l \quad (2.2.4)$$

where, C_v is calculated as ρC_p (ρ is the sample density, 5.6 g/cm³ and C_p is the specific heat capacity). The phonon mean free path is calculated to be ~ 68.35 Å and ~ 12.90 Å along the in-plane and cross-plane directions, respectively. The high phonon mean free path (~ 17 times than that of $a = b = 4.005$ Å) along the in-plane direction means the flow of heat through the plane is seamless and corroborates with our high κ_{lat} value in that direction. While the phonon mean free path along the cross-plane direction is less than the lattice parameter along the c-direction (16.640 Å) which means most of the phonons gets attenuated in the interlayer barrier and hence the heat flow through this direction is found to be very limited.

Room temperature Terahertz-Time Domain Spectroscopy (THz-TDS) of β -InSe has been performed to experimentally investigate its vibrational characteristics. THz radiation mainly detects IR active optical phonon modes in semiconductor. For β -InSe, we observe several absorption peaks below 5 THz indicating the presence of multiple soft phonon optical modes (Figure 6). These optical phonon modes can couple with the heat

carrying acoustics modes and scatter them, thereby lowering the κ_{lat} of β -InSe as observed.

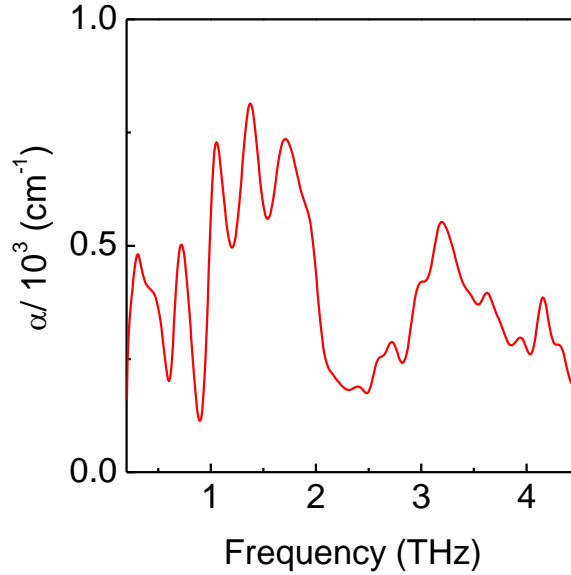


Figure 2.2.6. THz-TDS spectrum of InSe at room temperature in reflection geometry.

2.2.4. Conclusion

β -InSe shows highly anisotropic κ_{lat} due to their highly strong bond overlap within the layers, whereas in between layers only weak vdW type interaction is present. The presence of such bonding heterogeneity is observed from charge density functional analysis and IFC values. Phonon dispersion indicated the presence of anisotropic cut-off frequencies of acoustic modes with high cut-off ($> 60 \text{ cm}^{-1}$) frequency is observed in the in-plane layer direction and low cut-off frequency ($< 20 \text{ cm}^{-1}$) is observed in the cross-plane direction. These are further corroborated using the sound velocity measurements and phonon mean free path calculations. Phonon mean free path revealed very high phonon mean free paths along the layers while traversing the layers, the phonon mean free paths are found to be very low ($\sim 12.90 \text{ \AA}$). Further we have observed the presence of very soft phonon modes through THz-TDS measurements. All these findings are suggestive of a very anisotropic phonon conduction through β -InSe and indeed we found an anisotropic ratio of 8.25 at room temperature along the two directions. The κ_{lat} is found to have a high value of 10.43 W/mK at room temperature when measured \perp to the c-axis,

while \parallel to the c -axis the κ_{lat} found to be low, around 1.26 W/mK at room temperature. The anisotropic κ_{lat} in β -InSe arises due to the interlayer barrier between two layers which impedes the lattice vibrations and thus limiting its κ_{lat} .

2.2.5. References

- [1] J. Wu, Y. Chen, J. Wu and K. Hippalgaonkar, *Adv. Electron. Mater.*, 2018, **4**, 1800248.
- [2] S. J. Kim, K. Choi, B. Lee, Y. Kim and B. H. Hong, *Annu. Rev. Mater. Res.*, 2015, **45**, 63-84.
- [3] B. Poudel, Q. Hao, Y. Ma, Y. Lan, A. Minnich, B. Yu, X. Yan, D. Wang, A. Muto, D. Vashaee, X. Chen, J. Liu, M. S. Dresselhaus, G. Chen and Z. Ren, *Science*, 2008, **320**, 634.
- [4] B. Zhu, X. Liu, Q. Wang, Y. Qiu, Z. Shu, Z. Guo, Y. Tong, J. Cui, M. Gu and J. He, *Energy Environ. Sci.*, 2020, **13**, 2106-2114.
- [5] B. Qin, D. Wang, X. Liu, Y. Qin, J.-F. Dong, J. Luo, J.-W. Li, W. Liu, G. Tan, X. Tang, J.-F. Li, J. He and L.-D. Zhao, *Science*, 2021, DOI: 10.1126/science.abi8668.
- [6] W. He, D. Wang, H. Wu, Y. Xiao, Y. Zhang, D. He, Y. Feng, Y.-J. Hao, J.-F. Dong, R. Chetty, L. Hao, D. Chen, J. Qin, Q. Yang, X. Li, J.-M. Song, Y. Zhu, W. Xu, C. Niu, X. Li, G. Wang, C. Liu, M. Ohta, S. J. Pennycook, J. He, J.-F. Li and L.-D. Zhao, *Science*, 2019, **365**, 1418.
- [7] J.-S. Rhyee, K. H. Lee, S. M. Lee, E. Cho, S. I. Kim, E. Lee, Y. S. Kwon, J. H. Shim and G. Kotliar, *Nature*, 2009, **459**, 965-968.
- [8] M. Samanta, T. Ghosh, S. Chandra and K. Biswas, *J. Mater. Chem. A*, 2020, **8**, 12226-12261.
- [9] Q. D. Gibson, T. Zhao, L. M. Daniels, H. C. Walker, R. Daou, S. Hébert, M. Zanella, M. S. Dyer, J. B. Claridge, B. Slater, M. W. Gaultois, F. Corà, J. Alaria and M. J. Rosseinsky, *Science*, 2021, DOI: 10.1126/science.abh1619, eabh1619.
- [10] N. P. Padture, M. Gell and E. H. Jordan, *Science*, 2002, **296**, 280.
- [11] S. Roychowdhury, T. Ghosh, R. Arora, M. Samanta, L. Xie, N. K. Singh, A. Soni, J. He, U. V. Waghmare and K. Biswas, *Science*, 2021, **371**, 722.
- [12] B. Jiang, Y. Yu, J. Cui, X. Liu, L. Xie, J. Liao, Q. Zhang, Y. Huang, S. Ning, B. Jia, B. Zhu, S. Bai, L. Chen, S. J. Pennycook and J. He, *Science*, 2021, **371**, 830.
- [13] M. Dutta, D. Sarkar and K. Biswas, *Chem. Commun.*, 2021, **57**, 4751-4767.

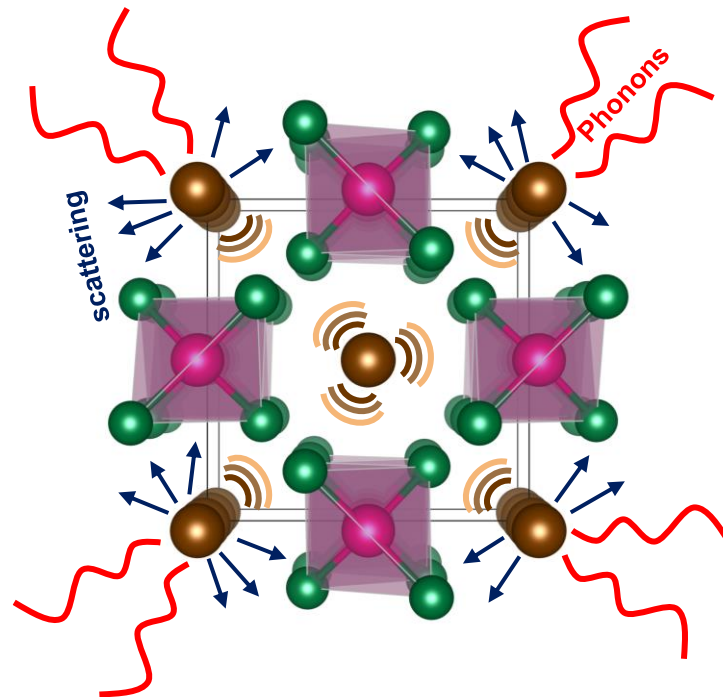
- [14] R. W. Damon and R. W. Redington, *Phys. Rev.*, 1954, **96**, 1498-1500.
- [15] M. V. Andriyashik, M. Yu. Sakhnovskii, V. B. Timofeev and A. S. Yakimova, *Phys. Status Solidi B*, 1968, **28**, 277-285.
- [16] T.-R. Wei, M. Jin, Y. Wang, H. Chen, Z. Gao, K. Zhao, P. Qiu, Z. Shan, J. Jiang, R. Li, L. Chen, J. He and X. Shi, *Science*, 2020, **369**, 542.
- [17] S. R. Tamalampudi, Y.-Y. Lu, R. K. U, R. Sankar, C.-D. Liao, K. M. B, C.-H. Cheng, F. C. Chou and Y.-T. Chen, *Nano Lett.*, 2014, **14**, 2800-2806.
- [18] K. Iordanidou, M. Houssa, J. Kioseoglou, V. V. Afanas'ev, A. Stesmans and C. Persson, *ACS Appl. Nano Mater.*, 2018, **1**, 6656-6665.
- [19] A. Segura, J. P. Guesdon, J. M. Besson and A. Chevy, *J. Appl. Phys.*, 1983, **54**, 876-888.
- [20] F. Chen, A. Cui, X. Wang, C. Gao, L. Xu, K. Jiang, J. Zhang, Z. Hu and J. Chu, *Nanotechnology*, 2020, **31**, 335702.
- [21] X. Hou, S. Chen, Z. Du, X. Liu and J. Cui, *RSC Adv.*, 2015, **5**, 102856-102862.
- [22] S. Shigetomi and T. Ikari, *J. Appl. Phys.*, 2003, **93**, 2301-2303.
- [23] H. Shi, D. Wang, Y. Xiao and L.-D. Zhao, *Aggregate*, 2021, **n/a**, e92.
- [24] K. H. Lee, M.-W. Oh, H.-S. Kim, W. H. Shin, K. Lee, J.-H. Lim, J.-i. Kim and S.-i. Kim, *Inorg. Chem. Front.*, 2019, **6**, 1475-1481.
- [25] Z. Chang, K. Yuan, Z. Sun, X. Zhang, Y. Gao, G. Qin and D. Tang, *Phys. Chem. Chem. Phys.*, 2021, **23**, 13633-13646.
- [26] S.-s. Choo, S.-w. Hong, H.-S. Kim and S.-i. Kim, *Korean J. Met. Mater.*, 2020, **58**, 348-352.
- [27] J. Yoo, J.-i. Kim, H.-j. Cho, S.-s. Choo, S.-i. Kim, K. Lee, W. H. Shin, H.-S. Kim and J. W. Roh, *J. Korean Phys. Soc.*, 2018, **72**, 775-779.
- [28] J.-i. Kim, H.-S. Kim and S.-i. Kim, *J. Phys. D: Appl. Phys.*, 2019, **52**, 295501.
- [29] L. W. Sprague, C. Huang, J.-P. Song and B. M. Rubenstein, *J. Phys. Chem. C*, 2019, **123**, 25437-25447.
- [30] R. Haleoot and B. Hamad, *Phys. B (Amsterdam, Neth.)*, 2020, **587**, 412105.

-
- [31] P. Gomes da Costa, R. G. Dandrea, R. F. Wallis and M. Balkanski, *Phys. Rev. B*, 1993, **48**, 14135-14141.
- [32] G. Kresse and J. Furthmüller, *Phys. Rev. B: Condens. Matter Mater. Phys.*, 1996, **54**, 11169.
- [33] G. Kresse and J. Furthmüller, *Comput. Mater. Sci.*, 1996, **6**, 15-50.
- [34] P. E. Blöchl, *Phys. Rev. B*, 1994, **50**, 17953-17979.
- [35] G. Kresse and D. Joubert, *Phys. Rev. B*, 1999, **59**, 1758.
- [36] J. P. Perdew, K. Burke and M. Ernzerhof, *Phys. Rev. Lett.*, 1996, **77**, 3865.
- [37] J. P. Perdew, A. Ruzsinszky, G. I. Csonka, O. A. Vydrov, G. E. Scuseria, L. A. Constantin, X. Zhou and K. Burke, *Phys. Rev. Lett.*, 2008, **100**, 136406.
- [38] A. Togo and I. Tanaka, *Scr. Mater.*, 2015, **108**, 1-5.
- [39] J. F. Nye, *Physical Properties of Crystals: Their Representation by Tensors and Matrices*, Oxford Press, Oxford, 1957.
- [40] G. R. Yettapu, D. Talukdar, S. Sarkar, A. Swarnkar, A. Nag, P. Ghosh and P. Mandal, *Nano Lett.*, 2016, **16**, 4838-4848.
- [41] M. Dutta, S. Matteppanavar, M. V. D. Prasad, J. Pandey, A. Warankar, P. Mandal, A. Soni, U. V. Waghmare and K. Biswas, *J. Am. Chem. Soc.*, 2019, **141**, 20293-20299.
- [42] P. U. Jepsen, D. G. Cooke and M. Koch, *Laser Photonics Rev.*, 2011, **5**, 124-166.
- [43] S. M. Atakishiev, D. S. Abdinov and G. A. Akhundov, *phys. stat. sol. (b)*, 1968, **28**, K47-K50.
- [44] W. Kim, *J. Mater. Chem. C*, 2015, **3**, 10336-10348.
- [45] E. Rathore, R. Juneja, S. P. Culver, N. Minafra, A. K. Singh, W. G. Zeier and K. Biswas, *Chem. Mater.*, 2019, **31**, 2106-2113.
- [46] D. G. Cahill, S. K. Watson and R. O. Pohl, *Phys. Rev. B*, 1992, **46**, 6131-6140.
- [47] M. K. Jana and K. Biswas, *ACS Energy Lett.*, 2018, **3**, 1315-1324.

PART 3

**Elucidating the Origin of Low Lattice
Thermal Conductivity through
Synchrotron X-ray Pair Distribution
Function (PDF) and Inelastic
Neutron Scattering (INS**

Chapter 3.1



**Evidence of Highly Anharmonic Soft
Lattice Vibrations in a Zintl Rattler**

Evidence of Highly Anharmonic Soft Lattice Vibrations in a Zintl Rattler[†]

Summary

In this chapter, we present lattice dynamics associated with the local chemical bonding hierarchy in Zintl compound TlInTe₂, which cause intriguing phonon excitations and strongly suppress the lattice thermal conductivity to an ultralow value (0.46 - 0.31 W/mK) in the 300–673 K. We established an intrinsic rattling nature in TlInTe₂ by studying the local structure and phonon vibrations using synchrotron X-ray pair distribution function (PDF) (100–503 K) and inelastic neutron scattering (INS) (5–450 K), respectively. We showed that while 1D chain of covalently bonded [InTe₂]_n⁻ⁿ transport heat with Debye type phonon excitation, ionically bonded Tl rattles with a frequency ca. 30 cm⁻¹ inside distorted Thompson cage formed by [InTe₂]_n⁻ⁿ. This highly anharmonic Tl rattling causes strong phonon scattering and consequently phonon lifetime reduces to ultralow value of ca. 0.66(6) ps, resulting in ultralow thermal conductivity in TlInTe₂.

[†]M. Dutta, M. Samanta, T. Ghosh, D. J. Voneshen and K. Biswas. *Angew. Chem. Int. Ed.*, 2021, **60**, 4259–4265.

3.1.1. Introduction

Heat propagation in crystalline solids is a coveted research area for its wide-ranging applications from heat dissipation in miniaturized electronic devices and photovoltaics to the use of ultralow thermal conducting materials in thermoelectric energy conversion,¹⁻³ thermal barriers⁴ or refractories. Primarily for energy applications like thermoelectrics, the main pre-requisite of a material is to achieve low thermal conductivity without compromising the electrical properties, i.e., to limit the flow of heat via lattice (or phonon) vibrations.⁵ The magnitude of such lattice vibrations in a material is determined by their short and long range chemical bonding interactions, and thus understanding the nature of bonding and lattice dynamics together with their influence on phonon transport is essential to explore and design new crystalline solids with low lattice thermal conductivity (κ_{lat}).⁶ Traditionally, external inclusion of nano/meso precipitates or all-scale hierarchical nano-structuring are employed to lower κ_{lat} , which comes at a cost of deteriorating charge carrier flow to some extent.⁷⁻⁹

Slack envisioned a material system called “Phonon Glass Electron Crystals (PGEC)” in which the electronic and phonon transports are essentially decoupled such that the material provides a smooth conduction pathways for electrical charge carriers while effectively blocking the heat carrying phonons.¹⁰ Recently, it has been realized that, rather than extrinsic (nano/meso-structuring) phonon transport manipulation strategies, the deployment of intrinsic material properties to block heat transport is effective to achieve PGEC like properties.⁵ This leads to a recent surge in the discovery of intrinsically low thermal conducting materials. Various intrinsic effects like stereochemically active lone pairs,¹¹ inherent bonding heterogeneity,¹²⁻¹⁴ layered 2D structures like SnSe,¹⁵⁻¹⁷ SnS,¹⁸ BiSe¹⁹ and BiTe²⁰, complex crystal structures,^{21, 22} ferroelectric instability^{23,24} or part crystalline-part liquid states²⁵⁻²⁷ etc. have been employed to achieve an intrinsically low κ_{lat} . Low thermal conductivity has been observed in skutterudites²⁸ and clathrates^{29, 30} wherein a host element rattles independently in an oversized cage.

Zintl compounds like InTe,³¹ TlSe,³² NaCoO₂³³ and TlInTe₂³⁴⁻³⁶ possess intrinsically low κ_{lat} . These compounds have covalent (stronger) and ionic (weaker) substructures within them. The presence of such hierarchically bonded sublattices makes Zintl compounds ideal for intrinsically ultra-low thermal conductivity. TlInTe₂ has been recently found to possess intrinsically low κ_{lat} .³⁴ Room temperature κ_{lat} of TlInTe₂ is ~ 0.46 W/mK which further decreases to ~ 0.31 W/mK at 673 K, lying close to its theoretical minimum of thermal conductivity (κ_{min}). TlInTe₂ undergoes both electronic and structural phase transitions above room temperature.^{37, 38} Furthermore, TlInTe₂ also shows a pressure induced semiconductor to semimetal and semimetal to superconductor transitions.³⁹ Therefore, fundamental understanding of the local structural evolution of TlInTe₂ with temperature and its correlation with low energy phonon modes are critical in understanding the intrinsically low κ_{lat} of TlInTe₂.

Herein, we investigate the fundamental origin of the ultra-low κ_{lat} in the Zintl compound TlInTe₂. We have performed temperature dependent (100 K – 503 K) synchrotron X-ray atomic Pair Distribution Function (PDF) and Inelastic Neutron Scattering (INS) analysis to uncover the relationship between local structure and lattice dynamics for the experimentally observed intrinsically low κ_{lat} in TlInTe₂. Our analysis of local crystal structure of TlInTe₂ using PDF reveals that all the constituent atoms have anisotropic thermal vibrations. However, Tl atoms vibrate at a greater amplitude indicating the rattling behaviour inside the Thomson cage created by $[\text{InTe}_2]_{\text{n}}^{-\text{n}}$ tetrahedra. We have observed the presence of bonding heterogeneity (coexisting covalent and ionic bonding) which further aids to the lowering of κ_{lat} . The analysis of thermal vibration of Tl atoms indicates that its rattling behaviour generates low energy Einstein mode around ~ 30 cm⁻¹. We have experimentally verified the presence of such low energy phonon modes using temperature dependent neutron-weighted phonon density of states (PhDOS) by INS. We have observed several low energy peaks in PhDOS at ~ 28 cm⁻¹, 45 cm⁻¹ and 77 cm⁻¹ which are responsible for such low κ_{lat} of TlInTe₂.⁴⁰⁻⁴³ These modes

broaden dramatically on heating, confirming the presence of strong phonon-phonon scattering.

3.1.2. Methods

Synthesis. Synthesis of polycrystalline TlInTe₂ ingots were done via melting stoichiometric amounts of high purity Thallium (Tl), Indium (In) and Tellurium (Te) (12 g total weight) in high vacuum (10⁻⁵ torr) sealed carbon-coated quartz tube. These ampules were then heated to 1123 K in 7 hr, subsequently soaked for 10 hr and then cooled to room temperature in 15 hr.

Synchrotron X-ray Pair Distribution Function (PDF). For performing synchrotron X-ray PDF, samples were finely ground with agate mortar pestle and then filled in capillary of 0.6 mm diameter. Both ends of capillaries were sealed using adhesive. Low temperature measurements (100 – 400 K) are done using Cryostream, and for high temperature measurements (293 – 503 K), hot air blower was used. Perkin Elmer image plate detector was used to record the diffraction data. To subtract the background, data sets of empty capillaries was performed. Dark measurement prior to each data collection was done and Lanthanum Hexaboride (LaB₆) was taken as standard for calibration. The energy of the beam was fixed at 59.83 keV was used.

$G(r)$, which tells us about the probability of finding nearest neighbour bonding at a certain distance r in the material, was obtained via Fourier transformation of scattering structure function, $F(Q)$ ⁴⁴

$$G(r) = \frac{2}{\pi} \int_{Q_{min}}^{\infty} F(Q) \sin Qr dQ \quad (3.1.1)$$

where Q represents the momentum transfer of the scattering particle. $F(Q)$ is obtained from scattering data and is related to structure function $S(Q)$ as $F(Q) = Q[S(Q)-1]$.

Simulation of the experimental PDF data was done using PDFgui⁴⁵ software. All the datasets from 100 K – 503 K were initially modelled using a tetragonal $I4/mcm$ model. The refinement parameters were the scale, correlation parameter, lattice parameter, and

the thermal displacement values. The first peak of the $G(r)$ vs r plot represents the nearest atom - atom correlation, the second peak corresponds to second nearest atom-atom distances and so on.

For calculating θ_E and θ_D , the experimental PDF data is fitted using $I4/mcm$ space group of $TlInTe_2$ with isotropic atomic displacement parameter (U_{iso}). The U_{iso} values were refined considering the constraint that U_{iso} of In and Te is equal but different from that of Tl. PDF data is taken in beamline P02.1, PETRA III, Germany.

Inelastic Neutron Scattering (INS). 10 g of polycrystalline $TlInTe_2$ was wrapped in thin Al foil and formed into an annulus approximately 2 mm thick with an outer diameter of 45 mm. This was mounted inside a top-loading CCR with hot stage (5 - 450 K) on MARI. MARI is a Time-Of-Flight neutron spectrometer at the ISIS pulsed neutron source. MARI was set up with the Gd chopper running at 200 Hz allowing for two incident energies of 35 meV and 6 meV to be measured simultaneously. Data collected was reduced with the Mantid package⁴⁶ and analysed with custom python scripts.

For each temperature measured, a corresponding empty sample can was also measured. This empty can was subtracted from the data after scaling to 95 % of its original value (this scaling was determined by the strength of the Al Bragg reflections) to account for the increase in scattering when the rather absorbing sample is removed from the can. A linear scaling factor is reasonably appropriate as the majority of the Al scattering is not from the sample can but the cryostat tails. This approximation breaks down at very low or high 2θ where scattered neutron could pass back through the sample. For this reason, data integrations have excluded the very lowest angle detectors. This linear scaling is still an approximation and leads to a slight over-subtraction at large energy transfers where scattering from the sample can is then strongly absorbed by the sample.

Phonon scattering grows in intensity as the square of the momentum transfer Q and so the data was divided through by this. The Debye-Waller factor also applies to phonon scattering causing a drop-in intensity with Q . Due to the anisotropic displacements and the large differences between sites this was not possible to correct for.

No further corrections were applied to data which was subsequently fitted. The intensities of the middle peak ($\sim 45 \text{ cm}^{-1}$) were not well behaved at high temperature. For the phonon density-of-states, the data was also multiplied through by the energy the scattering was observed at and corrected for Bose statistics.

To extract a scattering rate from the fitted data the 5 K data was assumed to be the resolution function. Additional broadening at higher temperature was assumed to arise from phonon-phonon scattering and for the widths to add in quadrature. The phonon scattering was then given by:

$$\sigma_{scat} = \sqrt{\sigma_T^2 - \sigma_{5K}^2}. \quad (3.1.2)$$

With errors calculated as

$$\Delta\sigma_{scat} = \sqrt{\left(\Delta\sigma_T \left(\frac{\sigma_T}{\sqrt{\sigma_T^2 - \sigma_{5K}^2}}\right)\right)^2 + \left(\Delta\sigma_{5K} \left(\frac{\sigma_{5K}}{\sqrt{\sigma_T^2 - \sigma_{5K}^2}}\right)\right)^2}, \quad (3.1.3)$$

where σ_{5K} is the width at base temperature, σ_T the width at higher temperatures and $\Delta\sigma_i$ is the error in the corresponding parameter. The INS measurements are done in collaboration with Dr. D. J. Voneshen at MARI, ISIS-RAL, UK.

3.1.3. Results and Discussion

TlInTe₂ has a body-centred tetragonal crystal structure with space group $I4/mcm$ at ambient conditions. The tetragonal structure comprises tetrahedral $[\text{InTe}_2]_n^{-n}$ 1D chains propagating along the crystallographic c -direction (Figure 3.1.1).³⁴ Each tetrahedron is connected to another one via corner shared Te atoms, while the In³⁺ reside in the middle of the tetrahedra. The In-Te bond distance is around 2.82 Å, which is close to the sum (2.80 Å) of covalent radii of In (1.42 Å) and Te (1.38 Å). The Tl⁺ reside in the 4a Wyckoff position and are surrounded by 8 Te atoms, forming a slightly deformed Thompson cage (Figure 3.1.1a). The Tl-Te bond distance is around 3.59 Å, much larger than the sum (2.83 Å) of covalent radii of Tl (1.45 Å) and Te (1.38 Å), but close to their

ionic bond distance of 3.71 Å [ionic radius (r_{ion}) of Tl^+ is 1.64 Å; r_{ion} of Te^{2-} is 2.07 Å]. The presence of such heterogeneous bonding environment (i.e., the presence of both covalent and ionic bond) is known to lower the lattice thermal conductivity due to enhanced phonon scattering.¹² Furthermore, in TlInTe_2 , the Tl^+ contains a $6s^2$ lone pair of electrons which further enhances phonon scattering due to lone pair induced anharmonic lattice vibration.

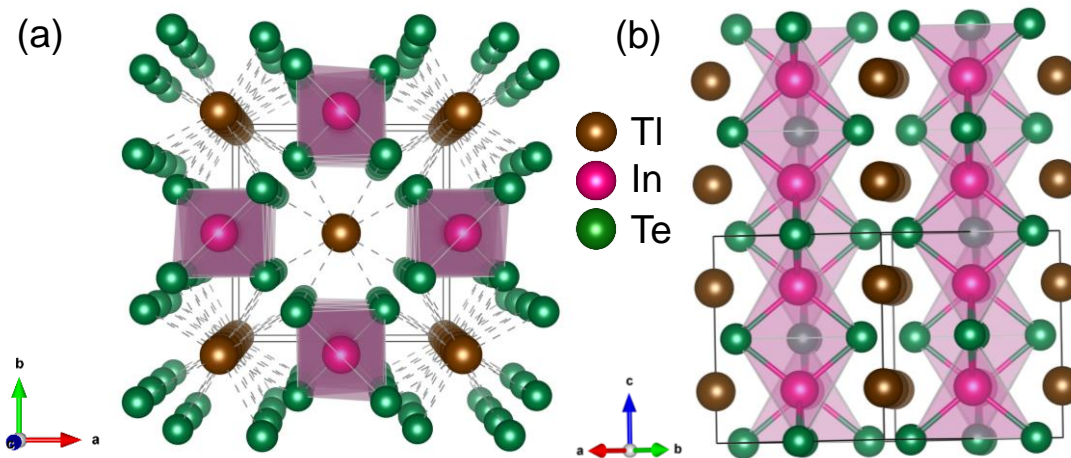


Figure 3.1.1. (a) Room temperature tetragonal crystal structure (space group: $I4/mcm$) of TlInTe_2 viewed along c -axis. Dashed lines signify weak electrostatic interaction between Tl and Te . (b) Room temperature tetragonal crystal structure of TlInTe_2 exhibiting In-Te polyhedra encompasses weakly bonded Tl in the lattice.

X-ray atomic Pair Distribution Function (PDF) analysis, being a total diffraction technique, provides information for both the local (diffuse diffraction) and average (Bragg diffraction) structure of a material and is ideal to study rattling and anisotropic thermal vibrations.⁴⁷ We have analysed the synchrotron X-ray PDF data of TlInTe_2 in the temperature range of 100 K – 503 K. Figure 3.1.2a represents a typical PDF data ($G(r)$ vs. r) of TlInTe_2 taken at 300 K and the fit using the $I4/mcm$ space group. The first few peaks in Figure 3.1.2a in the low r range ($r < 5$ Å) provides information about the local structure while the peaks in the high r range describes the average structure of TlInTe_2 . Absence of any significant peak anomaly and overall good fitting ($R_w = 0.108$) of the

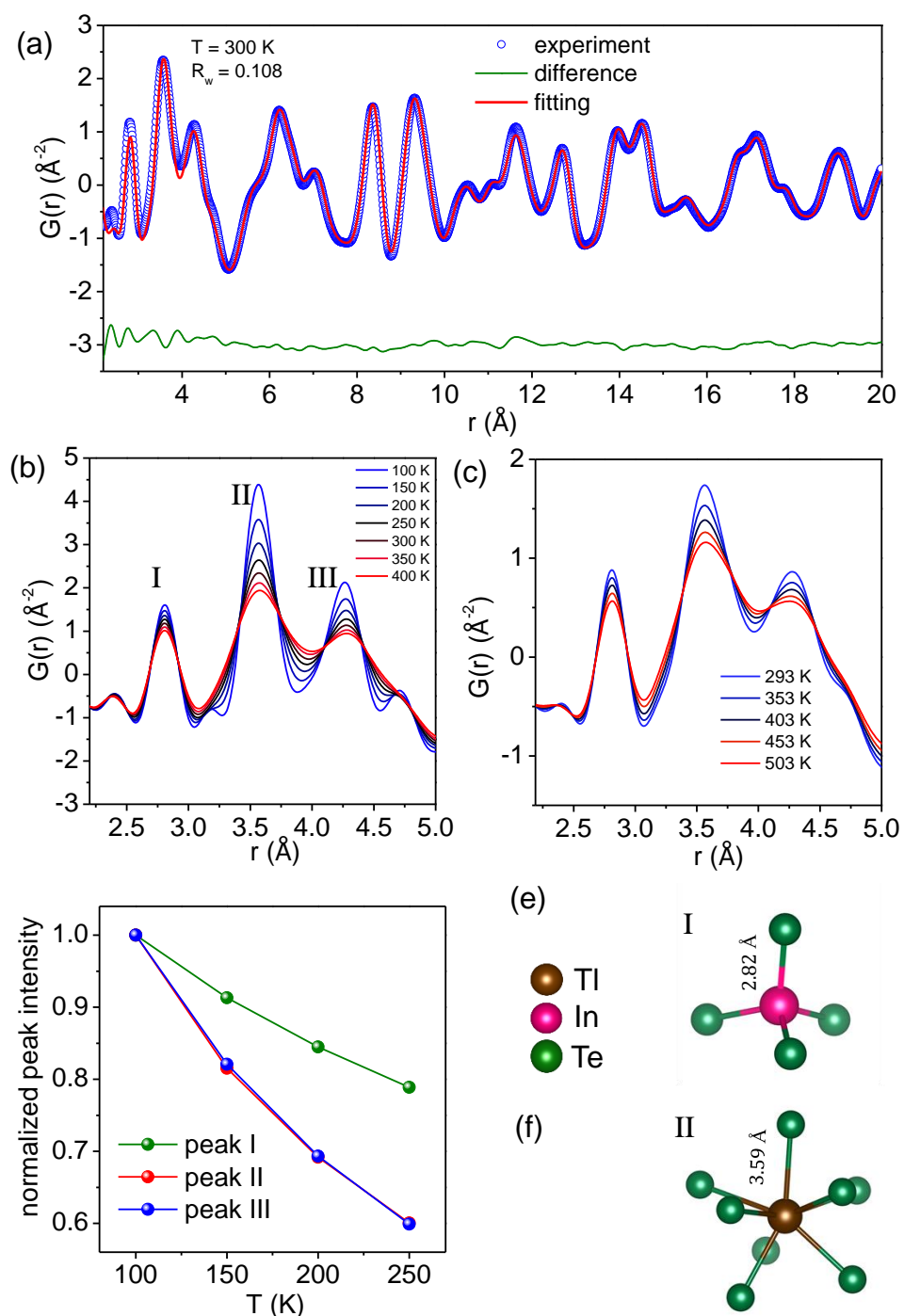


Figure 3.1.2. (a) Synchrotron X-ray PDF data of TlInTe_2 at 300 K fitted using $I4/mcm$ space group. (b) and (c) Temperature dependent $G(r)$ of TlInTe_2 for the first few peaks. (d) Normalized peak intensity for the first three peaks. (e) The In-Te chemical bonding

environment contributing to the first peak in $G(r)$. (f) The Tl-Te chemical environment majorly contributing to the second peak in $G(r)$. The third peak has major contributions from Tl-In correlations.

PDF data over a wide r range using the $I4/mcm$ space group confirms that the compound is indeed pure TlInTe_2 with body-centred tetragonal structure. Figure 3.1.2b, c, exhibit the temperature dependent (100 K – 503 K) PDF data of first few peaks ($r < 5 \text{ \AA}$) which provides information for the temperature evolution of the local crystal structure of the compound. The first peak at around 2.82 \AA corresponds to the nearest neighbour In-Te correlation. This bond is formed by In and Te in the $[\text{InTe}_2]_n^-$ tetrahedra as shown in Figure 3.1.2e. The second peak at $\sim 3.6 \text{ \AA}$ corresponds mainly to the nearest neighbour Tl-Te bond (Figure 3.1.2f). The third peak at 4.24 \AA is predominantly constituted by nearest-neighbour In and Tl interactions. Decrease in peak intensity and increase in peak width with increasing temperature is observed for all these local structural peaks which can be attributed to the increased thermal vibrations. The intensity of the second and third peaks, however, decreases much faster than the first peak with increasing temperature (Figure 3.1.2d). The sharp decrease in intensity of the second peak as compared to the first peak is a direct consequence of the heterogeneous bonding environment within TlInTe_2 . The nearest neighbour In-Te bond has a strong covalent character and thus, shows a higher resistance to change with increase in temperature. Whereas, the nearest neighbour Tl-Te bond being weaker (ionic) in nature, vibrates with greater intensity as temperature increases. This direct evidence of bonding heterogeneity obtained from temperature dependent PDF data confirms the theoretical observations obtained from charge density and electron localization function (ELF).³⁴ Such bonding heterogeneity leads to enhanced phonon scattering and results in low κ_{lat} in TlInTe_2 .

To investigate the nature of atomic vibrations in TlInTe_2 , we have critically examined the local crystal structure of the compound. The refinement of synchrotron X-ray PDF data of TlInTe_2 at 300 K for the whole range evidence that all the constituent atoms, Tl, In and Te vibrate anisotropically. This is in contrast to the earlier reports

obtained from Rietveld refinement of room temperature powder X-ray diffraction data from laboratory diffractometer, which showed anisotropic vibration only for Tl while vibration of In and Te remained isotropic in nature.³⁴ The room temperature atomic displacement parameter (U) of Tl along the crystallographic c -direction (U_{33}) is found to be 0.038 \AA^2 , whereas the values along the crystallographic a - and b -directions ($U_{11} = U_{22}$) are found to be 0.035 \AA^2 . Similarly, at 300 K, the U_{33} values for In and Te are 0.015 \AA^2 and 0.014 \AA^2 , respectively, whereas the $U_{11} = U_{22}$ values are 0.021 \AA^2 and 0.022 \AA^2 , respectively.

To further understand the nature of atomic vibration in TlInTe_2 , we have modelled the first two $G(r)$ peaks at room temperature (local structure) using two different models. Firstly, we used anisotropic U values only for Tl ($U_{33} = 0.074 \text{ \AA}^2$ and $U_{11} = U_{22} = 0.027 \text{ \AA}^2$) while keeping the atomic vibration of In ($U_{11} = U_{22} = U_{33} = 0.016 \text{ \AA}^2$) and Te ($U_{11} = U_{22} = U_{33} = 0.023 \text{ \AA}^2$) isotropic as reported in the previous Rietveld refinement of room temperature PXRD data.³⁴ The resultant fit is shown in Figure 3.1.3a, which exhibits that this model gives reasonably accurate description of the second peak, which is dominated mainly via Tl-Te correlations. However, fit of the first peak, which is dominated by the nearest neighbour In-Te bonding, is poor. The fit improves considerably when we remove the restriction of isotropic vibration for In and Te and replacing the isotropic values with the anisotropic values obtained from the PDF fitting over the whole r range (Figure 3.1.3b). The R_w value also decreases from 0.148 for the first model to 0.117 in the second one, indicating a better fit when anisotropic thermal vibration is considered for all the constituent elements. The temperature evolution of R_w for the whole structural fitting (i.e., $2.2 - 20 \text{ \AA}$) is shown in Figure 3.1.3c, exhibits a gradual increase of R_w with increasing temperature. R_w increases monotonously from 0.079 at 100 K to 0.140 at 503 K. The gradual increase of R_w in the 100 K to 503 K temperature range with increasing temperature is an indication that the structure is slowly deviating from its tetragonal symmetry, however, we have not observed any local symmetry breaking within this temperature range.

To further investigate the origin of such increase, we have divided the PDF spectra into two parts: 2.2 – 5 Å and 5 – 20 Å and estimated the R_w value for these two regions separately keeping all the refined parameters constant as obtained from whole structural fitting (i.e., 2.2 – 20 Å). We observed that for the 5 – 20 Å range (Figure 3.1.3c) which provides information for the average structure, the R_w values remains quite low and varies from 0.07 at 100 K to 0.11 at 503 K, indicating that the average structure remains in the tetragonal $I4/mcm$ symmetry. However, R_w in the 2.2 – 5 Å range increases greatly from 0.12 at 100 K to 0.21 at 503 K (Figure 3.1.3c). Such an increase in R_w value for the local geometry of $TlInTe_2$ has a marked effect on the total structural modelling (i.e., 2.2 – 20 Å) and the increase in its R_w value (Figure 3.1.3c) is mainly attributed to the rapid increase in the R_w value of the local structure. High R_w value for the low r range peaks (2.2 – 5 Å) indicates that the crystallographic information obtained from the fitting of the average structure are a poor descriptor of the local structural features. It infers that the effects of temperature evolution on the low r range peaks position, intensity and width is much stronger and asymptotically different as compared to the average structure. It likely entails that either the crystal structure is locally perturbed as observed previously in well-known thermoelectric compounds like PbQ ($Q = S/Se/Te$),^{48, 49} $SnTe$ ⁵⁰ etc. or the atomic species vibrate with greater anharmonicity within the lattice. Since we have not observed any peak asymmetry with increase in temperature which is an indicator for local structural distortion, it is likely that the high R_w values for first few peaks are due to the enhanced anharmonicity within the lattice. The increase of R_w with increasing temperature then signifies that the anharmonicity increases with increasing temperature which also corroborates with the rapid decrease (increase) in the peak intensity (width) for the second peak as shown in Figure 3.1.2b, c. This evidence of significant anharmonicity is also in accordance with the theoretical prediction of a high Gruneisen parameter.^{34, 35}

Temperature evolution of lattice parameters show a monotonous increment with increasing temperature throughout the whole temperature range of 100 - 503 K (Figure 3.1.4a). The lattice parameter along the crystallographic c -direction increases from 7.17 Å at 100 K to 7.20 Å at 503 K. Similarly, along the crystallographic a - and b -axis ($a = b$

for the tetragonal structure of TlInTe_2 the lattice parameter varies from 8.43 Å to 8.54 Å within the same temperature range.

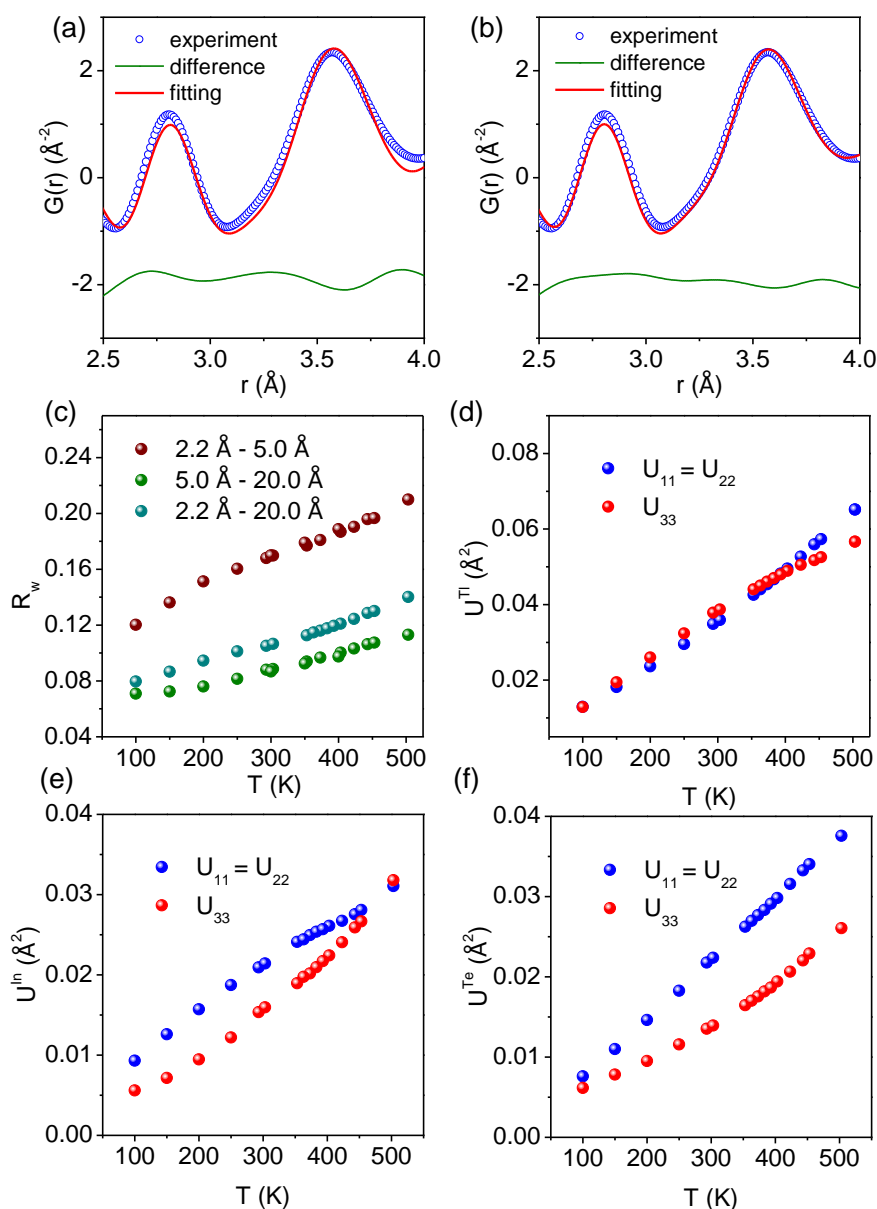


Figure 3.1.3. Local structural ($2.5 \text{ \AA} - 4 \text{ \AA}$) modelling of 300 K synchrotron X-ray PDF data considering (a) anisotropy in the vibration of Tl only, and (b) anisotropic vibration for all the constituent elements Tl, In and Te. (c) Temperature dependent goodness of fit (R_w) for local ($2.2 - 5 \text{ \AA}$), average ($5 - 20 \text{ \AA}$) and total ($2.2 - 20 \text{ \AA}$) structural X-ray PDF data. Atomic displacement parameters of (d) Tl, (e) In and (f) Te along crystallographic a , b ($U_{11} = U_{22}$) and c (U_{33}) directions.

The temperature dependent U values for Tl, In and Te is shown in Figure 3.1.3d - f. At 100 K, the Tl vibration is nearly isotropic having value of 0.013 \AA^2 . The low temperature isotropic nature of Tl vibration is in accordance with the spherical $6s^2$ lone pair of electrons around Tl obtained from ELF.³⁴ This further confirms that Tl resides in an isotropic void created by the Thompson cages of $[\text{InTe}_2]_n^{-n}$ tetrahedra and all the Tl-Te bonds are equal in distance. With increase in temperature, U becomes gradually anisotropic with U_{33} showing slightly higher values as compared to $U_{11} = U_{22}$ (Figure 3.1.3d) in the temperature range of 100 – 393 K. However, as the temperature increases above 393 K, Tl atom shows a greater degree of thermal vibration along the crystallographic a and b -axis as compared to the crystallographic c -direction (Figure 3.1.3d). The thermal expansion along a -(b) direction is also higher compared to c -direction as seen from the temperature dependent a/c ratio (Figure 3.1.4b), which also corroborates with higher $U_{11} = U_{22}$ values for Tl at high temperatures (393 – 503 K) as compared to U_{33} value (Figure 3.1.3d). Due to thermal expansion, the electrostatic repulsion between Tl and Te ions weakens which results in a higher rate of thermal vibration along the crystallographic a - and b -axis, whereas the propensity of Tl^+ to migrate along c -axis increases. This migration will lead to $\text{Tl}^+ - \text{Tl}^+$ electrostatic repulsion along this c -directional Tl chain and might be the reason for the rate of decrease in the increase of U_{33} value at high temperatures. In and Te also show anisotropic values with $U_{11} = U_{22}$ being higher than U_{33} (Figure 3.1.3e, f). The higher value of $U_{11} = U_{22}$ as compared to U_{33} for In and Te is due to the absence of bonding of $[\text{InTe}_2]_n^{-n}$ tetrahedra along the crystallographic a - and b -axis, whereas it forms a 1D linear chain along the crystallographic c -axis. This anisotropic thermal vibration along with bonding heterogeneity of TlInTe_2 observed directly from PDF measurements explain the reason for low and anisotropic thermal conductivity observed in this compound.

To further elucidate the rattling behaviour of Tl atoms in TlInTe_2 , we have critically examined the temperature dependence of the isotropic thermal displacement parameter of Tl. If an atom resides in an oversized cage, it often resembles to that of an Einstein oscillator. These Einstein oscillators vibrate independently to one another and

with identical frequency.⁵¹ For such quantized oscillators, temperature dependence of U at high temperature is given by:⁵¹

$$U_{\text{iso}} = \frac{h^2 T}{(4\pi^2 m \kappa_B \theta_E^2)} \quad (3.1.4)$$

where, m , h , κ_B and θ_E corresponds to reduced mass, Planck constant, Boltzmann constant and Einstein temperature, respectively. Temperature dependence of U_{iso} for Tl in TlInTe₂ exhibits linear behaviour with a slope of $1.277 \times 10^{-4} \text{ \AA}^2/\text{K}$ and an intercept of almost zero (Figure 3.1.4c). Zero intercept signifies the lack of any static disorder in the Tl sublattice. From the linear temperature dependence of U_{iso} , we obtained $\theta_E \sim 43(2) \text{ K}$ ($\sim 30(1.4) \text{ cm}^{-1}$), which corresponds to E_{1g} mode obtained from theoretical prediction and it is highly Tl rich in nature.³⁶ Similarly, using $U_{\text{iso}} = 3h^2 T / (4\pi^2 m \kappa_B \theta_D^2)$ for the $[\text{InTe}_2]_n^{-n}$ tetrahedra, where m is the average mass, Debye temperature (θ_D) of 136.7 1(7) K is obtained which is in fair agreement to theoretically calculated θ_D value of 146.7 K .³⁶ This confirms that while the vibration of the $[\text{InTe}_2]_n^{-n}$ tetrahedra which forms the Thomson cage is correlated in nature giving rise to the Debye type phonon excitation in TlInTe₂, the localized rattling of Tl atoms residing inside those Thompson cages generates soft and highly anharmonic vibrations.

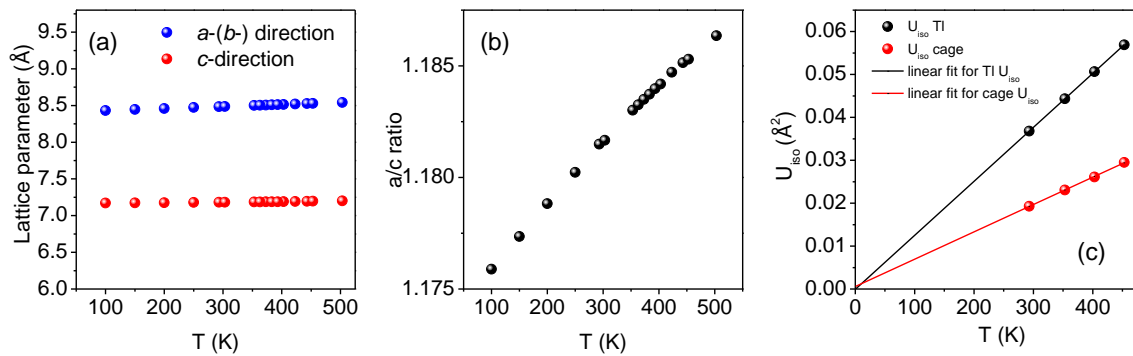


Figure 3.1.4. (a) Temperature dependent lattice parameter of TlInTe₂ obtained from fitting of PDF data (average structure). (b) Ratio of lattice parameter along crystallographic a- (b-) direction with respect to crystallographic c-direction. (c) Linear fitting for U_{iso} values of Tl and the $[\text{InTe}_2]_n^{-n}$ Thompson cage.

Such localized rattling of Tl atoms should give rise to enhanced phonon density of states (phDOS) at low energies with highly anharmonic phonon modes. To experimentally uncover the presence of such low energy modes, we have performed a temperature dependent Inelastic Neutron Scattering (INS) experiment.⁵² Neutron-weighted phDOS over the whole frequency region is shown at Figure 3.1.5a at 5 K. Figure 3.1.5b exhibits the low energy neutron-weighted phDOS from 5 K to 450 K range using neutrons with an incident energy of 280 cm^{-1} . The overall features of the neutron-weighted phDOS compare favorably with the previous theoretically calculated phDOS of TlInTe_2 (Figure 3.1.5c).³⁶ However, this data does not have sufficient resolution to probe the very low energy parts of the DOS (elastic FWHM = 8 cm^{-1}). An additional incident energy of 48 cm^{-1} was also used with much better resolution (elastic FWHM = 2.4 cm^{-1}), however no additional peaks were observed above background. At 5K, there are 3 separate peaks in the neutron-weighted phDOS below 100 cm^{-1} (Figure 3.1.5). The first low energy peak in neutron weighted phDOS is found at 28.3(4) cm^{-1} , which corresponds well to the θ_E value of 30(1.4) cm^{-1} obtained from the temperature dependent U_{iso} of Tl in PDF data indicating the dominant contribution in the low energy phDOS peak comes from the Tl rattlers.

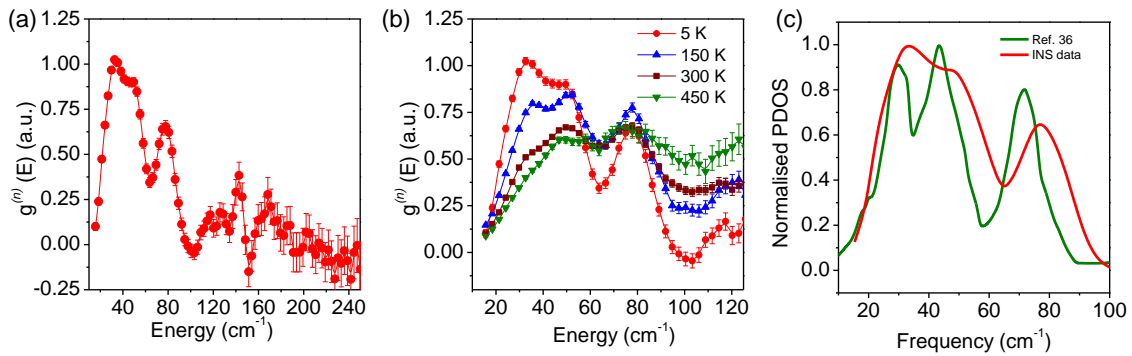


Figure 3.1.5. (a) The neutron-weighted DOS measured on MARI at 5 K. (b) Temperature dependence of the low energy neutron-weighted phonon DOS. (c) Comparison of observed DOS from INS with calculated DOS³⁶ of TlInTe_2 .

Temperature evolution of neutron-weighted phDOS (Figure 3.1.5a) exhibits that the low energy phonon modes broaden dramatically with increasing temperature and by 450 K there are only a few distinct features remaining. There is also significant drop in peak intensity (after correction for Bose statistics) which is likely due to the Debye-Waller factor. Attempts to correct the data with a single isotropic Debye-Waller factor produced unphysical results which is in line with the PDF results. In an attempt to quantify the evolution with temperature, the data, prior to conversion to phDOS were integrated from 2.75 to 6.75 \AA^{-1} and fitted. At each temperature, a one-sided exponential convolved with a Gaussian was used to approximate the shape of the elastic line, and three Gaussians each Bose weighted to appear on both the energy gain and energy loss sides. At 5 K these Gaussians were centered at 28.3(4), 45(1) and 77.2(3) cm^{-1} respectively. Figure 3.1.6a shows the evolution of peak position with temperature. Generally, phonons would be expected to soften with increasing temperature, however, in the presence of anharmonic potentials they can harden. Here, we have observed slight hardening in the case of 45 cm^{-1} mode which is consistent with previous predictions of mode hardening in guest field clathrate rattlers.⁵³ Furthermore, the shifts in the other two modes although in the conventional direction, are large at around 8% by 450 K.

If there were strong phonon-phonon scattering one might expect that the phDOS would show significant broadening as the temperature is increased. This broadening could be related to phonon-phonon scattering rates, however, in a powder dataset the large number of different values and their overlap make extraction very challenging. We have assumed that additional broadening from phonon scattering can be described by adding Gaussian widths in quadrature where the underlying resolution is given by the widths obtained at 5 K (see methods for detail). The extracted broadening from phonon-phonon scattering (σ_{scat}) is shown in Figure 3.1.6b. When allowed to vary freely the 45 cm^{-1} mode loses significant intensity and narrows with increasing temperature in an unphysical manner. Thus, its width was constrained to not fall more than 10 % below its 5 K value (corresponding to the size of error in this parameter). Even so, by 450 K its intensity

(Figure 3.1.6c) is behaving unphysically and so no attempt to extract a width has been made for this mode at any temperature.

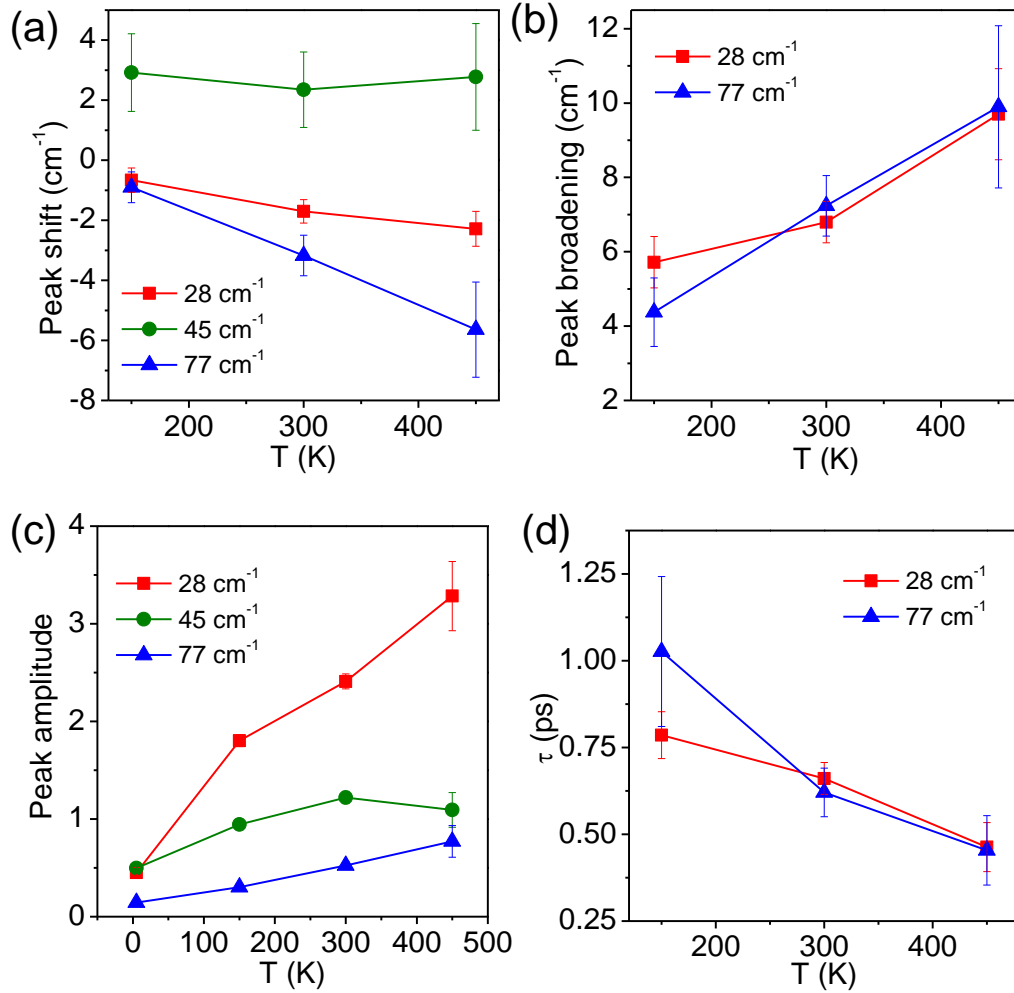


Figure 3.1.6. (a) The shifts in peak position with increasing temperature. The temperature dependence of extracted (b) broadening (FWHM) (c) amplitude and (d) phonon lifetimes.

From the widths extracted for the other two modes however, it is possible to compute a typical phonon lifetime. The inverse lifetime (τ) is obtained by

$$\tau^{-1} = 2.355\pi\sigma_{\text{scat}} \quad (3.1.5)$$

Applying this to our results at 300 K we find phonon lifetime of 0.66(6) ps for the 28 cm^{-1} mode. Phonon lifetime estimated from the average sound velocity obtained from phonon dispersion of TlInTe_2 is found to be 0.72 ps,³⁴ which is similar to that of the measured value from INS. Phonon lifetime for the two modes (28 cm^{-1} and 77 cm^{-1}) along with their temperature dependence shown in Figure 3.1.6d. This is much shorter than the observed values in other thermoelectric materials.⁵⁴ Given the rather simplistic assumptions, it is also in remarkable agreement with the previous theoretical results.³⁶ The ultra-short phonon life time is indicative of strong anharmonic phonon-phonon scattering and would explain the ultralow lattice thermal conductivity of TlInTe_2 .

3.1.4. Conclusion

In conclusion, we have investigated the temperature dependent structural evolution of TlInTe_2 in terms of its local bonding environment and experimental phonon density of states to uncover the origin of its ultralow thermal conductivity. Our microscopic insights into the TlInTe_2 crystal structure using synchrotron X-ray PDF analysis revealed the presence bonding hierarchy between Tl-Te and In-Te, anisotropic vibration of atoms and enhanced anharmonicity. Local structural analysis yielded the information regarding enhanced anharmonic vibration of Tl atoms which is associated with its rattling characteristics. Neutron-weighted phonon DOS obtained from INS measurements further confirmed the presence of low-lying phonon modes and their mode-hardening with increasing temperature evidenced for the presence of high anharmonicity in TlInTe_2 . The temperature dependent X-ray PDF and INS investigations provided conclusive evidence for the origin of low thermal conductivity in TlInTe_2 . Thus, critical examination of chemical bonding, local structure and experimental determination of phonon DOS should be the way forward to explore the fundamental origin of low thermal conductivity in crystalline material.

3.1.5. References

- [1] L.-D. Zhao, V. P. Dravid and M. G. Kanatzidis, *Energy Environ. Sci.*, 2014, **7**, 251-268.
- [2] G. Tan, L.-D. Zhao and M. G. Kanatzidis, *Chem. Rev.*, 2016, **116**, 12123-12149.
- [3] Y. Xiao and L.-D. Zhao, *Science*, 2020, **367**, 1196.
- [4] N. P. Padture, M. Gell and E. H. Jordan, *Science*, 2002, **296**, 280.
- [5] M. K. Jana and K. Biswas, *ACS Energy Lett.*, 2018, **3**, 1315-1324.
- [6] Z. Chen, X. Zhang and Y. Pei, *Adv. Mater.*, 2018, **30**, 1705617.
- [7] K. Biswas, J. He, I. D. Blum, C.-I. Wu, T. P. Hogan, D. N. Seidman, V. P. Dravid and M. G. Kanatzidis, *Nature*, 2012, **489**, 414.
- [8] J. Zhang, D. Wu, D. He, D. Feng, M. Yin, X. Qin and J. He, *Adv. Mater.*, 2017, **29**, 1703148.
- [9] B. Poudel, Q. Hao, Y. Ma, Y. Lan, A. Minnich, B. Yu, X. Yan, D. Wang, A. Muto, D. Vashaee, X. Chen, J. Liu, M. S. Dresselhaus, G. Chen and Z. Ren, *Science*, 2008, **320**, 634.
- [10] G. A. Slack and D. Rowe, *CRC handbook of thermoelectrics*, CRC press Boca Raton, FL, 1995.
- [11] D. T. Morelli, V. Jovovic and J. P. Heremans, *Phys. Rev. Lett.*, 2008, **101**, 035901.
- [12] M. Dutta, K. Pal, U. V. Waghmare and K. Biswas, *Chem. Sci.*, 2019, **10**, 4905-4913.
- [13] P. Acharyya, T. Ghosh, K. Pal, K. Kundu, K. Singh Rana, J. Pandey, A. Soni, U. V. Waghmare and K. Biswas, *J. Am. Chem. Soc.*, 2020, **142**, 15595-15603.
- [14] S. Lee, K. Esfarjani, T. Luo, J. Zhou, Z. Tian and G. Chen, *Nat. Commun.*, 2014, **5**, 3525.

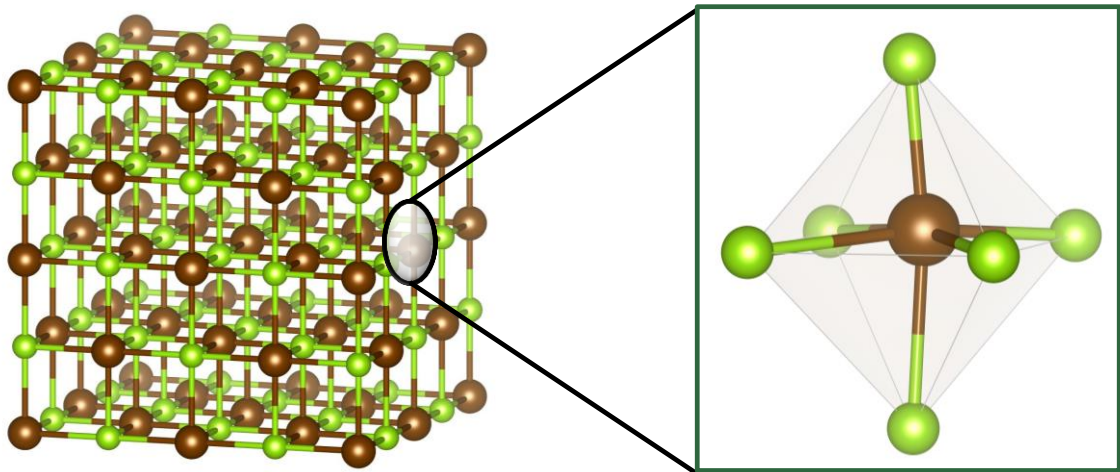
- [15] L.-D. Zhao, S.-H. Lo, Y. Zhang, H. Sun, G. Tan, C. Uher, C. Wolverton, V. P. Dravid and M. G. Kanatzidis, *Nature*, 2014, **508**, 373.
- [16] C. Chang, M. Wu, D. He, Y. Pei, C.-F. Wu, X. Wu, H. Yu, F. Zhu, K. Wang, Y. Chen, L. Huang, J.-F. Li, J. He and L.-D. Zhao, *Science*, 2018, **360**, 778.
- [17] Y. K. Lee, Z. Luo, S. P. Cho, M. G. Kanatzidis and I. Chung, *Joule*, 2019, **3**, 719-731.
- [18] W. He, D. Wang, H. Wu, Y. Xiao, Y. Zhang, D. He, Y. Feng, Y.-J. Hao, J.-F. Dong, R. Chetty, L. Hao, D. Chen, J. Qin, Q. Yang, X. Li, J.-M. Song, Y. Zhu, W. Xu, C. Niu, X. Li, G. Wang, C. Liu, M. Ohta, S. J. Pennycook, J. He, J.-F. Li and L.-D. Zhao, *Science*, 2019, **365**, 1418.
- [19] M. Samanta, K. Pal, P. Pal, U. V. Waghmare and K. Biswas, *J. Am. Chem. Soc.*, 2018, **140**, 5866-5872.
- [20] M. Samanta, K. Pal, U. V. Waghmare and K. Biswas, *Angew. Chem. Int. Ed.*, 2020, **59**, 4822-4829.
- [21] G. J. Snyder and E. S. Toberer, *Nat. Mater.*, 2008, **7**, 105.
- [22] X. Li, P.-F. Liu, E. Zhao, Z. Zhang, T. Guidi, M. D. Le, M. Avdeev, K. Ikeda, T. Otomo, M. Kofu, K. Nakajima, J. Chen, L. He, Y. Ren, X.-L. Wang, B.-T. Wang, Z. Ren, H. Zhao and F. Wang, *Nat. Commun.*, 2020, **11**, 942.
- [23] A. Banik, T. Ghosh, R. Arora, M. Dutta, J. Pandey, S. Acharya, A. Soni, U. V. Waghmare and K. Biswas, *Energy Environ. Sci.*, 2019, **12**, 589-595.
- [24] D. Sarkar, T. Ghosh, S. Roychowdhury, R. Arora, S. Sajan, G. Sheet, U. V. Waghmare and K. Biswas, *J. Am. Chem. Soc.*, 2020, **142**, 12237-12244.
- [25] H. Liu, X. Shi, F. Xu, L. Zhang, W. Zhang, L. Chen, Q. Li, C. Uher, T. Day and G. J. Snyder, *Nat. Mater.*, 2012, **11**, 422.
- [26] S. Ishiwata, Y. Shiomi, J. S. Lee, M. S. Bahramy, T. Suzuki, M. Uchida, R. Arita, Y. Taguchi and Y. Tokura, *Nat. Mater.*, 2013, **12**, 512.
- [27] B. Li, H. Wang, Y. Kawakita, Q. Zhang, M. Feygenson, H. L. Yu, D. Wu, K. Ohara, T. Kikuchi, K. Shibata, T. Yamada, X. K. Ning, Y. Chen, J. Q. He, D. Vaknin, R. Q. Wu, K. Nakajima and M. G. Kanatzidis, *Nat. Mater.*, 2018, **17**, 226-230.

- [28] X. Shi, J. Yang, J. R. Salvador, M. Chi, J. Y. Cho, H. Wang, S. Bai, J. Yang, W. Zhang and L. Chen, *J. Am. Chem. Soc.*, 2011, **133**, 7837-7846.
- [29] T. Takabatake, K. Suekuni, T. Nakayama and E. Kaneshita, *Rev. Mod. Phys.*, 2014, **86**, 669-716.
- [30] T. J. Slade, T. P. Bailey, J. A. Grovogui, X. Hua, X. Zhang, J. J. Kuo, I. Hadar, G. J. Snyder, C. Wolverton, V. P. Dravid, C. Uher and M. G. Kanatzidis, *Adv. Energy Mater.*, 2019, **9**, 1901377.
- [31] M. K. Jana, K. Pal, U. V. Waghmare and K. Biswas, *Angew. Chem. Int. Ed.*, 2016, **55**, 7792-7796.
- [32] M. Dutta, S. Matteppanavar, M. V. D. Prasad, J. Pandey, A. Warankar, P. Mandal, A. Soni, U. V. Waghmare and K. Biswas, *J. Am. Chem. Soc.*, 2019, **141**, 20293-20299.
- [33] D. J. Voneshen, K. Refson, E. Borissenko, M. Krisch, A. Bosak, A. Piovano, E. Cemal, M. Enderle, M. J. Gutmann, M. Hoesch, M. Roger, L. Gannon, A. T. Boothroyd, S. Uthayakumar, D. G. Porter and J. P. Goff, *Nat. Mater.*, 2013, **12**, 1028.
- [34] M. K. Jana, K. Pal, A. Warankar, P. Mandal, U. V. Waghmare and K. Biswas, *J. Am. Chem. Soc.*, 2017, **139**, 4350-4353.
- [35] G. Ding, J. He, Z. Cheng, X. Wang and S. Li, *J. Mater. Chem. C*, 2018, **6**, 13269-13274.
- [36] M. Wu, Enamullah and L. Huang, *Phys. Rev. B*, 2019, **100**, 075207.
- [37] O. Z. Alekperov, A. I. Najafov, E. Nakhmedov, O. A. Samedov, N. A. Aliyeva and G. Jafarova, *J. Appl. Phys.*, 2018, **123**, 135701.
- [38] O. Zeynal, E. Nakhmedov, A. Najafov, O. Samedov, X. Nadirova, V. Gasymov and G. Mahmudova, *J. Phys. D: Appl. Phys.*, 2019, **53**, 035103.
- [39] S. Yesudhas, N. Yedukondalu, M. K. Jana, J. Zhang, J. Huang, B. Chen, H. Deng, R. Sereika, H. Xiao, S. Sinogeikin, C. Kenney-Benson, K. Biswas, J. B. Parise, Y. Ding and H.-k. Mao, *arXiv preprint arXiv:2003.09804*, 2020.

- [40] O. Delaire, J. Ma, K. Marty, A. F. May, M. A. McGuire, M. H. Du, D. J. Singh, A. Podlesnyak, G. Ehlers, M. D. Lumsden and B. C. Sales, *Nat. Mater.*, 2011, **10**, 614-619.
- [41] M. E. Manley, O. Hellman, N. Shulumba, A. F. May, P. J. Stonaha, J. W. Lynn, V. O. Garlea, A. Alatas, R. P. Hermann, J. D. Budai, H. Wang, B. C. Sales and A. J. Minnich, *Nat. Commun.*, 2019, **10**, 1928.
- [42] M. E. Manley, S. Shapiro, Q. Li, A. Llobet and M. E. Hagen, *J. Appl. Phys.*, 2011, **109**, 083722.
- [43] J. Ma, O. Delaire, A. F. May, C. E. Carlton, M. A. McGuire, L. H. VanBebber, D. L. Abernathy, G. Ehlers, T. Hong, A. Huq, W. Tian, V. M. Keppens, Y. Shao-Horn and B. C. Sales, *Nat. Nanotechnol.*, 2013, **8**, 445-451.
- [44] T. Proffen, S. J. L. Billinge, T. Egami and D. Louca, *Z. Kristallogr. Cryst. Mater.*, 2003, **218**, 132.
- [45] C. L. Farrow, P. Juhas, J. W. Liu, D. Bryndin, E. S. Božin, J. Bloch, P. Th and S. J. L. Billinge, *J. Phys: Condens. Matter*, 2007, **19**, 335219.
- [46] J. Taylor, O. Arnold, J. Bilheaux, A. Buts, S. Campbell, M. Doucet, N. Draper, R. Fowler, M. Gigg, V. Lynch and others, *Bull. Am. Phys. Soc.*, 2012, **57**.
- [47] T. Egami and S. J. Billinge, *Underneath the Bragg peaks: structural analysis of complex materials*, Elsevier, 2003.
- [48] E. S. Božin, C. D. Malliakas, P. Souvatzis, T. Proffen, N. A. Spaldin, M. G. Kanatzidis and S. J. L. Billinge, *Science*, 2010, **330**, 1660.
- [49] R. Yu, E. S. Bozin, M. Abeykoon, B. Sangiorgio, N. A. Spaldin, C. D. Malliakas, M. G. Kanatzidis and S. J. L. Billinge, *Phys. Rev. B*, 2018, **98**, 144108.
- [50] K. R. Knox, E. S. Bozin, C. D. Malliakas, M. G. Kanatzidis and S. J. L. Billinge, *Phys. Rev. B*, 2014, **89**, 014102.
- [51] B. C. Sales, D. G. Mandrus and B. C. Chakoumakos, in *Semiconductors and Semimetals*, ed. T. M. Tritt, Elsevier, 2001, vol. 70, pp. 1-36.
- [52] K. Biswas, M. Dutta, S. Roychowdhury, M. Samanta and D. Voneshen, *STFC ISIS Neutron and Muon Source*, 2016, DOI: doi.org/10.5286/ISIS.E.RB1868000, doi.org/10.5286/ISIS.E.RB1868000.

-
- [53] M. Christensen, A. B. Abrahamsen, N. B. Christensen, F. Juranyi, N. H. Andersen, K. Lefmann, J. Andreasson, C. R. H. Bahl and B. B. Iversen, *Nat. Mater.*, 2008, **7**, 811-815.
- [54] P.-F. Lory, S. Pailhès, V. M. Giordano, H. Euchner, H. D. Nguyen, R. Ramlau, H. Borrmann, M. Schmidt, M. Baitinger, M. Ikeda, P. Tomeš, M. Mihalkovič, C. Allio, M. R. Johnson, H. Schober, Y. Sidis, F. Bourdarot, L. P. Regnault, J. Ollivier, S. Paschen, Y. Grin and M. de Boissieu, *Nat. Commun.*, 2017, **8**, 491.

Chapter 3.2



**Local Cation Off-centering Induces
Glass-like Thermal Conduction in
AgSbSe₂**

Local Cation Off-centering Induces Glass-like Thermal Conduction in AgSbSe_2^\dagger

Summary

Lattice vibrations or phonons are one of the major thermal conductors in a crystalline solid. The magnitude of lattice vibrations in a solid is ensured by its periodicity and chemical bonding, thereby, understanding the relationship between local vs. global structure and lattice dynamics is critical in achieving intrinsically low thermal conductivity, which is essential for thermoelectrics, thermal barrier coating and optical phase-change applications. In this chapter, we demonstrate a local cationic off-centering within the global rock salt structure of AgSbSe_2 by using the total structural analysis through temperature dependent (100 – 300 K) synchrotron X-ray pair distribution function (PDF) experiments, which unravel the fundamental origin of its “glass-like” lattice thermal conductivity (κ_{lat}) (~ 0.4 W/mK at 300 K). The cations (Ag/Sb) are distorted along the crystallographic $\langle 100 \rangle$ direction by a factor of ~ 0.2 Å locally, which averages out as rock-salt structure on the global scale. Phonon dispersion based on density functional theory (DFT) shows the presence of weakly imaginary phonon modes signifying that the structure is unstable in its high symmetric rock salt form and validating our experimental results. Electron localization function (ELF) revealed that the local structural distortion arises from the $5s^2$ lone pairs of Sb. Raman spectroscopy exhibits the presence of forbidden low energy Raman modes, concurring with local structural distortion in global cubic structure. Thereby, the low κ_{lat} in AgSbSe_2 originates from the local off-centering of cations driven by the presence of stereochemically active $5s^2$ lone pair of Sb within the global rock salt structure and its significantly high lattice anharmonicity.

[†]M. Dutta, M. V. D. Prasad, J. Pandey, A. Soni, U. V. Waghmare and K. Biswas. *Manuscript under preparation.*

3.2.1. Introduction

Heat propagation through a material is one of its fundamental properties and has a wide array of applications. Inorganic solids with low thermal conductivity find its usefulness in thermoelectrics,¹⁻⁵ phase change memory devices⁶ and thermal insulators⁷ while high thermal conductivity are useful as heat sinks in photovoltaics and electrical devices.^{8, 9} For thermoelectrics, one key requirement is to have a crystalline semiconductor with ultralow lattice thermal conductivity, which is achievable via limiting the heat transport through lattice vibrations (phonons).^{3, 10} The extent of heat carried by these phonons is related to the chemical bonding interactions within the material and the periodicity of the lattice. In absence of homogeneous chemical bonding or lack of local periodicity, the phonon propagation gets hindered and consequently lowers the thermal conductivity. Hence, to interpret the origin of low lattice thermal transport in a crystalline solid, atomistic insights into the local and global structure and their chemical bonding interactions stands crucial.^{11, 12}

Conventionally lowering of the lattice thermal conductivity (κ_{lat}) is mainly focused on minimising the phonon propagation via externally incorporating point defects, nano/meso structures, hierarchical architectures etc.^{10, 13-16} which although impedes phonon propagations but also has detrimental effect on carrier mobility (μ). Thus, to overcome such adverse effects it is essential to furnish compounds which by their own structural design shows intrinsically low κ_{lat} . In this regard several intrinsic approaches have been implemented like introducing bonding hierarchy,^{17, 18} rattling of guest atoms in filled Skutterudites and clathrates,^{19, 20} liquid like cationic motion inside a rigid anionic framework,^{21, 22} presence of high anharmonicity in 2D layered structure^{3, 23-25} and intrinsic rattler atom in Zintl compounds²⁶⁻²⁹. All of these approaches are governed by the presence of crystallographic inhomogeneity with rigid and soft bonding interactions.¹² Other intrinsic phenomena like resonant bonding,¹⁸ lone pair induced anharmonicity,³⁰⁻³² ferroelectric instability,³³ locally distorted lattice framework³⁴⁻³⁹ also shown to efficiently constrain the phonon propagation and thereby lowering the κ_{lat} . Crystalline compounds with site disorder like those of rock-salt I-V-VI₂ chalcogenides (I = Cu, Ag or alkali metal, V = As, Sb, Bi, VI = S, Se, Te) contains high lattice anharmonicity induced by the

presence of positionally disordered atoms and electrostatic repulsion of the cationic ns^2 lone pair of electrons.⁴⁰⁻⁴³

I-V-VI₂ compounds are regarded as one of the promising candidates to achieve high thermoelectric performance by virtue of possessing such low intrinsic κ_{lat} .^{31, 40-42, 44, 45} AgSbSe₂ a globally rock-salt cubic material, belongs to this family exhibits exceptionally low κ_{lat} of 0.42 – 0.36 W/mK at 295 - 710 K and excellent thermoelectric properties for a Te free material.^{41, 46-49} The low κ_{lat} in this compound was previously attributed to the high anharmonicity generated due to the presence of $5s^2$ lone pair on Sb.³¹ The presence of ns^2 lone pair induces significant electrostatic repulsion to the bonding pairs formed by Sb – Se. Popular thermoelectric material PbQ (Q = S, Se, Te) crystallises as similar rock-salt structure that shows high anharmonicity and subsequent low κ_{lat} arising from the presence of $6s^2$ lone pair of electrons on Pb. Recently, it has been found that PbQ shows “emphanitic behaviour” indicating the formation of locally distorted low symmetric structure inside a globally high symmetric rock salt structure on warming.^{34, 35} Presence of such local distortion is known to impede the phonon transport and thereby lowering the κ_{lat} in PbQ. AgSbSe₂ which is globally iso-structural to PbTe, contains $5s^2$ lone pair of electrons on Sb and exhibits a much greater lattice anharmonicity,³¹ thus making it essential to probe into the local structural environment of AgSbSe₂ and understand the underlying correlation between bonding and heat flow in this compound.

Herein, we report fundamental origin of the ultralow lattice thermal conductivity of AgSbSe₂ by performing the complete structural (local and global) analysis using synchrotron X-ray Pair Distribution Function (PDF) analysis. The average structure of AgSbSe₂ do reside in a high symmetric rock salt structure (space group, $Fm\bar{3}m$), but the local structure of AgSbSe₂ is distorted to a lower symmetric structure. Local structural analysis disclose that the cations (Ag/Sb) are off-centred from their mean position along $\langle 100 \rangle$ direction by a factor of ~ 0.20 Å. Phonon dispersion of AgSbSe₂ from the first principles density functional theory (DFT) exhibits imaginary phonon mode at L-point of the Brillouin Zone (BZ), indicating that the structure is unstable in its high symmetric rock salt form. Analysis of the double-well potential involving this imaginary mode reveals that the instability is caused by pair-wise interactions of Ag-Se and Sb-Se bonds.

Stereochemically active $5s^2$ lone-pair of Sb visualized using electron localization function (ELF) is found to responsible this local structural distortion. Furthermore, such local distortions are verified through Raman spectroscopic measurements, wherein we have observed several low energy optical phonon modes which ideally should be Raman inactive in nature. The presence of such local distortion in AgSbSe_2 disrupts the facile conduit required for the phonons to propagate and as a result leads to lowering of its κ_{lat} .

3.2.2. Methods

Synthesis. High quality polycrystalline AgSbSe_2 were prepared by vacuum sealed melting process. Stoichiometric quantities of silver (Sigma Aldrich, 99.99%), antimony (Alfa Aesar 99.9999%) and selenium (Alfa Aesar, 99.9999) (total weight of 6 g) were taken in a quartz ampoule, sealed during high vacuum of 10^{-6} Torr. The contents were then slowly heated up to 673 K over 12 h, then heated up to 1123 K over 4 h, soaked for 10 h, and subsequently cooled to room temperature in 15 hours. The melt was shaken multiple times during the reaction process to ensure homogeneity.

Pair Distribution Function (PDF). X-ray PDF was performed on P02.1 beamline of Petra III, DESY, Germany.⁵⁰ The samples were finely ground using agate mortar pestle and the powder crystals were then filled in a capillary having diameter of 0.6 mm and is sealed on ends using adhesive. Cryostream was used for the temperature dependent measurement within the range (100 K – 300 K). The Perkin Elmer detector was placed at ~ 230 mm from the sample and data sets were obtained at regular interval of 20 K. A dark measurement was performed prior to every data set, and to obtain the background data sets from empty capillary was taken after each sample. Lanthanum Hexaboride (LaB_6) was used as a standard for calibration purposes in our experiment. The beam spot size had a dimension of $0.5 \times 0.5 \text{ mm}^2$ and a fixed energy of 59.83 keV was used.

Processing and normalization of data provided us with $G(r)$, which gives the probability of finding nearest neighbour atoms at a distance r in the material. $G(r)$ is obtained via Fourier transformation of scattering structure function $F(Q)$, using the formula⁵¹

$$G(r) = \frac{2}{\pi} \int_{Q_{min}}^{\infty} F(Q) \sin QrdQ \quad (3.2.1)$$

Where Q is the momentum transfer of the scattering particle. $F(Q)$ is related to structure function $S(Q)$ which is attained from proper correction of scattering data via the relation $F(Q) = Q[S(Q)-1]$.

Modelling of the PDF data was performed using PDFgui⁵² software. All the datasets from 100 K – 300 K were initially modelled using a rock-salt cubic model. The refinement parameters were the scale, lattice parameter, and the U_{iso} values. The first peak of the $G(r)$ vs r plot represents the nearest atom - atom distance, similarly the second peak corresponds to second nearest atom distances (i.e., cation - cation or anion - anion distance) and so on.

For investigating the local off-centering of cations, only scale, peak correlation factor and co-ordinates were refined. Other parameters like the lattice parameters and U_{iso} etc. obtained from cubic fit were fixed. The r range was taken between 2.5 - 4.5 Å. PDF measurements were done at beamline P02.1, PETRA III, DESY, Germany.

Powder X-ray diffraction (PXRD). Room temperature PXRD measurements were recorded on Rigaku SmartLab SE diffractometer using $Cu K\alpha$ ($\lambda = 1.5406$ Å) radiation.

DFT calculation details. Phonon properties are calculated using first-principles pseudo potentials within density functional theory (DFT) as implemented in Quantum Espresso⁵³ code. In DFT calculations, we employed a local density approximation (LDA) to the exchange correlation energy functional and used projector augmented wave (PAW) pseudo-potentials to treat the interactions between ionic cores and valence electrons, and a plane wave basis with an energy cut off of 50 Ry (200 Ry) in representation of Kohn-Sham wave functions (density). Brillouin zone of the tetragonal unit cell is sampled with a uniform $6 \times 6 \times 6$ k-point mesh. The discontinuity in the occupation numbers of electronic states near the gap was smeared with Fermi-Dirac distribution function with a broadening of $k_B T = 0.003$ Ry. Our optimized lattice parameters are in reasonable agreement with the experimental values. Theoretical calculations are done in collaboration with Prof. U. V. Waghmare, JNCASR, India.

Eigen vector modulation. Since the unstable phonon modes appear at L-point $[0, 0, 1/2]$ of primitive cell of $Fd\bar{3}m$ structure, we calculated its potential energy surface by displacing atoms by $\frac{A}{\sqrt{N_a m_j}} \text{Re}[\exp(i\phi)e_j \exp(q \cdot r_{jl})]$ where A is the amplitude, ϕ is the phase, N_a is the number of atoms in the supercell, m_j is the atomic mass, q is the q-point specified, r_{jl} is the position of the j^{th} atom in the l^{th} unit cell, and e_j is the j^{th} atom component of eigenvector. We used Phonopy⁵⁴ tool to modulate the eigen vector.

Thermal conductivity. The thermal diffusivity, D , was measured between 290 K and 723 K using laser flash diffusivity technique in Netzsch LFA-457 instrument. Disc-shaped pellets with ca. 10 mm x 2 mm dimensions were used for thermal transport measurement. Total thermal conductivity (κ) was estimated using the relation, $\kappa = D \times C_p \times \rho$, where ρ is the density (> 98%) of the sample and C_p is the heat capacity (C_p) estimated using the reference Pyroceram. Lattice thermal conductivity (κ_{lat}) is extracted by subtracting electronic thermal conductivity (κ_{el}) from total thermal conductivity. κ_{el} is calculated using the Wiedemann Franz law, $\kappa_{\text{el}} = L\sigma T$, where σ is the electrical conductivity and L is the temperature dependent Lorentz number obtained by fitting the Seebeck coefficient to the reduced chemical potential⁵⁵. Low temperature thermal conductivity data was extracted from a previous report.³¹

Electrical properties. Electrical conductivity (σ) and Seebeck coefficient (S) were simultaneously measured under He-atmosphere from 290 K up to 823 K using ULVAC-RIKO ZEM-3 instrument. Rectangular bar shaped samples (ca. $2 \times 2 \times 9 \text{ mm}^3$) were used for the electrical measurements.

3.2.3. Results and Discussion

Polycrystalline AgSbSe_2 is synthesized via high temperature melting process under vacuum ($\sim 10^{-6}$ Torr) in sealed fused silica tube and is found to crystallise in face-centred cubic ($Fm\bar{3}m$) NaCl type average structure. Powder X-ray diffraction (PXRD) confirms the formation of pure crystalline AgSbSe_2 as we have not detected any secondary peaks within the instrumental detection limit (Figure 3.2.1a). The cations Ag

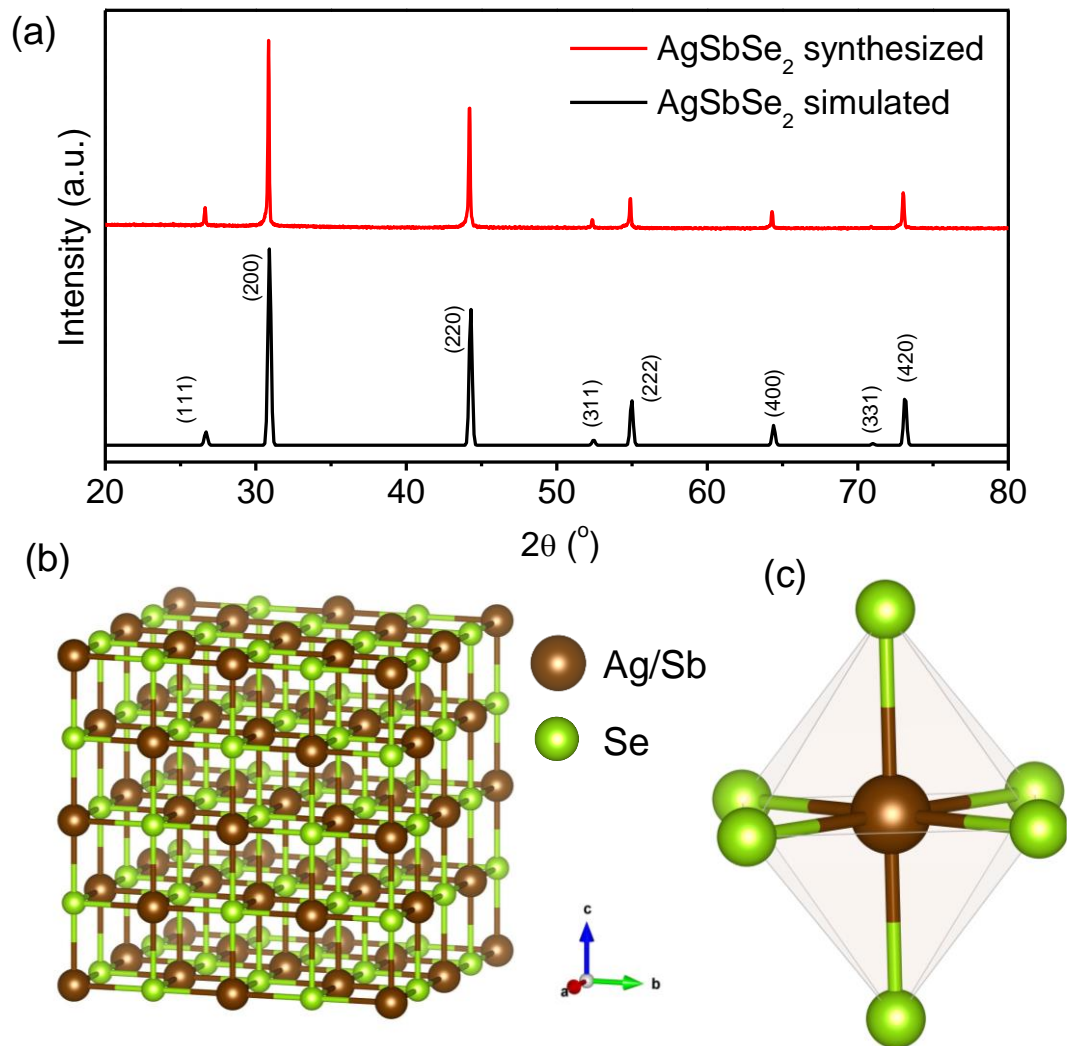


Figure 3.2.1. Room temperature PXRD data of AgSbSe_2 . (b) Rock-salt type structure of AgSbSe_2 . (c) Ag/Sb octahedrally coordinated with 6 Se atoms.

and Sb in AgSbSe_2 reside in the (0, 0, 0) crystallographic site in a random positional disorder, and are surrounded by 6 Se atoms (which take up the $(\frac{1}{2}, \frac{1}{2}, \frac{1}{2})$ crystallographic position) in an octahedral fashion (Figure 3.2.1b, c). The occurrence of such positionally disordered cations induces additional phonon scattering via site scattering mechanism and are beneficial in lowering of the κ_{lat} of a material.¹⁷ Indeed it is found that pristine AgSbSe_2 shows ultralow κ_{tot} and κ_{lat} within the measured temperature range (Figure 3.2.2). The κ_{lat} of AgSbSe_2 is found to be 0.42 – 0.36 W/mK in the temperature range of 295 – 711 K and lies close to the theoretical minimum thermal conductivity (κ_{min}) calculated using the Cahill's model which is given by,^{56,57}

$$\kappa_{min} = \frac{3}{2} \left(\frac{\pi}{6} \right)^{1/3} k_B n^{2/3} v_m \quad (3.2.2)$$

where, k_B is the Boltzmann constant, n is the number density of atoms and v_m is the mean sound velocity calculated using the formula,

$$v_m^3 = \frac{3}{v_l^{-3} + v_{t1}^{-3} + v_{t2}^{-3}} \quad (3.2.3)$$

where v_l ($v_l = 3433$ m/s) and v_t ($v_{t1} = 1362$ m/s and $v_{t2} = 2105$ m/s) are the longitudinal and transverse sound velocities, respectively. κ_{min} for AgSbSe₂ using equation (3.2.2) and (3.2.3) is found to be 0.355 W/mK, thus making the κ_{lat} to be “glass-like”. This indicates that the thermal conductivity of globally crystalline AgSbSe₂ resembles to that of amorphous compounds which are devoid of long-range periodicity. This necessitates investigating the periodicity of AgSbSe₂ in atomic scales to explain such glass-like κ_{lat} phenomenon.

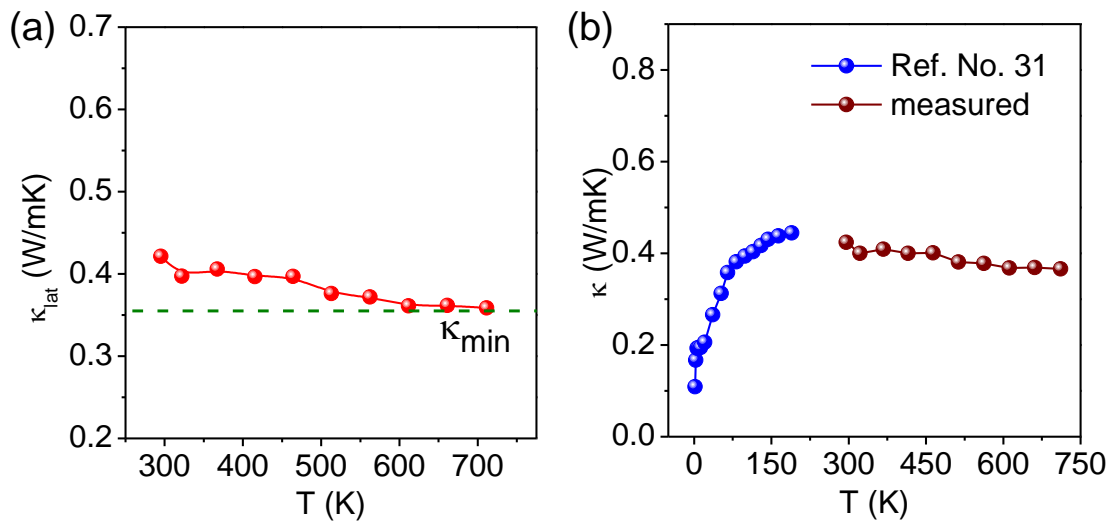


Figure 3.2.2. (a) Temperature dependent total thermal conductivity (κ) of AgSbSe₂. The low temperature data (below 250 K) are taken from supplementary reference 31. (b) Temperature dependent lattice thermal conductivity (κ_{lat}) of AgSbSe₂.

Pair distribution function (PDF) analysis of synchrotron X-ray data provides bonding and structural information in both local and global length scales⁵⁸ and hence is a powerful tool to study the detailed structure of AgSbSe₂ which can reveal the actual origin of its glass-like κ_{lat} . Figure 3.2.3a (top) shows the synchrotron X-ray PDF data ($G(r)$ vs. r) of AgSbSe₂ up to a radial distance of 20 Å at 300 K. The blue circle represents the

experimental data, which have been fitted using a cubic $Fm\bar{3}m$ model and is shown by the red line. The difference between experimentally obtained PDF data and simulated data is given by the green line offset at some distance for clarity (Figure 3.2.3a (top)). The partial simulated profile of the atom-atom correlation is given in Figure 3.2.3a (bottom). It is evident from Figure 3.2.3a (bottom) that the first peak corresponds to nearest Ag (Sb) – Se correlation while the second peak corresponds to Ag (Sb) – Sb (Ag) or Se – Se correlation and so on. The information regarding the local structural environment is contained within the first few peaks (generally $r < 5 \text{ \AA}$), while peaks at high r range provide us with the global structural information. From Figure 3.2.3a two things become evident: (1) experimental data at high r values ($r > 4.5 \text{ \AA}$) provides an excellent agreement to the simulated curve, indicating that AgSbSe₂ do remain in average cubic structure (Figure 3.2.3b). (2) The first peak which correspond to nearest cation – anion correlation is asymmetrical and do not agree with the simulated curve of rock salt cubic model (Figure 3.2.3c). These findings are also corroborated by the goodness of fit (R_w) values which provides a quantitative parameter to the nature of the refinement. Refinement of the total PDF data at 300 K (Figure 3.2.3a), using the conventional cubic $Fm\bar{3}m$ yielded a decent R_w value of 11.14% having lattice parameter value of $\sim 5.79 \text{ \AA}$, and isotropic atomic displacement parameter (U_{iso}) value of $\sim 0.036 \text{ \AA}^2$ and 0.047 \AA^2 for cation Ag/Sb and anion Se respectively. When simulated for the global structure ($4.5 \text{ \AA} < r < 20 \text{ \AA}$) with all the refined parameters constant to that obtained from the total structural refinement, this R_w value decreases to 4.56 % (Figure 3.2.3b), concurring with the global average cubic structure of AgSbSe₂ as obtained from the laboratory PXRD data (Figure 3.2.1a). The R_w value for the local structure ($r < 4.5 \text{ \AA}$), using the same cubic model is found to be as high as 23.92 %, implying that the cubic model is insufficient to explain the crystallographic information contained in the local geometry of AgSbSe₂ (Figure 3.2.3c). The first peak shows a clear asymmetry and can be inferred as incompletely resolved short and long cation-anion bond lengths (Figure 3.2.3c). Such asymmetry in the nearest neighbour peak indicates that the octahedra around the central atom might remain distorted contrary to the ideal octahedron as shown in Figure 3.2.1b. Such distortion in the octahedra arises from the off-centering of the central ion from its mean position and can give rise to enhanced anharmonicity in the lattice.⁵⁹

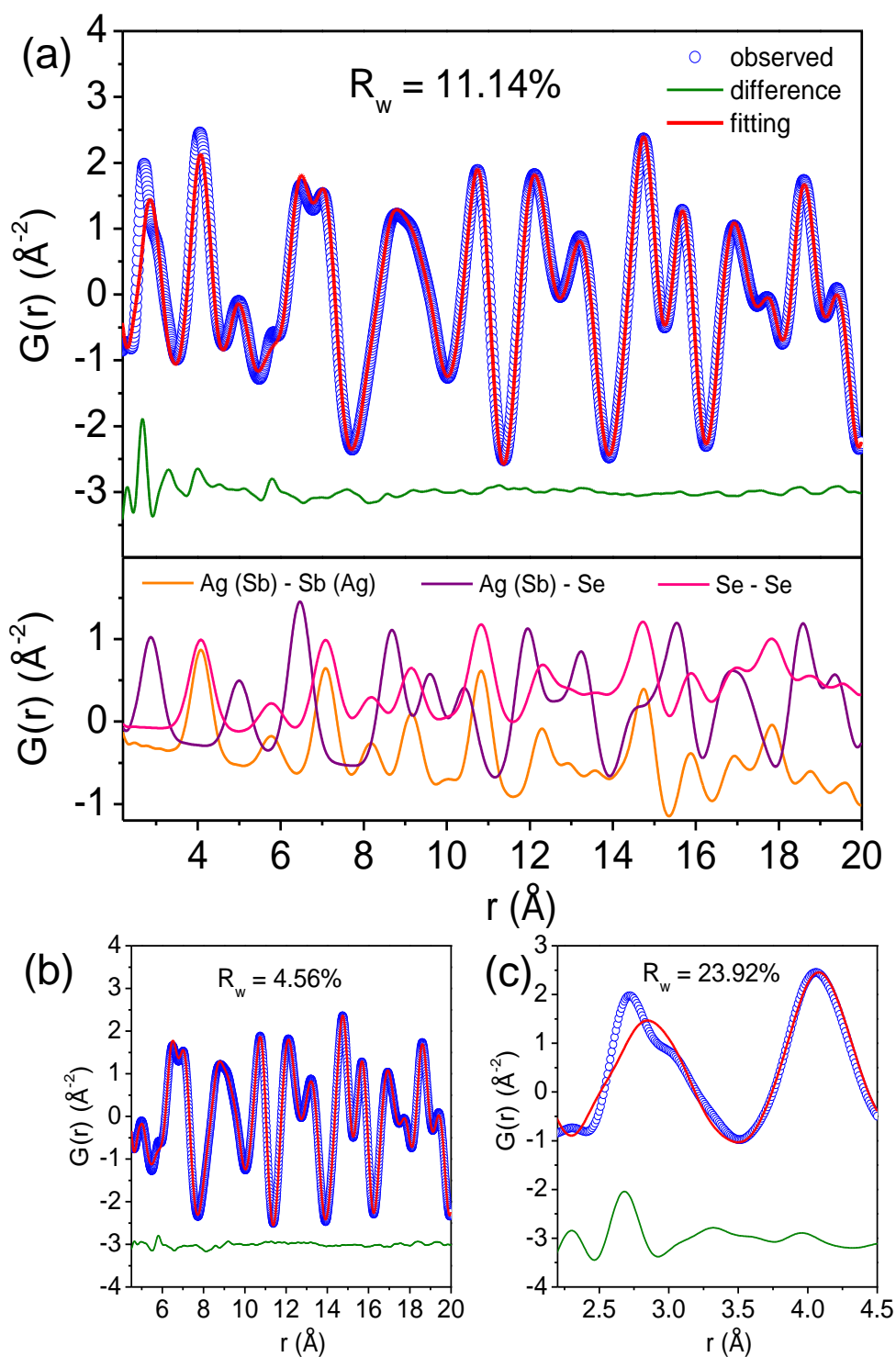


Figure 3.2.3. (a) X-ray pair distribution function (PDF) plot of AgSbSe_2 at 300 K fitted against the cubic $Fm\bar{3}m$ model for the total structure (2.2 - 20 \AA) (top) and partial PDF simulated plot for different atom-atom correlations (bottom). PDF plot of AgSbSe_2 at 300 K fitted against the cubic $Fm\bar{3}m$ model (b) average structure (4.5 - 20 \AA), and (c) local structure (2.2 - 4.5 \AA).

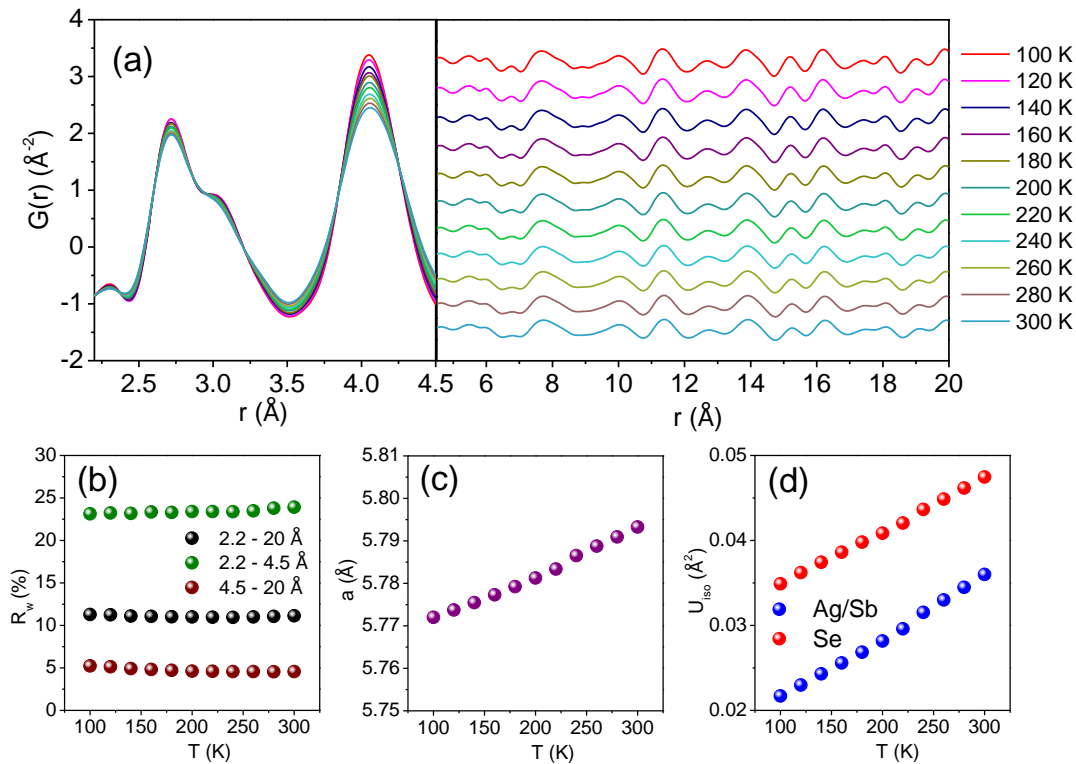


Figure 3.2.4. Temperature dependent (a) Experimental $G(r)$ plots for low r (2.2 – 4.5 Å; left) and high r (4.5 – 20 Å; right), (b) goodness of fit (R_w %), (c) lattice parameter, and (d) isotropic atomic displacement parameter (U_{iso}) of AgSbSe_2 . (b - d) is obtained from refinement of the X-ray PDF data (2.2 - 20 Å) with cubic $Fm\bar{3}m$ model.

Temperature dependent (100 K – 300 K) PDF data is shown in Figure 3.2.4a. The peak asymmetry is evident from the first peak in Figure 3.2.4a (left) and persists up to room temperature. The decrease in intensity with temperature is due to increased thermal motion of the atoms (Figure 3.2.4a). The R_w value for total scattering (2.2 Å < r < 20 Å) remains almost identical from 11.29 % at 100 K to 11.14 % at 300 K (Figure 3.2.4b) when fitted with cubic model. Similarly, for the global structure (4.5 Å < r < 20 Å) R_w values ranges from 5.23 % at 100 K to 4.56 % at 300 K. The R_w value for low r range (2.2 – 4.5 Å) ranges from 23.12% to 23.92% at 100 K and 300 K respectively (Figure 3.2.4b) using the same cubic model. Only a slight change in the R_w value with temperature infers that the structure does not undergo any temperature dependent structural phase transition locally or globally within the measured temperature range (Figure 3.2.4b). Temperature dependent lattice parameter (a) obtained via refining the total structure (2.2 Å < r < 20 Å) using the cubic model is found to increase with increase in temperature (Figure 3.2.4c).

The lattice parameter increases from 5.77 Å at 100 K to 5.79 Å at 300 K and can be attributed to normal thermal expansion and no anomaly has been found to suggest any phase transition within this temperature. U_{iso} is also seen to increase with increase in the temperature when refined using cubic model for the full r range (2.2 – 20 Å). Se atoms as predicted possess greater U_{iso} compared to Ag/Sb, due to its lighter atomic mass. U_{iso} of Se increases from 0.035 Å² to 0.047 Å² in the temperature range of 100 – 300 K, whereas U_{iso} of Ag/Sb increases from 0.021 Å² to 0.036 Å² within the same temperature range (Figure 3.2.4d). The increase in U_{iso} with increase in temperature for all atoms is expected as with warming thermal vibration enhances too.

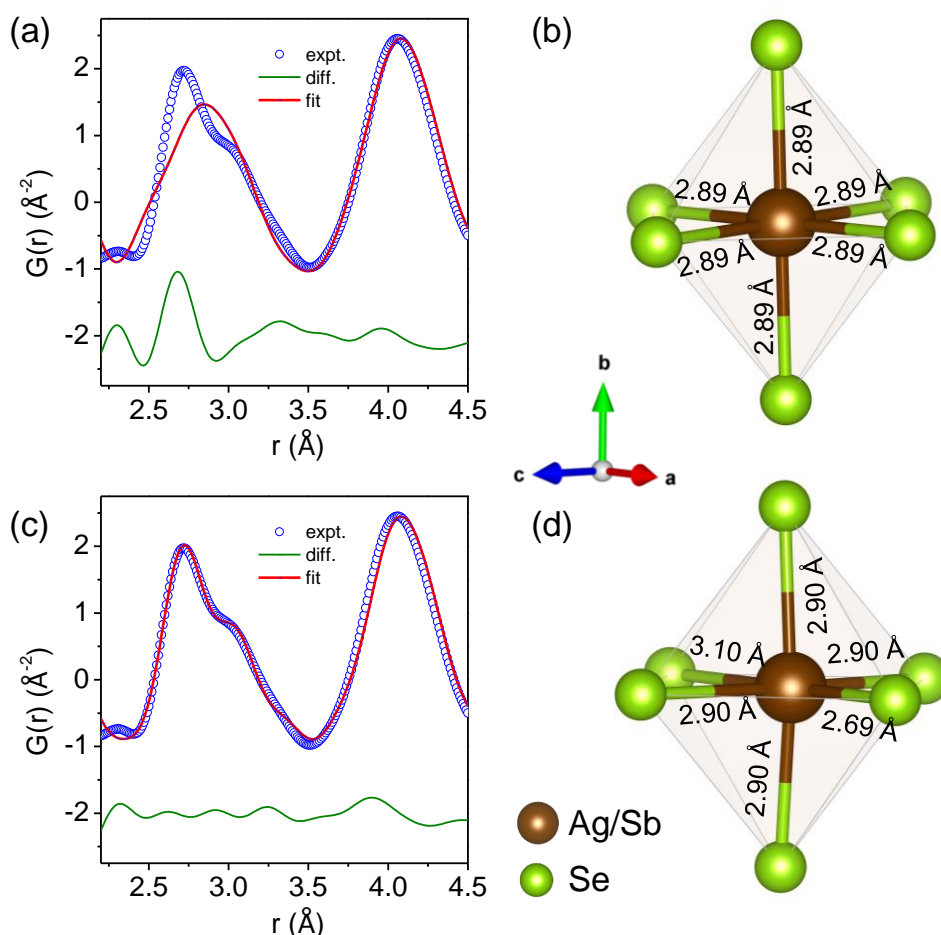


Figure 3.2.5. (a) Refinement of the X-ray PDF data using undistorted Ag/Sb cations at 300 K. (b) Co-ordination around the undistorted Ag/Sb with corresponding bond distances. (c) Refinement of the X-ray PDF data using Ag/Sb cations displaced along $\langle 100 \rangle$ direction at 300 K. (d) Co-ordination around the $\langle 100 \rangle$ distorted Ag/Sb with corresponding bond distances.

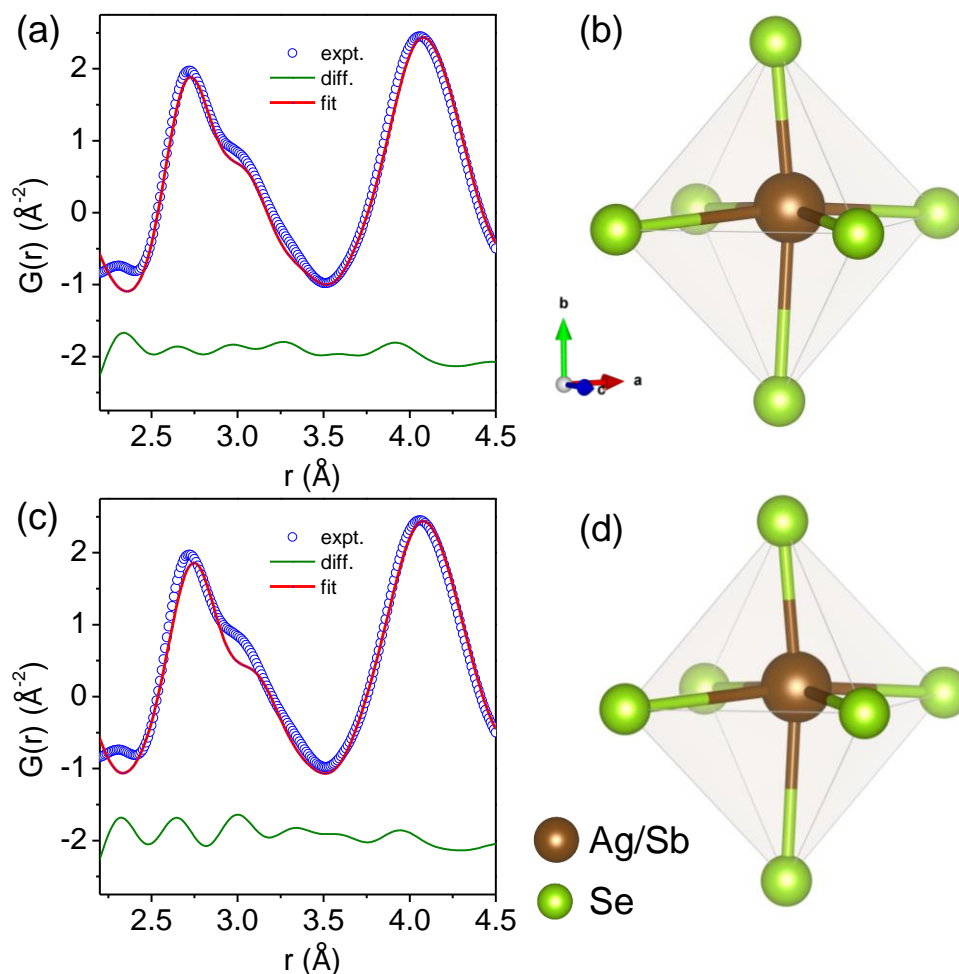


Figure 3.2.6. (a) Refinement of the 300 K X-ray PDF data using Ag/Sb cations displaced along $\langle 110 \rangle$ direction. (b) Co-ordination around the $\langle 110 \rangle$ distorted Ag/Sb. (c) Refinement of the 300 K X-ray PDF data using Ag/Sb cations displaced along $\langle 111 \rangle$ direction. (d) Co-ordination around the $\langle 111 \rangle$ distorted Ag/Sb.

To elucidate the local structure (r ranging from 2.2 – 4.5 \AA) of AgSbSe_2 , several prototypical models by off-centering Ag/Sb from their mean position were used and fitted. Figure 3.2.5a represents the simulated curve at 300 K wherein Ag/Sb are kept undistorted in their mean position. In this model, all the six (Ag/Sb)-Se bonds are identical having bond distance of ~ 2.89 \AA (Figure 3.2.5b). As expected, the simulated curve in figure 3.2.5a, shows a single symmetrical Gaussian curve peaking at ~ 2.89 \AA indicating same bonding environment along all sides of the octahedron as seen in Figure 3.2.5b. On off-centering the Ag/Sb cations along $\langle 100 \rangle$, the simulated data undergoes dramatic improvement and reasonably describes the asymmetry observed in the experimental first

peak (Figure 3.2.5c). Off-centering the cations along $\langle 100 \rangle$, *i.e.*, along the corner of the (Ag/Sb)-Se₆ octahedron leads to one short (~ 2.69 Å), one long (~ 3.10 Å) and 4 medium (~ 2.90 Å) sized bonds (Figure 3.2.5d). Off-centering the cations along $\langle 110 \rangle$ crystallographic direction, *i.e.*, towards the edge of Ag/Sb-Se₆ octahedron, lead to formation of 2 short (~ 2.69 Å), 2 long (~ 3.11 Å) and 2 medium (~ 2.91 Å) sized bonds. Similarly, off-centering along $\langle 111 \rangle$ direction, *i.e.*, along the face of the Ag/Sb-Se₆ octahedron, lead to formation to 3 shorter (~ 2.73 Å) and 3 longer (~ 3.09 Å) bonds. Although the simulated curve for both $\langle 110 \rangle$ and $\langle 111 \rangle$ cation displacement improves the first peak (Figure 3.2.6a, c) fitting but is little worse compared to $\langle 100 \rangle$ cation displacement. The visualization of the distorted octahedron along $\langle 110 \rangle$ and $\langle 111 \rangle$ is given in Figure 3.2.6b, d, respectively. The R_w values for these four models at 300 K are given in figure 3.2.7a. It is clearly evident from the R_w values that off-centering the cations along $\langle 100 \rangle$ crystallographic direction provides the best description of the local environment of AgSbSe₂ as compared to other models. The R_w value of $\langle 100 \rangle$ off-centering is found to be 8.90% at 300 K, which is significantly lower than that of the undistorted cubic AgSbSe₂ ($R_w = 23.92\%$). Displacing Ag/Sb along the other two crystallographic directions, *viz.*, $\langle 110 \rangle$ and $\langle 111 \rangle$ lead to R_w values of 11.23% and 13.09% respectively at 300 K (Figure 3.2.7a). It implies that the displacement of Ag/Sb is likely to be along $\langle 100 \rangle$ direction locally, *i.e.*, along the corner of the octahedron.

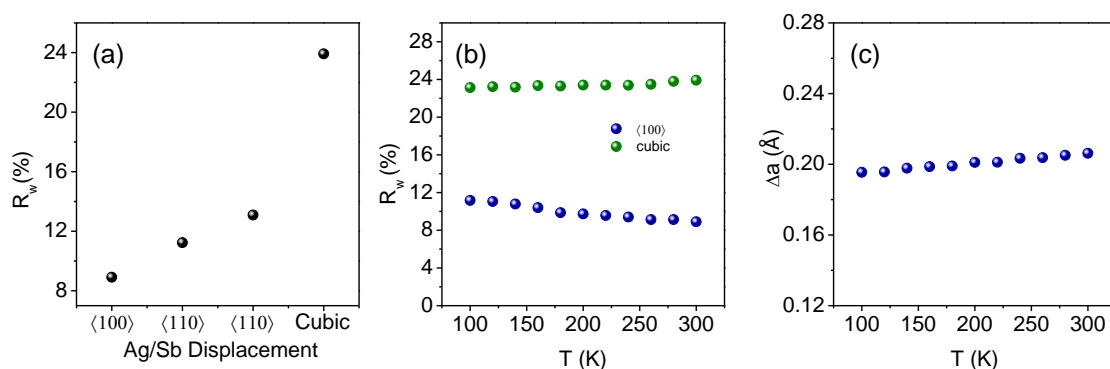


Figure 3.2.7. (a) Goodness of fit (R_w %) obtained for AgSbSe₂ for the undistorted and cation distorted models for the first two peaks. Temperature dependent (b) goodness of fit (R_w %) for (2.2 Å $< r < 4.5$ Å), and (c) magnitude of cation off-centering, for the locally distorted AgSbSe₂ along $\langle 100 \rangle$ direction.

To investigate the temperature evolution of local displacement of Ag/Sb, we have performed fitting of temperature dependent (100 – 300 K) X-ray PDF data ($2.2 \text{ \AA} < r < 4.5 \text{ \AA}$) by the distorted model (along $\langle 100 \rangle$) of local structure. It has been found that the R_w values decreases from 11.17 % at 100 K to 8.90 % at 300 K (Figure 3.2.7b). The cation displacement along $\langle 100 \rangle$ direction remains almost temperature independent with slight increase from 0.19 \AA at 100 K to 0.20 \AA at 300 K (Figure 3.2.7c). Such independent off-centering of cations with temperature suggest that the off-centering of Ag/Sb is static and persists even up to high temperatures. Such local off-centering gives rise to significant lattice anharmonicity^{59, 60} within the lattice and is responsible for the lowering of κ_{lat} in AgSbSe₂. It is to be mentioned that Ag and Sb by virtue of having similar X-ray scattering factors are difficult to differentiate using the conventional PDFgui suite. Individual displacement of Ag and Sb lead to almost identical results to that of combined displacement of Ag and Sb. Hence, such individual PDF fitting data are not shown as it cannot be established with upmost certainty as to which cation is responsible for the off-centering from PDFgui alone.

In order to unravel which of Ag and Sb cations drive the local structural symmetry breaking of AgSbSe₂, we have calculated its phonon spectrum using first-principles DFT. Phonon dispersion of $Fd\bar{3}m$ AgSbSe₂ (Figure 3.2.8a) exhibits weakly unstable doubly degenerate modes at L-point at frequency $\omega = 0.86i$ THz (29i cm⁻¹), in agreement with earlier calculations.³¹ These indicate that AgSbSe₂ is unstable in the reference high symmetry structure, and is likely to distort to a lower symmetry structures. To further understand the nature of this phonon instability, we have calculated potential energy surface of L1 mode as a function of normal mode amplitude, η , by simulating a 2x2x2 supercell. With increase in η , the potential energy decreases and clearly exhibits an anharmonic double-well form (Figure 3.2.8b) with a minimum energy of -2.9 meV/unit cell. To identify the interatomic interactions governing this instability, we determined energetics of distortions corresponding to different components of the L1 instability (Figure 3.2.8b). We find that off-centering distortions corresponding to displacements of Ag-Se and Sb-Se pairs (orange and magenta lines) exhibit the double-well character, whereas the individual atomic, and Ag-Sb pairwise off-centering displacements are stable with a parabolic energy well. This shows that the cation-anion interactions cause the

anharmonic energy profile and in contrast to halide perovskites (CsSnBr_3),³⁷ where the Cs atom's off-centering alone results in an anharmonic double-well potential.

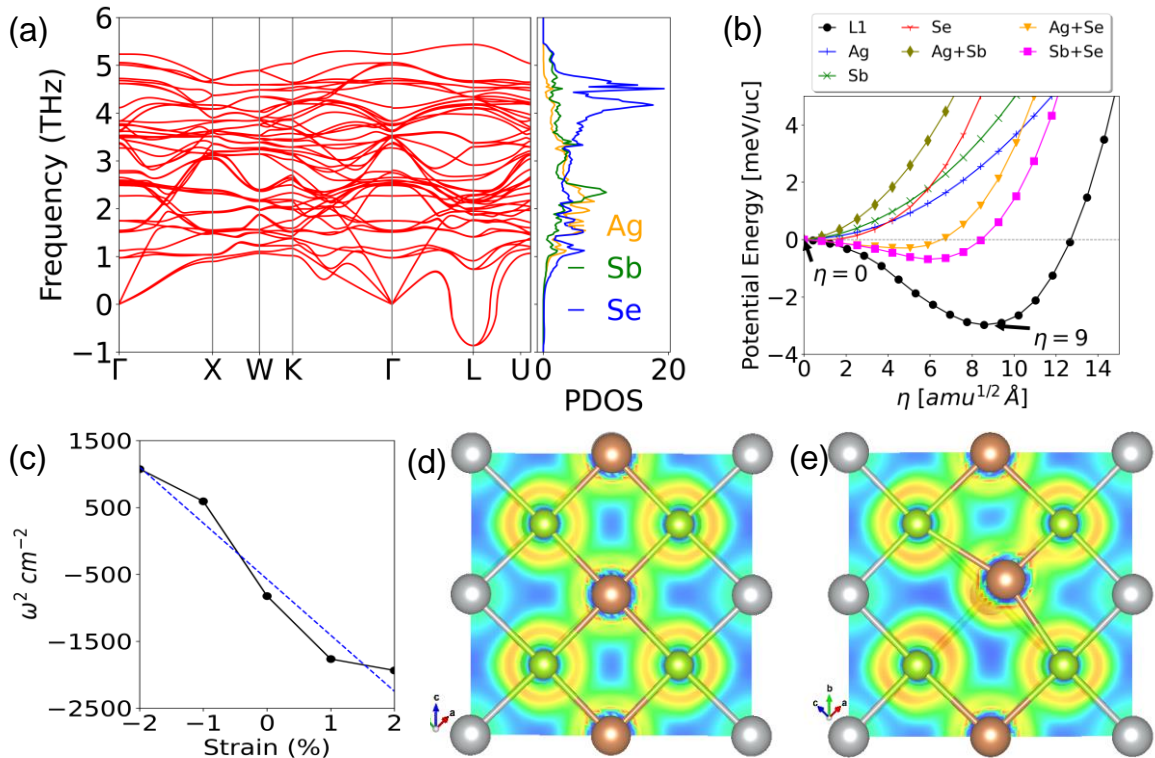


Figure 3.2.8. (a) Calculated phonon dispersion of AgSbSe_2 in $Fd\bar{3}m$ structure (left), along with phonon density of states on the right, Unstable phonon modes (given as $\omega < 0$) at L point $[0, 0, 1/2]$ of the Brillouin Zone (BZ) reveal structural instability of $Fd\bar{3}m$ AgSbSe_2 . (b) Potential energy of structural distortions driven by the unstable mode at L point calculated with $2 \times 2 \times 2$ supercell as a function of normal mode amplitude. Strain-phonon coupling given by the changes in phonon frequencies with hydrostatic strain (c). Contour maps of electron localization function (ELF) of (d) undistorted and (e) Sb off-centered structures of AgSbSe_2 . Contour levels shown are between 0 (blue) and 1 (red) to poorly localized and highly localized electronic regions, respectively. The grey, orange and green spheres represent Ag, Sb and Se atoms respectively.

To assess the strength of anharmonic interactions further, we determined the frequency of unstable mode, ω , at different hydrostatic strains, ϵ . (Figure 3.2.8c). Our estimate of the strain-phonon coupling, $\frac{\partial \omega(\epsilon)}{\partial \epsilon}$, used as a measure of anharmonicity, is 831 cm^{-1} , which is comparable to that in highly anharmonic compounds like SnTe .⁶¹

To gain insights into role of chemical bonding of AgSbSe_2 , we examine the electron localization function (ELF) of the two structural models. First is the undistorted AgSbSe_2 model through which the Sb atoms are displaced by 3% along [100] direction but keeping the cell parameters unchanged. In the first case, $5s^2$ lone pair localized with spherical symmetry around Sb atoms indicating no stereochemical activity (Figure 3.2.8d). In the Sb off-centered distorted structure (Figure 3.2.8e), we find formation of localized lone pair along the off-centering displacements of Sb atoms, indicating that the stereochemical activity results in lone pair - bond pair repulsion and local off-centering of Sb in AgSbSe_2 . This off-centering of Sb in the SbSe_6 octahedra will result in formation of short and long Sb–Se bonds, and such local bonding heterogeneity will have a ripple effect on the neighbouring octahedra of AgSe_6 , as they share the same Wyckoff position. This might be the reason we see slight stabilisation of Ag–Se bonding interactions with increasing η while Sb–Se bonding exhibits much deeper anharmonic well, indicating that the instability originates from the lone pair of Sb (Figure 3.2.8b).

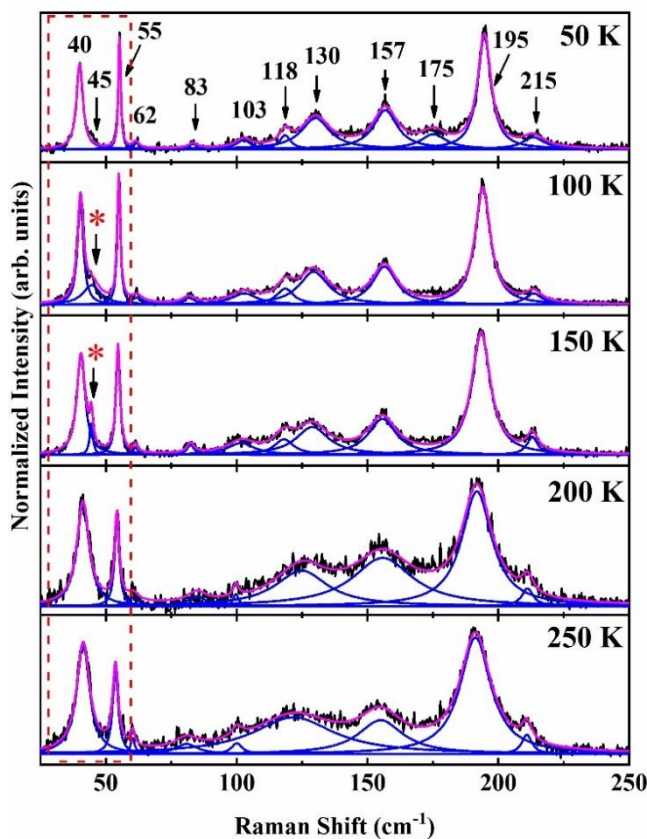


Figure 3.2.9. Temperature dependent Raman spectra of AgSbSe_2 from 50 to 250 K.

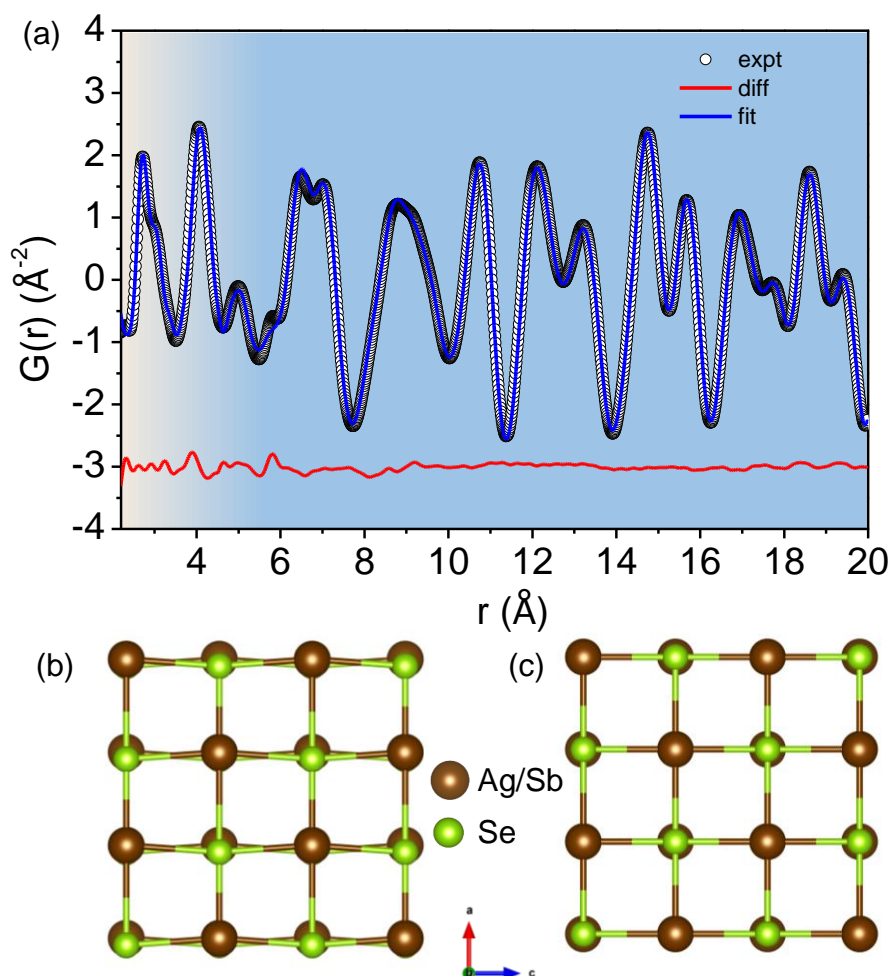


Figure 3.2.10. (a) X-ray PDF data plotted for locally distorted Ag/Sb cations in the low r (2.2 – 4.5 Å) range and undistorted $Fm\bar{3}m$ structure in the high r (4.5 – 20 Å) range. Excellent fitting in both the regions indicates a local structural distortion within an average cubic $AgSbSe_2$. (b), (c) Structure for distorted and undistorted $AgSbSe_2$ respectively.

Temperature dependent (50 – 250 K) Raman spectroscopy was performed for further insight into the structure of $AgSbSe_2$ (Figure 3.2.9). Raman measurements revealed several low energy modes ($< 100\text{ cm}^{-1}$) which the factor group analysis of the average cubic structure indicates that they should be Raman inactive. The presence of such low energy Raman forbidden modes indicates that the local structure deviates from the average cubic symmetry and concords with our PDF and theoretical observations. The appearance of these modes resembles the Raman spectra of $CsPbBr_3$, where such low energy modes indicate the presence of locally non-cubic phases which on average appears

cubic in nature.^{37, 62} The high energy modes at ~ 118 and ~ 130 cm^{-1} shows vibration of Se atoms with A_1 and E_3 symmetry, respectively. Phonon modes at ~ 157 , 195 and 215 cm^{-1} represent vibration of Sb - Se bond.⁶³ The presence of such low frequency optical modes are beneficial for achieving low κ_{lat} as they couple with the heat carrying acoustic phonons and thereby enhances the phonon-phonon scattering.

3.2.4. Conclusion

Finally, it can be said that although AgSbSe_2 attains a global cubic structure, locally it remains distorted along $\langle 100 \rangle$ crystallographic direction. Such local off-centering is a result of the stereochemically active $5s^2$ lone pairs on Sb^{3+} , which exerts repulsive effect on the Sb-Se bonds and thus distorting the SbSe_6 octahedron. This lone pair induced off-centering is found to affect the neighbouring AgSe_6 octahedra as well, resulting in local displacement of Ag. This Sb (Ag) off-centering results in local bonding heterogeneity with shorter and longer Sb-Se (Ag-Se) bonding pairs. A complete picture of AgSbSe_2 can be understood on compiling the 2 models: local $\langle 100 \rangle$ distorted model ($r < 4.5$ Å) and cubic global model (4.5 Å $< r < 20$ Å) as shown in Figure 3.2.10. The excellent agreement of both local and global peaks exemplifies the local displacement of Sb/Ag within the average cubic sublattice. Raman analysis concords the presence of such locally distorted asymmetry in AgSbSe_2 though the presence of several low energy Raman inactive modes. This local distortion induces a significant lattice strain, and in conjunction with the high anharmonicity and low energy optical phonon modes enhances the phonon scattering which ultimately results in the intrinsically ultralow lattice thermal conductivity of AgSbSe_2 . Our findings open up a new paradigm for understanding how the local structure influences the thermal property of a material and should be considered as an essential criterion when establishing structure-property relationship of thermoelectric material.

3.2.5. References

- [1] X.-L. Shi, J. Zou and Z.-G. Chen, *Chem. Rev.*, 2020, **120**, 7399-7515.
- [2] G. Tan, L.-D. Zhao and M. G. Kanatzidis, *Chem. Rev.*, 2016, **116**, 12123-12149.
- [3] W. He, D. Wang, H. Wu, Y. Xiao, Y. Zhang, D. He, Y. Feng, Y.-J. Hao, J.-F. Dong, R. Chetty, L. Hao, D. Chen, J. Qin, Q. Yang, X. Li, J.-M. Song, Y. Zhu, W. Xu, C. Niu, X. Li, G. Wang, C. Liu, M. Ohta, S. J. Pennycook, J. He, J.-F. Li and L.-D. Zhao, *Science*, 2019, **365**, 1418.
- [4] S. Roychowdhury, T. Ghosh, R. Arora, M. Samanta, L. Xie, N. K. Singh, A. Soni, J. He, U. V. Waghmare and K. Biswas, *Science*, 2021, **371**, 722.
- [5] B. Jiang, Y. Yu, J. Cui, X. Liu, L. Xie, J. Liao, Q. Zhang, Y. Huang, S. Ning, B. Jia, B. Zhu, S. Bai, L. Chen, S. J. Pennycook and J. He, *Science*, 2021, **371**, 830.
- [6] K. Pielichowska and K. Pielichowski, *Prog. Mater. Sci.*, 2014, **65**, 67-123.
- [7] N. P. Padture, M. Gell and E. H. Jordan, *Science*, 2002, **296**, 280.
- [8] M. A. Green and S. P. Bremner, *Nat. Mater.*, 2017, **16**, 23-34.
- [9] F. Tian, B. Song, X. Chen, N. K. Ravichandran, Y. Lv, K. Chen, S. Sullivan, J. Kim, Y. Zhou, T.-H. Liu, M. Goni, Z. Ding, J. Sun, G. A. G. Udalamatta Gamage, H. Sun, H. Ziyae, S. Huyan, L. Deng, J. Zhou, A. J. Schmidt, S. Chen, C.-W. Chu, P. Y. Huang, D. Broido, L. Shi, G. Chen and Z. Ren, *Science*, 2018, **361**, 582.
- [10] K. Biswas, J. He, I. D. Blum, C. I. Wu, T. P. Hogan, D. N. Seidman, V. P. Dravid and M. G. Kanatzidis, *Nature*, 2012, **489**, 414-418.
- [11] M. K. Jana and K. Biswas, *ACS Energy Lett.*, 2018, **3**, 1315-1324.
- [12] M. Dutta, D. Sarkar and K. Biswas, *Chem. Commun.*, 2021, **57**, 4751-4767.
- [13] S. Roychowdhury, R. K. Biswas, M. Dutta, S. K. Pati and K. Biswas, *ACS Energy Lett.*, 2019, **4**, 1658-1662.
- [14] L. Fu, M. Yin, D. Wu, W. Li, D. Feng, L. Huang and J. He, *Energy Environ. Sci.*, 2017, **10**, 2030-2040.

- [15] B. Poudel, Q. Hao, Y. Ma, Y. Lan, A. Minnich, B. Yu, X. Yan, D. Wang, A. Muto, D. Vashaee, X. Chen, J. Liu, M. S. Dresselhaus, G. Chen and Z. Ren, *Science*, 2008, **320**, 634.
- [16] J. Ma, O. Delaire, A. F. May, C. E. Carlton, M. A. McGuire, L. H. VanBebber, D. L. Abernathy, G. Ehlers, T. Hong, A. Huq, W. Tian, V. M. Keppens, Y. Shao-Horn and B. C. Sales, *Nat. Nanotechnol.*, 2013, **8**, 445-451.
- [17] M. Dutta, K. Pal, U. V. Waghmare and K. Biswas, *Chem. Sci.*, 2019, **10**, 4905-4913.
- [18] S. Lee, K. Esfarjani, T. Luo, J. Zhou, Z. Tian and G. Chen, *Nat. Commun.*, 2014, **5**, 3525.
- [19] X. Shi, J. Yang, J. R. Salvador, M. Chi, J. Y. Cho, H. Wang, S. Bai, J. Yang, W. Zhang and L. Chen, *J. Am. Chem. Soc.*, 2011, **133**, 7837-7846.
- [20] M. Christensen, A. B. Abrahamsen, N. B. Christensen, F. Juranyi, N. H. Andersen, K. Lefmann, J. Andreasson, C. R. H. Bahl and B. B. Iversen, *Nat. Mater.*, 2008, **7**, 811-815.
- [21] H. Liu, X. Shi, F. Xu, L. Zhang, W. Zhang, L. Chen, Q. Li, C. Uher, T. Day and G. J. Snyder, *Nat. Mater.*, 2012, **11**, 422.
- [22] B. Li, H. Wang, Y. Kawakita, Q. Zhang, M. Feygenson, H. L. Yu, D. Wu, K. Ohara, T. Kikuchi, K. Shibata, T. Yamada, X. K. Ning, Y. Chen, J. Q. He, D. Vaknin, R. Q. Wu, K. Nakajima and M. G. Kanatzidis, *Nat. Mater.*, 2018, **17**, 226-230.
- [23] L.-D. Zhao, S.-H. Lo, Y. Zhang, H. Sun, G. Tan, C. Uher, C. Wolverton, V. P. Dravid and M. G. Kanatzidis, *Nature*, 2014, **508**, 373.
- [24] C. Chang, M. Wu, D. He, Y. Pei, C.-F. Wu, X. Wu, H. Yu, F. Zhu, K. Wang, Y. Chen, L. Huang, J.-F. Li, J. He and L.-D. Zhao, *Science*, 2018, **360**, 778.
- [25] Y. K. Lee, Z. Luo, S. P. Cho, M. G. Kanatzidis and I. Chung, *Joule*, 2019, **3**, 719-731.
- [26] M. Dutta, M. Samanta, T. Ghosh, D. J. Voneshen and K. Biswas, *Angew. Chem. Int. Ed.*, 2021, **60**, 4259-4265.
- [27] M. Dutta, S. Matteppanavar, M. V. D. Prasad, J. Pandey, A. Warankar, P. Mandal, A. Soni, U. V. Waghmare and K. Biswas, *J. Am. Chem. Soc.*, 2019, **141**, 20293-20299.

- [28] D. J. Voneshen, K. Refson, E. Borissenko, M. Krisch, A. Bosak, A. Piovano, E. Cemal, M. Enderle, M. J. Gutmann, M. Hoesch, M. Roger, L. Gannon, A. T. Boothroyd, S. Uthayakumar, D. G. Porter and J. P. Goff, *Nat. Mater.*, 2013, **12**, 1028.
- [29] W. Lee, H. Li, A. B. Wong, D. Zhang, M. Lai, Y. Yu, Q. Kong, E. Lin, J. J. Urban, J. C. Grossman and P. Yang, *Proc. Natl. Acad. Sci. U. S. A.*, 2017, **114**, 8693.
- [30] J. P. Heremans, *Nat. Phys.*, 2015, **11**, 990-991.
- [31] M. D. Nielsen, V. Ozolins and J. P. Heremans, *Energy Environ. Sci.*, 2013, **6**, 570-578.
- [32] E. J. Skoug and D. T. Morelli, *Phys. Rev. Lett.*, 2011, **107**, 235901.
- [33] D. Sarkar, T. Ghosh, S. Roychowdhury, R. Arora, S. Sajan, G. Sheet, U. V. Waghmare and K. Biswas, *J. Am. Chem. Soc.*, 2020, **142**, 12237-12244.
- [34] E. S. Božin, C. D. Malliakas, P. Souvatzis, T. Proffen, N. A. Spaldin, M. G. Kanatzidis and S. J. L. Billinge, *Science*, 2010, **330**, 1660.
- [35] R. Yu, E. S. Bozin, M. Abeykoon, B. Sangiorgio, N. A. Spaldin, C. D. Malliakas, M. G. Kanatzidis and S. J. L. Billinge, *Phys. Rev. B*, 2018, **98**, 144108.
- [36] Z.-Z. Luo, S. Hao, X. Zhang, X. Hua, S. Cai, G. Tan, T. P. Bailey, R. Ma, C. Uher, C. Wolverton, V. P. Dravid, Q. Yan and M. G. Kanatzidis, *Energy Environ. Sci.*, 2018, **11**, 3220-3230.
- [37] H. Xie, S. Hao, J. Bao, T. J. Slade, G. J. Snyder, C. Wolverton and M. G. Kanatzidis, *J. Am. Chem. Soc.*, 2020, **142**, 9553-9563.
- [38] S. Kastbjerg, N. Bindzus, M. Søndergaard, S. Johnsen, N. Lock, M. Christensen, M. Takata, M. A. Spackman and B. Brummerstedt Iversen, *Adv. Funct. Mater.*, 2013, **23**, 5477-5483.
- [39] X. Li, P.-F. Liu, E. Zhao, Z. Zhang, T. Guidi, M. D. Le, M. Avdeev, K. Ikeda, T. Otomo, M. Kofu, K. Nakajima, J. Chen, L. He, Y. Ren, X.-L. Wang, B.-T. Wang, Z. Ren, H. Zhao and F. Wang, *Nat. Commun.*, 2020, **11**, 942.
- [40] D. T. Morelli, V. Jovovic and J. P. Heremans, *Phys. Rev. Lett.*, 2008, **101**, 035901.
- [41] S. N. Guin, A. Chatterjee, D. S. Negi, R. Datta and K. Biswas, *Energy Environ. Sci.*, 2013, **6**, 2603-2608.

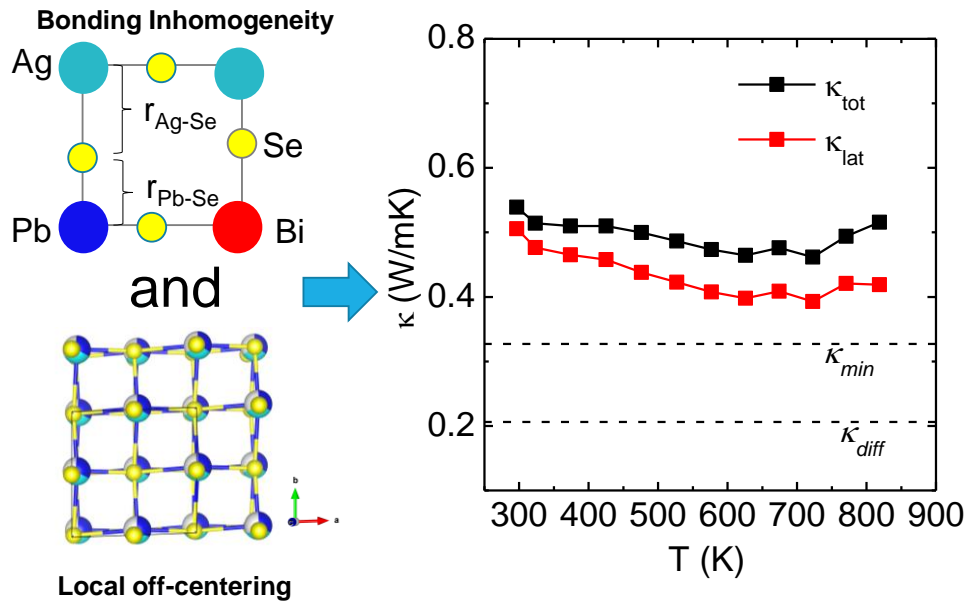
- [42] S. Roychowdhury, R. Panigrahi, S. Perumal and K. Biswas, *ACS Energy Lett.*, 2017, **2**, 349-356.
- [43] L.-H. Ye, K. Hoang, A. J. Freeman, S. D. Mahanti, J. He, T. M. Tritt and M. G. Kanatzidis, *Phys. Rev. B*, 2008, **77**, 245203.
- [44] E. Rathore, R. Juneja, S. P. Culver, N. Minafra, A. K. Singh, W. G. Zeier and K. Biswas, *Chem. Mater.*, 2019, **31**, 2106-2113.
- [45] T. Bernges, J. Peilstöcker, M. Dutta, S. Ohno, S. P. Culver, K. Biswas and W. G. Zeier, *Inorg. Chem.*, 2019, **58**, 9236-9245.
- [46] S. N. Guin, D. S. Negi, R. Datta and K. Biswas, *J. Mater. Chem. A*, 2014, **2**, 4324-4331.
- [47] D. Li, X. Y. Qin, T. H. Zou, J. Zhang, B. J. Ren, C. J. Song, Y. F. Liu, L. Wang, H. X. Xin and J. C. Li, *J. Alloys Compd.*, 2015, **635**, 87-91.
- [48] Z. Liu, J. Shuai, H. Geng, J. Mao, Y. Feng, X. Zhao, X. Meng, R. He, W. Cai and J. Sui, *ACS Appl. Mater. Interfaces*, 2015, **7**, 23047-23055.
- [49] W. Gao, Z. Wang, J. Huang and Z. Liu, *ACS Appl. Mater. Interfaces*, 2018, **10**, 18685-18692.
- [50] A.-C. Dippel, H.-P. Liermann, J. T. Delitz, P. Walter, H. Schulte-Schrepping, O. H. Seeck and H. Franz, *J. Synchrotron Rad.*, 2015, **22**, 675-687.
- [51] T. Proffen, S. J. L. Billinge, T. Egami and D. Louca, *Z. Kristallogr. Cryst. Mater.*, 2003, **218**, 132.
- [52] C. L. Farrow, P. Juhas, J. W. Liu, D. Bryndin, E. S. Božin, J. Bloch, P. Th and S. J. L. Billinge, *J. Phys: Condens. Matter*, 2007, **19**, 335219.
- [53] P. Giannozzi, S. Baroni, N. Bonini, M. Calandra, R. Car, C. Cavazzoni, D. Ceresoli, G. L. Chiarotti, M. Cococcioni, I. Dabo, A. Dal Corso, S. de Gironcoli, S. Fabris, G. Fratesi, R. Gebauer, U. Gerstmann, C. Gougoussis, A. Kokalj, M. Lazzeri, L. Martin-Samos, N. Marzari, F. Mauri, R. Mazzarello, S. Paolini, A. Pasquarello, L. Paulatto, C. Sbraccia, S. Scandolo, G. Sclauzero, A. P. Seitsonen, A. Smogunov, P. Umari and R. M. Wentzcovitch, *J. Phys.: Condens. Matter*, 2009, **21**, 395502.
- [54] A. Togo and I. Tanaka, *Scr. Mater.*, 2015, **108**, 1-5.
- [55] K. Biswas, J. He, I. D. Blum, C.-I. Wu, T. P. Hogan, D. N. Seidman, V. P. Dravid and M. G. Kanatzidis, *Nature*, 2012, **489**, 414.

-
- [56] D. G. Cahill, S. K. Watson and R. O. Pohl, *Phys. Rev. B*, 1992, **46**, 6131-6140.
- [57] M. T. Agne, R. Hanus and G. J. Snyder, *Energy Environ. Sci.*, 2018, **11**, 609-616.
- [58] T. Egami and S. J. Billinge, *Underneath the Bragg peaks: structural analysis of complex materials*, Elsevier, 2003.
- [59] K. M. Ø. Jensen, E. S. Božin, C. D. Malliakas, M. B. Stone, M. D. Lumsden, M. G. Kanatzidis, S. M. Shapiro and S. J. L. Billinge, *Phys. Rev. B*, 2012, **86**, 085313.
- [60] O. Delaire, J. Ma, K. Marty, A. F. May, M. A. McGuire, M. H. Du, D. J. Singh, A. Podlesnyak, G. Ehlers, M. D. Lumsden and B. C. Sales, *Nat. Mater.*, 2011, **10**, 614-619.
- [61] A. Banik, T. Ghosh, R. Arora, M. Dutta, J. Pandey, S. Acharya, A. Soni, U. V. Waghmare and K. Biswas, *Energy Environ. Sci.*, 2019, **12**, 589-595.
- [62] O. Yaffe, Y. Guo, L. Z. Tan, D. A. Egger, T. Hull, C. C. Stoumpos, F. Zheng, T. F. Heinz, L. Kronik, M. G. Kanatzidis, J. S. Owen, A. M. Rappe, M. A. Pimenta and L. E. Brus, *Phys. Rev. Lett.*, 2017, **118**, 136001.
- [63] J. Holubová, Z. Černošek and E. Černošková, *Optoelectron. Adv. Mat.*, 2007, **1**, 663-666.

PART 4

**Potential Use of Intrinsically Low
Lattice Thermal Conductive
Compound as Thermoelectric
Materials**

Chapter 4.1



Bonding Heterogeneity and Lone Pair Induced Anharmonicity Resulted in Ultralow Thermal Conductivity and Promising Thermoelectric Properties in n-type AgPbBiSe_3

Bonding Heterogeneity and Lone Pair Induced Anharmonicity Resulted in Ultralow Thermal Conductivity and Promising Thermoelectric Properties in *n*-type AgPbBiSe_3 [†]

Summary

*Efficiency in generation and utilization of energy is highly dependent on materials that have the ability to amplify or hinder the thermal conduction processes. A comprehensive understanding of the alliance between chemical bonding and structure impacting lattice waves (phonons) is quintessential to furnish compounds with ultralow lattice thermal conductivity (κ_{lat}) for important applications such as thermoelectrics. In this chapter, we demonstrate that *n*-type rock-salt AgPbBiSe_3 exhibits ultra-low κ_{lat} of 0.5-0.4 W/mK in the 290 - 820 K temperature range. We present detailed analysis to uncover the fundamental origin of such low κ_{lat} . First-principles calculations augmented with low temperature heat capacity measurements and experimentally determined synchrotron X-ray pair distribution function (PDF) reveal bonding heterogeneity within the lattice and lone pair induced lattice anharmonicity. Both of these factors enhance the phonon-phonon scattering, and are thereby responsible for suppressed κ_{lat} . Further optimization of the thermoelectric properties was performed by aliovalent halide doping and a thermoelectric figure of merit (zT) of 0.8 at 814 K was achieved in $\text{AgPbBiSe}_{2.97}\text{I}_{0.03}$ which is remarkable among *n*-type Te free thermoelectrics.*

[†]M. Dutta, K. Pal, U. V. Waghmare and K. Biswas. *Chem. Sci.*, 2019, **10**, 4905–4913.

4.1.1. Introduction

Almost all energy conversion processes liberate heat as its universal by-product of varying degrees. Minimizing this waste heat is thus of paramount importance, and a prime criterion for inhibiting such waste heat liberation is to have compounds that obstructs heat propagation. Hence compounds with innate low lattice thermal conductivity (κ_{lat}) are an intriguing prospect in this regard and can be utilized in the field of thermoelectrics,¹⁻³ Typically, in crystalline solids, phonons and free charges are the primary carriers of heat. Since charge carriers are essential for efficient electrical conduction, inhibiting the phonon propagation intrinsically is a primary pathway to reduce thermal conductivity, and is fostering significant attention towards developing materials with innately low κ_{lat} .⁴

Investigations into the phonon-transport processes in solids with intrinsically low κ_{lat} led to unearthing of various avenues to enhance the phonon scattering processes. Skutterudites⁵ and clathrates⁶ accommodate rattling guest atoms in hollow structural cages, thereby decreasing the κ_{lat} . Similarly, Zintl chalcogenides are known to contain weakly bonded rattling cations within a rigid covalent anionic sublattice.⁷⁻⁹ Dynamical movement of cations in a crystalline matrix also causes lowering of κ_{lat} via thermal damping effects.¹⁰⁻¹³ Site disorder and stereochemically active ns^2 lone electron pairs causes lattice anharmonicity, thus lowering the κ_{lat} .^{14, 15} Also, layered compounds are also known to have intrinsic ultralow κ_{lat} .^{3, 16} Several extrinsic approaches were also demonstrated to lower κ_{lat} of the compounds viz. alloying, nano/meso structuring etc.,¹⁷⁻¹⁹ but they come with a caveat of having to compromise on the electrical mobility. Thus, to develop compounds with intrinsically low κ_{lat} , a thorough investigation and fundamental understanding of their chemistry amongst bonding, lattice dynamics and thermal transport mechanisms is essential.

Herein, we observe ultralow κ_{lat} of *c.a.* 0.5 to 0.4 W/mK for *n*-type AgPbBiSe₃ in the temperature range of 290 K – 823 K. AgPbBiSe₃ adopts rock-salt type structure where the Ag/Pb/Bi cations remain statistically disordered in the 4a Wykoff position while the 4b Wykoff site is taken up by the anion Se.²⁰ Thermoelectric properties of the few compounds from AgPbBiQ₃ (Q = S/Se/Te) were previously measured in only low temperatures (2 - 300 K), but the *zT* remains very low and fundamental reasons behind

low κ_{lat} was not explored in detail.^{20, 21} To investigate the origin of low κ_{lat} of AgPbBiSe₃, we have performed low temperature heat capacity measurements, which reveal Einstein modes and hence the presence of low lying optical phonon. Using first-principles (DFT) calculations, we show a remarkable crystallographic inhomogeneity associated with distinct bonding environments of the statistically disordered cations (Ag/Pb/Bi) coordinated with anions (Se). We also find high mode Gruneisen parameters ($\gamma_{qv} \sim 20$), which are measure of lattice anharmonicity, and trace their origin to the presence of 6s² lone pairs on Pb and Bi. Pair distribution function (PDF) derived from the experimentally obtained synchrotron X-ray diffraction patterns enabled us to determine the bonding and lattice environment in terms of nearest neighbour atoms in real space, and obtain valuable microscopic insights into the mechanism behind low κ_{lat} . Results of the PDF analysis corroborate our theoretical inferences of bonding heterogeneity and presence of lone pairs, which are responsible for inhibition of the heat carrying acoustic phonons.

Demonstrating the low thermal conductivity, which is a prerequisite to realization of high thermoelectric performance, we have optimised the thermoelectric figure of merit (zT) of this *n*-type AgPbBiSe₃ via aliovalent halogen doping. We have observed a further reduction in the κ_{lat} of AgPbBiSe₃ to 0.23 W/mK at 823 K, which is attributed to point defect scattering. As a result, we report a two-fold increase in the zT from 0.43 for pristine AgPbBiSe₃ at 818 K to 0.8 for AgPbBiSe_{2.97}I_{0.03} at 814 K.

4.1.2. Methods

Reagents. Elemental silver (Sigma Aldrich, 99.99%), Lead (Alfa Aesar, 99.999%), bismuth (Sigma Aldrich, 99.999%), selenium (Alfa Aesar, 99.9999%) and BiX₃ (X= Cl, Br, I; Sigma Aldrich, 99.99%) were used as starting materials for the synthesis, without further purification.

Synthesis. Stoichiometric ratio of the reagents was taken to prepare ~10 g crystalline ingots of AgPbBiSe₃ and AgPbBiSe_{3-y}X_y (X = Cl, Br, I and y = 0.03 for Cl and I, 0.02 for Br). The reagents were poured into 8 mm inner diameter quartz ampoules and subsequently flame-sealed under high vacuum of 10⁻⁵ Torr. The vacuum-sealed ampoules were then heated gradually to 723 K in 12 h to minimize Se evaporation, followed by

heating up to 1223 K in 5 h. It was then soaked at that temperature for 10 h with constant shaking to ensure homogeneity in the sample. The following melt compound was then cooled slowly to room temperature in 15 h. Upon cooling the ingots obtained were cut into disk (having dimensions of 8 mm diameter and 2 mm thickness) and parallelepiped ($\sim 2 \times 3 \times 8 \text{ mm}^3$) shapes. The disk-shaped samples were used for thermal diffusivity measurements and the parallelepiped shaped samples were used for electrical transport measurements.

Powder X-ray Diffraction (PXRD). PXRD of the finely ground samples was done in Bruker D8 diffractometer instrument with Cu $K\alpha$ ($\lambda = 1.5406 \text{ \AA}$) being the radiation source, for all the as-synthesized samples.

Thermal conductivity. Disk shaped samples were used for the measurement of thermal diffusivity (D) via laser flash technique in Netzsch LFA 457 instrument under N_2 atmosphere. The obtained diffusivity was then used to measure the thermal conductivity of the samples using the formula $\kappa = DC_p\rho$, where ρ is the density of the measured samples and C_p is the heat capacity using Dulong-petit limit. All the measured samples have density greater than 94 %. The minimum lattice thermal conductivity is calculated via diffusion method²² using the formula $\kappa_{diff} \approx 0.76n^{(2/3)}k_Bv_s$, where n stands for number density of atoms, k_B is the Boltzmann factor and v_s is the mean velocity of sound derived from experimental heat capacity measurements (1710 m/s). The final value of κ_{diff} is found out to be 0.206 W/mK for undoped $AgPbBiSe_3$.

Electrical properties. Parallelepiped shaped samples were used for electric transport measurements. All the samples were measured under He atmosphere in ULVAC-RICO ZEM3 instrument. Both Seebeck coefficient and Electrical conductivity were measured simultaneously within the temperature range 290 K – 823 K.

Hall measurement. Room temperature hall measurement was performed in an in-house set up under a varying magnetic field of 0.0 – 0.57 T. The samples used are bar shaped and the current used is 75 mA.

Band gap measurement. Finely ground sample was used to obtain the optical band gap of the synthesized samples. The optical band gap was estimated in a FT-IR Bruker IFS 66V/S spectrometer within the range of 6000 – 400 cm^{-1} . Absorption (α/S) data were derived using Kubelka-Munk equation: $\alpha/S=(1-R)^2/(2R)$, where R is the reflectance, α and S corresponds to absorption and scattering coefficient, respectively. The energy band gaps were deduced from α/S vs E_g (eV) plot.

X-ray Pair Distribution Function (PDF). For performing X-ray PDF, the samples were finely ground using agate mortar pestle and the powder crystals were then filled in a capillary having diameter of 0.6 mm and is sealed on ends using adhesive. The capillaries then mounted on an instrument holder which is placed right in between the beam source and the image plate. Cryostream was used for the temperature dependent measurement within the range (100 K – 400 K). The Perkin Elmer detector was placed at 230 mm from the sample and data sets were obtained at regular interval of 50 K. A dark measurement was performed prior to every data set, and to obtain the background data sets from empty capillary was taken after each sample. Lanthanum Hexaboride (LaB_6) was used as a standard for calibration purposes in our experiment. The beam spot size had a dimension of 0.5 x 0.5 mm^2 and a fixed energy of 59.83 keV was used.

Processing and normalization of data provided us with $G(r)$, which gives the probability of finding nearest neighbor atoms at a distance r in the material. $G(r)$ is obtained via Fourier transformation of scattering structure function $F(Q)$, using the formula²³

$$G(r) = \frac{2}{\pi} \int_{Q_{min}}^{\infty} F(Q) \sin Qr dQ \quad (4.1.1)$$

Where Q is the momentum transfer of the scattering particle. $F(Q)$ is related to structure function $S(Q)$ which is attained from proper correction of scattering data via the relation $F(Q) = Q[S(Q)-1]$.

Modelling of the PDF data was performed using PDFgui²⁴ software. All the datasets from 100 K – 400 K were initially modeled using a rock-salt cubic model. The refinement parameters were the lattice parameter, and the ADP values. To minimize the correlation among the ADPs, first ADPs of all the cations (i.e., Ag/Pb/Bi) on the same

crystallographic sites were taken same and are refined. It was then followed by individual refinement of ADPs of the distinct atoms.

For investigating into the off-centering of the cations, ADPs obtained from cubic fit were fixed. The r range was taken 2.5 Å to 3.5 Å. The peak here corresponds to the nearest cation to anion distance (i.e., $a/2$, a corresponds to lattice distance). The parameters refined were lattice parameters and the cations position in $\langle 111 \rangle$ direction. PDF data is taken in beamline P02.1, PETRA III, Germany.

Computational Methods. Our first-principles calculations are based on density functional theory (DFT) using the Vienna Ab-initio Simulation Package (VASP).^{25,26} The potential energy of the interaction between ionic core of an atom and valence electrons was treated within the projected augmented wave (PAW)²⁷ method. Exchange and correlation energy of electrons was included within a generalized gradient approximated (GGA)²⁸ and functional parametrized by Perdew, Burke and Ernzerhof.²⁹ Expansions of electronic wave functions in plane wave basis was truncated with cut-off energy of 520 eV. Brillouin Zone (BZ) integrations were sampled on a uniform mesh of $8 \times 8 \times 8$ k-points, and discontinuity in occupations numbers of electronic states near across the gap was smeared with Fermi-Dirac distribution functions with a broadening of $k_B T = 0.04$ eV. To model AgPbBiSe_3 (in which Ag, Pb and Bi are statistically disordered at the cations sites) in our DFT calculations, we constructed an isotropic supercell containing 6 atoms (3 cations and 3 anions). This supercell basically consists of three primitive unit cells of a face centered cubic lattice. As there are three cations (Ag, Pb, and Bi) in the crystal structure, and three cation sites in our supercell, there would be a total six possible configurations. After fully optimizing all the structures, we found them to be iso-energetic (the energy difference between any two structure is less than 10^{-5} eV/f.u.). We took one of the structures to do further calculations. As phonon frequencies obtained using this supercell revealed imaginary phonon modes at several points (including the zone center i.e., Γ) in the Brillouin zone, we distorted the crystal structure by displacing atoms along the eigen vectors of the unstable phonon mode at Γ and relaxed atomic positions (the internal degrees of freedom the supercell. We used this relaxed supercell (which stabilizes

the Γ -point phonons) in further calculations to determine the electronic structure and lattice dynamical properties of AgPbBiSe_3 .

Phonon dispersion of AgPbBiSe_3 was determined using finite-displacement method using Phonopy³⁰ and VASP calculations on (2x2x2) supercell containing 48 atoms. Gruneisen parameter (γ) measures the degree of lattice anharmonicity in a material. We estimated mode Gruneisen parameter (γ_{qv}) of AgPbBiSe_3 using a central difference formula and phonon frequencies calculated at volumes ($1.02V_0$ and $0.98V_0$) around the equilibrium volume (V_0) of the supercell. While we included the effect of spin-orbit coupling (SOC) in the calculations of electronic structure, phonon frequencies were obtained without including the SOC in our calculations. To check the convergence of the phonon frequencies with respect to the supercell size, we took 3x3x3 supercell (with 162 atoms) and the same convergence criteria as above with a slightly reduced k-point grid (2x2x2). The changes in the phonon frequencies are not very significant particularly for the acoustic phonon branches. Hence, all the further calculations were performed using the (2x2x2) supercell. This work is done in collaboration with Prof. U. V. Waghmare of JNCASR, Bangalore.

4.1.3. Results and Discussion

High quality pure crystalline ingots of AgPbBiSe_3 were synthesized via melting process under high vacuum of 10^{-5} Torr. Figure 4.1.1a shows the Rietveld refinement of the powder-XRD data obtained in an in-house X-ray diffractometer (Cu $K\alpha$; $\lambda = 1.5406 \text{ \AA}$) with a cubic rock-salt model, which validates that AgPbBiSe_3 procures NaCl structure (space group, $Fm-3m$). The anion 4b Wyckoff site is occupied by the Se atoms whereas the cation 4a Wyckoff site is occupied by three cations in a statistical disorder (i.e., Ag, Bi and Pb) as shown in Figure 4.1.1b. The presence of 3 cations at the 4a Wyckoff site results in a greater degree of cation disorder in the crystal system. The global structure is apparently similar to LAST ($\text{AgPb}_m\text{SbTe}_{2+m}$ i.e. PbTe rich),³¹ where 3 cations Ag/Pb/Sb in same site provides enhanced scattering of phonons. Here too in Te free AgPbBiSe_3 , the positionally disordered cations in the same position expected to result in lowering of thermal conductivity to a certain extent via site scattering mechanism. Figure 4.1.1c depicts the temperature dependent total thermal conductivity (κ_{tot}) and κ_{lat} of AgPbBiSe_3 .

The κ_{lat} is found to be ultra-low and remains almost flat within the measured temperature range with values from 0.50 W/mK at 296 K to 0.41 W/mK at 818 K. The value although is ultra-low but is found to be higher than the minimum κ_{lat} (0.206 W/mK) derived using diffusion model²² as well as from Cahill's formulation (0.327 W/mK)³² which enhances the scope for further lowering of the κ_{lat} . The electronic contribution to the κ_{tot} is found to be very less and is given in Figure 4.1.1d.

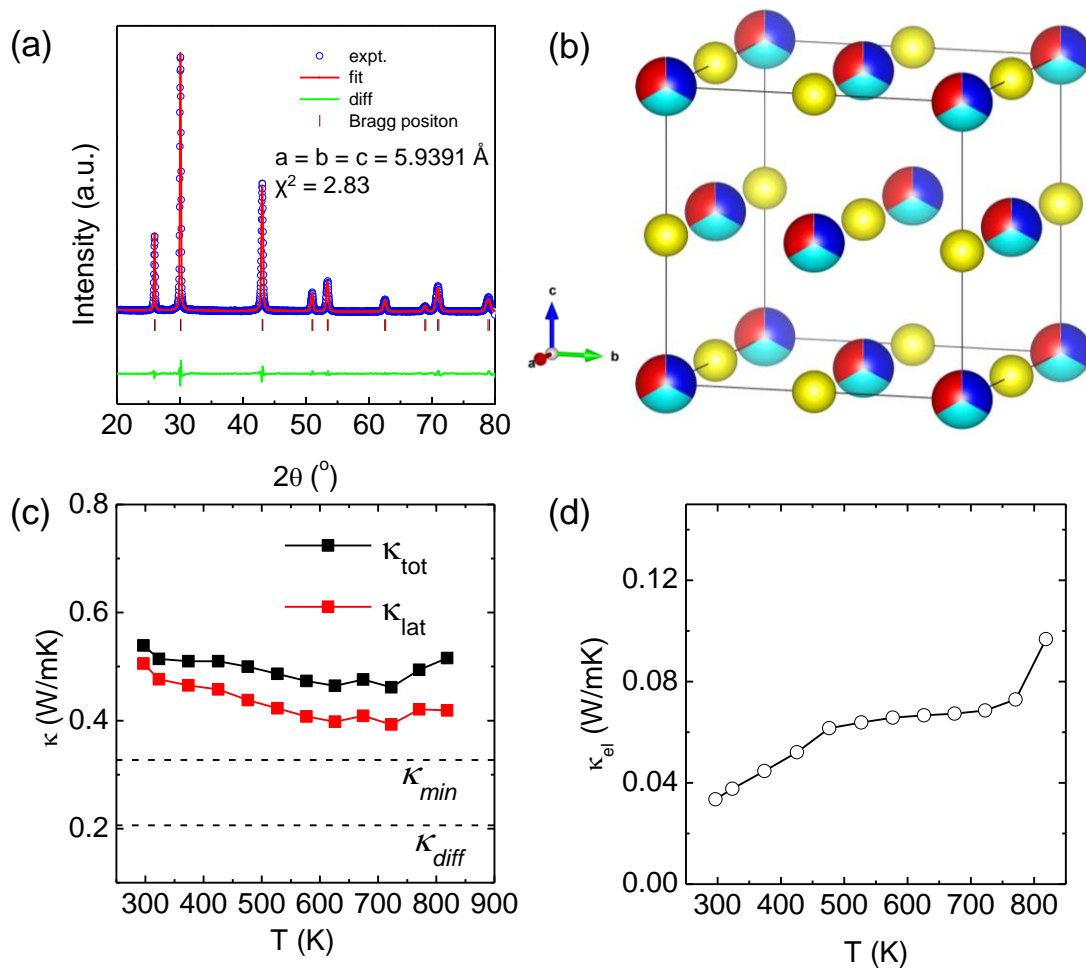


Figure 4.1.1. (a) Le Bail refinement of the powder XRD pattern of AgPbBiSe_3 . (b) Rock-salt structure of the compound AgPbBiSe_3 . Red, sky blue, blue, and yellow atoms represent Ag, Pb, Bi and Se respectively. (c) Temperature dependent total (black) and lattice (red) thermal conductivity of pristine AgPbBiSe_3 . (d) Temperature dependent κ_{el} data for pristine AgPbBiSe_3 .

For a better comprehension of this underlying ultralow lattice conductivity in AgPbBiSe_3 , we have measured low temperature Heat Capacity C_p (~ 2 K to ~ 200 K;

Figure 4.1.2a). Figure 4.1.2b represents C_p/T vs T^2 plot with temperature ranging from 2 K to 30 K. Modelling the plot using only Debye modes was insufficient, thus it was imperative to incorporate the Einstein oscillators for a proper analysis of the data. The combined Debye-Einstein model^{8, 10, 33} (Eqn. 4.1.2) is as follows.

$$\frac{C_p}{T} = \gamma + \beta T^2 + \sum_n \left(A_n (\theta_{E_n})^2 \cdot (T^2)^{-\frac{3}{2}} \cdot \frac{e^{\frac{\theta_{E_n}}{T}}}{\left(e^{\frac{\theta_{E_n}}{T}} - 1 \right)^2} \right) \quad (4.1.2)$$

This combined Debye-Einstein model is composed of three terms. The temperature independent part of the Eqn. 1, i.e., γ signifies electronic contribution. The second term β corresponds to contributions arising from Debye modes where,

$$\beta = B \cdot \left(12\pi^4 N_A \kappa_B / 5 \right) \cdot (\theta_D)^{-3} \quad (4.1.3)$$

N_A , κ_B and θ_D represents Avogadro number, Boltzmann constant and Debye temperature respectively. The term B in Eqn. 4.1.3 is given by, $B = 1 - \sum_n A_n / 3NR$, where N and R represents number of atoms per formula unit and universal gas constant ($8.314 \text{ J} \cdot \text{mol}^{-1} \cdot \text{K}^{-1}$) respectively. The final term takes care of the Einstein oscillators, where A_n is the Einstein pre-factor to the n^{th} Einstein mode (θ_{E_n}). A minimum of 2 Einstein modes along with the Debye modes were mandatory for a better fitting of the low temperature C_p data (Figure 4.1.2b). The individual contributions of each term are also plotted in Figure 4.1.2b. The fitting parameters that are obtained are provided in Table 4.1.1. The Debye Temperature (θ_D) derived for AgPbBiSe_3 is found to be 172 K. The characteristic temperature of the Einstein modes estimated from the fit are $\theta_{E1} = 35.6017 \text{ K}$ ($\sim 24 \text{ cm}^{-1}$) and $\theta_{E2} = 74.47509 \text{ K}$ ($\sim 51 \text{ cm}^{-1}$) which indicates the presence of low-lying optical modes. These low lying optical modes are pivotal for low κ_{lat} as they hinder the thermal flow via coupling with the heat-carrying acoustic phonons. We have determined the mean velocity of sound (v_s) using the formula $\kappa_B \theta_D = \hbar (6\pi^2 n)^{1/3} v_s$,²² where n is the number density of atoms and \hbar is the reduced Plank constant. The average or mean velocity of sound is derived to be $\sim 1710 \text{ m/s}$.

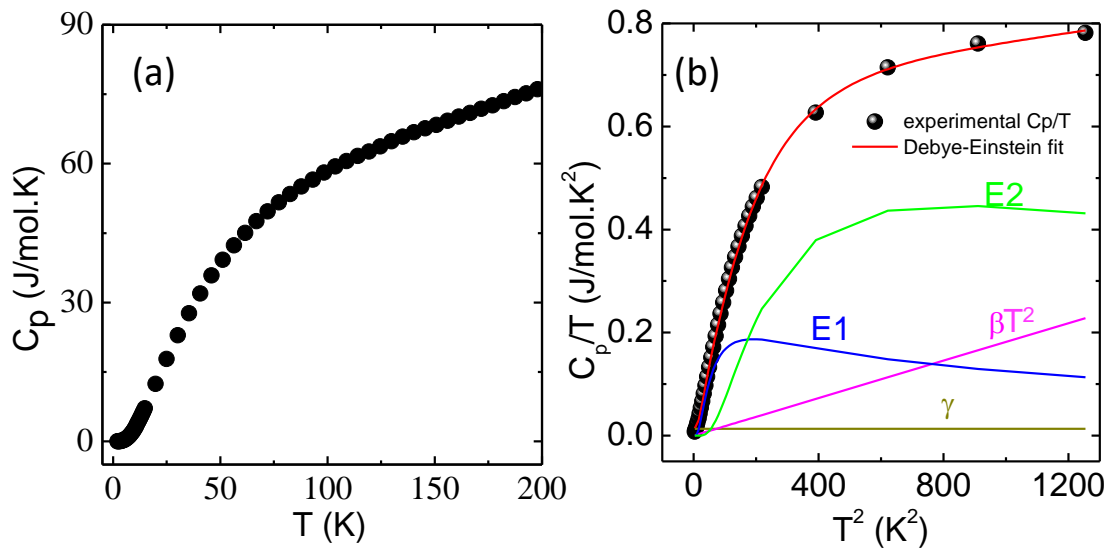


Figure 4.1.2. (a) Temperature dependent heat capacity. (b) C_p/T vs. T^2 plot within the 2–30 K range. The red line is the fit produced using the combined Debye–Einstein model. The individual contributions from electronic (γ), Debye (β) and the two Einstein terms (E1 and E2) are also plotted.

Table 4.1.1. Parameters obtained after fit in C_p/T vs T^2 plot.

Parameter	Values
γ / Jmol ⁻¹ K ⁻²	0.01333
β / Jmol ⁻¹ K ⁻⁴	1.81949 x 10 ⁻⁴
Θ_{E1} /K	35.6017
Θ_{E2} /K	74.47509
A_1	4.3697
A_2	21.80491
R^2	0.99974
χ^2	1.31538 x 10 ⁻⁵

To learn further about the bonding environment and atomic dynamics within the crystal structure and their role in suppressing the κ_{lat} of AgPbBiSe₃, we now present results of first-principles density functional theoretical (DFT) calculations using the Vienna Ab initio Simulation Package (VASP).^{25, 26} For the calculations, we took one of

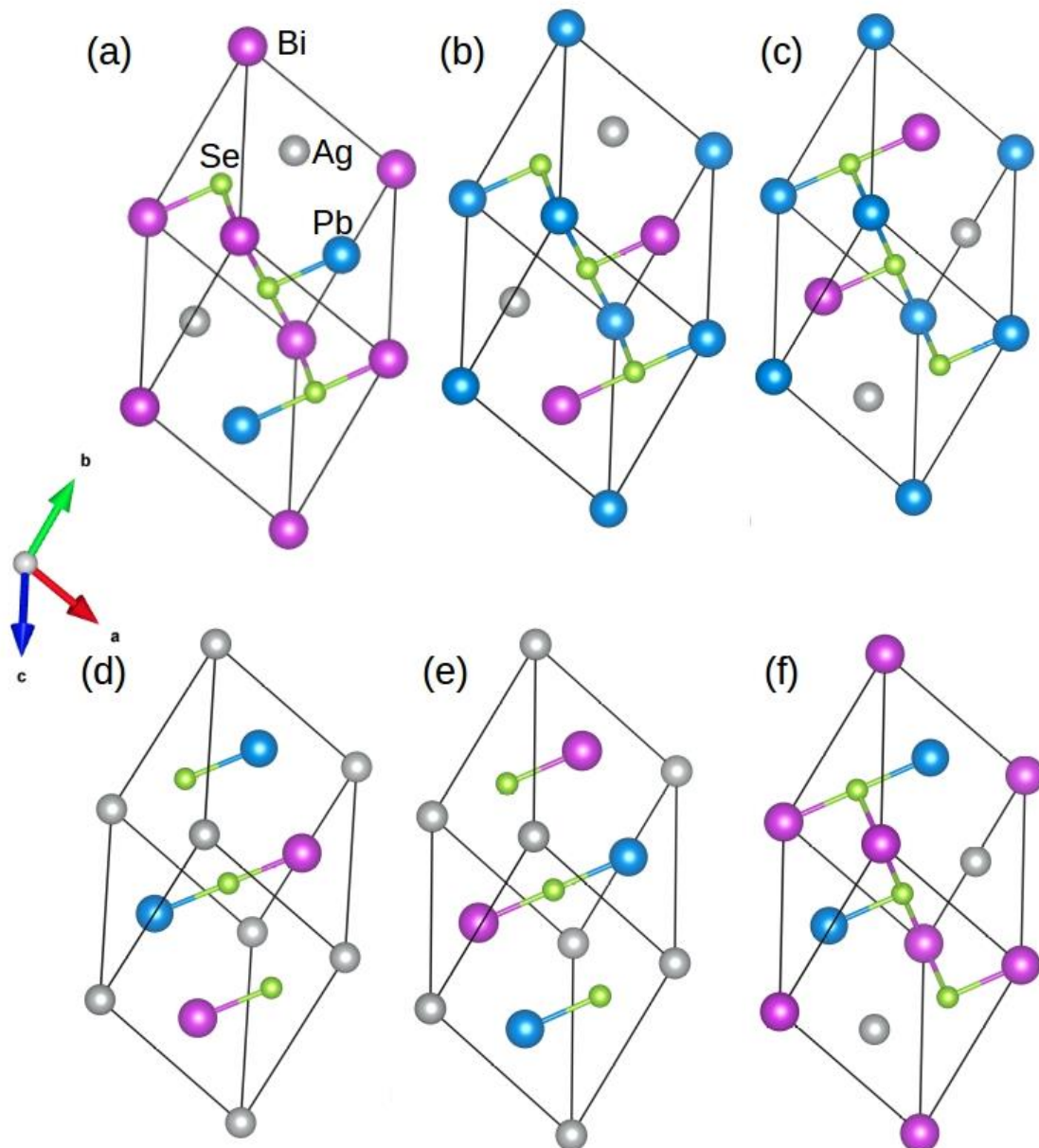


Figure 4.1.3. Six possible configurations of AgPbBiSe_3 where the cations are disordered. Our DFT calculations show that all the structures are energetically same. Silver, blue, violet and green spheres represent Ag, Pb, Bi and Se respectively.

six possible structures to do further calculations. We provide the lattice vectors, atomic positions and all six configurations of AgPbBiSe_3 in Figure 4.1.3. We analyse chemical bonding environment in AgPbBiSe_3 with real space charge density and electron localization function (ELF) created from a supercell containing three primitive fcc unit cell (Figure 4.1.4). Charge density analysis (Figure 4.1.4b) reveals that electronic clouds

of more electropositive Bi atoms strongly overlap with Se, suggesting a strong covalent character of bonding between them. On the other hand, the electronic clouds around less electropositive Ag and Pb cations overlap relatively weakly with the anions, indicating weaker bonding. Co-existence of such strong and weak bonding and cationic disorder give rise to crystallographic heterogeneity, resulting in low lattice thermal conductivity in materials.^{7, 8, 16, 34} To demonstrate the impact of bonding heterogeneity on the dynamics of the atoms, we calculated the potential energy (Figure 4.1.5a) landscape of atomic displacements around their equilibrium positions in x-, and z- directions. A shallow potential well of displacements of Ag atoms (see Figure 4.1.5a) signify the fact Ag atoms are loosely bound to the lattice, and their vibrations give greater dynamic structural disorder and entropy. Due to their relatively stronger bonding, Bi and Pb and Se atoms have deeper potential energy wells than that of Ag (Figure 4.1.5a). Larger amplitudes of atomic vibrations of Ag atoms than of Pb, Bi and Se are also evident in visualization of Eigen vectors of lowest energy optical phonons at Γ point (Figure 4.1.6). The visualization of the Eigen vectors at 30 cm^{-1} and 50 cm^{-1} (Figure 4.1.6) shows a greater vibration of Ag, which indicates that Ag is loosely bound to the lattice as compared to other cations that lead to the origin of these low lying optical phonons. These low energy Ag vibrations can be compared to the low lying optical modes derived from low temperature heat capacity (C_p) data.

We now present the crystal orbital Hamilton population (COHP) analysis, in which the energy of electronic states of a crystal is partitioned into pairwise orbital interactions, enabling quantification of the role of atomic orbitals in chemical bonding.^{35, 36} Moreover, the integrated COHP (iCOHP) gives the contribution of a chemical bond to the band energy, indicating its strength.^{37, 38} Here, we have used the LOBSTER code³⁵ COHP analysis of different nearest neighbor pairs of atoms of AgPbBiSe_3 . We find that the nearest neighbor Ag-Se interaction results in the weakest peak (Figure 4.1.5b) in COHP curves below the Fermi level, showing weaker interaction of Ag than the other cations. As expected, the integrated COHP for Ag-Se interaction is the smallest (see area under the curves in Figure 4.1.5c) confirming the weakest binding of Ag atoms to the lattice of AgPbBiSe_3 .

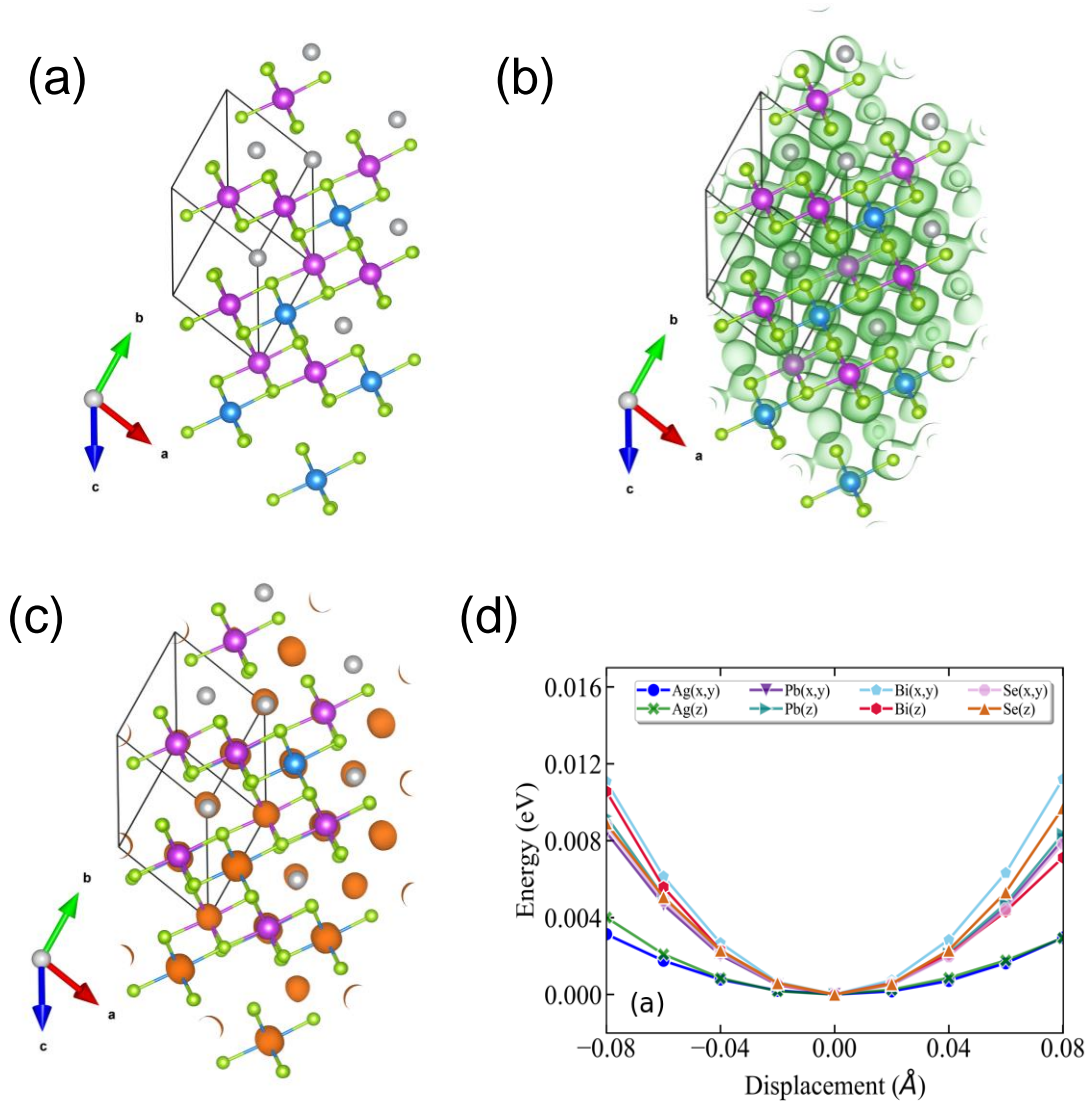


Figure 4.1.4. (a) Supercell containing three primitive fcc unit cells i.e., six atoms (Ag (cyan), Pb (violet), Bi (red) and three Se (green) atoms). (b) Total charge density of AgPbBiSe_3 visualized at an iso-value of 0.03 (minimum and maximum iso-values being -0.04 and 1.17, respectively) showing strong overlap of charge densities between Bi and Se atoms, relatively weak overlap between Pb and Se atoms, and almost no overlapping between Ag and Se atoms. (c) Electronic localization function (ELF) visualized at 91 % of the maximum iso-surface value reveals lone pair electrons around Pb and Bi atoms. (d) Potential energy curves of the constituent atoms in AgPbBiSe_3 as a function of displacement around their equilibrium positions along the x- and z-direction.

Visualization of electron localization function (Figure 4.1.4c) shows the presence of lone pairs around Bi and Pb atoms. Lone pairs are known to play important role in reducing the κ_{lat} in many well-known thermoelectric materials.^{14, 15} To quantify this effect

of the lone pairs in AgPbBiSe_3 , we calculated the mode Gruneisen parameters (γ_{qv}) which are a measure of the degree of anharmonicity in a lattice. They specifically give the third order interaction between phonons and acoustic waves (primary carriers of heat). Very high values of $\gamma_{qv} \sim 20$ (Figure 4.1.7a) of the lowest energy optical phonon and of phonons in the acoustic branches (Figure 4.1.7b), along several high symmetric directions (e.g., Γ -K1, Γ -K2 and Γ -K3) in the Brillouin zone indicate strong scattering of acoustic phonons by inhomogeneous strains associated with cationic disorder. Projected phonon density of states, DOS (Figure 4.1.8a) reveals that low frequency optical modes ($< 50 \text{ cm}^{-1}$) are dominated by vibrations of Ag atoms followed by the contributions from Pb and Bi atoms. This is also evident in the atom projected phonon dispersion curves (Figure 4.1.9). The role of the cations in the optical-acoustic phonon scattering processes is evident from the avoided crossing between the branches of acoustic and low frequency optical modes in the phonon dispersion (Figure 4.1.7c). Thus, lone pairs of Bi and Pb atoms cause strengthening of their bonds with Se by off-centering, and consequent weakening of Ag-Se bonds. This results in a combination of chemical and structural heterogeneity at atomic scales, leading to suppression of relaxation times of acoustic phonon scattering and hence low κ_{lat} of AgPbBiSe_3 .

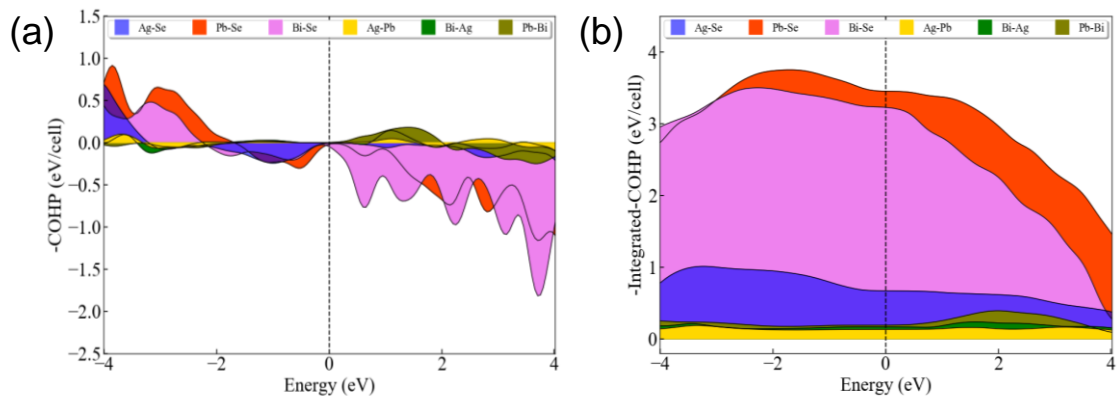


Figure 4.1.5. (a) Crystal orbital Hamilton population (COHP) and (b) integrated COHP (iCOHP) for the nearest neighbour atomic pairs of AgPbBiSe_3 . The smaller peak in (a) below the Fermi level and smallest area under the curve in (b) of Ag–Se interaction shows that the Ag atoms have the weakest bonding to the lattice.

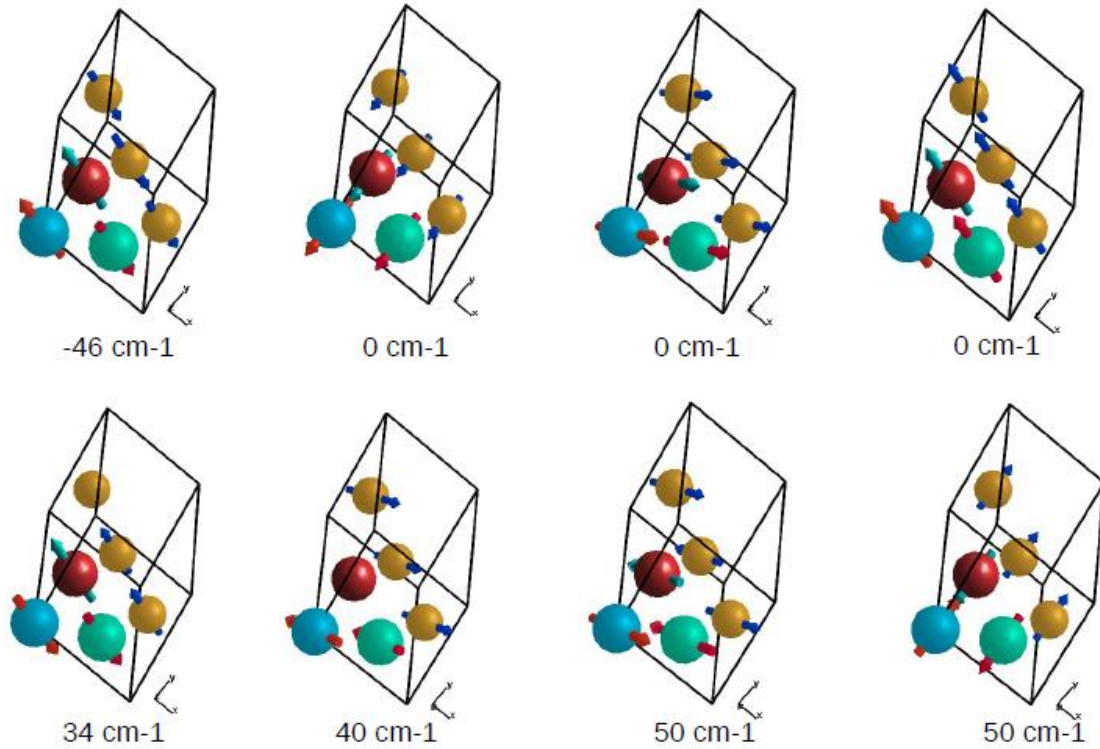


Figure 4.1.6. Visualizations of the atomic vibrations for the phonon modes at Γ point calculated at the optimized lattice constant. Red, Yellow, Cyan and Blue symbolizes Ag, Se, Pb and Bi respectively.

Calculated phonon dispersion (Figure 4.1.8b) shows that the cut-off frequencies of the acoustic modes are quite low ($< 50 \text{ cm}^{-1}$), suggesting low sound velocity that further contribute to lowering thermal conductivity in AgPbBiSe_3 , through quadratic dependence (within the kinetic theory): $\kappa_{lat} = 0.33C_v v_s^2 \tau$. Here, C_v corresponds to heat capacity at constant volume, v_s is the average sound velocity and τ denotes phonon relaxation time. In Table 4.1.2, the cut-off frequencies for the longitudinal (LA) and two transverse (TA1 and TA2) acoustic modes for the in-plane and out-of-plane directions in the Brillouin zone are listed. The low cut-off frequency points are due to the presence of heavy atoms and the bonding inhomogeneity amongst them. Average sound velocity (v_s) of AgPbBiSe_3 is 1860 m/s, calculated using $v_s = \frac{1}{3} \left(\frac{1}{v_l} + \frac{2}{v_t^2} \right)^{-\frac{1}{3}}$, which agrees well with the sound velocity (1710 m/s) derived from the C_p measurements. We estimated the longitudinal ($v_l = 3310 \text{ m/s}$) and transverse ($v_t = 1610 \text{ m/s}$) sound velocities of this compound through the relations:

$$v_l = \sqrt{\left(B + \frac{4}{3}G\right)/\rho} \text{ and } v_t = \sqrt{G/\rho},$$

where B , G , ρ denotes the bulk modulus, shear modulus and density of the material respectively.

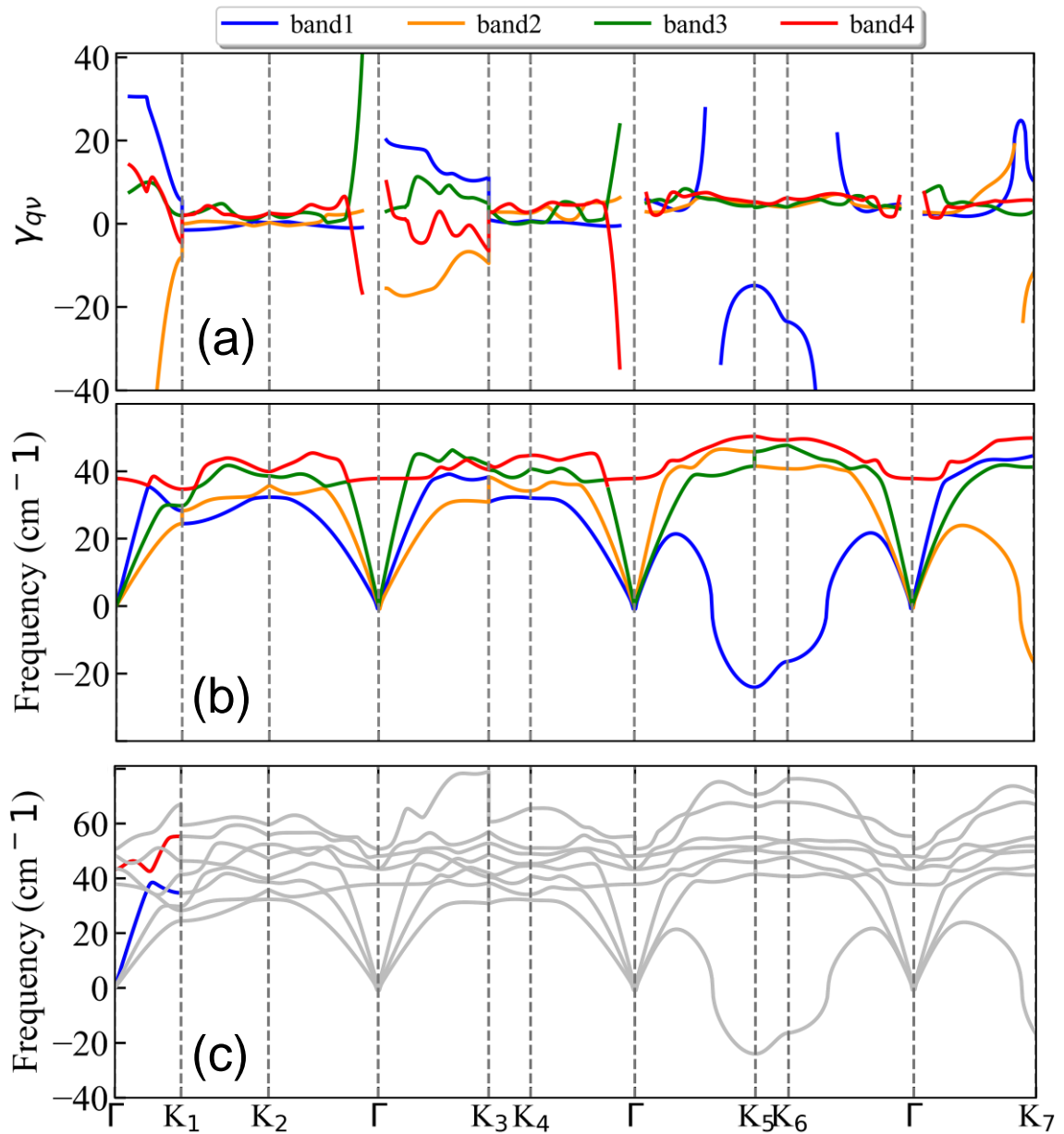


Figure 4.1.7. (a) Mode Gruneisen parameter (γ_{qv}), calculated for the four lowest frequency phonon branches along high symmetric directions in the Brillouin zone. Very high values of γ_{qv} (~ 20) of the acoustic modes indicate the lattice anharmonicity in AgPbBiSe_3 induced by the cation disorder in the unit cell as well as by the electrostatic

repulsions of their lone pairs. (b) Zoomed in frequency of the first four phonon bands (3 acoustic and 1 optical phonons). (c) Strong anharmonicity leads to enhanced scattering rate in the lattice, which is also manifested by the avoided crossing between the acoustic (blue line segment) and low frequency optical (red line segment) modes.

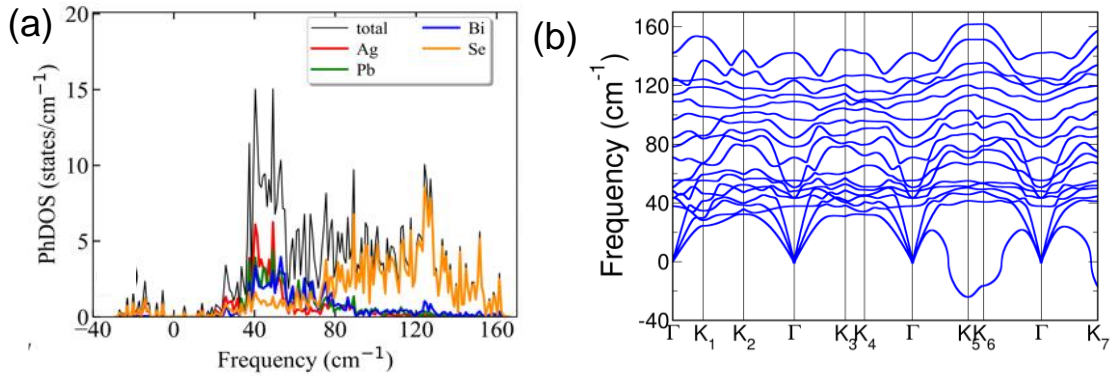


Figure 4.1.8. (a) Atom projected phonon density of states reveals that low frequency optical modes ($<50 \text{ cm}^{-1}$) originate largely due to the vibrations of the Ag atoms followed by contributions from Pb and Bi atoms. (b) Phonon dispersion of AgPbBiSe_3 showing that the acoustic branches have low cut-off frequencies ($<50 \text{ cm}^{-1}$).

In mixed-valence systems, phonon scattering is enhanced by the electron charge transfer which contributes to further reduction of κ_{lat} .²⁰ To unravel if there is any charge transfer occurring in AgPbBiSe_3 , we calculated the dynamical (Born effective) charges (Z^*), and find significant deviations from the nominal valence charges of each atom: (Ag: $Z^*_{xx(yy)} = 2.3$, $Z^*_{zz} = 2.1$; Pb: $Z^*_{xx(yy)} = 4.3$, $Z^*_{zz} = 5.1$; Bi: $Z^*_{xx(yy)} = 6.4$, $Z^*_{zz} = 5.9$; Se: $Z^*_{xx(yy)} = -6$, $Z^*_{zz} = -1.6$). Such anomalously large positive charges of the cations and negative charges of the anions indicate dynamical (hopping) transfer of electronic charge from cations to the anions during polar vibrations.

An in-depth experimental analysis of the structure for this ensuing low κ_{lat} is complicated due to presence of disordered cations which might induce lattice strain. It infers that the local bonding environment might be different from the average/global structure. Hence it is paramount to augment the traditional crystallographic measurements with local structure measuring techniques. Atomic pair distribution function (PDF) specializes in providing both diffuse scattering (which gives information regarding the

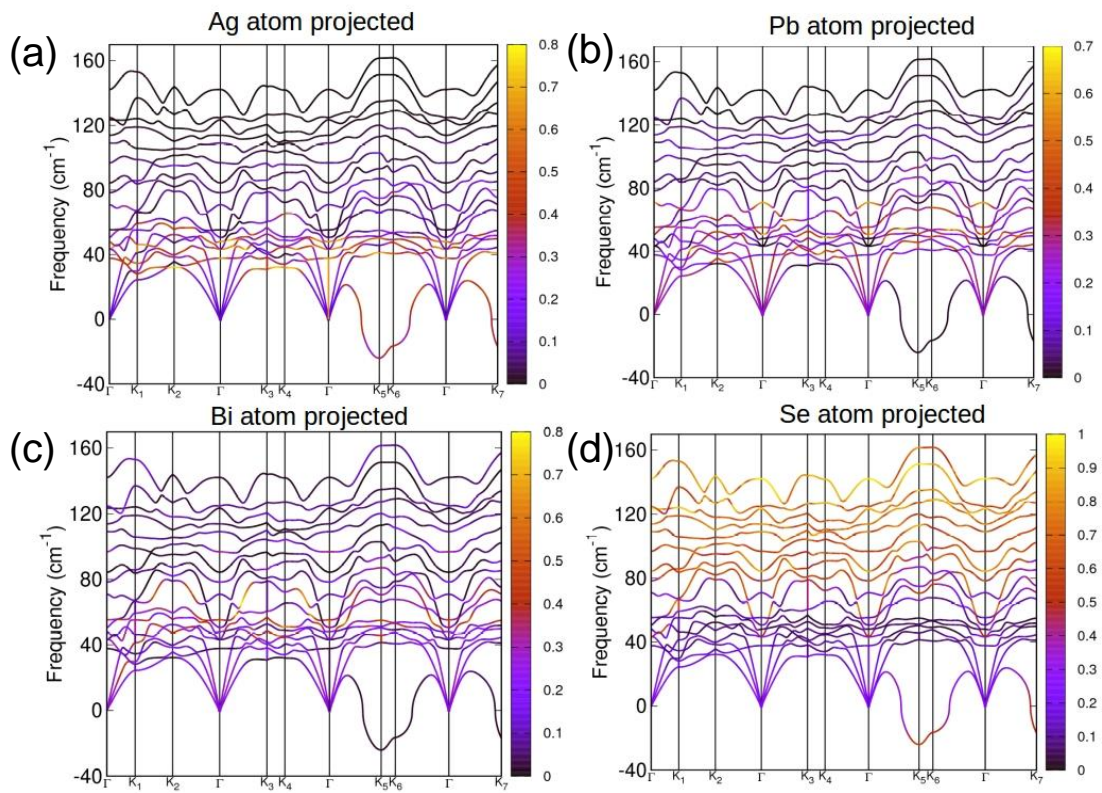


Figure 4.1.9. Atom projected phonon dispersion curves show that while (a) Ag, (b) Pb and (c) Bi atoms primarily contributes to the low frequency ($< 50 \text{ cm}^{-1}$) optical phonon branches, (d) Se atom being the lightest element mainly involved in the high frequency ($> 50 \text{ cm}^{-1}$) phonon modes in the spectrum.

Table 4.1.2. Cut off frequencies of different in-plane and out-of-plane directions in AgPbBiSe_3

AgPbBiSe_3 (ω / cm^{-1})			
	TA 1	TA 2	LA
Γ -K1	21	27	34
Γ -K3	27	35	42
Γ -K5	19	31	37

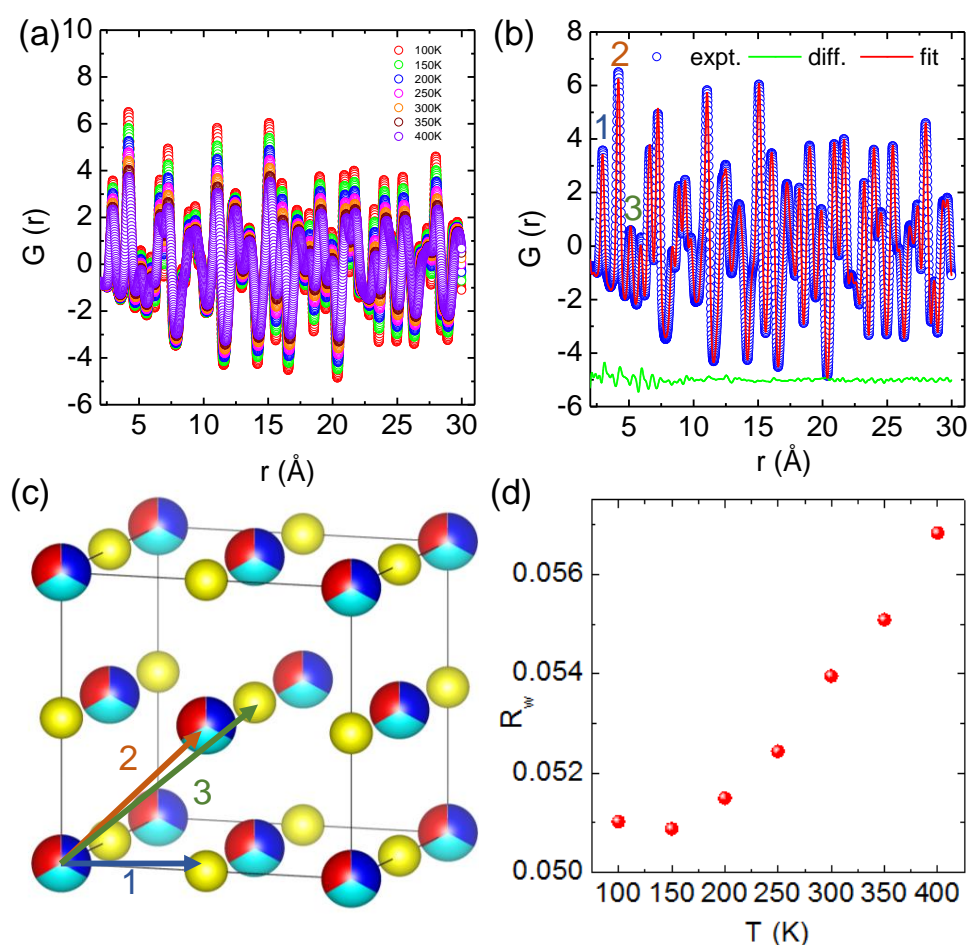


Figure 4.1.10. (a) Temperature dependent atomic PDF $G(r)$ plots of AgPbBiSe_3 . (b) $G(r)$ plot which depicts the nearest atom-atom bond distances (part (a)). The peaks marked as 1, 2 and 3 corresponds to cation - anion, anion - anion (or cation - cation) and cation-anion distances as shown in (c) of the figure. (d) Temperature dependent R_w obtained from refinement of PDF data using undistorted cubic $Fm\bar{3}m$ model.

structure at an atomic level) and Bragg scattering (which provides information regarding the global atomic structure), thus providing us microscopic insights into the role that the structure Figure 4.1.10a depicts the temperature dependent synchrotron X-ray PDF data from 100 K 400 K at an equal interval of 50 K as a function of r (in Å). A decrease in intensity and broadening of the peaks were observed, which is normally due to the enhanced thermal vibrations with increasing temperature. The PDF data is fitted with a cubic $Fm\bar{3}m$ model which is given by the red curve in Figure 4.1.10b. The residual of the experimental and simulated profile is given below in green. The first peak of the $G(r)$ vs r plot represents the nearest atom - atom distance, similarly the second peak

corresponds to second nearest atom distances (i.e., cation - cation or anion - anion distance) and so on (Figure 4.1.10c). The goodness of fit (R_w) of the temperature dependent PDF data when fitted using the cubic model of AgPbBiSe_3 is shown in Figure 4.1.10d.

Table 4.1.3. Temperature dependent ADP values.

T (K)	U_{iso} values (\AA^2)			
	Ag	Pb	Bi	Se
100	0.02662	0.01278	0.01277	0.02063
150	0.03042	0.01467	0.01467	0.02321
200	0.03431	0.01688	0.01686	0.02587
250	0.03816	0.01917	0.01931	0.02871
300	0.04191	0.02145	0.0216	0.0316
350	0.04605	0.0239	0.0239	0.03476
400	0.04981	0.02605	0.02606	0.03725

The temperature dependent lattice parameter, a are given in Figure 4.1.11a and is shown to linearly increase with temperature. The thermal parameter (U_{iso}) obtained from the refinement clearly shows a higher ADP values for Ag compared to Se, with Bi and Pb having the lowest ADP values (Figure 4.1.11b). ADPs of Pb is actually almost same as that of Bi and as a result ADPs of Bi overlaps with that of Pb. The similar ADP values of both Pb and Bi is due to similar size among them and the values are presented in Table 4.1.3. The high ADP values of Ag compared to other atoms corroborates with the theoretical prediction that the Ag atoms are loosely bonded in the crystal lattice and contributes to the anharmonicity and thereby suppressing κ_{lat} . Figure 4.1.12a, b represents first peak (which provides information of the nearest atom-atom correlations) and total peak fitting using the cubic model respectively at 100 K. It can be clearly seen that although the total average structure gives a good fit to the cubic model, the first peak

which corresponds to the nearest anion to cation distance (i.e., at a distance of $a/2$) could not be properly fitted using the cubic model. To understand the local dynamics of the structure and subsequently their role in the low κ_{lat} of the compound, we tried to refine the first peak as it tells us about any local distortion in the system. We have observed that the best fit is possible when the cations are displaced from their native place in the $\langle 111 \rangle$ direction.

Although the first peak gave a very good account for the local distortion, the overall fitting was worse compared to the cubic model as evident from the corresponding R_w values. Figure 4.1.12c, d shows the fitting using the locally distorted cubic structure, for the first atom-atom correlation and the total fit respectively. It has been observed that by distorting Pb and Bi to a higher degree compared to Ag, the nature of the first peak fits better. Figure 4.1.13a shows first peak fitting at 100 K and can be compared with the first peak fitting at 400 K (Figure 4.1.13b). The fitting of the first peak at these two temperatures (100 K and 400 K) were possible by off-centering Pb and Bi by 0.047 Å at 100 K and by 0.21 Å at 400 K. Ag gets off-centered to a lesser degree from 0.018 Å to 0.06 Å at 100 K and 400 K respectively. The higher magnitude of off-centering in Pb and Bi might be due to the presence of $6s^2$ lone pair electrons, which is similar to that of PbTe and PbS, where it was argued that the stereochemical activity of $6s^2$ lone pairs of Pb^{2+} contributed to the off-centering of Pb and subsequent suppression of the κ_{lat} .³⁹ Thus, lone pairs of Bi^{3+} and Pb^{2+} can be presumed to play a prominent role in suppressing κ_{lat} *via* inducing strong lattice anharmonicity.

Hence, it can be argued that the low κ_{lat} in AgPbBiSe_3 is a combination of bonding heterogeneity whereby Ag being loosely bonded are effective in scattering heat carrying phonons as well as due to lone pairs of electrons on Pb and Bi which induces anharmonicity in the lattice.

Since materials with low κ_{lat} has its usefulness in waste heat management, we have further improved the thermoelectric figure of merit in this *n*-type AgPbBiSe_3 via aliovalent halogen doping. Thermoelectric figure of merit (zT) of thermoelectric materials is determined using the formula,

$$zT = \frac{\sigma S^2}{\kappa} T \quad (4.1.4)$$

where, σ and S represents electrical conductivity and Seebeck coefficient respectively. κ is the thermal conductivity which constitutes of electronic (κ_{el}) and lattice (κ_{lat}) contributions, i.e., $\kappa = \kappa_{el} + \kappa_{lat}$. PXRD of all the halide doped compounds can be indexed according to the cubic rock-salt structure (Figure 4.1.14a) and shows no presence of second phase peaks within the detection limit.

Band gap measurement reveal that *n*-type AgPbBiSe₃ has a band gap (E_g) of 0.46 eV which is consistent with the earlier reported E_g of 0.48 eV.²⁰ Halide doping in AgPbBiSe₃ do not show any significant change in band gap as shown in Figure 4.1.14b and the band gap values are given in Table 4.1.4. Electronic structure (Figure 4.1.15a) of AgPbBiSe₃ determined from DFT calculations including spin-orbit coupling reveals that it possesses a small E_g of 0.14 eV. Theoretical calculations are known to underestimate band gaps of the compounds and thus shows lower value compared to the experimentally observed band gap. Atom projected electronic density of states (Figure 4.1.15b) and projected electronic structure (Figure 4.1.16) shows that while valence bands just below the Fermi level are primarily constituted of orbital contributions of the Se atoms, the conduction bands above the Fermi level have contributions from all the atoms.

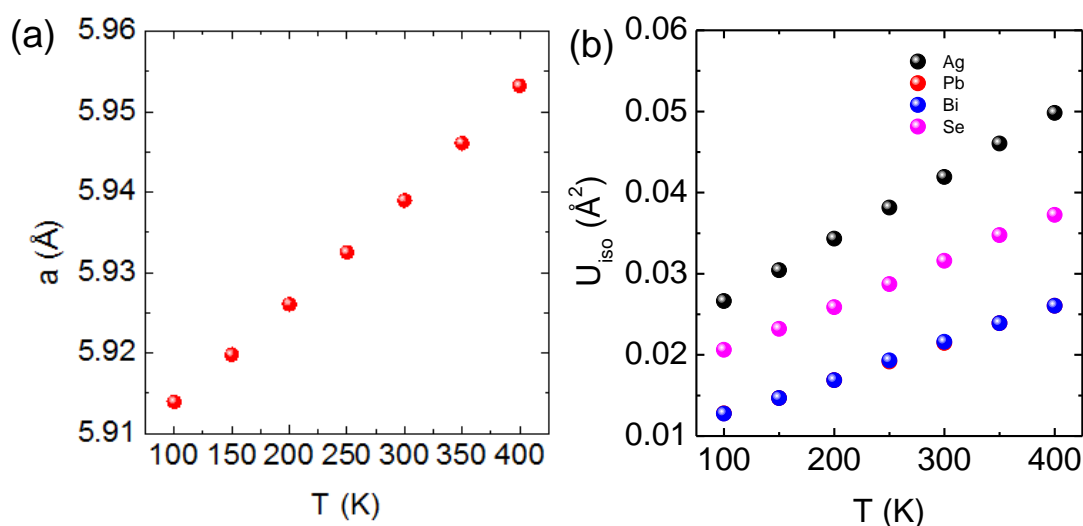


Figure 4.1.11. Temperature dependent (a) lattice parameter (a) and isotropic thermal parameters obtained from the full fitting the undistorted cubic $Fm\bar{3}m$ model.

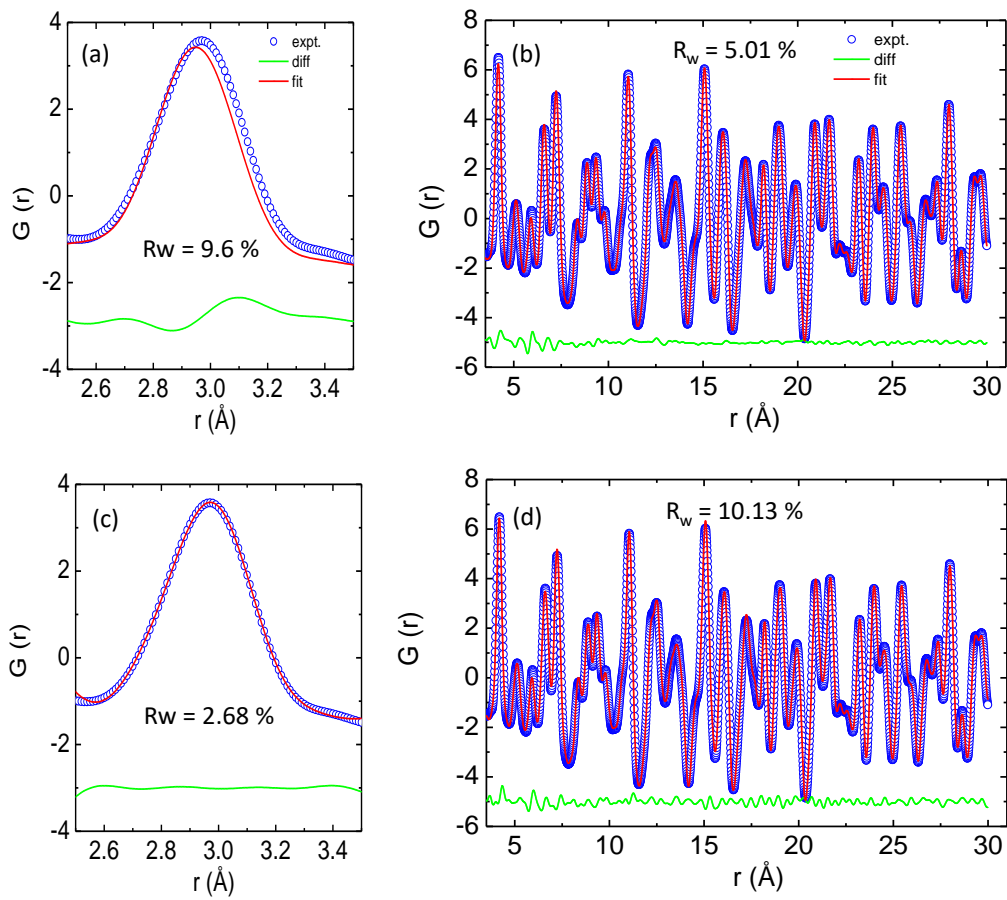


Figure 4.1.12. X-ray PDF data: (a) first peak and (b) total peak fitting using the cubic model. (c) First peak and (d) total peak fitting using the locally distorted model. The experimental data used at a temperature of 100 K.

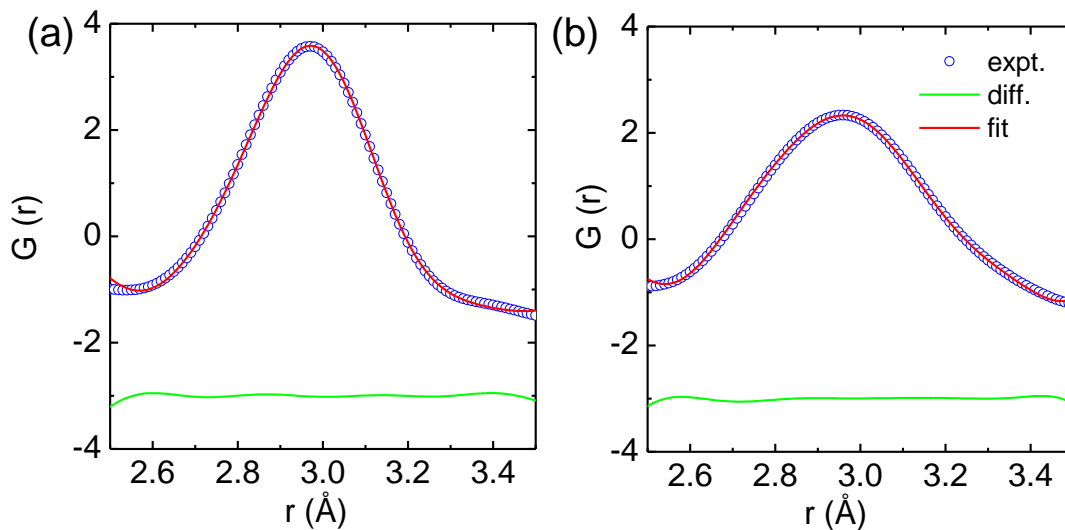


Figure 4.1.13. Local structure fit done at (a) 100 K and (b) 400 K. Fit is obtained by shifting the cations (Ag/Pb/Bi) in the $\langle 111 \rangle$ direction.

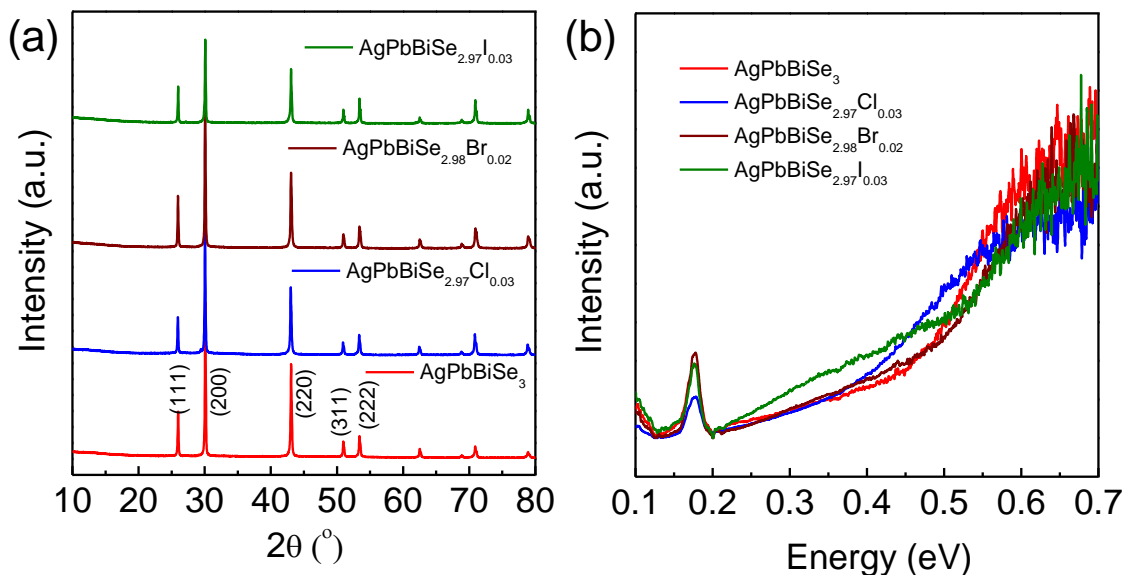


Figure 4.1.14. (a) PXRD pattern of halogen doped compounds. All the compounds pertain rock-salt cubic structure. (b) Bandgap of the pristine and doped AgPbBiSe_3 .

Table 4.1.4. Band-gap values for the pristine and doped AgPbBiSe_3 .

Compound	Band gap (eV)
AgPbBiSe_3	0.46
$\text{AgPbBiSe}_{2.97}\text{Cl}_{0.03}$	0.42
$\text{AgPbBiSe}_{2.98}\text{Br}_{0.02}$	0.50
$\text{AgPbBiSe}_{2.97}\text{I}_{0.03}$	0.52

Electrical transport measurement has been performed for all the samples within the temperature range of 290 K – 823 K. Electrical conductivity (σ) as expected, increases with halogen doping as it imparts an extra electron and can be understood via simple valance counting. For pristine AgPbBiSe_3 , the electrical conductivity at room temperature value is 63 S/cm and rises slightly up to 72 S/cm at 818 K (Figure 4.1.17a). Cl doped $\text{AgPbBiSe}_{2.97}\text{Cl}_{0.03}$ contributes the most in enhancing the electrical property. Doping with

Cl increases the electrical conductivity to 263 S/cm at 297 K and 240 S/cm at 813 K compared to the pristine AgPbBiSe₃ which has considerably lower σ (Figure 4.1.17a). Doping with Br and I increases the electrical conductivity too but is considerably less compared to Cl (Figure 4.1.17a). The difference in electrical conductivity with various doping is due to the respective size of the halogens. Cl whose size is smaller and similar to Se as compared to Br and I, thereby Cl goes easily to Se lattice and impart the extra electron with better efficiency than Br or I. The carrier concentration and mobility of the doped AgPbBiSe₃ are presented in Table 4.1.5 also resembles to the electrical conductivity trend. The carrier concentration for pristine AgPbBiSe₃ at room temperature is $1.44 \times 10^{18} \text{ cm}^{-3}$, which increases to $1.34 \times 10^{19} \text{ cm}^{-1}$ for AgPbBiSe_{2.97}Cl_{0.03} (Table 4.1.5). Similarly, seebeck coefficient (S) value measured for pristine AgPbBiSe₃ is $-131 \mu\text{V/K}$ at 296 K which increases to $-204 \mu\text{V/K}$ at 770 K (Figure 4.1.17b). The negative sign in Seebeck coefficient value corresponds to *n*-type conduction which is also corroborated from the Hall measurement data. The S value decreases with the doping concentration which is in line with the electrical conductivity and carrier concentration (*n*) trend. The electrical conductivity and seebeck co-efficient results in a power factor of $1.09 \mu\text{W/cmK}^2$ at 296 K and increases to $2.71 \mu\text{W/cmK}^2$ at 818 K for pristine AgPbBiSe₃ (Figure 4.1.17c). The power factor of the doped compounds are understandably higher compared to the pristine sample with maximum power factor of *ca.* $5.15 \mu\text{W/cmK}^2$ at 813 K for the Cl doped AgPbBiSe_{2.97}Cl_{0.03} (Figure 4.1.17c) is obtained.

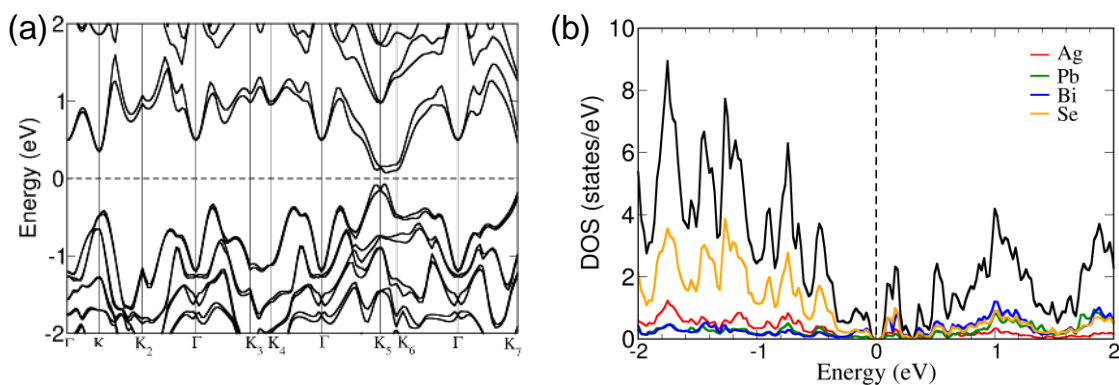


Figure 4.1.15. (a) Electronic structure of AgPbBiSe₃ calculated with spin-orbit coupling (SOC) shows that it is a small band gap semiconductor with multiple bands near the Fermi level. (b) Projected density of states reveals that the valence and conduction bands around the Fermi level mainly constitute bonding and anti-bonding states arising from

the hybridization of atomic orbitals between Bi and Se atoms. While Ag atoms have the weakest bonding in the lattice, the bonding between Pb and Se atoms are also relatively weak.

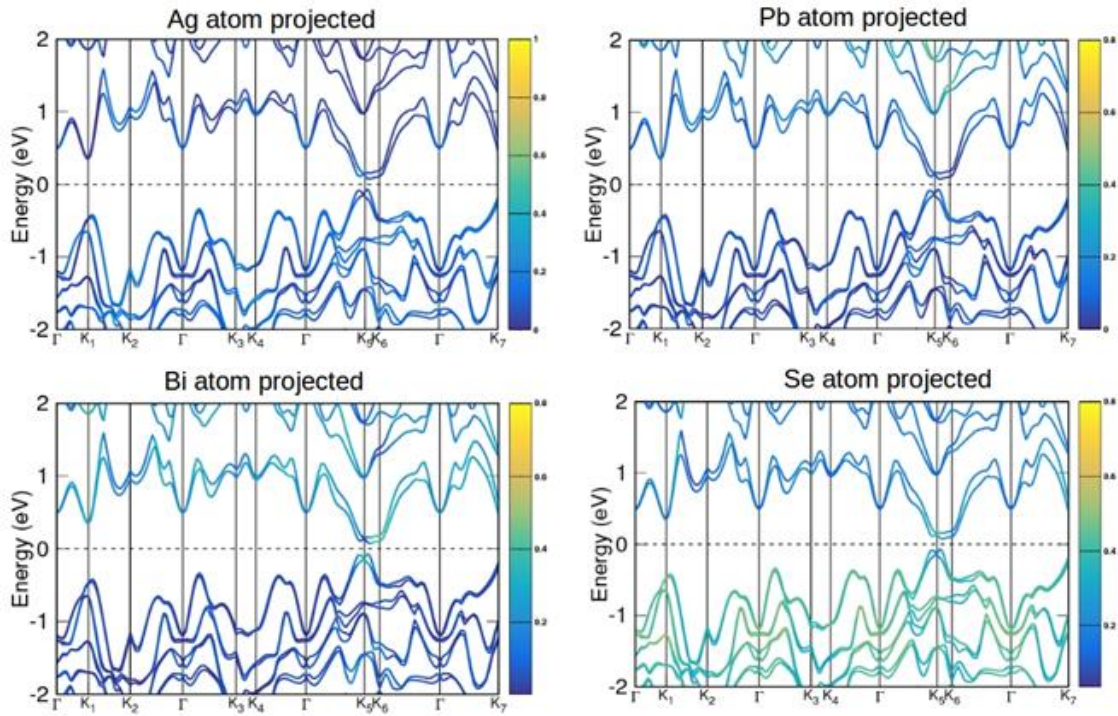


Figure 4.1.16. Atom projected electronic structure of AgPbBiSe_3 reveals that while the valence bands just below the Fermi level have highest contributions from the Se atoms, the conduction bands just above the Fermi level have larger contributions coming from the Bi atoms. Ag and Pb atoms have little contributions to the bands in the vicinity of the Fermi level suggesting that they do not actively participate in bonding.

Table 4.1.5. Carrier concentration and mobilities for the pristine and doped AgPbBiSe_3 .

Compound	Carrier concentration (cm^{-3}) $\times 10^{18}$	Mobility, μ_H ($\text{cm}^2\text{V}^{-1}\text{S}^{-1}$)
AgPbBiSe_3	1.32	298
$\text{AgPbBiSe}_{2.97}\text{Cl}_{0.03}$	13.63	120
$\text{AgPbBiSe}_{2.98}\text{Br}_{0.02}$	6.84	191
$\text{AgPbBiSe}_{2.97}\text{I}_{0.03}$	5.29	197

Figure 4.1.17d and 4.1.17e depicts total thermal conductivity and lattice thermal conductivity for the doped compounds. It has been observed that the lattice thermal conductivity of the halogen doped AgPbBiSe_3 decreases from 0.6 W/mK at 290 K to around c.a. 0.23 W/mK at 823 K. The decrease in the lattice thermal conductivity compared to the pristine counterpart is due point defects arising from halogen doping which scatters the high frequency phonons.

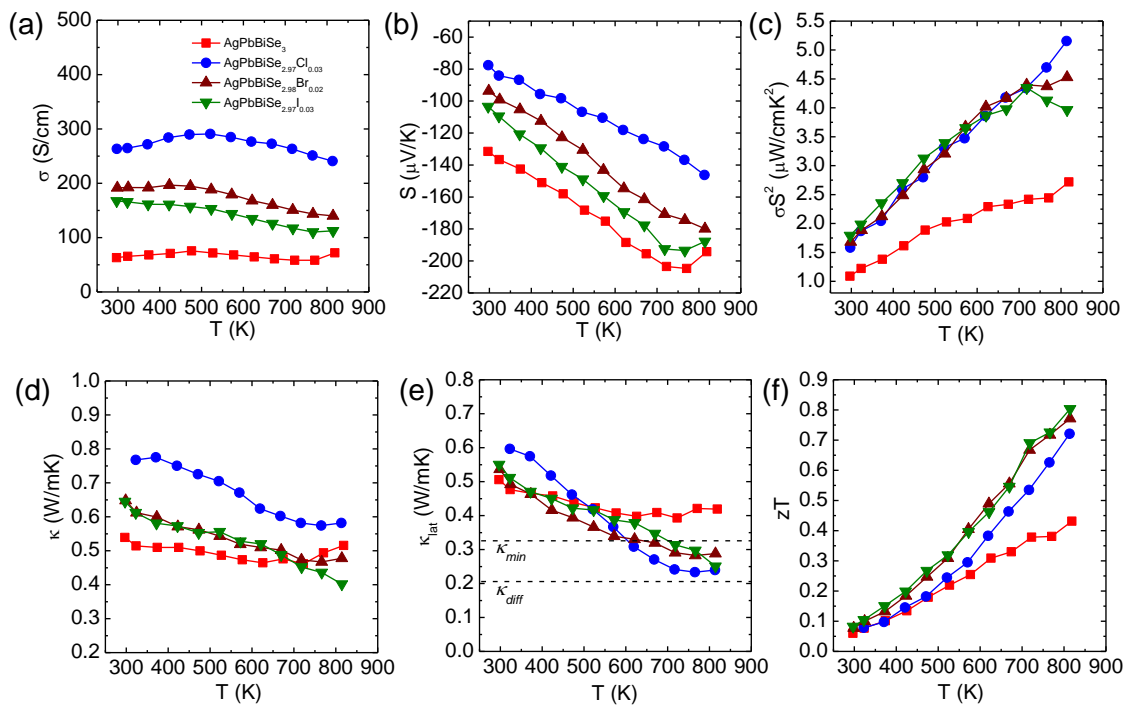


Figure 4.1.17. Temperature dependent (a) electrical conductivity, (b) Seebeck coefficient, (c) power factor, (d) thermal conductivity, (e) lattice thermal conductivity and (f) thermoelectric figure of merit (zT) for pristine and halogen doped AgPbBiSe_3 .

The thermoelectric figure of merit (zT) which takes into account the power factor and the thermal conductivity is found to be 0.43 for pristine AgPbBiSe_3 at 818 K and it increases almost two-fold to 0.8 at 814 K in $\text{AgPbBiSe}_{2.97}\text{I}_{0.03}$, which is considerably high in n -type Te free compounds (Figure 4.1.17f). For comparison, n -type AgBiSe_2 have a peak zT of ~ 0.9 at 810 K⁴⁰ and n -type $(\text{GeSe})_{0.50}(\text{AgBiSe}_2)_{0.50}$ exhibits a zT of 0.45 677 K⁴¹. n -type BiSe have achieved a zT of 0.8 at 425 K via Sb substitution¹⁶. Polycrystalline n -type PbSe on the other hand achieved a peak zT of ~ 1.8 at 723 K for $\text{PbSe}_{0.998}\text{Br}_{0.002}$ -2% Cu_2Se ⁴². Although PbSe based n -type thermoelectrics provide a much better zT , it is

worth noting that it took almost a decade to reach this type of zT values in PbSe. Our compound AgPbBiSe₃ on the other hand is in its nascent stage and with further optimization of its electronic properties, higher zT can also be achieved in AgPbBiSe₃.

4.1.4. Conclusion

AgPbBiSe₃ exhibits ultralow lattice thermal conductivity in the temperature range 290 - 823 K. Low temperature heat capacity experiment proved the presence of low lying optical phonon modes which are pivotal in scattering the heat-carrying acoustic phonons. Theoretical probe into the phonon mechanism using first principles DFT calculations revealed high degree of anharmonicity arising from the chemical disorder of cations. The compound possesses bonding inhomogeneity wherein the Ag atoms are weakly bonded as compared to Pb and Bi in the lattice. Electron localization function analysis reveals the presence of $6s^2$ lone pairs in Pb and Bi which induce strong variation in chemical bonding of cations, and hence the lattice anharmonicity. Thus, the synergistic presence of bonding heterogeneity and lattice anharmonicity arising from $6s^2$ lone pairs of Bi and Pb fosters low lattice thermal conductivity of 0.5 W/mK at 296 K which further decreases to c.a. 0.4 W/mK at 818 K. Further reduction of this low thermal conductivity and enhancement in the power factor in *n*-type AgPbBiSe₃ compound have been strategized by halogen substitution, and we achieve a high zT of 0.8 at 814 K in AgPbBiSe_{2.97}I_{0.03}. We hope that this fundamental understanding of the lattice thermal conductivity and its interplay with the structural aspects, chemical bonding and lattice dynamics will guide in designing and furnishing new materials having low intrinsic thermal conductivity.

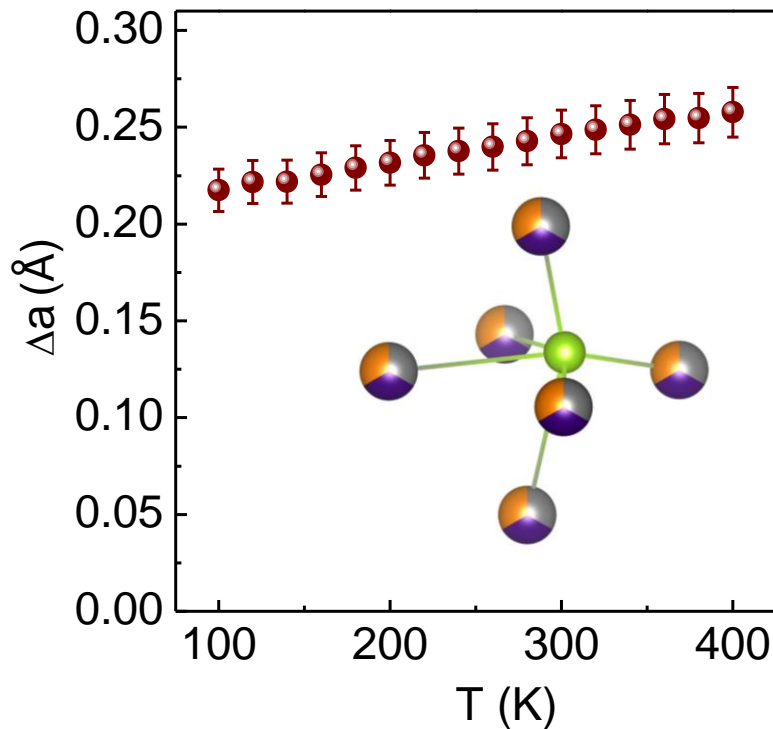
4.1.5. References

- [1] G. Tan, L.-D. Zhao and M. G. Kanatzidis, *Chem. Rev.*, 2016, **116**, 12123-12149.
- [2] L.-D. Zhao, V. P. Dravid and M. G. Kanatzidis, *Energy Environ. Sci.*, 2014, **7**, 251-268.
- [3] C. Chang, M. Wu, D. He, Y. Pei, C.-F. Wu, X. Wu, H. Yu, F. Zhu, K. Wang, Y. Chen, L. Huang, J.-F. Li, J. He and L.-D. Zhao, *Science*, 2018, **360**, 778.
- [4] M. K. Jana and K. Biswas, *ACS Energy Lett.*, 2018, **3**, 1315-1324.
- [5] X. Shi, J. Yang, J. R. Salvador, M. Chi, J. Y. Cho, H. Wang, S. Bai, J. Yang, W. Zhang and L. Chen, *J. Am. Chem. Soc.*, 2011, **133**, 7837-7846.
- [6] T. Takabatake, K. Suekuni, T. Nakayama and E. Kaneshita, *Rev. Mod. Phys.*, 2014, **86**, 669-716.
- [7] M. K. Jana, K. Pal, U. V. Waghmare and K. Biswas, *Angew. Chem. Int. Ed.*, 2016, **55**, 7792-7796.
- [8] M. K. Jana, K. Pal, A. Warankar, P. Mandal, U. V. Waghmare and K. Biswas, *J. Am. Chem. Soc.*, 2017, **139**, 4350-4353.
- [9] S. Mukhopadhyay, D. S. Parker, B. C. Sales, A. A. Puretzky, M. A. McGuire and L. Lindsay, *Science*, 2018, **360**, 1455.
- [10] H. Liu, X. Shi, F. Xu, L. Zhang, W. Zhang, L. Chen, Q. Li, C. Uher, T. Day and G. J. Snyder, *Nat. Mater.*, 2012, **11**, 422.
- [11] S. Roychowdhury, M. K. Jana, J. Pan, S. N. Guin, D. Sanyal, U. V. Waghmare and K. Biswas, *Angew. Chem. Int. Ed.*, 2018, **57**, 4043-4047.
- [12] S. N. Guin, J. Pan, A. Bhowmik, D. Sanyal, U. V. Waghmare and K. Biswas, *J. Am. Chem. Soc.*, 2014, **136**, 12712-12720.
- [13] B. Li, H. Wang, Y. Kawakita, Q. Zhang, M. Feygenson, H. L. Yu, D. Wu, K. Ohara, T. Kikuchi, K. Shibata, T. Yamada, X. K. Ning, Y. Chen, J. Q. He, D. Vaknin, R. Q. Wu, K. Nakajima and M. G. Kanatzidis, *Nat. Mater.*, 2018, **17**, 226-230.
- [14] S. N. Guin, A. Chatterjee, D. S. Negi, R. Datta and K. Biswas, *Energy Environ. Sci.*, 2013, **6**, 2603-2608.

-
- [15] D. T. Morelli, V. Jovovic and J. P. Heremans, *Phys. Rev. Lett.*, 2008, **101**, 035901.
- [16] M. Samanta, K. Pal, P. Pal, U. V. Waghmare and K. Biswas, *J. Am. Chem. Soc.*, 2018, **140**, 5866-5872.
- [17] K. Biswas, J. He, I. D. Blum, C.-I. Wu, T. P. Hogan, D. N. Seidman, V. P. Dravid and M. G. Kanatzidis, *Nature*, 2012, **489**, 414.
- [18] B. Poudel, Q. Hao, Y. Ma, Y. Lan, A. Minnich, B. Yu, X. Yan, D. Wang, A. Muto, D. Vashaee, X. Chen, J. Liu, M. S. Dresselhaus, G. Chen and Z. Ren, *Science*, 2008, **320**, 634.
- [19] M. Samanta and K. Biswas, *J. Am. Chem. Soc.*, 2017, **139**, 9382-9391.
- [20] S. Sportouch, M. Basteat, P. Brazis, J. Ireland, C. R. Kannewurf, C. Uher and M. G. Kanatzidis, *MRS Online Proc. Libr.*, 1998, **545**, 123-130.
- [21] D. P. Spitzer, *J. Phys. Chem. Solids*, 1970, **31**, 19-40.
- [22] M. T. Agne, R. Hanus and G. J. Snyder, *Energy Environ. Sci.*, 2018, **11**, 609-616.
- [23] T. Proffen, S. J. L. Billinge, T. Egami and D. Louca, *Z. Kristallogr. Cryst. Mater.*, 2003, **218**, 132.
- [24] C. L. Farrow, P. Juhas, J. W. Liu, D. Bryndin, E. S. Božin, J. Bloch, P. Th and S. J. L. Billinge, *J. Phys: Condens. Matter*, 2007, **19**, 335219.
- [25] G. Kresse and J. Hafner, *Phys. Rev. B*, 1993, **48**, 13115-13118.
- [26] G. Kresse and J. Furthmüller, *Comput. Mater. Sci.*, 1996, **6**, 15-50.
- [27] P. E. Blöchl, *Phys. Rev. B*, 1994, **50**, 17953-17979.
- [28] X. Hua, X. Chen and W. A. Goddard, *Phys. Rev. B*, 1997, **55**, 16103-16109.
- [29] J. P. Perdew, K. Burke and M. Ernzerhof, *Phys. Rev. Lett.*, 1996, **77**, 3865-3868.
- [30] A. Togo, F. Oba and I. Tanaka, *Phys. Rev. B*, 2008, **78**, 134106.
- [31] K. F. Hsu, S. Loo, F. Guo, W. Chen, J. S. Dyck, C. Uher, T. Hogan, E. K. Polychroniadis and M. G. Kanatzidis, *Science*, 2004, **303**, 818.
- [32] D. G. Cahill, S. K. Watson and R. O. Pohl, *Phys. Rev. B*, 1992, **46**, 6131-6140.

-
- [33] H. Liu, J. Yang, X. Shi, S. A. Danilkin, D. Yu, C. Wang, W. Zhang and L. Chen, *J. Materiomics*, 2016, **2**, 187-195.
- [34] K. Pal, J. He and C. Wolverton, *Chem. Mater.*, 2018, **30**, 7760-7768.
- [35] R. Dronskowski and P. E. Bloechl, *J. Phys. Chem.*, 1993, **97**, 8617-8624.
- [36] V. L. Deringer, A. L. Tchougréeff and R. Dronskowski, *J. Phys. Chem. A*, 2011, **115**, 5461-5466.
- [37] S. Maintz, V. L. Deringer, A. L. Tchougréeff and R. Dronskowski, *J. Comput. Chem.*, 2013, **34**, 2557-2567.
- [38] A. Lücke, U. Gerstmann, T. D. Kühne and W. G. Schmidt, *J. Comput. Chem.*, 2017, **38**, 2276-2282.
- [39] E. S. Božin, C. D. Malliakas, P. Souvatzis, T. Proffen, N. A. Spaldin, M. G. Kanatzidis and S. J. L. Billinge, *Science*, 2010, **330**, 1660.
- [40] S. N. Guin, V. Srihari and K. Biswas, *J. Mater. Chem. A*, 2015, **3**, 648-655.
- [41] S. Roychowdhury, T. Ghosh, R. Arora, U. V. Waghmare and K. Biswas, *Angew. Chem. Int. Ed.*, 2018, **57**, 15167-15171.
- [42] C. Zhou, Y. Yu, Y. K. Lee, O. Cojocar-Mirédin, B. Yoo, S.-P. Cho, J. Im, M. Wuttig, T. Hyeon and I. Chung, *J. Am. Chem. Soc.*, 2018, **140**, 15535-15545.

Chapter 4.2



**Emphasis in Cubic
 $(\text{SnSe})_{0.5}(\text{AgSbSe}_2)_{0.5}$: Dynamical off-centering of Anion Leads to Low Thermal Conductivity and High Thermoelectric Performance**

Emphanisis in Cubic $(\text{SnSe})_{0.5}(\text{AgSbSe}_2)_{0.5}$: Dynamical off-centering of Anion Leads to Low Thermal Conductivity and High Thermoelectric Performance[†]

Summary

The structural transformation generally occurs from lower symmetric to higher symmetric structure on heating. However, the formation of locally broken asymmetric phases upon warming has been evidenced in PbQ ($Q = \text{S, Se, Te}$), a rare and unusual phenomenon called emphanisis, which has significant effect on their thermal transport and thermoelectric properties. $(\text{SnSe})_{0.5}(\text{AgSbSe}_2)_{0.5}$ exhibits in rock-salt cubic average structure, with the three cations occupying the same Wyckoff site (4a) and Se in the anion position (Wyckoff site: 4b). Using synchrotron X-ray pair distribution function (XPDF) analysis, in this chapter, we show that the local structure of $(\text{SnSe})_{0.5}(\text{AgSbSe}_2)_{0.5}$ gradually deviates further from its overall average cubic rock-salt structure with warming, which resembles to the emphanisis. The local structural analysis indicate that Se atoms remain off-centered position by a magnitude of $\sim 0.25 \text{ \AA}$ at 300 K along the [111] direction and the magnitude of the distortion is found to increase with increasing the temperature. This provides three short and three long $M\text{-Se}$ bonds ($M = \text{Sn/Ag/Sb}$) within the average rock-salt lattice, which hinders the phonon propagation and lowers the lattice thermal conductivity (κ_{lat}) to $0.49 - 0.39 \text{ W/mK}$ in the $295 - 725 \text{ K}$ range. Phonon dispersion based on density functional theory (DFT) shows highly anharmonic low energy optical modes which are primarily contributed by the localized Ag and Se vibrations. Emphanisis induced low κ_{lat} and favourable electronic structure with multiple valence band extrema withinin close energy concurrently give rise to a promising thermoelectric figure of merit (ZT) of ~ 1 at 706 K in p-type carrier optimized Ge doped new rock-salt phase of $(\text{SnSe})_{0.5}(\text{AgSbSe}_2)_{0.5}$.

[†]M. Dutta, K. Pal, M. Etter, U. V. Waghmare and K. Biswas. *J. Am. Chem. Soc.*, 2021, **143**, 16839–16848.

4.2.1. Introduction

Structural transformation is an intrinsic property of a material and is subjected to huge introspection in chemistry due to its fundamental interests in both academic and applied fields. Typically, the structural transformation occurs from a low symmetric ground state to a higher symmetry state upon heating.¹ This happens because as the temperature increases, the system favours a more disordered state, i.e., a high symmetric phase.^{2, 3} However, recently it has been observed in few high symmetric materials, the formation of locally broken asymmetric phases upon warming, an unusual phenomenon called “*emphanisis*”.⁴⁻⁶ Emphanisis means transformation of a high symmetric to a lower symmetric structure with warming, which is driven largely by the presence of stereochemically active lone pair of electrons as seen in the case for IV-VI chalcogenides like PbQ ($Q= S, Se, Te$),^{4, 5, 7} $SnTe$ ⁶ or in perovskite halides like $CsSnBr_3$ etc.^{8, 9} Such local off-centering of atoms creates multiple short and long bonds in its local environment thereby inducing a local aperiodicity which impede the phonon propagation, thus leading to low lattice thermal conductivity (κ_{lat}).¹⁰⁻¹⁴

Such materials exhibiting low κ_{lat} are essential for thermal management applications like thermoelectrics,¹⁵⁻¹⁹ thermal barriers,²⁰ thermo-galvanic cells²¹ etc and hence rigorous investigations are being pursued to understand the nature of phonon propagation in solids. Conventional approaches to lower κ_{lat} of material includes external doping/alloying,^{22, 23} introducing nanoprecipitates into the parent matrix^{24, 25}, forming all-scale hierarchical architectures²⁶ or through intrinsic phonon propagating pathways²⁷ like bonding hierarchy,²⁸ intrinsic rattling^{29, 30} or lone pair induced anharmonicity³¹ etc. $SnSe$ for example consists of stacked layers along the crystallographic a -direction which consists of weak intralayer bonding. Such weak bonding disrupts the phonon flow and ultimately decreases the phonon group velocity, thereby lowering the κ_{lat} .³²⁻³⁵ $AgSbSe_2$ which comprises of $5s^2$ lone pair on Sb , induces significant lattice anharmonicity which disrupts the phonon propagation.^{31, 36, 37} Both these compounds, $SnSe$ and $AgSbSe_2$ are found to possess intrinsically ultralow κ_{lat} of < 0.5 W/mK throughout the measured temperature. Both $SnSe$ and $AgSbSe_2$ are predicted to have distorted polyhedron around them mainly to accommodate the active lone pair of electrons on Sn^{2+} and Sb^{3+} cations.^{31, 38} Thereby, temperature dependent local vs. global structure, thermal conductivity and

thermoelectric properties investigations of the compounds in compositions $(\text{SnSe})_{1-x}(\text{AgSbSe}_2)_x$ ^{39, 40} and more importantly in $(\text{SnSe})_{0.5}(\text{AgSbSe}_2)_{0.5}$ (*i.e.*, $\text{SnSe}:\text{AgSbSe}_2 = 1:1$) is worth exploring.

Here, we demonstrate that $(\text{SnSe})_{0.5}(\text{AgSbSe}_2)_{0.5}$ exhibits overall average rock-salt structure, but its local structure is found to deviate from the average structure by analysing the temperature dependent X-ray Pair Distribution Function (XPDF). The local structure distortion shows significant effect on its thermal transport and thermoelectric properties. $(\text{SnSe})_{0.5}(\text{AgSbSe}_2)_{0.5}$ exists in rock-salt cubic average structure, with the three cations occupying the same Wyckoff site (4a) and Se in the anion position (Wyckoff site: 4b). The local structural analysis indicate that Se atoms remain off-centered position by a magnitude of $\sim 0.25 \text{ \AA}$ at 300 K along the [111] direction and the magnitude of the distortion is found to increase with increasing the temperature. This increase in the local distortion of Se with increase in temperature, lowers the local symmetry with warming, which resembles to a rare phenomenon called “*emphanisis*”. This local off-centering of Se leads to local bonding hierarchy with three short and three long M – Se bonds (M = Sn/Ag/Sb) within the average rock-salt lattice, which hinders the phonon propagation and lowers the lattice thermal conductivity (κ_{lat}) to an ultralow value. First principal density functional theory (DFT) based phonon calculations exhibit low energy optical modes which are primarily contributed by Ag and Se vibrations. Furthermore, the lattice is characterised by a high degree of anharmonicity as seen from very high mode-Gruneisen parameters. All these factors lead to enhance phonon scattering in $(\text{SnSe})_{0.5}(\text{AgSbSe}_2)_{0.5}$, which decreases its κ_{lat} to 0.49 – 0.39 W/mK in the 295 – 725 K temperature range. Combined with a favourable electronic band structure with multiple valence band extrema having very little energy off-sets ($\Delta E \sim 15 \text{ meV}$), $(\text{SnSe})_{0.5}(\text{AgSbSe}_2)_{0.5}$ shows a good thermoelectric power factor of $5.27 \mu\text{W}/\text{cmK}^2$ at 725 K, and a p-type zT of 0.77 at 725 K. With further optimization via Ge doping, a high zT of ~ 1 is found for $(\text{SnSe})_{0.5}(\text{AgSb}_{1-x}\text{Ge}_x\text{Se}_2)_{0.5}$ ($x = 0.06$) at 706 K which is significant for a lead free new Se based thermoelectric material.

4.2.2. Methods

Synthesis. High quality polycrystalline $(\text{SnSe})_{0.5}(\text{AgSbSe}_2)_{0.5}$ and its derivatives were prepared by vacuum sealed melting. Used stoichiometric quantities of high-purity Sn (> 99.99%, Alfa Aesar), Ag (99.99%, Sigma Aldrich), Sb (Alfa Aesar 99.9999%), Ge (Sigma Aldrich 99.999%) and Se (99.9999%, Alfa Aesar) (total weight of 7 g) in a quartz ampoule, sealed during high vacuum of 10^{-5} torr. The contents were heated up to 723 K in 12 hours, then ramped to 1223 K in 5 hours, followed by dwelling at this temperature for 10 hours, and then cooled to room temperature in 12 hours. The as-synthesized samples were then cut into appropriate shapes for transport measurements.

Powder X-ray diffraction (PXRD). Room temperature PXRD measurements of finely ground samples were recorded on Rigaku SmartLab SE diffractometer using Cu $K\alpha$ ($\lambda = 1.54059 \text{ \AA}$) radiation.

Thermal conductivity. The thermal diffusivity, D , was measured between 290 K and 730 K using laser flash diffusivity technique in Netzsch LFA-457 instrument. Disc-shaped pellets with ca. 8 mm x 2 mm dimensions were used for thermal transport measurement. Total thermal conductivity (κ_{tot}) was estimated using the relation, $\kappa = D \times C_p \times \rho$, where ρ is the density (> 97%) of the sample and C_p is the heat capacity (C_p) estimated from the Dulong Petit limit. Lattice thermal conductivity (κ_{lat}) is extracted by subtracting electronic thermal conductivity (κ_{el}) from total thermal conductivity. κ_{el} is calculated using the Wiedemann Franz law, $\kappa_{\text{el}} = L\sigma T$, where σ is the electrical conductivity and L is the temperature dependent Lorenz number obtained by fitting the Seebeck coefficient to the reduced chemical potential.²⁶

Electronic properties. Electrical conductivity (σ) and Seebeck coefficient (S) were simultaneously measured under He-atmosphere from 290 K up to 730 K using ULVAC-RIKO ZEM-3 instrument. Rectangular bar shaped samples of dimension 9 mm x 2 mm x 2 mm were used for the measurements.

Hall Measurements. Room temperature hall measurement was performed for all the samples in an in-house set up under a varying magnetic field of 0.0 – 1.0 T. The samples used are bar shaped and the current used is 100 mA.

X-ray Pair Distribution Function (XPDF). For performing synchrotron X-ray PDF, samples were finely ground with agate mortar pestle and then filled in capillary of 0.6 mm diameter. Both ends of capillaries were sealed using adhesive. Perkin Elmer image plate detector was used to record the diffraction data. To subtract the background, data sets of empty capillaries was performed. Dark measurement prior to each data collection was done and Lanthanum Hexaboride (LaB₆) was taken as standard for calibration. The wavelength of the beam was fixed at 0.20742 Å. The data was taken in P02.1 beamline of PETRA III, DESY, Germany.⁴¹

$G(r)$, which tells us about the probability of finding nearest neighbour bonding at a certain distance r in the material, was obtained via Fourier transformation of scattering structure function, $F(Q)$ ⁴²

$$G(r) = \frac{2}{\pi} \int_{Q_{min}}^{\infty} F(Q) \sin Qr \, dQ \quad (4.2.1)$$

where Q represents the momentum transfer of the scattering particle. $F(Q)$ is obtained from scattering data and is related to structure function $S(Q)$ as $F(Q) = Q[S(Q)-1]$. Initial data reduction was done using DAWN⁴³ and PDFgetx3⁴⁴ softwares.

Simulation of the experimental PDF data was done using PDFgui⁴⁵ software. All the datasets from 100 K – 400 K were initially modelled using a cubic $Fm\bar{3}m$ model. The refinement parameters were the scale, correlation parameter, lattice parameter, and the thermal displacement values. The first peak of the $G(r)$ vs r plot represents the nearest atom - atom correlation, the second peak corresponds to second nearest atom-atom distances and so on.

Computational details. All density functional theory (DFT) calculations were performed using the Vienna Ab-initio Simulation Package (VASP).^{46, 47} We used the PBEsol⁴⁸ generalized gradient approximation (GGA)⁴⁹ to the exchange-correlation energy functional and the projector augmented wave (PAW)^{50, 51} potentials for Ag (4p⁶ 4d¹⁰ 5s¹), Sn (4d¹⁰ 5s² 5p²), Sb (5s² 5p³) and Se (4s² 4p⁴). To model the disordered structure of

(SnSe)_{0.5}(AgSbSe₂)_{0.5}, we used a special quasi random structure (SQS) of the compound generated with the ATAT code⁵² using a 54 atom supercell having 9 Sn, 9 Ag, 9 Sb and 27 Se atoms. We calculated the electronic structure and density of states of (SnSe)_{0.5}(AgSbSe₂)_{0.5} using the SQS structure. While doping with Ge, we substituted 1 Ge (2 Ge) atoms with 1 Sb (2 Sb) atoms in the 54 atom SQS structure, that leads to 3.7% (7.4%) doping concentrations of Ge at the cation sites. We used a kinetic energy cut-off of 400 eV and a k-point mesh of 6 x 6 x 6 for all calculations.

To calculate the phonon dispersion, we used an ordered structure of (SnSe)_{0.5}(AgSbSe₂)_{0.5} having 6 atoms (1 Ag, 1 Sn, 1 Sb and 3 Se atoms) since the calculations of the phonons using the 54-atom disordered structure would be computationally very expensive. All the structures were fully relaxed before calculating their electronic structures (that include spin-orbit coupling) and phonon dispersions (that does not include spin-orbit coupling). The phonon dispersions were calculated using 2×2×2 supercell (containing 48 atoms) of the ordered structure (having 6 atoms) using Phonopy.⁵³ We determined the mode Grüneisen parameters of (SnSe)_{0.5}(AgSbSe₂)_{0.5} using a finite difference method where we have calculated the phonon frequencies of the compound at two different volumes (1.02V₀ and 0.98V₀, V₀ being the equilibrium unit cell volume) and utilized the formula $\gamma_{qv} = - \frac{d \ln \omega_{qv}}{d \ln V}$, where γ_{qv} , V and ω_{qv} denote Grüneisen parameter, unit cell volume, and frequency of a phonon mode at wavevector q for branch v, respectively. Theoretical calculations are done in collaboration with Prof. U. V. Waghmare, JNCASR, India.

Calculation of minimum thermal conductivity: Minimum thermal conductivity of (SnSe)_{0.5}(AgSbSe₂)_{0.5} is calculated via diffuson process using the formula,⁵⁴

$$\kappa_{diff} = 0.76n^{2/3}k_B v_{ave} \quad (4.2.2)$$

where k_B is the Boltzmann constant, n is the number density and v_{ave} is the mean sound velocity calculated using the formula⁵⁵

$$v_{ave} = \frac{3}{v_l^{-3} + 2v_t^{-3}} \quad (4.2.3)$$

where, v_l and v_t is calculated theoretically to be 3890 m/s and 2020 m/s respectively. The average sound velocity (v_{ave}) is calculated to be 2260 m/s.

4.2.3. Results and Discussion

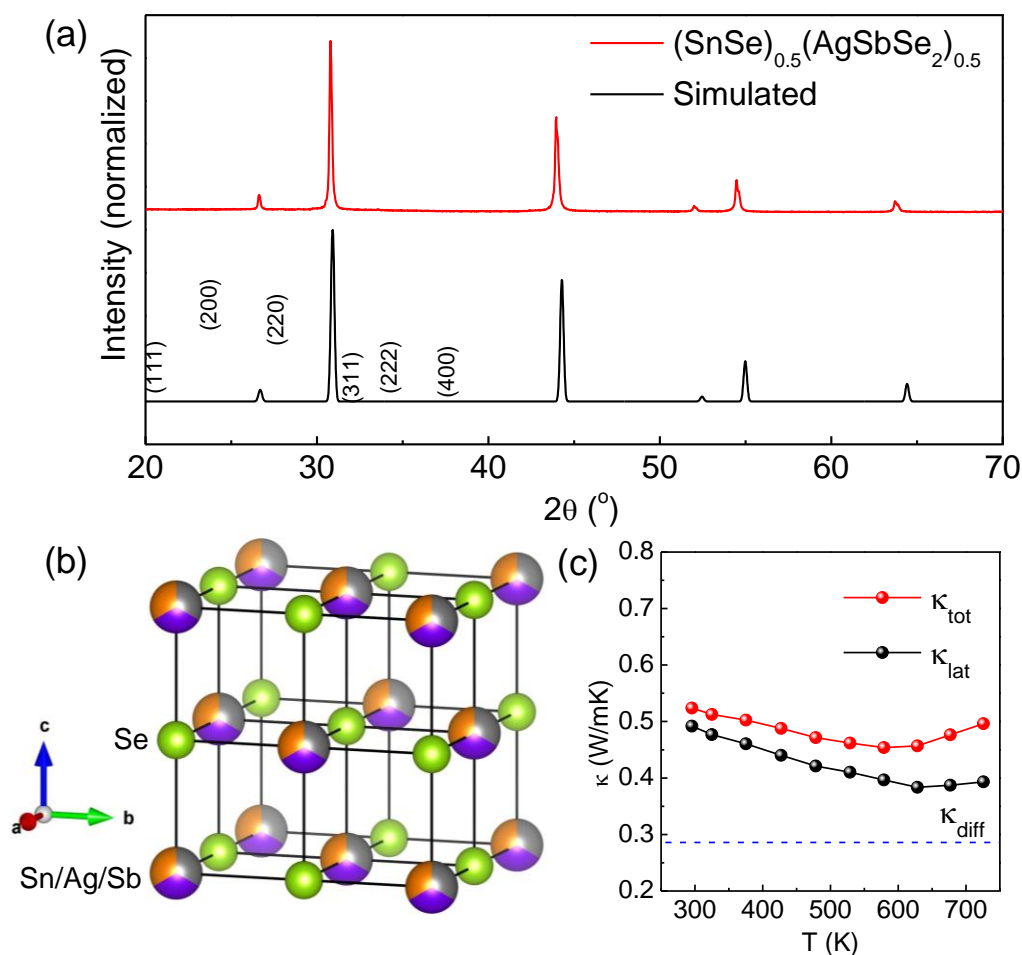


Figure 4.2.1. (a) Room temperature PXRD of $(\text{SnSe})_{0.5}(\text{AgSbSe}_2)_{0.5}$. (b) Rock-salt cubic structure of $(\text{SnSe})_{0.5}(\text{AgSbSe}_2)_{0.5}$. (c) Temperature dependent total thermal conductivity (κ_{tot}) and lattice thermal conductivity (κ_{lat}) of $(\text{SnSe})_{0.5}(\text{AgSbSe}_2)_{0.5}$.

Polycrystalline ingots of $(\text{SnSe})_{0.5}(\text{AgSbSe}_2)_{0.5}$ were synthesized via melting of individual elements in sealed quartz tube at high vacuum ($\sim 10^{-5}$ Torr). Room temperature powder X-ray diffraction (PXRD) data indicates that the as synthesized compound can be indexed using rock-salt cubic structure (space group; $Fm\bar{3}m$), with no observable secondary phase impurities (Figure 4.2.1a). The cation site is occupied by Sn/Ag/Sb in a positional disorder while the Se atoms take up the anion position (Figure 4.2.1b). The presence of three distinct atoms in the same position generates a greater degree of disorder

in the system which should provide enhanced phonon scattering. The total thermal conductivity (κ_{tot}) is found to be 0.52 W/mK at 295 K and decreases very slightly with temperature, with value reaching up to 0.45 W/mK at 579 K (Figure 4.2.1c). The lattice thermal conductivity (κ_{lat}) which is derived using the formula $\kappa_{\text{lat}} = \kappa_{\text{tot}} - L\sigma T$ (L = Lorenz number), is found to be 0.49 W/mK at 295 K and decreases slightly with increase in temperature to 0.39 W/mK at 725 K (Figure 4.2.1c), lying higher than the minimum thermal conductivity (κ_{diff}) of 0.286 W/mK calculated using the diffuson model.⁵⁴

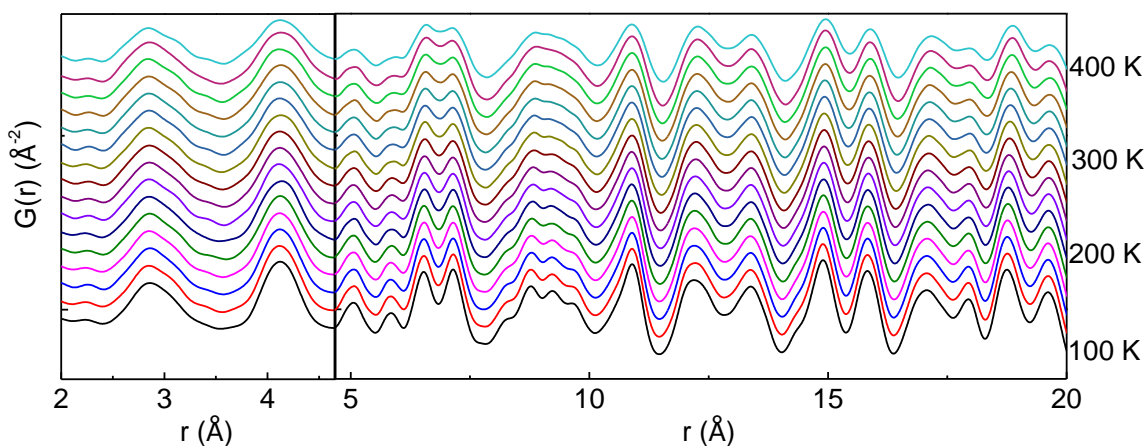


Figure 4.2.2. Temperature dependent XPDF data of $(\text{SnSe})_{0.5}(\text{AgSbSe}_2)_{0.5}$.

To elucidate the structural origin of low κ_{lat} in $(\text{SnSe})_{0.5}(\text{AgSbSe}_2)_{0.5}$, we have analysed its crystal structure using synchrotron X-ray Pair Distribution Function (X-PDF) in the temperature range 100–400 K (Figure 4.2.2). Figure 4.2.3a represents the X-PDF plot of $(\text{SnSe})_{0.5}(\text{AgSbSe}_2)_{0.5}$ up to 20 Å at 400 K, fitted with a rock-salt cubic model. The blue open circles represent the experimental data which has been fitted with a simulated profile given by red line. The residual between the experimental and simulated curve is given by green line and has been offset for clarity. The individual contributions of cation–anion pairs as obtained from the above fitting is also shown in Figure 4.2.3b. Being a total scattering technique X-PDF provides information regarding both local structure as well as the average structure of a solid.⁵⁶ Thus, for an in-depth understanding of the chemical bonding in $(\text{SnSe})_{0.5}(\text{AgSbSe}_2)_{0.5}$, we have separated the X-PDF data into two sections: (1) The first two peaks ($r = 2.0 - 4.66$ Å) which will provide information regarding local

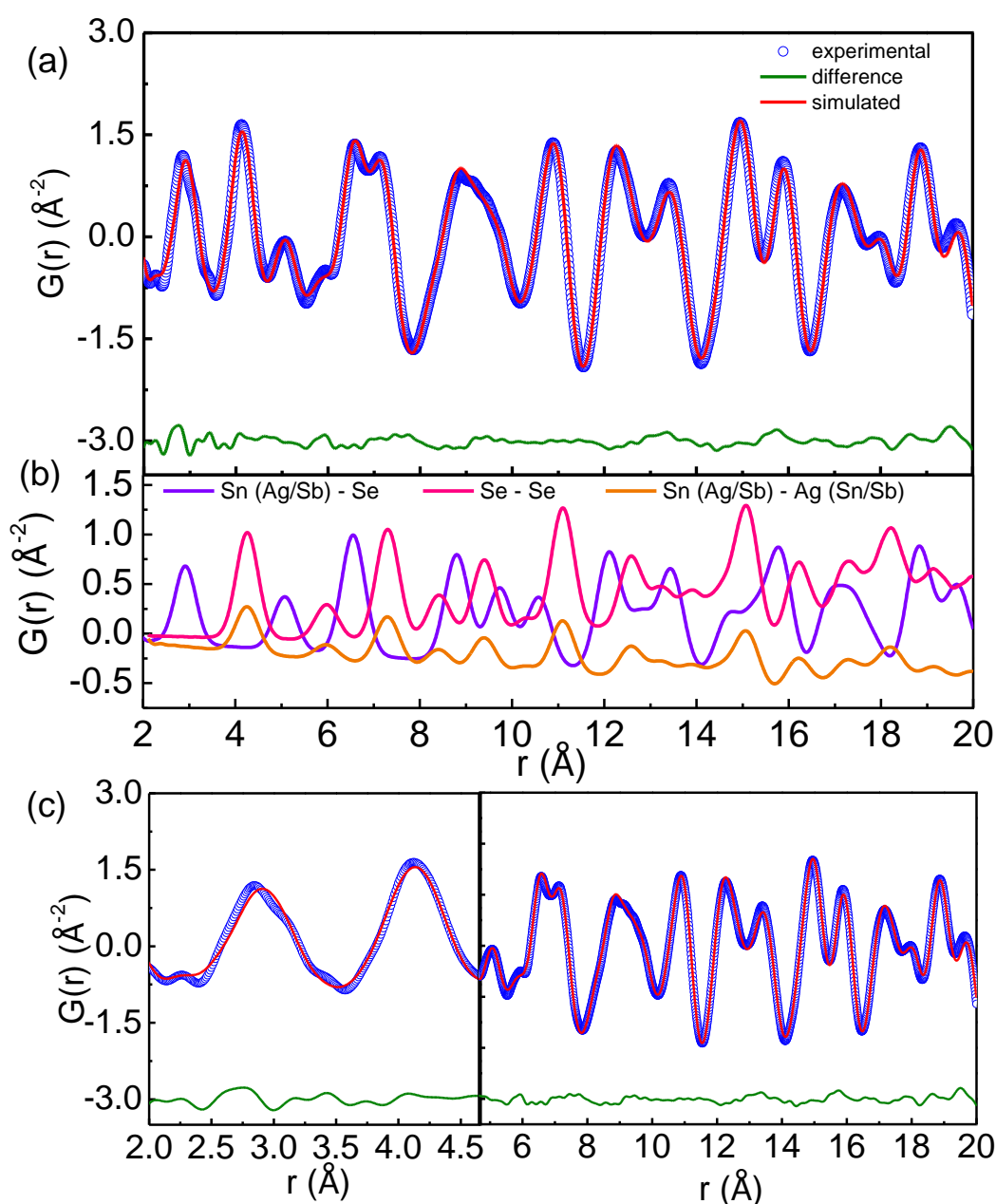


Figure 4.2.3. (a) XPDF data of $(\text{SnSe})_{0.5}(\text{AgSbSe}_2)_{0.5}$ at 400 K fitted with cubic rock-salt model. (b) Individual atom-atom pair correlations at 400 K. (c) XPDF of $(\text{SnSe})_{0.5}(\text{AgSbSe}_2)_{0.5}$ divided into two parts signifying local (left) and average (right) structure.

bonding interactions (i.e., local structure), and (2) the high r peaks ($r = 4.66 - 20 \text{\AA}$), which provides information regarding the average structure (i.e., global structure) of $(\text{SnSe})_{0.5}(\text{AgSbSe}_2)_{0.5}$ as shown in Figure 4.2.3c. From Figure 4.2.3c it is evident that

although the high r peaks provide a good description of the rock-salt structure, the experimental low r peaks deviate significantly from the simulated profile for the rock-salt cubic model. This is further verified from the goodness of fit (R_w) value. The R_w value for high r peaks ($r = 4.66 - 20 \text{ \AA}$) is 0.079 compared to 0.124 for $r = 2.0 - 4.66 \text{ \AA}$ at 400 K. Furthermore, clear asymmetry in the first peak (signifying the first co-ordination sphere) can be observed, which seems to become more prominent with warming (Figure 4.2.4). Such asymmetry has been attributed to multiple unresolved long and short bond lengths present between the atoms. This local structural distortion can give rise to additional phonon-phonon scattering, which can reduce the κ_{lat} of this material.

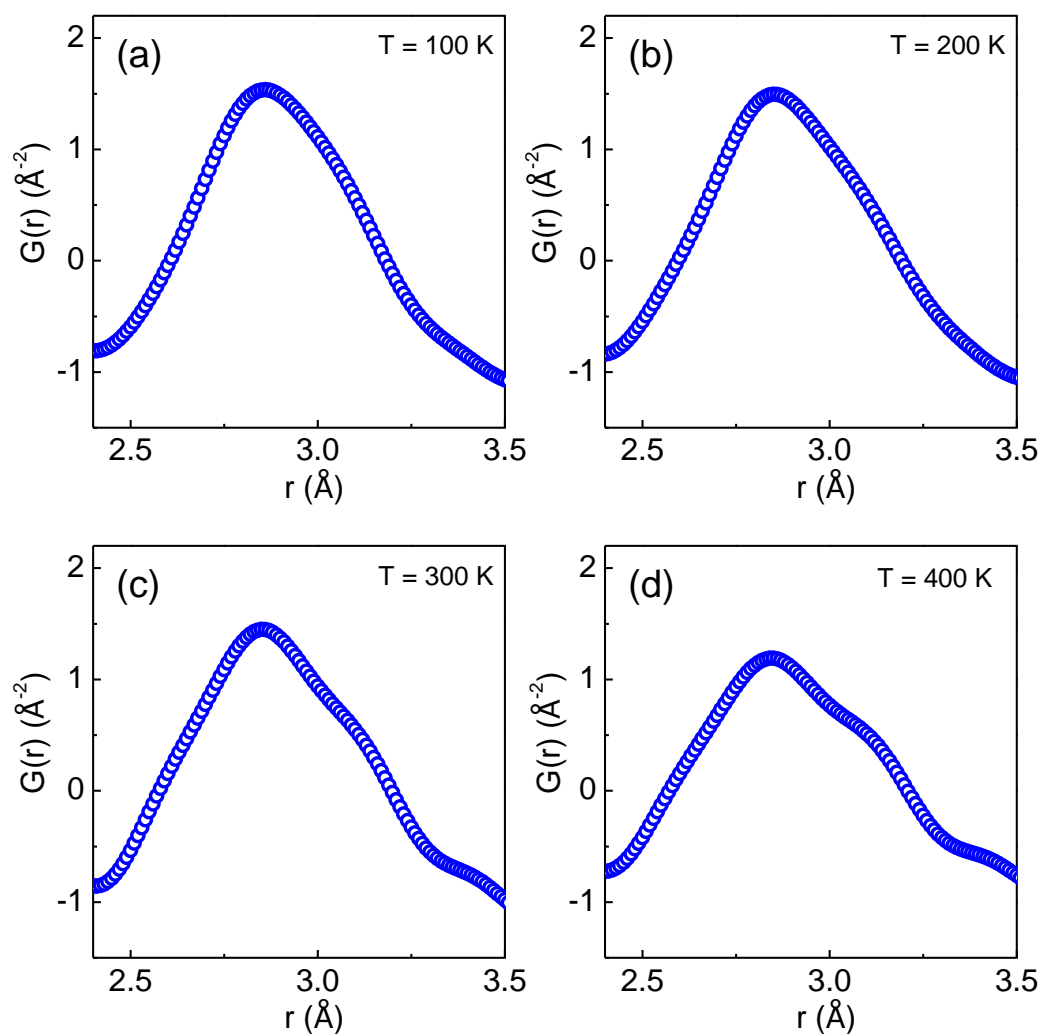


Figure 4.2.4. First peak XPDF data showing increase in peak asymmetry with temperatures at (a) 100 K, (b) 200 K, (c) 300 K and (d) 400 K.

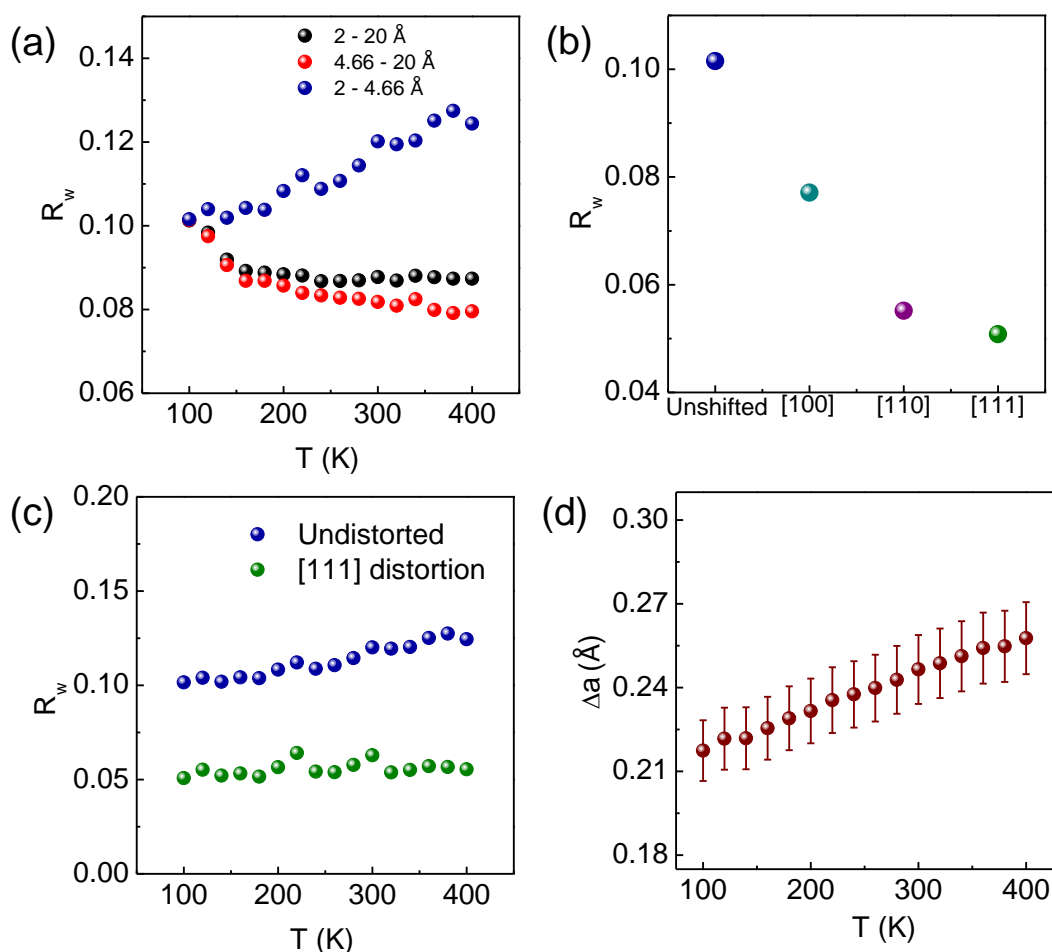


Figure 4.2.5. (a) Temperature dependent goodness of fit (R_w) value obtained from the rock-salt modelling of the XPDF data of $(\text{SnSe})_{0.5}(\text{AgSbSe}_2)_{0.5}$ for different r range. (b) Goodness of fit (R_w) value for the local structure ($r = 2.0 - 4.66$ Å) of $(\text{SnSe})_{0.5}(\text{AgSbSe}_2)_{0.5}$ at 100 K with Se being off-centered along the different crystallographic directions. (c) Temperature dependent R_w value for the local structure ($r = 2.0 - 4.66$ Å) for undistorted and [111] distortion of Se from its mean position. (d) Magnitude of Se distortion along [111] direction.

Temperature dependent (100 – 400 K) total X-PDF data ($r = 2.0 - 20$ Å) fitted using rock-salt model indicated that the overall structure becomes more cubic with the increase in temperature as evident from the R_w data (Figure 4.2.5a). The R_w value decreases from 0.101 at 100 K to 0.087 at 400 K. The lattice parameter and the atomic displacement parameters obtained through cubic fitting are found to increase with temperature as expected (Figure 4.2.6). R_w values for the low r peaks ($r = 2.0 - 4.66$ Å) and high r peaks ($r = 4.66 - 20$ Å) however shows contradictory trend (Figure 4.2.5a).

The R_w values for the average structure, $r = 4.66 - 20 \text{ \AA}$, is found to vary from 0.101 at 100 K to 0.079 at 400 K, indicating the structure globally becomes more symmetric with temperature. However, for the local structure *i.e.*, $r = 2.0 - 4.66 \text{ \AA}$, the R_w values increases from 0.101 at 100 K to 0.124 at 400 K, thus suggesting that the local structure deviates from the high symmetric cubic phase on warming (Figure 4.2.5a). Ideally, a structure transforms from low symmetric ground state to high symmetric state on warming, however, the evolution of the local structure from high symmetric phase to low symmetric phase on warming is rare and unusual, and is termed as “*emphanisis*”.⁴ Recently *emphanisis* is seen for Pb Chalcogenides, where the Pb^{2+} is found to off-center with temperature.⁴⁻⁶ Such local off-centering is known to disrupt the phonon flow through a material and lower the lattice thermal conductivity.^{11-14, 28}

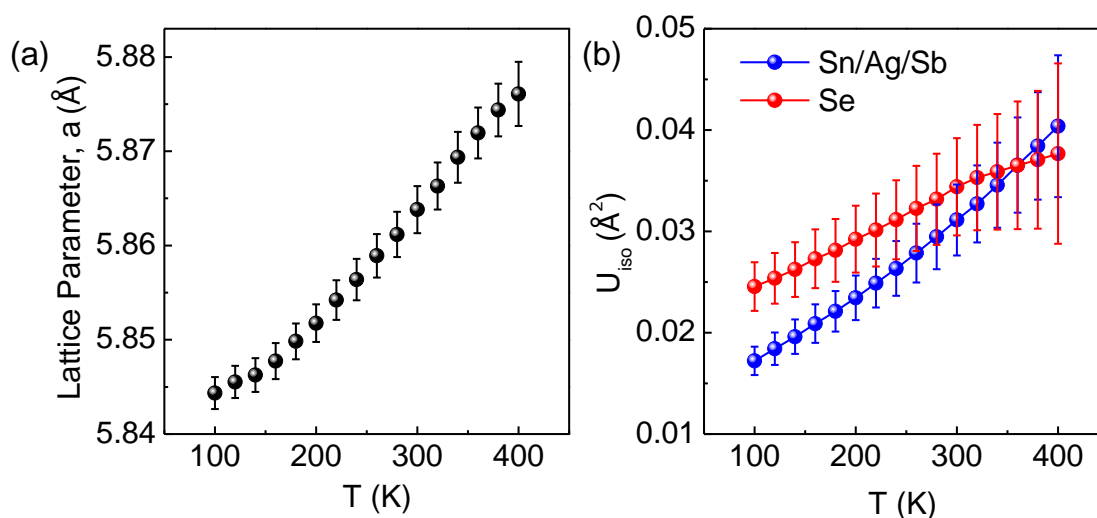


Figure 4.2.6. Temperature dependent (a) lattice parameter, and (b) isotropic atomic displacement parameters (U_{iso}), of $(\text{SnSe})_{0.5}(\text{AgSbSe}_2)_{0.5}$ obtained from cubic fitting of the XPDF data.

To investigate the local environment of $(\text{SnSe})_{0.5}(\text{AgSbSe}_2)_{0.5}$ ($r = 2.0 - 4.66 \text{ \AA}$) we have off-centered the anion Se along different crystallographic direction ([100], [110] and [111]) as shown in Figure 4.2.7. The off-centering of Se is motivated by phonon dispersion of $(\text{SnSe})_{0.5}(\text{AgSbSe}_2)_{0.5}$ (discussed later). The simulation becomes instantly better for all the three distorted models compared to the undistorted case as is apparent

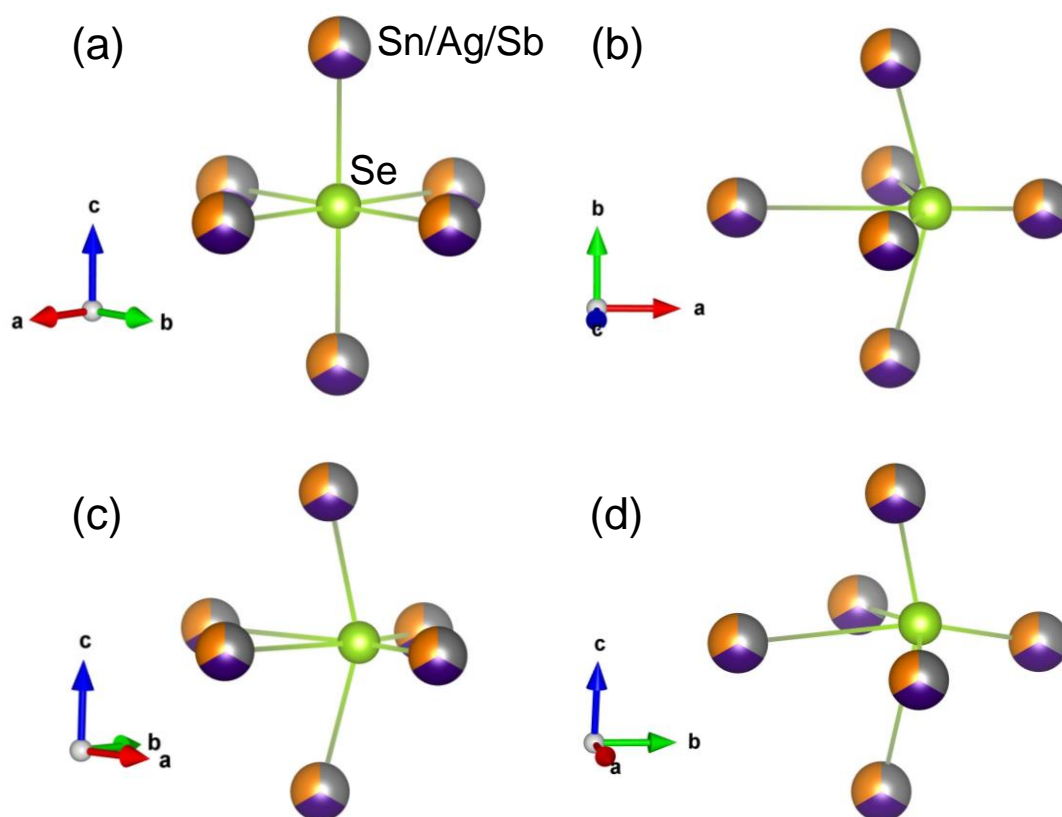


Figure 4.2.7. Representative diagram of the octahedral co-ordination of Se, where the Se is present in the (a) undistorted position, (b) distorted along $[100]$ direction, (c) distorted along $[110]$ direction and (d) distorted along $[111]$ direction.

from their R_w value (Figure 4.2.5b). The R_w value of undistorted model at 100 K is 0.101 which decreases to 0.077, 0.055 and 0.051 for $[100]$, $[110]$ and $[111]$ respectively at 100 K (Figure 4.2.5b). This indicates that the Se atom is most likely off-centered along $[111]$ direction and this local off-centering appreciably describes the peak asymmetry found for the nearest atom pair correlation compared to the undistorted peak (Figure 4.2.8a, b). The simulated profiles of the local structure for the other two models, *i.e.*, along $[100]$ and $[110]$ directions are given in Figure 4.2.8c, d. Off-centering of Se atom along $[111]$ direction will lead to formation of 3 short and 3 long bonds, thus resulting in a local structural distortion in the lattice which can disrupt the phonon transport. Temperature dependent analysis of the local structure ($r = 2.0 - 4.66 \text{ \AA}$), indicate that the $[111]$ distorted structure provides better description to the peak asymmetry throughout the measured range. Temperature dependent R_w values corroborates with the observed

improvement in the fitting (Figure 4.2.5c). The Se atom is found to off-center by ~ 0.21 Å at 100 K which increases to ~ 0.26 Å at 400 K (Figure 4.2.5d). This increase in the magnitude of off-centering for Se with increasing temperature indicates that the local structure is slowly deviating from the rock-salt structure on warming, thus showing “*emphanitic*” behaviour. The presence of such off-centering and consequent local bonding heterogeneity is a determining factor for low κ_{lat} as observed for $(\text{SnSe})_{0.5}(\text{AgSbSe}_2)_{0.5}$.

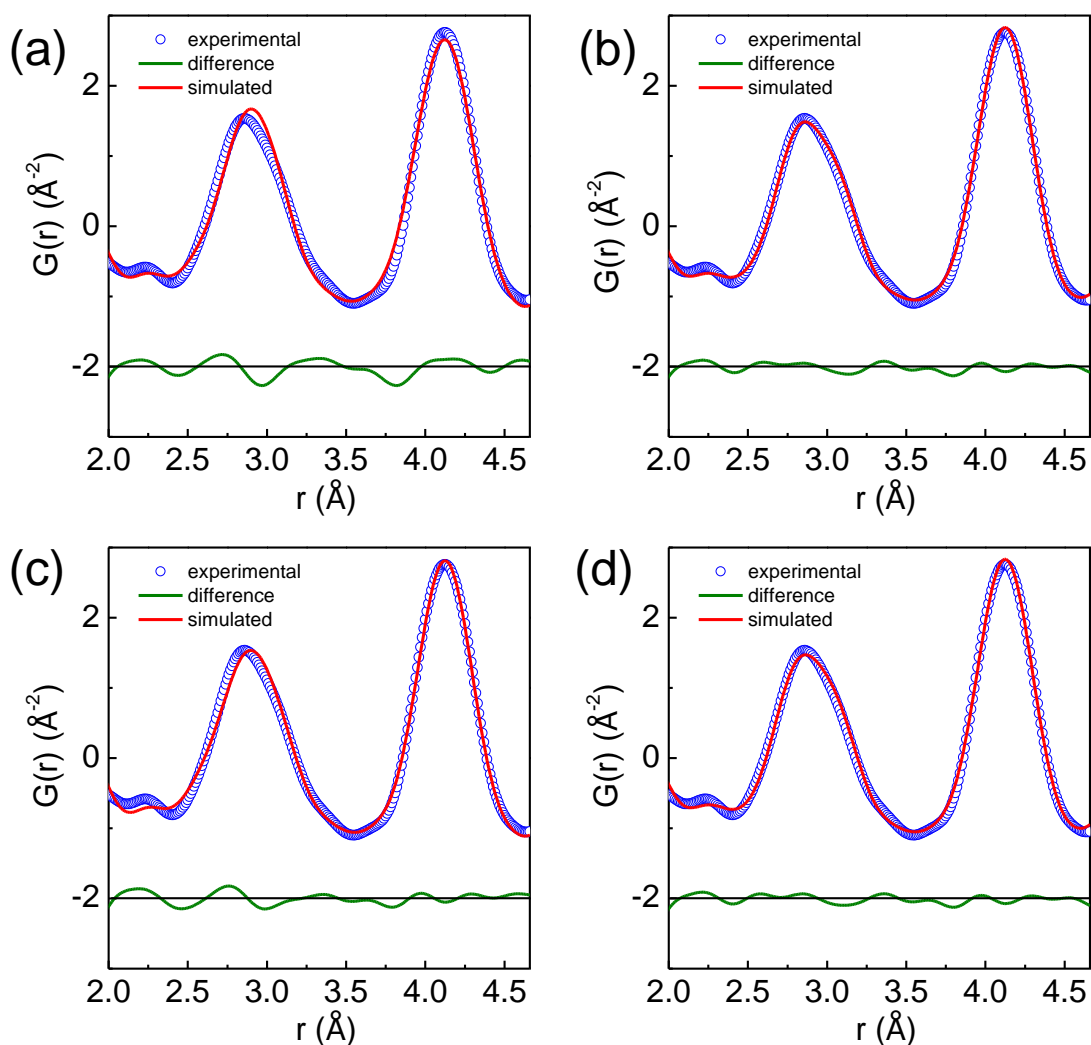


Figure 4.2.8. XPDF fitting of the local structure ($r = 2.0 - 4.66$ Å) of $(\text{SnSe})_{0.5}(\text{AgSbSe}_2)_{0.5}$ at 100 K for (a) undistorted Se, (b) distortion of Se along $[111]$ direction, (c) distortion of Se along $[100]$ direction and (d) distortion of Se along $[110]$ direction. The first peak asymmetry can be accounted for using the distorted model.

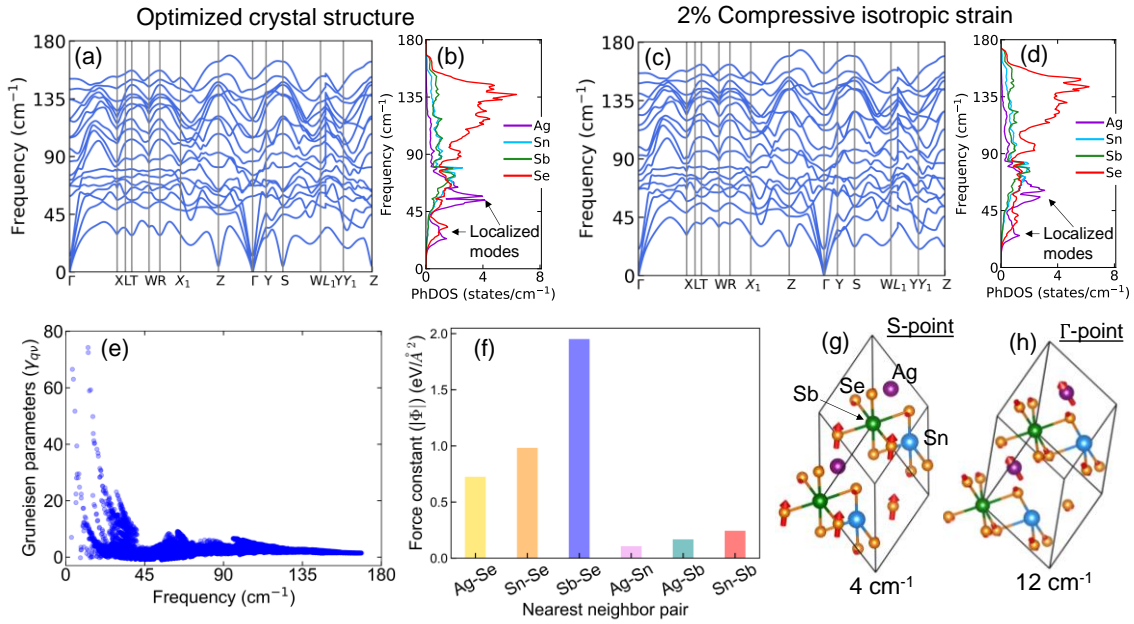


Figure 4.2.9. Phonon dispersions and atom-resolved phonon density of states for (a, b) the optimized and ordered structure of $(\text{SnSe})_{0.5}(\text{AgSbSe}_2)_{0.5}$ and (c, d) the isotropically strained (compressive) ordered structure of $(\text{SnSe})_{0.5}(\text{AgSbSe}_2)_{0.5}$. (e) Calculated mode-Grüneisen parameters and (f) harmonic interatomic force constants for the nearest neighbor atoms. Visualizations of some of the low-frequency optical phonon modes are shown in (g) and (h), where the red arrow indicates the direction and magnitude of the displacement of an atom.

To further understand the origin of the ultralow κ_{lat} of $(\text{SnSe})_{0.5}(\text{AgSbSe}_2)_{0.5}$, we have analysed its lattice dynamics. The calculated phonon dispersion at the optimized lattice constants (Figure 4.2.9a) exhibits a localized low-frequency optical phonon branch ($\sim 30 \text{ cm}^{-1}$) that primarily originates due to the vibrations of Ag and Se atoms (see phonon density of states in Figure 4.2.9b). The low-frequency localized phonon modes can effectively scatter the heat-carrying phonons, inducing a low κ_{lat} in crystalline solids.^{57, 58} Interestingly, the low-energy phonon branch also exhibits damped phonon vibrations at the zone boundary (S and Z points) at very low-frequency ($\sim 4 \text{ cm}^{-1}$) which becomes effective in reducing κ_{lat} of $(\text{SnSe})_{0.5}(\text{AgSbSe}_2)_{0.5}$ in the similar way the overdamped phonons induce ultralow κ_{lat} in CsPbBr_3 .⁵⁹ This 4 cm^{-1} mode involves vibration of Se atom, which prompted us to off-centre Se during XPDF analysis. In addition, another group of localized phonon modes appear at a slightly higher energy ($\sim 55 \text{ cm}^{-1}$) which primarily involve the vibrations of Ag atoms. The low-energy optical phonon branch near

55 cm^{-1} exhibits a strong strain-phonon coupling, where the phonon modes are significantly hardened after the application of 2% compressive strain on the unit cell volume of the optimized cell (Figure 4.2.9c). This indicates that this low-frequency phonon modes are strongly anharmonic which has been verified by calculation of mode Gruneisen parameters (γ_{qv}) that reveals high values (~ 80) of γ_{qv} for the acoustic and low-energy optical phonons (Figure 4.2.9e). Since the phonon scattering rates (inversely proportional to the phonon lifetime) increase with the inverse square of γ_{qv} ,⁶⁰ the presence of such a strong anharmonicity attributes to ultralow κ_{lat} in $(\text{SnSe})_{0.5}(\text{AgSbSe}_2)_{0.5}$. Even after the application of strain, the localization of the phonon modes persists in $(\text{SnSe})_{0.5}(\text{AgSbSe}_2)_{0.5}$ as seen in the phonon density of states in Figure 4.2.9d.

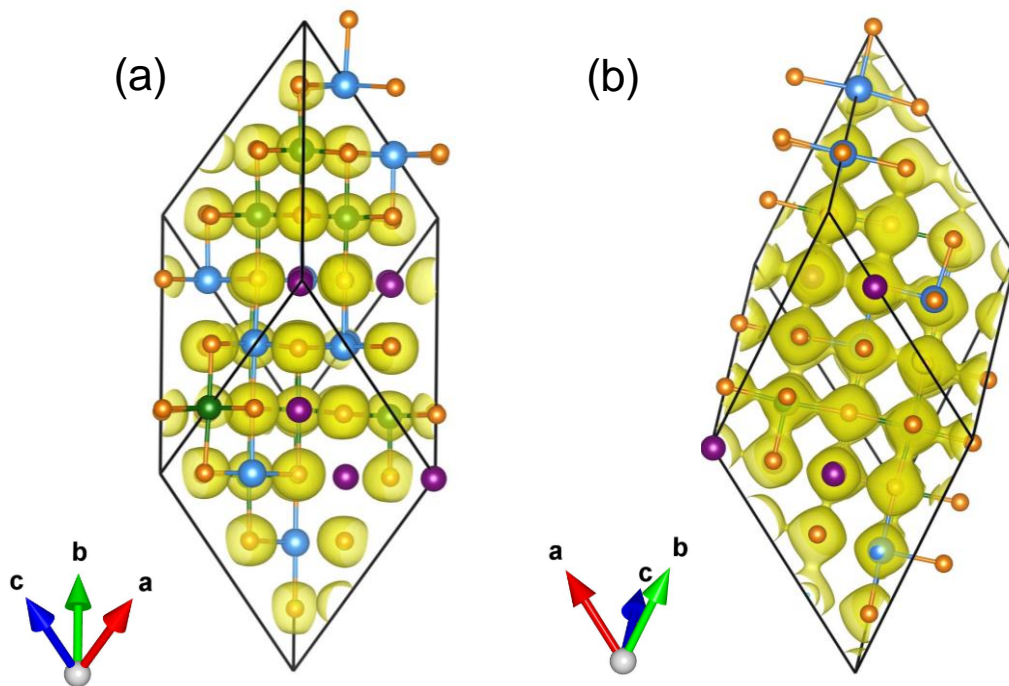


Figure 4.2.10. Analysis of chemical bonding on the SQS of $(\text{SnSe})_{0.5}(\text{AgSbSe}_2)_{0.5}$. (a) Iso-surfaces of electron localization function (visualized on at an iso-value which is 77% of the maximum) reveal the lone pair of electrons ($5s^2$) around Sb atoms. (b) Iso-surfaces of total charge density plot visualized at an iso-value of 0.04 (minimum = -0.05, maximum = 2.28) which reveals stronger Sb-Se bonding compared to Ag-Se and Sn-Se bonds due to relatively stronger overlap of the charge densities between Sb and Se atoms. Colour code: Sn – Cyan, Ag – Purple, Sb – Green, Se – Brown.

To quantify the bond-strengths, we have analysed the harmonic interatomic force constants (IFCs) between the nearest-neighbour pair of atoms in the structure of $(\text{SnSe})_{0.5}(\text{AgSbSe}_2)_{0.5}$, which shows (Figure 4.2.9f) that Ag and Se have the weakest bonding compared to Sb-Se and Sn-Se bond strengths. The IFC values are further corroborated from the charge density and electron localization function plot (ELF), where stronger overlap between Sb-Se evidence for its high IFC value (Figure 4.2.10). Ag is found to have weaker interaction with Se and hence corresponds to the low IFC values. These analyses rationalize the appearance of the low-frequency and localized phonon modes contributed by Ag and Se in the phonon dispersion of $(\text{SnSe})_{0.5}(\text{AgSbSe}_2)_{0.5}$. Finally, we show atomic displacement pattern for (i) the damped phonon mode (4 cm^{-1}) at S point where only the Se atoms vibrate (Figure 4.2.9g) and (ii) localized phonon mode (12 cm^{-1}) at Γ point in Figure 4.2.9h, where the Ag atoms have the largest displacements. Such localized phonon modes are the strong source of phonon-scattering processes in a material.^{57, 58} Hence the presence of such localized low frequency optical modes, high anharmonicity within the lattice and local off-centering of Se atom contribute heavily to scatter the heat carrying acoustic phonons and as a result low κ_{lat} is observed for $(\text{SnSe})_{0.5}(\text{AgSbSe}_2)_{0.5}$.

Since crystalline materials with low κ_{lat} are highly advantageous for thermoelectrics, we have measured the electrical properties of $(\text{SnSe})_{0.5}(\text{AgSbSe}_2)_{0.5}$. Electrical conductivity (σ) of $(\text{SnSe})_{0.5}(\text{AgSbSe}_2)_{0.5}$ is found to be 66 S/cm at room temperature which increases to 90 S/cm at 725 K (Figure 4.2.12a). It has a room temperature *p*-type carrier concentration (n) of $1.82 \times 10^{19} \text{ cm}^{-3}$. The Seebeck co-efficient (S) is found to be 194 $\mu\text{V/K}$ at 295 K which increase to 242 $\mu\text{V/K}$ at 725 K (Figure 4.2.12b). The positive S values indicate that hole is the majority carrier which is consistent with our Hall data. As a result, a decent power factor of $5.27 \mu\text{W/cmK}^2$ is obtained at 725 K (Figure 4.2.12c). The thermoelectric figure of merit (ZT) of $(\text{SnSe})_{0.5}(\text{AgSbSe}_2)_{0.5}$ is found to be 0.77 at 725 K which is mainly due to its low κ_{lat} and favourable electrical transport values (Figure 4.2.12f).

To improve the thermoelectric properties of $(\text{SnSe})_{0.5}(\text{AgSbSe}_2)_{0.5}$, we have doped Ge into the lattice. Room temperature PXRD indicates the presence of no impurity phases with Ge doping within the instrumental detection limit (Figure 4.2.11). With Ge doping

the σ of the compound increases from 66 S/cm for pristine $(\text{SnSe})_{0.5}(\text{AgSbSe}_2)_{0.5}$ to 361 S/cm for $(\text{SnSe})_{0.5}(\text{AgSb}_{1-x}\text{Ge}_x\text{Se}_2)_{0.5}$ ($x = 0.08$) at room temperature (Figure 4.2.12a). The p-type carrier concentration also similarly changes from $1.82 \times 10^{19} \text{ cm}^{-3}$ for $(\text{SnSe})_{0.5}(\text{AgSbSe}_2)_{0.5}$ to $6.25 \times 10^{19} \text{ cm}^{-3}$ for $(\text{SnSe})_{0.5}(\text{AgSb}_{1-x}\text{Ge}_x\text{Se}_2)_{0.5}$ ($x = 0.10$) (Table 4.2.1). The S value decreases from 194 $\mu\text{V/K}$ for pristine $(\text{SnSe})_{0.5}(\text{AgSbSe}_2)_{0.5}$ to 78 $\mu\text{V/K}$ for $(\text{SnSe})_{0.5}(\text{AgSb}_{1-x}\text{Ge}_x\text{Se}_2)_{0.5}$ ($x = 0.08$) (Figure 4.2.12b) and is in line with the conductivity trend. As a result of the improvement in the σ value, a high power factor of 7.88 $\mu\text{W/cmK}^2$ is obtained for $(\text{SnSe})_{0.5}(\text{AgSb}_{1-x}\text{Ge}_x\text{Se}_2)_{0.5}$ ($x = 0.06$) at 706 K (Figure 4.2.12c).

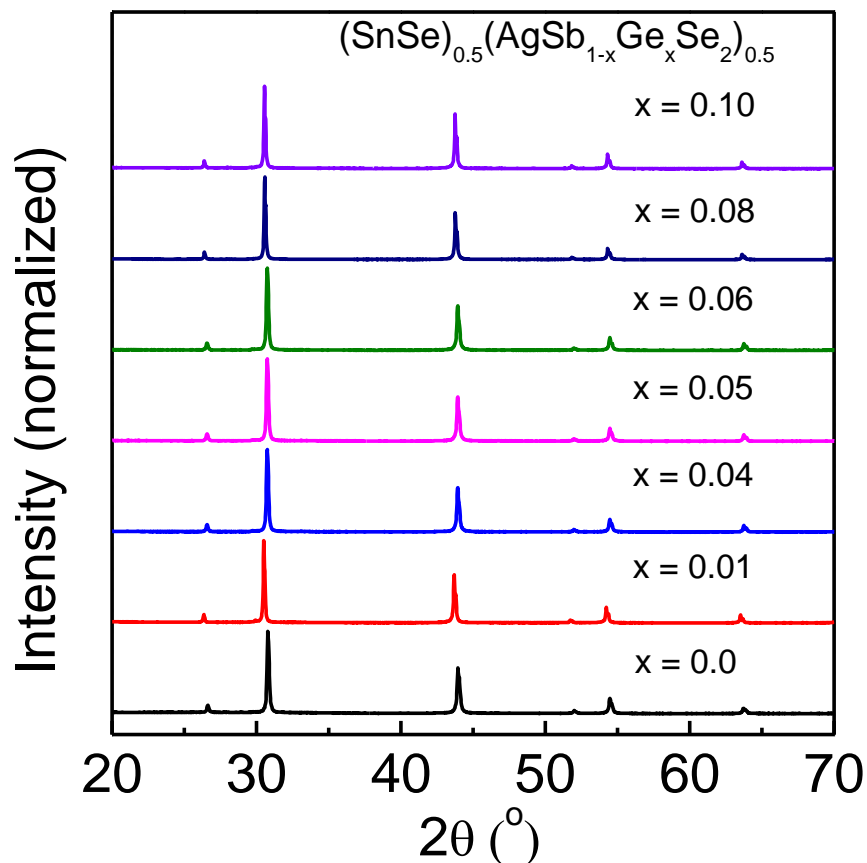


Figure 4.2.11. Room temperature PXRD of $(\text{SnSe})_{0.5}(\text{AgSb}_{1-x}\text{Ge}_x\text{Se}_2)_{0.5}$ ($x = 0.0 - 0.10$).

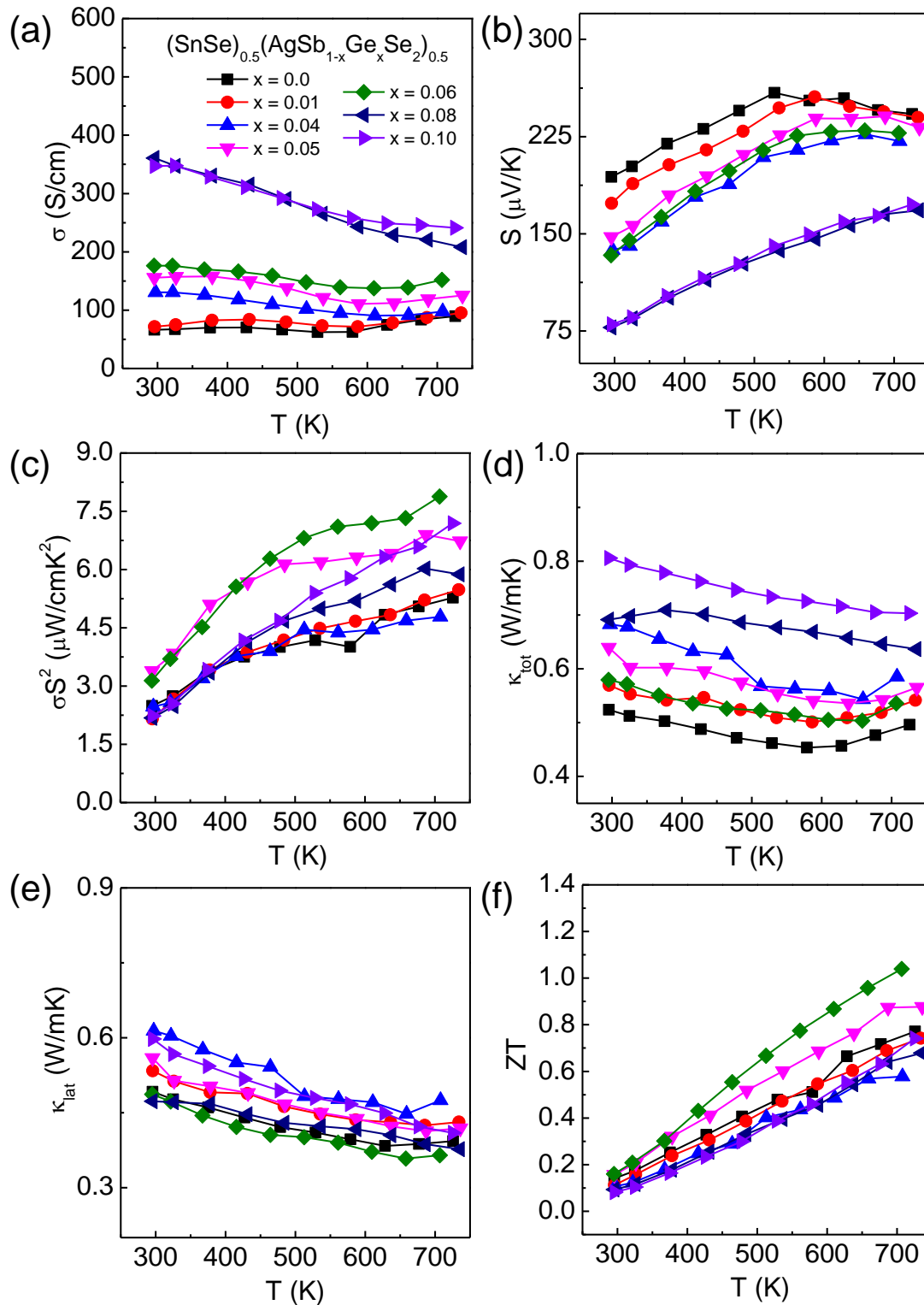


Figure 4.2.12. Temperature dependent (a) electrical conductivity (σ), (b) Seebeck coefficient (S), (c) power factor (σS^2), (d) total thermal conductivity (κ_{tot}), (e) lattice thermal conductivity (κ_{lat}) and (f) thermoelectric figure of merit (ZT) of $(\text{SnSe})_{0.5}(\text{AgSb}_{1-x}\text{Ge}_x\text{Se}_2)_{0.5}$ ($x = 0.0 - 0.10$).

Table 4.2.1. Room temperature carrier concentration and mobility for $(\text{SnSe})_{0.5}(\text{AgSb}_{1-x}\text{Ge}_x\text{Se}_2)_{0.5}$.

Compound $(\text{SnSe})_{0.5}(\text{AgSb}_{1-x}\text{Ge}_x\text{Se}_2)_{0.5}$	Carrier concentration ($\times 10^{19}$) cm^{-3}	Mobility (cm^2/Vs)
x = 0%	1.82	22
x = 1%	2.70	17
x = 4%	3.31	24
x = 5%	3.71	26
x = 6%	4.13	26
x = 8%	5.62	40
x = 10%	6.25	35

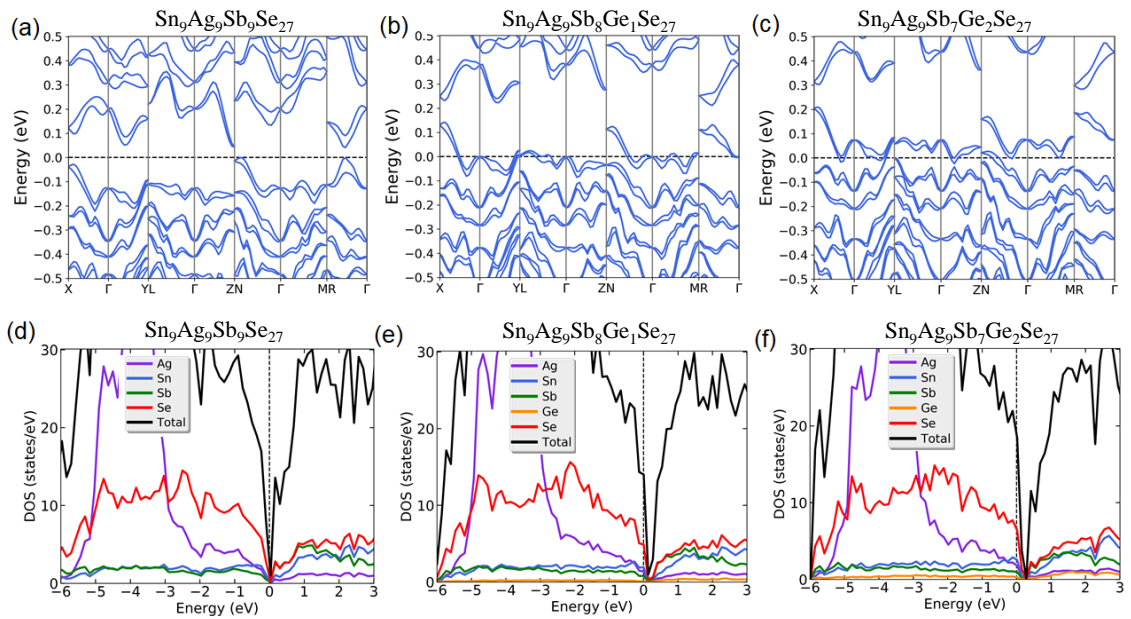


Figure 4.2.13. Spin-orbit coupled electronic structures and density of states of disordered (a, d) $\text{Sn}_9\text{Ag}_9\text{Sb}_9\text{Se}_{27}$, (b, e) $\text{Sn}_9\text{Ag}_9\text{Sb}_8\text{Ge}_1\text{Se}_{27}$, and (c, f) $\text{Sn}_9\text{Ag}_9\text{Sb}_7\text{Ge}_2\text{Se}_{27}$. The dashed line in the figures at 0 eV denotes the Fermi level. The density of states at the Fermi level increases as the Ge-doping concentration increases, leading to an enhancement of the hole concentration and electrical conductivity.

To understand the role of Ge in $(\text{SnSe})_{0.5}(\text{AgSbSe}_2)_{0.5}$, we have calculated the electronic structure of $(\text{SnSe})_{0.5}(\text{AgSbSe}_2)_{0.5}$ and Ge doped $(\text{SnSe})_{0.5}(\text{AgSbSe}_2)_{0.5}$. The

DFT-calculated electronic structure for pristine $(\text{SnSe})_{0.5}(\text{AgSbSe}_2)_{0.5}$ exhibits a small direct band gap (~ 41 meV, Figure 4.2.13a), where the valence bands are dominated by contributions from the Ag and Se atoms and the conduction bands primarily consists of the Sn, Sb and Se atoms (Figure 4.2.13d). The top valence band exhibits multiple band extrema (along the Γ -X, Γ -R, and Γ -N lines) within a very small energy window (~ 15 meV) that can lead to effective band convergence and hence, a high Seebeck coefficient ($194 \mu\text{V/K}$ at 300 K) was observed in the experiment. However, the electrical conductivity of the pristine samples remains low. In order to boost the electrical conductivity (σ), $(\text{SnSe})_{0.5}(\text{AgSbSe}_2)_{0.5}$ was doped with Ge, which introduced holes into the system and enhanced its σ significantly. Our calculations show that upon doping with 1 Ge atom instead of Sb in the calculated unit cell of $(\text{SnSe})_{0.5}(\text{AgSbSe}_2)_{0.5}$, the Fermi level is pushed inside the valence band (Figure 4.2.13b). This strongly increases the density of states (DOS) at the Fermi level (Figure 4.2.13e), which increases its σ as is also observed from our experimental data (Figure 4.2.12a). The projected DOS also shows that the contributions from Ge atoms are delocalized around Fermi level, which becomes quite effective in enhancing the hole concentrations and electrical conductivity. Increasing the Ge inclusion to 2 atoms further pushes the Fermi level deeper into the valence band (Figure 4.2.13c), amplifies the electronic DOS at the Fermi level (Figure 4.2.13f), which are consistent with our experimental observations. However, the Seebeck coefficient of the doped samples decreases due to the increase in carrier concentration. Overall, the ensuing power factor of Ge-doped $(\text{SnSe})_{0.5}(\text{AgSbSe}_2)_{0.5}$ increases significantly due to the large enhancement of its electrical conductivity with doping.

The total thermal conductivity of Ge doped $(\text{SnSe})_{0.5}(\text{AgSbSe}_2)_{0.5}$ is found to increase on Ge doping. The κ_{tot} increases from 0.52 W/mK for pristine $(\text{SnSe})_{0.5}(\text{AgSbSe}_2)_{0.5}$ to 0.80 W/mK for $(\text{SnSe})_{0.5}(\text{AgSb}_{1-x}\text{Ge}_x\text{Se}_2)_{0.5}$ ($x = 0.10$) at room temperature (Figure 4.2.12d) and is mainly due to the enhanced contribution of electronic part of the thermal conductivity (κ_{el}). The κ_{lat} remains almost same with Ge doping with room temperature κ_{lat} value remains between 0.49 to 0.59 W/mK for all the Ge doped $(\text{SnSe})_{0.5}(\text{AgSb}_{1-x}\text{Ge}_x\text{Se}_2)_{0.5}$ ($x = 0.05$) samples (Figure 4.2.12e). The thermoelectric figure of merit (ZT) reaches a high value of 1.04 at 706 K for 6 mol% Ge doped

$(\text{SnSe})_{0.5}(\text{AgSb}_{1-x}\text{Ge}_x\text{Se}_2)_{0.5}$, which is significant for a lead free Se based thermoelectric material (Figure 4.2.12f).

4.2.4. Conclusion

In conclusion, globally rock-salt $(\text{SnSe})_{0.5}(\text{AgSbSe}_2)_{0.5}$ exhibits rare *emphanitic* behaviour, wherein the Se atoms gets locally distorted along [111] direction from its parent position. Through synchrotron X-ray PDF total scattering we observed that local distortion of Se is found to increase with increase in temperature indicating that the local structure further deviates from its global cubic structure with warming. Phonon dispersion revealed the presence of localized low frequency optical modes which are mainly comprised of Se and Ag atoms, which aids in scattering the phonon transport through the lattice. The crystal lattice is also composed of a high degree of anharmonicity and bonding heterogeneity, both adds to additional phonon scattering and thus decreasing the κ_{lat} . As a result, ultralow κ_{lat} of 0.49 – 0.39 W/mK in 295 – 725 K range has been achieved in $(\text{SnSe})_{0.5}(\text{AgSbSe}_2)_{0.5}$. Electronic band structure calculations via DFT shown the presence of multiple bands near the valence band maxima with very little energy offsets ($\Delta E = 0.15$ eV) which are found to beneficial for enhanced electronic transport. As a result, a promising thermoelectric figure of merit (ZT) of ~ 0.77 is obtained at 725 K for $(\text{SnSe})_{0.5}(\text{AgSbSe}_2)_{0.5}$. Further optimization of electrical properties via Ge doping led to increase in the electrical conductivity which enhanced the zT value to 1.04 at 706 K for $(\text{SnSe})_{0.5}(\text{AgSb}_{1-x}\text{Ge}_x\text{Se}_2)_{0.5}$ ($x = 0.06$).

4.2.5. References

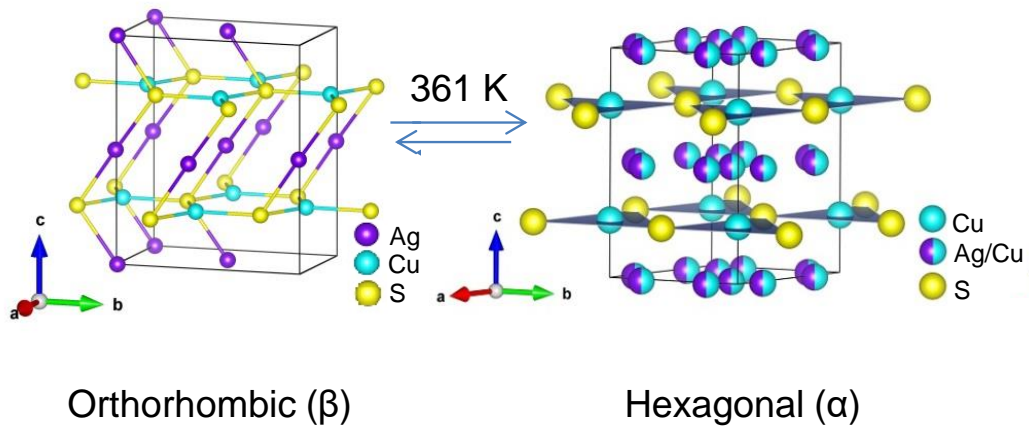
- [1] C. N. R. Rao, *Acc. Chem. Res.*, 1984, **17**, 83-89.
- [2] E. K. H. Salje, *Acta Cryst.*, 1991, **47**, 453-469.
- [3] E. K. H. Salje, in *digital Encyclopedia of Applied Physics*, Wiley-VCH Verlag GmbH & Co. KGaA, 2003, DOI: 10.1002/3527600434.eap320.
- [4] E. S. Božin, C. D. Malliakas, P. Souvatzis, T. Proffen, N. A. Spaldin, M. G. Kanatzidis and S. J. L. Billinge, *Science*, 2010, **330**, 1660.
- [5] R. Yu, E. S. Bozin, M. Abeykoon, B. Sangiorgio, N. A. Spaldin, C. D. Malliakas, M. G. Kanatzidis and S. J. L. Billinge, *Phys. Rev. B*, 2018, **98**, 144108.
- [6] K. R. Knox, E. S. Bozin, C. D. Malliakas, M. G. Kanatzidis and S. J. L. Billinge, *Phys. Rev. B*, 2014, **89**, 014102.
- [7] S. Kastbjerg, N. Bindzus, M. Søndergaard, S. Johnsen, N. Lock, M. Christensen, M. Takata, M. A. Spackman and B. Brummerstedt Iversen, *Adv. Funct. Mater.*, 2013, **23**, 5477-5483.
- [8] D. H. Fabini, G. Laurita, J. S. Bechtel, C. C. Stoumpos, H. A. Evans, A. G. Kontos, Y. S. Raptis, P. Falaras, A. Van der Ven, M. G. Kanatzidis and R. Seshadri, *J. Am. Chem. Soc.*, 2016, **138**, 11820-11832.
- [9] G. Laurita, D. H. Fabini, C. C. Stoumpos, M. G. Kanatzidis and R. Seshadri, *Chem. Sci.*, 2017, **8**, 5628-5635.
- [10] A. Banik, T. Ghosh, R. Arora, M. Dutta, J. Pandey, S. Acharya, A. Soni, U. V. Waghmare and K. Biswas, *Energy Environ. Sci.*, 2019, **12**, 589-595.
- [11] H. Xie, S. Hao, J. Bao, T. J. Slade, G. J. Snyder, C. Wolverton and M. G. Kanatzidis, *J. Am. Chem. Soc.*, 2020, **142**, 9553-9563.
- [12] M. Dutta, R. K. Biswas, S. K. Pati and K. Biswas, *ACS Energy Lett.*, 2021, **6**, 1625-1632.
- [13] J. M. Hodges, S. Hao, J. A. Grovogui, X. Zhang, T. P. Bailey, X. Li, Z. Gan, Y.-Y. Hu, C. Uher, V. P. Dravid, C. Wolverton and M. G. Kanatzidis, *J. Am. Chem. Soc.*, 2018, **140**, 18115-18123.

- [14] Z.-Z. Luo, S. Hao, X. Zhang, X. Hua, S. Cai, G. Tan, T. P. Bailey, R. Ma, C. Uher, C. Wolverton, V. P. Dravid, Q. Yan and M. G. Kanatzidis, *Energy Environ. Sci.*, 2018, **11**, 3220-3230.
- [15] G. Tan, L.-D. Zhao and M. G. Kanatzidis, *Chem. Rev.*, 2016, **116**, 12123-12149.
- [16] X.-L. Shi, J. Zou and Z.-G. Chen, *Chem. Rev.*, 2020, **120**, 7399-7515.
- [17] Y. Xiao and L.-D. Zhao, *Science*, 2020, **367**, 1196.
- [18] S. Roychowdhury, T. Ghosh, R. Arora, M. Samanta, L. Xie, N. K. Singh, A. Soni, J. He, U. V. Waghmare and K. Biswas, *Science*, 2021, **371**, 722.
- [19] B. Jiang, Y. Yu, J. Cui, X. Liu, L. Xie, J. Liao, Q. Zhang, Y. Huang, S. Ning, B. Jia, B. Zhu, S. Bai, L. Chen, S. J. Pennycook and J. He, *Science*, 2021, **371**, 830.
- [20] N. P. Padture, M. Gell and E. H. Jordan, *Science*, 2002, **296**, 280.
- [21] H. Ma, X. Wang, Y. Peng, H. Peng, M. Hu, L. Xiao, G. Wang, J. Lu and L. Zhuang, *ACS Energy Lett.*, 2019, **4**, 1810-1815.
- [22] L. Fu, M. Yin, D. Wu, W. Li, D. Feng, L. Huang and J. He, *Energy Environ. Sci.*, 2017, **10**, 2030-2040.
- [23] S. Roychowdhury, R. K. Biswas, M. Dutta, S. K. Pati and K. Biswas, *ACS Energy Lett.*, 2019, **4**, 1658-1662.
- [24] B. Poudel, Q. Hao, Y. Ma, Y. Lan, A. Minnich, B. Yu, X. Yan, D. Wang, A. Muto, D. Vashaee, X. Chen, J. Liu, M. S. Dresselhaus, G. Chen and Z. Ren, *Science*, 2008, **320**, 634.
- [25] K. Biswas, J. He, Q. Zhang, G. Wang, C. Uher, V. P. Dravid and M. G. Kanatzidis, *Nat. Chem.*, 2011, **3**, 160.
- [26] K. Biswas, J. He, I. D. Blum, C.-I. Wu, T. P. Hogan, D. N. Seidman, V. P. Dravid and M. G. Kanatzidis, *Nature*, 2012, **489**, 414.
- [27] M. Dutta, D. Sarkar and K. Biswas, *Chem. Commun.*, 2021, **57**, 4751-4767.
- [28] M. Dutta, K. Pal, U. V. Waghmare and K. Biswas, *Chem. Sci.*, 2019, **10**, 4905-4913.
- [29] M. Christensen, A. B. Abrahamsen, N. B. Christensen, F. Juranyi, N. H. Andersen, K. Lefmann, J. Andreasson, C. R. H. Bahl and B. B. Iversen, *Nat. Mater.*, 2008, **7**, 811-815.

- [30] D. J. Voneshen, K. Refson, E. Borissenko, M. Krisch, A. Bosak, A. Piovano, E. Cemal, M. Enderle, M. J. Gutmann, M. Hoesch, M. Roger, L. Gannon, A. T. Boothroyd, S. Uthayakumar, D. G. Porter and J. P. Goff, *Nat. Mater.*, 2013, **12**, 1028.
- [31] M. D. Nielsen, V. Ozolins and J. P. Heremans, *Energy Environ. Sci.*, 2013, **6**, 570-578.
- [32] Y. K. Lee, Z. Luo, S. P. Cho, M. G. Kanatzidis and I. Chung, *Joule*, 2019, **3**, 719-731.
- [33] C. Chang, M. Wu, D. He, Y. Pei, C.-F. Wu, X. Wu, H. Yu, F. Zhu, K. Wang, Y. Chen, L. Huang, J.-F. Li, J. He and L.-D. Zhao, *Science*, 2018, **360**, 778.
- [34] S. Chandra and K. Biswas, *J. Am. Chem. Soc.*, 2019, **141**, 6141-6145.
- [35] L.-D. Zhao, G. Tan, S. Hao, J. He, Y. Pei, H. Chi, H. Wang, S. Gong, H. Xu, V. P. Dravid, C. Uher, G. J. Snyder, C. Wolverton and M. G. Kanatzidis, *Science*, 2016, **351**, 141.
- [36] S. N. Guin, A. Chatterjee, D. S. Negi, R. Datta and K. Biswas, *Energy Environ. Sci.*, 2013, **6**, 2603-2608.
- [37] W. Gao, Z. Wang, J. Huang and Z. Liu, *ACS Appl. Mater. Interfaces*, 2018, **10**, 18685-18692.
- [38] Y. Zhou and L.-D. Zhao, *Adv. Mater.*, 2017, **29**, 1702676.
- [39] Y. Luo, S. Hao, S. Cai, T. J. Slade, Z. Z. Luo, V. P. Dravid, C. Wolverton, Q. Yan and M. G. Kanatzidis, *J. Am. Chem. Soc.*, 2020, **142**, 15187-15198.
- [40] D. P. Spitzer, *J. Phys. Chem. Solids*, 1970, **31**, 19-40.
- [41] A.-C. Dippel, H.-P. Liermann, J. T. Delitz, P. Walter, H. Schulte-Schrepping, O. H. Seeck and H. Franz, *J. Synchrotron Rad.*, 2015, **22**, 675-687.
- [42] T. Proffen, S. J. L. Billinge, T. Egami and D. Louca, *Z. Kristallogr. Cryst. Mater.*, 2003, **218**, 132.
- [43] M. Basham, J. Filik, M. T. Wharmby, P. C. Y. Chang, B. El Kassaby, M. Gerring, J. Aishima, K. Levik, B. C. A. Pulford, I. Sikharulidze, D. Sneddon, M. Webber, S. S. Dhesi, F. Maccherozzi, O. Svensson, S. Brockhauser, G. Naray and A. W. Ashton, *J. Synchrotron Rad.*, 2015, **22**, 853-858.

- [44] P. Juhas, T. Davis, C. L. Farrow and S. J. L. Billinge, *J. Appl. Crystallogr.*, 2013, **46**, 560-566.
- [45] C. L. Farrow, P. Juhas, J. W. Liu, D. Bryndin, E. S. Božin, J. Bloch, P. Th and S. J. L. Billinge, *J. Phys: Condens. Matter*, 2007, **19**, 335219.
- [46] G. Kresse and J. Furthmüller, *Comput. Mater. Sci.*, 1996, **6**, 15-50.
- [47] G. Kresse and J. Furthmüller, *Phys. Rev. B: Condens. Matter Mater. Phys.*, 1996, **54**, 11169.
- [48] J. P. Perdew, K. Burke and M. Ernzerhof, *Phys. Rev. Lett.*, 1996, **77**, 3865.
- [49] J. P. Perdew, A. Ruzsinszky, G. I. Csonka, O. A. Vydrov, G. E. Scuseria, L. A. Constantin, X. Zhou and K. Burke, *Phys. Rev. Lett.*, 2008, **100**, 136406.
- [50] P. E. Blöchl, *Phys. Rev. B*, 1994, **50**, 17953-17979.
- [51] G. Kresse and D. Joubert, *Phys. Rev. B*, 1999, **59**, 1758.
- [52] A. Van De Walle, M. Asta and G. Ceder, *Calphad*, 2002, **26**, 539-553.
- [53] A. Togo and I. Tanaka, *Scr. Mater.*, 2015, **108**, 1-5.
- [54] M. T. Agne, R. Hanus and G. J. Snyder, *Energy Environ. Sci.*, 2018, **11**, 609-616.
- [55] E. Rathore, R. Juneja, S. P. Culver, N. Minafra, A. K. Singh, W. G. Zeier and K. Biswas, *Chem. Mater.*, 2019, **31**, 2106-2113.
- [56] T. Egami and S. J. Billinge, *Underneath the Bragg peaks: structural analysis of complex materials*, Elsevier, 2003.
- [57] K. Pal, Y. Xia, J. He and C. Wolverton, *Chem. Mater.*, 2019, **31**, 8734-8741.
- [58] K. Pal, Y. Xia and C. Wolverton, *npj Comput. Mater.*, 2021, **7**, 5.
- [59] T. Lanigan-Atkins, X. He, M. J. Krogstad, D. M. Pajerowski, D. L. Abernathy, G. N. M. N. Xu, Z. Xu, D. Y. Chung, M. G. Kanatzidis, S. Rosenkranz, R. Osborn and O. Delaire, *Nat. Mater.*, 2021, **20**, 977-983.
- [60] D. T. Morelli, V. Jovovic and J. P. Heremans, *Phys. Rev. Lett.*, 2008, **101**, 035901.

Chapter 4.3



Tuning of *p-n-p*-Type Conduction in AgCuS through Cation Vacancy: Thermopower and Positron Annihilation Spectroscopy Investigations

Tuning of *p-n-p*-Type Conduction in AgCuS through Cation Vacancy: Thermopower and Positron Annihilation Spectroscopy Investigations[†]

Summary

*Understanding the complex phenomenon behind the structural transformations is a key requisite to developing important solid-state materials with better efficacy such as transistors, resistive switches, thermoelectrics, etc. AgCuS, a superionic semiconductor, exhibits temperature dependent *p-n-p*-type conduction switching and a colossal jump in thermopower during an orthorhombic to hexagonal superionic transition. Tuning of *p-n-p*-type conduction switching in superionic compounds is fundamentally important to realize the correlation between electronic/phonon dispersion modulation with changes in the crystal structure and bonding, which might contribute to the design of better thermoelectric materials. In this chapter, we have created extrinsic Ag/Cu non stoichiometry in AgCuS, which resulted in the vanishing of *p-n-p*-type conduction switching and improved its thermoelectric properties. We have performed the selective removal of cations and measured their temperature-dependent thermopower and Hall coefficient, which demonstrates only *p*-type conduction in the $\text{Ag}_{1-x}\text{CuS}$ and $\text{AgCu}_{1-x}\text{S}$ samples. The removal of Cu is much more efficient in arresting conduction switching, whereas in the case of Ag vacancy, *p-n-p*-type conduction switching vanishes at higher vacant concentrations. Positron annihilation spectroscopy measurements have been done to shed further light on the mechanisms behind this structural transition-dependent conduction switching. Cation (Ag^+/Cu^+) non stoichiometry in AgCuS significantly increases the vacancy concentration, hence, the *p*-type carriers, which is confirmed by positron annihilation spectroscopy and Hall measurement. The $\text{Ag}_{1-x}\text{CuS}$ and $\text{AgCu}_{1-x}\text{S}$ samples exhibit ultralow thermal conductivity ($\sim 0.3\text{--}0.5$ W/mK) in the 290–623 K temperature range because of the low-energy cationic sublattice vibration that arises as a result of the movement of loosely bound Ag/Cu within the stiff S sublattice.*

[†]M. Dutta, D. Sanyal and K. Biswas. *Inorg. Chem.*, 2018, **57**, 7481–7489.

4.3.1. Introduction

Structural phase transformations remain one of the most intrigued phenomena for the modern day inorganic and solid state chemistry, primarily because it acts as a podium for furnishing materials with a plethora of novel physical properties,¹ viz. superconductivity,² superionic conduction,³⁻⁶ the photoelectronic effect,^{7, 8} optical storage,⁹ giant magnetoresistance,¹⁰ *p-n* and *p-n-p* type conduction switching,^{3, 11-15} and thermoelectricity.^{6, 16-20} Apart from the changes in crystal structure, phase transformation also lead to changes in the orientation of electron clouds which in turn influences their spin states. These deformations result in evolving of the electronic structures and phonon dispersions. Among these novel attributes, temperature-dependent *p-n-p* type conduction switching is relatively unexplored and can potentially find its usage in temperature controlled diode and transistor devices, which can operate efficiently and reversibly near room temperatures.²¹

Silver and copper chalcogenides, chalcogenides, and halides have garnered interest over the past few years due to their tendency to exhibit mixed ionic and electronic conduction in the superionic phases.^{3, 4, 13, 22} These compounds are composed of cationic and anionic substructures which are weakly coupled. Structural transition of these compounds leads to a superionic phase at high temperatures which can primarily be attributed to the formation of a substructure of mobile cations. AgCuS belongs to these family, and shows several temperature dependent structural transitions.^{13, 23} Recently we have shown that AgCuS undergoes a *p-n-p* type conduction switching coupled with a colossal change of thermopower in the vicinity of orthorhombic to hexagonal structural transition.¹³ The switching of conduction type can be attributed to the change in electronic structure and the Ag vacancy concentration during the first superionic structural transition at ~ 360 K. Room temperature orthorhombic phase, β -AgCuS (*Cmc*2₁) is composed of distorted hexagonal close packing (hcp) of sulphur atoms (Figure 4.3.1).²³ The Cu atoms lie within the distorted hcp S layer and form three co-ordinated structure. Ag atoms form loosely bound face-centered-cubic (fcc) framework, alternating with those of CuS, which are bonded to two S atoms with near-linear geometry (Figure 4.3.1).²⁴ Hexagonal (α phase at 361 K) and cubic (δ phase at 439 K) are the high-temperature superionic phases with space groups *P*6₃/*mmc* and *Fm* $\bar{3}$ *m* respectively. AgCuS undergoes structural phase

transformations at 361 K ($\beta \rightarrow \alpha$) and further at 439 K ($\alpha \rightarrow \delta$). The high temperature hexagonal (α) phase composed of partially disordered Ag and Cu, with S atoms preserving the hcp sublattice (Figure 4.3.1).²⁴ The cubic (δ phase) phase is the other high-temperature structure where all the cations (Ag^+/Cu^+) are randomly distributed at tetrahedral and octahedral sites of the rigid S fcc sublattice (Figure 4.3.1).²⁴ In general, anion sublattice lattice is crystalline, while cation mobilizes with increase in temperature, akin to liquid-like disorder within the crystalline chalcogenide/chalcohalide framework, which leads to p - n and p - n - p type conduction switching and important thermoelectric properties in AgCuS , AgCuSe , $\text{Ag}_{10}\text{Te}_4\text{Br}_3$ and AgBiSe_2 .^{10, 12-14}

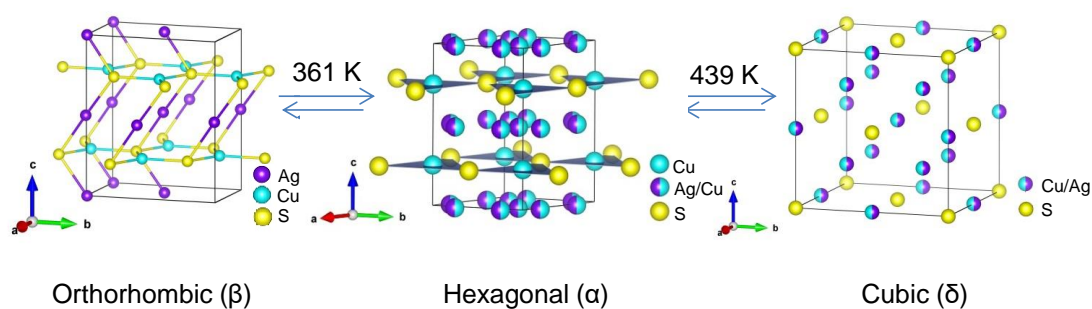


Figure 4.3.1. (a) Temperature-driven structural transformations for AgCuS . AgCuS undergoes phase transition from an ordered orthorhombic phase to a partially cation-disordered hexagonal phase to finally a fully cation-disordered cubic phase.

Tuning of p - n - p type conduction switching in superionic compounds is fundamentally important to realize the correlation between electronic/phonon dispersion modulation with the change in crystal structure and bonding, which might furnish designing better thermoelectric materials. Recently, tuning of p - n - p conduction switching in AgCuS has been performed by reducing the grain size to nanoscale, which opens up the band gap and increases the Ag vacancy concentration, thereby alters the conduction switching.²⁵ Interestingly, in AgBiSe_2 , the p - n - p conduction switching vanishes for its bulk counterpart.¹⁷ Crystallite size here plays a prominent role in conduction switching as it modifies the electronic structure. Tuning of conduction switching has also been seen in anion substituted $\text{Ag}_{10}\text{Te}_4\text{Br}_3$,²⁶ where the substitution influences the carrier transport and electronic structure, which lead to a shift in the phase transition temperature. p -type

conduction in β -AgCuS results due to intrinsic Ag vacancy, which provides an effective path for the Ag^+ ion migration during superionic phase transition.¹³ The presence of hybridized Cu-S orbitals in the intermediate semi-metallic electronic structure state contributes to n -type conduction, which is responsible for the p - n - p type conduction switching in AgCuS.¹³ Purposeful creation of non-stoichiometry or cation (Ag^+/Cu^+) vacancy may result in a change in p - n - p type conduction switching in AgCuS. The findings will not only help us to gain insight into the pertinent mechanism for the conduction switching but also show its usefulness in developing better thermoelectric materials.

Herein, we demonstrate an innovative way to tune p - n - p conduction in AgCuS, whilst trying to keep the grain size intact. Ag vacancy concentration and Cu-S hybridized states are pivotal for p - n - p conduction switching in AgCuS. Thus, we intentionally created extrinsic Ag and Cu vacancies in AgCuS in order to tune the conduction switching. In the case of Ag vacancies, the p - n - p conduction switching vanishes at $\text{Ag}_{0.85}\text{CuS}$ whereas, for Cu, p - n - p vanishes even at only 1 mol% Cu vacant samples. Nature of the vacancy and relative concentrations with increasing respective cation (Ag^+/Cu^+) non-stoichiometry in AgCuS has been analyzed by the positron annihilation lifetime and shape parameter (S). Increase in the positron annihilation lifetime and decrease in S parameter with the increase in Ag^+/Cu^+ vacancy concentration indicates the enhancement of p -type carrier in non-stoichiometric AgCuS, which was also further confirmed by the Hall measurement at room temperature. Change in thermopower (ΔS) during orthorhombic to hexagonal superionic transition decreases with increasing cation deficiency. Superionic phase transition temperature is independent of vacancy concentrations in AgCuS which is confirmed by differential scanning calorimetric (DSC) analysis. All the samples exhibit ultralow thermal conductivity ($\sim 0.3 - 0.5 \text{ W/mK}$) in the temperature region of 290 K – 623 K which is due to the dynamic movement of the cations within the rigid anion sublattice. The $\text{Ag}_{0.85}\text{CuS}$ exhibits a maximum thermoelectric figure of merit (zT) of ~ 0.15 which is significantly higher than that of pristine AgCuS.

4.3.2. Methods

Starting materials. Elemental Ag ($\geq 99.99\%$, Sigma Aldrich), Cu (99.999 %, Alfa Aesar) and S (99.999 %, Alfa Aesar) were used in stoichiometric amounts for the synthesis of the compounds. They were used as obtained and no further purification has been done.

Synthesis. Ingots ($\sim 7\text{g}$) of $\text{Ag}_{1-x}\text{CuS}$ ($x = 0.01, 0.1$ and 0.15) and $\text{AgCu}_{1-x}\text{S}$ ($x = 0.01, 0.02$ and 0.04) were prepared by taking stoichiometric amounts of Ag, Cu and S. They were transferred in quartz ampoules and subsequently flame-sealed under high vacuum ($\sim 10^{-5}$ Torr). These vacuum sealed ampoules were then heated slowly up to 773 K over 12 hours to minimize any sulfur evaporation, and then gradually heated to 1223 K in 5 hours followed by soaking for 24 hours and finally air-quenched to room temperature. Each ingot was subsequently cut and polished into a parallelepiped ($\sim 2 \times 3 \times 8 \text{ mm}^3$) and thin coin shaped (8 mm diameter and 2 mm thick) samples for performing electrical transport and thermal diffusivity measurements respectively.

Powder X-ray diffraction (XRD). The samples were finely ground using an agate mortar and were used for powder X-ray Diffraction. Powder-XRD was done under room temperature conditions using Cu $K\alpha$ radiation source ($\lambda = 1.5406 \text{ \AA}$) on a Bruker D8 diffractometer. Temperature dependent powder-XRD was carried out using Rigaku Smart-lab X-ray diffractometer, the radiation source being Cu $K\alpha$ ($\lambda = 1.5406 \text{ \AA}$). The temperature ramp rate during heating and cooling cycles were kept at 5 K/min with an additional 2 min for steadying the temperature. The scanning rate was kept at 1° per minute. Temperature dependent powder XRD was done with the help of Prof. R. Ranjan from IISc, Bangalore.

Seebeck coefficient and electrical conductivity. Seebeck coefficients and electrical conductivity of the samples were measured from room temperature to 550 K under helium atmosphere using ULVAC-RIKO ZEM-3 instrument.

Thermal conductivity. Thin coin shaped samples were used for thermal diffusivity, D measurements in Netzsch LFA 457 under N_2 atmosphere. The total thermal conductivity was then calculated using the equation $\kappa_{total} = DC_p\rho$, where ρ is the density of the measured samples. C_p is the heat capacity which is obtained using the reference pyroceram. All the samples have density greater than 96% of the theoretical density.

Hall measurement. Parallelepiped shaped samples were used for hall measurement. The measurement was carried out in an in-house set up developed by Excel Instruments, using a varying magnetic field of 0.0 - 0.57 T and a dc current of 50 mA. For high temperature measurements the ramp rate was kept at a steady 1 K/min, with a fluctuation limit of 1 K during the measurements.

Differential scanning calorimetry (DSC). Finely powdered samples were used for DSC measurements. The measurements were carried out on TA DSC Q2000 instrument with a heating rate of 5 K/min within the temperature range 290 K to 550 K.

Positron annihilation spectroscopy (PAS). Positron annihilation measurements have been carried out using a $^{22}NaCl$ source (strength $\sim 10 \mu Ci$) and sealed in a thick nickel foil (1.5 μm). The sealed source has been placed amidst two identical plane faced samples (8 mm diameter X 1 mm thick pellet) for both the positron annihilation lifetime (PAL) as well as Doppler broadening measurements. The PAL have been calculated with a conventional fast-fast coincidence assembly which comprises of two gamma-ray detectors (25 mm long and 25 mm tapered to 13 mm diameter BaF_2 scintillator, optically coupled with XP2020 Q photomultiplier tube) and two differential discriminators having constant fraction (Fast ComTech; model 7029A) which has time resolution (full width at half maximum) of ~ 220 ps measured by the prompt gamma ray of ^{60}Co source. Approximately ten million coincidence counts have been detected and recorded in a multichannel analyzer. The recorded lifetime spectrum has been examined using the computer code PATFIT-88 with proper source corrections. Doppler broadening of positron annihilation radiation (DBPAR) experiment has been carried out at room temperature by a single HPGe detector (*Efficiency*: 12 %; *Type*: PGC 1216 sp of DSG,

Germany) which have an energy resolution of 1.15 keV at 514 keV of ^{85}Sr . The DBPAR spectra have been recorded in a dual ADC based multi-parameter data acquisition system (MPA-3 of FAST ComTec, Germany). The Doppler broadening of annihilation at 511 keV γ -ray spectrum has been examined by evaluating the line-shape parameters (S -parameter).^{27, 28} The S -parameter is defined as the ratio of counts in the central area under the photo peak ($|511 \text{ keV} - E_\gamma| \leq 0.85 \text{ keV}$) to the whole area under the photo peak ($|511 \text{ keV} - E_\gamma| \leq 4.25 \text{ keV}$). The S -parameter mainly tells us about the fraction of positrons that are being annihilated by the lower momentum electrons with reference to the total electrons annihilated. The contribution of the S -parameter is crucial because of the occurrence of open volume defects where the positrons get annihilated. The PAS measurements were done in collaboration with Dr. Dirtha Sanyal of VECC, Kolkata.

4.3.3. Results and Discussion

Non-stoichiometric $\text{Ag}_{1-x}\text{CuS}$ ($x = 0.01, 0.1$ and 0.15) and $\text{AgCu}_{1-x}\text{S}$ ($x = 0.01, 0.02$ and 0.04) were synthesized by vacuum sealed tube melting reaction of Ag, Cu and S. Figure 4.3.2a and b, show the powder X-ray diffraction pattern of $\text{Ag}_{1-x}\text{CuS}$ ($x = 0.01, 0.10$ and 0.15) and $\text{AgCu}_{1-x}\text{S}$ ($x = 0.01, 0.02$ and 0.03) samples respectively. The samples were found to procure orthorhombic β - AgCuS structure ($\text{Cmc}2_1$) in low concentration of Ag/Cu vacancy. When the Ag/Cu vacancy concentration is increased significantly, we observe minute second phase of Cu_2S ($\text{P}4_32_12$, marked in asterisk, Figure 4.3.2a and b) along with β - AgCuS . It has been observed that for both the cation (Ag^+/Cu^+) deficient samples, interestingly Cu_2S gets isolated as the minor second phase, where the common perception is that in case of $\text{AgCu}_{1-x}\text{S}$, Ag_2S or elemental Ag should contribute to any second phase.

Further, temperature dependent structural transition in non-stoichiometric $\text{Ag}_{1-x}\text{CuS}$ ($x = 0.01, 0.15$) and $\text{AgCu}_{1-x}\text{S}$ ($x = 0.01, 0.02$) has been studied via DSC measurement (Figure 4.3.3a and b). The heating curve of DSC shows a strong peak around 369 K which corresponds to the first high temperature orthorhombic to hexagonal ($\beta \rightarrow \alpha$) phase transition. The peak around 404 K could be attributed to the low-temperature boundary region for the second high-temperature hexagonal to cubic ($\alpha \rightarrow \delta$) phase transition.²³ Although on hindsight $\alpha \rightarrow \delta$ transition shows no peak in the Ag

deficient $\text{Ag}_{1-x}\text{CuS}$, zoomed in version of $\text{Ag}_{0.99}\text{CuS}$ and $\text{Ag}_{0.85}\text{CuS}$ DSC Data around 404 K suggests that there is a presence of the $\alpha \rightarrow \delta$ transition peak (Figure 4.3.3a, inset). The DSC data further provides information that there is no shift in the transition temperature with varying vacancy concentration. This finding is of fundamental interest as it shows, unlike $\text{Ag}_{10}\text{Te}_4\text{Br}_3$ where the transition temperature shift with anion substitution,²⁶ here the transition is immune to vacancies. The presence of a peak at 369 K depicts that the phase transition does take place in all the samples, but with an increase of Ag vacancy in $\text{Ag}_{1-x}\text{CuS}$ which imparts p -type conduction, the formation of semi-metallic states are not enough for the change in conduction switching. In case of $\text{AgCu}_{1-x}\text{S}$ samples, although the ($\beta \rightarrow \alpha$) transition takes place at around 369 K as shown in the DSC plot, the absence of Cu-S hybridized bonds becomes a contributing factor for the tuning of p - n - p conduction switching. The cooling data shows a peak around 440 K for $\text{Ag}_{1-x}\text{CuS}$ and 425 K for $\text{AgCu}_{1-x}\text{S}$ samples. These peaks can be attributed to the ($\alpha \rightarrow \delta$) phase transition. The peak around 380 K is two-phase boundary region of the ($\alpha \rightarrow \delta$) transition. The region in between the aforementioned two peaks (425 K and 380 K) in the cooling cycle contains both hexagonal (α) and cubic (δ) forms.

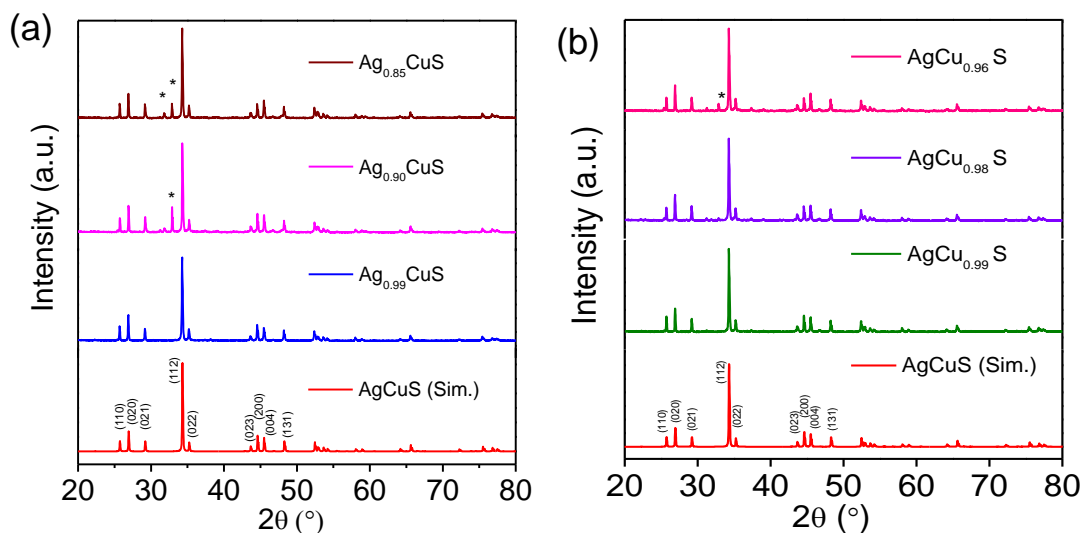


Figure 4.3.2. (b and c) Powder XRD patterns for the different Ag and Cu-deficient AgCuS , respectively. Extra peak(s) (marked by asterisks) at higher deficiencies is (are) due to the presence of Cu_2S .

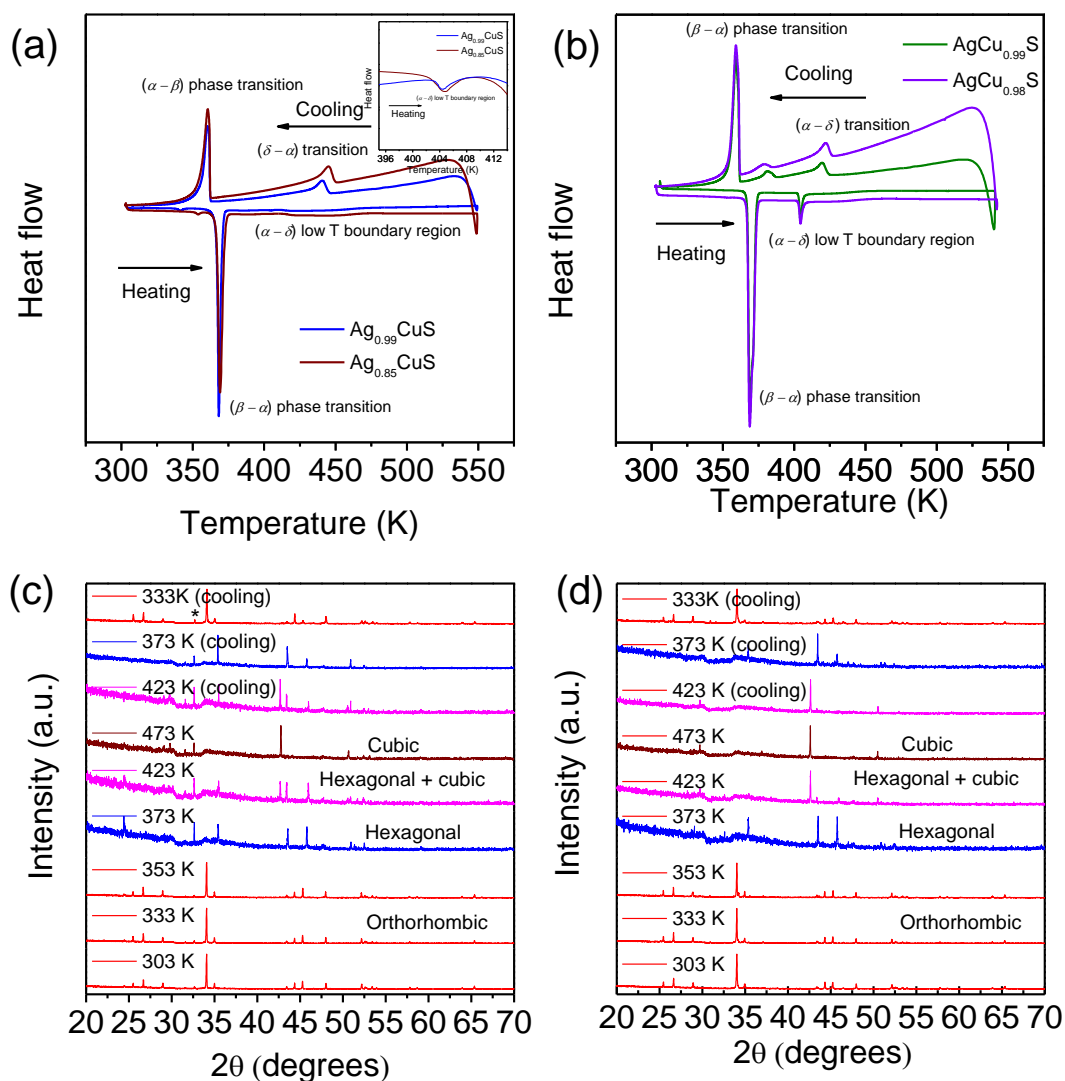


Figure 4.3.3. DSC curves for (a) $\text{Ag}_{1-x}\text{CuS}$ ($x = 0.01$ and 0.15) and (b) $\text{AgCu}_{1-x}\text{S}$ ($x = 0.01$ and 0.02). There is no apparent shift in the phase transition temperature in any of the vacant samples. The inset of part a contains zoomed-in versions of hexagonal to cubic phase transitions around 404 K. Temperature-dependent heating and cooling powder XRD data for (c) $\text{Ag}_{0.85}\text{CuS}$ and (d) $\text{AgCu}_{0.98}\text{S}$. Both samples show reversible phase transitions. The peak marked with an asterisk (*) in part a is due to the presence of a Cu_2S second phase.

To further corroborate the DSC findings, the temperature dependent powder-XRD has also been carried out to provide conclusive evidence of the phase transition taking place in the cation vacant samples. We have performed temperature dependent powder-XRD for two samples *i.e.*, $\text{Ag}_{0.85}\text{CuS}$ and $\text{AgCu}_{0.98}\text{S}$ (Figure 4.3.3c and d). The presence

of different phases with changes in temperature provides us conclusive proof of the phase transformations in these cation vacant samples. For both the samples we have observed temperature dependent phase transitions from orthorhombic (room temperature) to hexagonal (~370 K) to a mixture of hexagonal and cubic (~423 K) to finally fully cubic phase. The heating and cooling cycles prove that the phase transitions in cation (Ag^+/Cu^+) vacant AgCuS samples are reversible in nature, which complements our DSC results. For the silver vacant sample (i.e., $\text{Ag}_{0.85}\text{CuS}$), we observe that the presence of minor second Cu_2S phase which do not undergo any noticeable phase transition within the measured temperature range.

Table 4.3.1. Room temperature Carrier Concentrations for the Different Cation (Ag^+ and Cu^+) Vacant Compounds.

Sample	Carrier concentration (cm^{-3})
AgCuS	1.3×10^{15}
$\text{Ag}_{0.99}\text{CuS}$	1.09×10^{16}
$\text{Ag}_{0.90}\text{CuS}$	1.27×10^{17}
$\text{Ag}_{0.85}\text{CuS}$	1.02×10^{17}
$\text{AgCu}_{0.99}\text{S}$	7.11×10^{15}
$\text{AgCu}_{0.98}\text{S}$	9.26×10^{15}
$\text{AgCu}_{0.96}\text{S}$	5.37×10^{15}

The p -type conduction in the orthorhombic phase is due to the intrinsic Ag vacancies which act as an effective route for the hopping of the Ag^+ ions to these inherent vacant positions.¹³ Here, we have extrinsically created Ag vacancies by using stoichiometric amounts of Ag, Cu and S in the appropriate ratio to form compounds with the nominal composition of $\text{Ag}_{1-x}\text{CuS}$ ($x = 0.01, 0.10$ and 0.15). The motive behind this was to create more vacancies for the Ag^+ ions to migrate, which may tune the conduction switching property in AgCuS. As it has already been understated that Ag vacancies are

responsible for the p -type conduction in β -AgCuS at room temperature, thus creating more such vacancies will lead to predominantly p -type conduction throughout the temperature range. We have measured the carrier type and concentrations of $\text{Ag}_{1-x}\text{CuS}$ samples by Hall coefficient measurement at room temperature (Table 4.3.1). Pristine AgCuS exhibits p -type carrier concentration of $1.3 \times 10^{15} \text{ cm}^{-3}$, which significantly increases to $1.27 \times 10^{17} \text{ cm}^{-3}$ in $\text{Ag}_{0.9}\text{CuS}$.

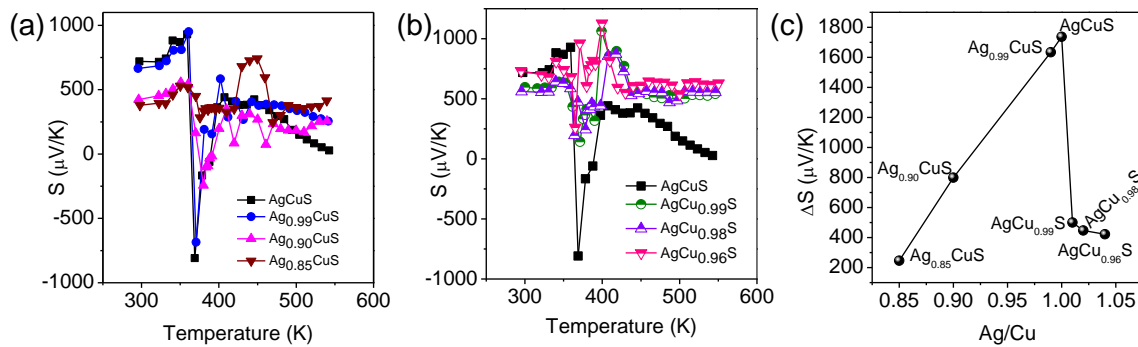


Figure 4.3.4. Temperature-dependent Seebeck coefficient values for (a) $\text{Ag}_{1-x}\text{CuS}$ (where $x = 0, 0.01, 0.10, \text{ and } 0.15$). The p - n - p -type conduction switching is tuned and eliminated at $x = 0.15$. Temperature-dependent Seebeck coefficient values for (b) $\text{AgCu}_{1-x}\text{S}$ (where $x = 0, 0.01, 0.02, \text{ and } 0.04$). Here the p - n - p -type conduction switching vanished at low deficiencies only. (c) Change in the thermopower (ΔS) versus vacancy concentration. ΔS decreases with increasing vacancy.

Figure 4.3.4a shows the temperature dependent thermopower (S) for the $\text{Ag}_{1-x}\text{CuS}$ samples. The room temperature Seebeck coefficient value decreases from $719 \mu\text{V/K}$ in pristine AgCuS, to $378 \mu\text{V/K}$ for $\text{Ag}_{0.85}\text{CuS}$ (Figure 4.3.4a). Such decrease in thermopower with the increase in the Ag vacancy concentration in $\text{Ag}_{1-x}\text{CuS}$, can be attributed to the increase in the p -type carrier concentrations (Table 4.3.1). With an initial increase in temperature, thermopower increases gradually followed by a sudden colossal jump ($\Delta S = 1737 \mu\text{V/K}$) accompanying with it the change in conduction type from p - to n -during orthorhombic to hexagonal superionic transition ($\sim 367 \text{ K}$) in pristine AgCuS. Further increase in the temperature, the thermopower reverts back to p -type and stays p -type throughout afterwards. With the gradual increment in Ag vacancy, the change in thermopower (ΔS) during the superionic phase transition decreases (Figure 4.3.4c). This decrease in the change of ΔS value can be attributed to the increase in p -type carrier

(Table 4.3.1) which nullifies some of the effective n -type carriers during the phase transition. For the $\text{Ag}_{0.85}\text{CuS}$ sample, the absence of such p - n - p type conduction switching is observed and the compound remains predominantly p -type throughout the measured temperature. Although there is a slight drop in the thermopower at the vicinity of the orthorhombic (β) to hexagonal (α) phase transition, the drop is not sufficient enough to cause a change in the conduction type. The hump around 450 K in the thermopower value for $\text{Ag}_{0.85}\text{CuS}$ is most likely due to the pronounced effect of hexagonal (α) to (hexagonal (α) + cubic (δ)) to finally fully cubic (δ) phase transition, which is present in other samples too but the hump is not as prominent as that of $\text{Ag}_{0.85}\text{CuS}$, which is not clear at this moment. Thus, we were able to tune the p - n - p type conduction switching in AgCuS to fully p -type conduction via non-stoichiometric $\text{Ag}_{1-x}\text{CuS}$.

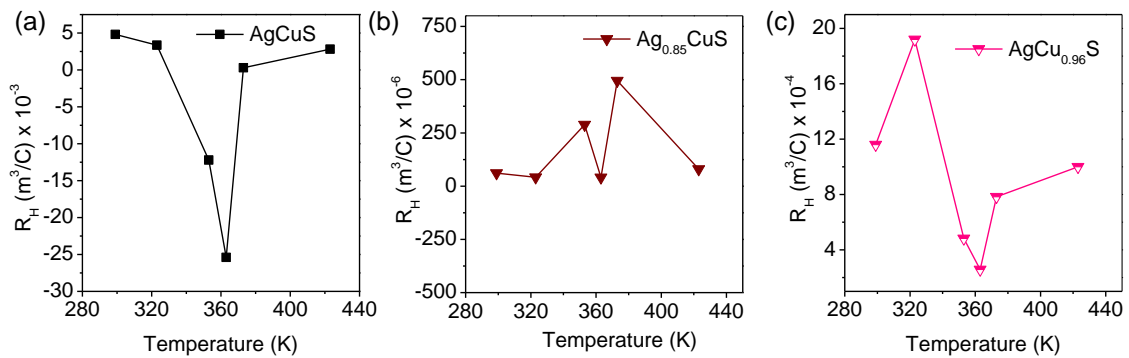


Figure 4.3.5. Temperature dependent Hall coefficient (R_H) data for (a) Pristine AgCuS , (b) $\text{Ag}_{0.85}\text{CuS}$ and, (c) $\text{AgCu}_{0.96}\text{S}$. Pristine AgCuS undergoes change in conduction from p -type to n -type and then back to p -type, whereas (b) and (c) do not undergo change in conduction.

We have conducted temperature dependent Hall measurements for both the pristine AgCuS and $\text{Ag}_{0.85}\text{CuS}$ sample (Figure 4.3.5 a, b). We have seen a similar trend in sign of Hall coefficient (R_H) which gives the indication regarding the nature of conduction in a material. In case of pristine AgCuS , the R_H is initially positive (p -type conduction), then changes to negative (n -type) during the $\beta \rightarrow \alpha$ phase transition and revert back to positive value (p -type). In the case of cation vacant $\text{Ag}_{0.85}\text{CuS}$, the R_H remains positive (p -type) within the measurement range indicating that $\text{Ag}_{0.85}\text{CuS}$ is a fully p -type

conductor which supports the temperature dependent Seebeck coefficient data. The temperature dependent carrier concentration data is given in Table 4.3.2 and Table 4.3.3.

Table 4.3.2. Temperature dependent carrier concentration for pristine AgCuS. Carrier type *p* denotes hole conduction, whereas *n* denotes electron conduction.

Temperature (K)	Carrier concentration (cm ⁻³)	Carrier type
299	1.3 x 10 ¹⁵	<i>p</i>
323	1.86 x 10 ¹⁵	<i>p</i>
353	5.13 x 10 ¹⁴	<i>n</i>
363	2.46 x 10 ¹⁴	<i>n</i>
373	2.16 x 10 ¹⁶	<i>p</i>
423	2.22 x 10 ¹⁵	<i>p</i>

Table 4.3.3. Temperature dependent carrier concentration for Ag_{0.85}CuS

Temperature (K)	Carrier concentration (cm ⁻³)	Carrier type
299	1.02 x 10 ¹⁷	<i>p</i>
323	1.5 x 10 ¹⁷	<i>p</i>
353	2.16 x 10 ¹⁶	<i>p</i>
363	1.54 x 10 ¹⁷	<i>p</i>
373	1.26 x 10 ¹⁶	<i>p</i>
423	7.82 x 10 ¹⁶	<i>p</i>

Hybridized Cu-S orbitals in AgCuS forms the semi-metallic intermediate electronic state during orthorhombic (β) to hexagonal (α), which provides *n*-type conduction at ~ 365 K.¹³ To understand the role of Cu vacancy, we extrinsically created Cu vacant samples by using stoichiometric amounts of Ag, Cu and S in the appropriate

ratio to form compounds with the nominal composition $\text{AgCu}_{1-x}\text{S}$ ($x = 0.01, 0.02$ and 0.04). Interestingly, Cu non-stoichiometry does not increase much the p -type carrier concentration in $\text{AgCu}_{1-x}\text{S}$ compared to that of Ag vacant samples (Table 4.3.1). For example, the p -type carrier concentration of $5.37 \times 10^{15} \text{ cm}^{-3}$ was obtained in $\text{AgCu}_{0.96}\text{S}$, which is much lower as compared to that of $\text{Ag}_{1-x}\text{CuS}$.

Figure 4.3.4b shows the temperature dependent thermopower (S) for the $\text{AgCu}_{1-x}\text{S}$ samples. Unlike the Ag vacant samples, where the tuning of the conduction switching was possible to attain only at higher vacancy (e.g., $\text{Ag}_{0.85}\text{CuS}$), here we observed complete loss of p - n - p type conduction switching at lower Cu vacancies i.e., in $\text{AgCu}_{0.99}\text{S}$. This can be attributed to the fact that the hybridized Cu-S states are the prime factor for the formation of n -type semi-metallic state electronic during the ($\beta \rightarrow \alpha$) phase transition, which can be perturbed by creating a small amount of Cu vacancy. Moreover, partial density of states in electronic structure clearly showed that the Cu 3d orbital resides near the Fermi level during the p - n conduction switching,¹³ making the contribution from Cu towards the conduction switching is much more prevalent than its Ag counterpart in $\text{Ag}_{1-x}\text{CuS}$. Since the Cu 3d orbitals reside so close to the Fermi level, that a little perturbation in them might hinder the overlapping of the valence and conduction bands during the phase transition, which actually makes $\text{AgCu}_{1-x}\text{S}$ a fully p -type semiconductor. Typically, $\text{AgCu}_{0.96}\text{S}$ exhibits S value of $733 \mu\text{V/K}$ at room temperatures remains p -type throughout and have a S value of $630 \mu\text{V/K}$ at 550 K . Here the change is thermopower with increasing vacancy is much more gradual. The ΔS value for $\text{AgCu}_{0.99}\text{S}$ is $500 \mu\text{V/K}$, which decreases gradually to $422 \mu\text{V/K}$ for $\text{AgCu}_{0.96}\text{S}$ (Figure 4.3.4c). Temperature dependent Hall coefficient data of $\text{AgCu}_{0.96}\text{S}$ is also consistent with the observed Seebeck coefficient, which confirms that $\text{AgCu}_{0.96}\text{S}$ is indeed a fully p -type semiconductor (Figure 4.3.5c). The temperature dependent carrier concentration data is given in Table 4.3.4.

Although the presence of minor second phase of Cu_2S in the non-stoichiometric AgCuS could contribute to the tuning of p - n - p transition as significant amount of it is present in high cation (Ag^+/Cu^+) vacant samples, it is to be noted that in $\text{AgCu}_{0.90}\text{S}$, the presence of Cu_2S do not inhibit the change in conduction type. In case of $\text{AgCu}_{0.99}\text{S}$, p - n - p conduction switching vanishes although there is no such Cu_2S phase is observed. Thus,

the presence of Cu_2S might not play a profound role in the tuning of the p - n - p type conduction switching.

Table 4.3.4. Temperature dependent carrier concentration for $\text{AgCu}_{0.96}\text{S}$

Temperature (K)	Carrier concentration (cm^{-3})	Carrier type
299	5.37×10^{15}	p
323	3.26×10^{15}	p
353	1.3×10^{16}	p
363	2.43×10^{16}	p
373	7.98×10^{15}	p
423	6.23×10^{15}	p

$\text{Ag}_{1-x}\text{CuS}$ ($x = 0.01, 0.10$ and 0.15) and $\text{AgCu}_{1-x}\text{S}$ ($x = 0.01, 0.02$ and 0.04) samples exhibit ultralow thermal conductivity (κ_{tot}) of $0.3 - 0.5$ W/mK in the $290 \text{ K} - 623 \text{ K}$ range, which is slightly lower than that of pristine AgCuS (Figure 4.3.6a and b). The total thermal conductivity is given as a summation of both electrical and lattice thermal conductivity ($\kappa_{\text{tot}} = \kappa_{\text{lat}} + L\sigma T$, where L is the Lorenz number). Since the electrical conductivity (σ) of the samples are very low, the total conductivity is effectively comprised of lattice thermal conductivity (κ_{lat}). A rational explanation for such a low thermal conductivity is probably due to the effective phonon scattering by the mobile cations which shows dynamic disorder inside the rigid sulphur sub-lattice. With the increase of vacancy the relative ease of hopping increases which might be the possible reason for having lower thermal conductivity than that of pristine AgCuS . Also, the previous first principle calculations on AgCuS provides us with phonon dispersion plot which reveals a distinct separation of the two energy modes.¹³ The low lying phonon-modes are primarily constituted of the loosely bound cations. This low lying acoustic phonon modes is indicative of the softness of AgCuS and hence the low thermal conductive nature. Since the electronic transport is governed predominantly by the rigid

sulfur sublattice and the low thermal conductivity is due to loosely bound cation sublattice, an effective decoupling has been observed between the electrical and phonon transports in AgCuS, which is essential for thermoelectrics. With the increase in vacancy, the electrical conductivity too increases, due to the apparent increase in *p*-type carrier concentration (Table 4.3.1), which results in a thermoelectric figure of merit (*zT*) of ~ 0.15 at 445 K for the Ag_{0.85}CuS sample. For the AgCu_{0.96}S sample, a *zT* of ~ 0.12 is achieved at 400 K. The *zT* of ~ 0.15 in Ag_{0.85}CuS and ~ 0.12 in AgCu_{0.96}S is observed which is due to the low κ_{lat} and increase in carrier concentration of the samples.

Positron annihilation spectroscopy (PAS) has been a cornerstone in recent history for characterizing and identifying the chemical nature of the defects in different solids.^{12, 13, 27-30} The positron annihilation lifetime (PAL) and Doppler broadening (DB) measurements of the Ag_{1-x}CuS and AgCu_{1-x}S samples are the two principal techniques; one probe the electron density distribution whilst the other probes the electron momentum distribution in the studied material. Structural phase transitions in different sulfide samples using these two positron annihilation techniques have been studied successfully.^{13, 25}

We have characterized all the as synthesized samples (Ag_{0.85}CuS, Ag_{0.90}CuS, Ag_{0.99}CuS, AgCu_{0.99}S, AgCu_{0.98}S and AgCu_{0.96}S) by positron lifetime spectroscopy and Doppler broadening of positron annihilation radiation spectroscopy. The entire lifetime spectrum has been analyzed by PATFIT 88 program with proper source correction. The best fit of the spectrum (variance of fit < 1 per channel) is with three lifetime components fitting, having a long lifetime of 1.3 ns with 4 % intensity. This lifetime component is due to the formation of positronium at the surfaces or at the void spaces inside the sample. Figure 4.3.7a represents the positron annihilation lifetime spectrum for Ag_{0.99}CuS and AgCu_{0.96}S samples. The shortest lifetime component (τ_1) of about 156 ps, is attributed to the free annihilation of the positron. The intermediate lifetime component (τ_2) is due to the positron annihilation at defect sites. In the present studies, the intermediate lifetime (τ_2) component is in the range of 321 ± 5 to 347 ± 5 ps with the relative intensity of 43 to 53 %.

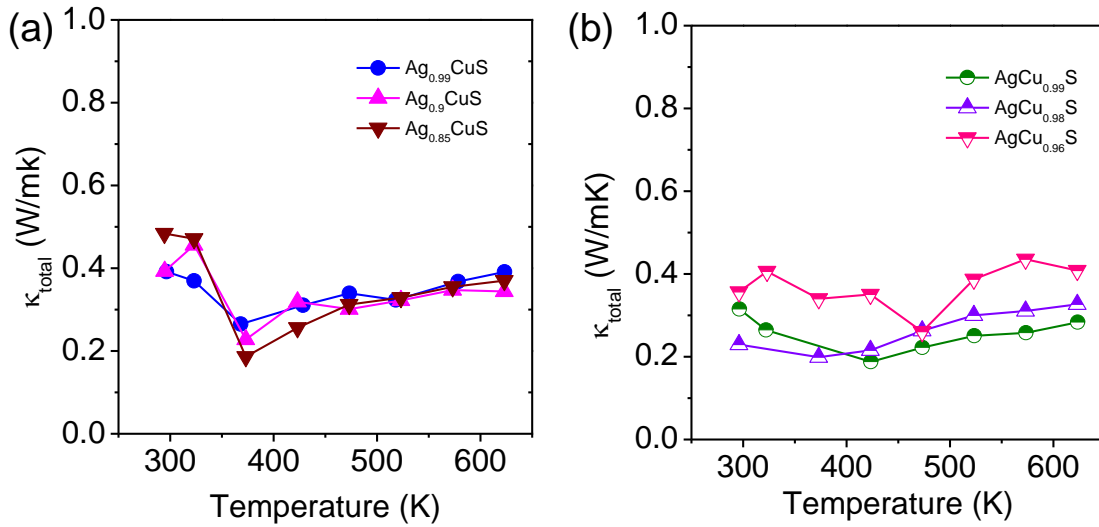


Figure 4.3.6. Temperature-dependent total thermal conductivity plots for (a) Ag-deficient $Ag_{1-x}CuS$ samples and (b) Cu-deficient $AgCu_{1-x}S$ samples. Temperature dependent (c) electrical conductivity (σ) and (d) thermoelectric figure of merit (zT) for $Ag_{0.85}CuS$ and $AgCu_{0.96}S$ samples.

Figure 4.3.7b represents the variation of τ_2 with the stoichiometric ratio of Ag and Cu (*i.e.*, Ag/Cu) in $AgCuS$ sample. It has already been observed earlier that for a high-quality crystalline ingot of $AgCuS$, the value of τ_2 is about 272 ps, and had been identified as Ag vacancy.¹³ It is interesting that τ_2 is minimum around Ag/Cu ~ 1 . Upon decreasing the Ag/Cu ratio to values less than unity, τ_2 , there is a gradual increase from 343 ps for $Ag_{0.99}CuS$ to 346 ps for $Ag_{0.90}CuS$ and then slightly decreases to 339 ps for $Ag_{0.85}CuS$, while the increment of τ_2 is relatively faster in case of Cu vacant samples (320 ps for $AgCu_{0.99}S$ to 339 ps for $AgCu_{0.96}S$). The increase of τ_2 suggests the agglomeration of cation defects at a particular defect site and hence increases of positron lifetime value, which indicates towards an increase in cation vacancy in $Ag_{1-x}CuS$ and $AgCu_{1-x}S$ samples. The intensity of the intermediate positron lifetime (I_2), is directly proportional to the defect concentration, is also plotted for all the samples (inset of Figure 4.3.7b). This also suggests that the cation defect concentration is more when the stoichiometry is changed in either way. Average positron lifetime and the bulk positron lifetime were further calculated using the formula $\langle\tau\rangle = (\tau_1 \times I_1 + \tau_2 \times I_2)/(I_1 + I_2)$ and $\tau_B = (I_1/\tau_1 + I_2/\tau_2)^{-1} \times (I_1 + I_2)$ respectively and plotted against the stoichiometry as Figure 4.3.7c. The nature of both the graphs is similar and as typical, the value of τ_B is more than $\langle\tau\rangle$, indicating

the presence of a vacancy defect in the sample, which increases with increasing the non-stoichiometry in AgCuS that has a significant impact on the vanishing p - n - p conduction switching in $\text{Ag}_{1-x}\text{CuS}$ and $\text{AgCu}_{1-x}\text{S}$ samples.

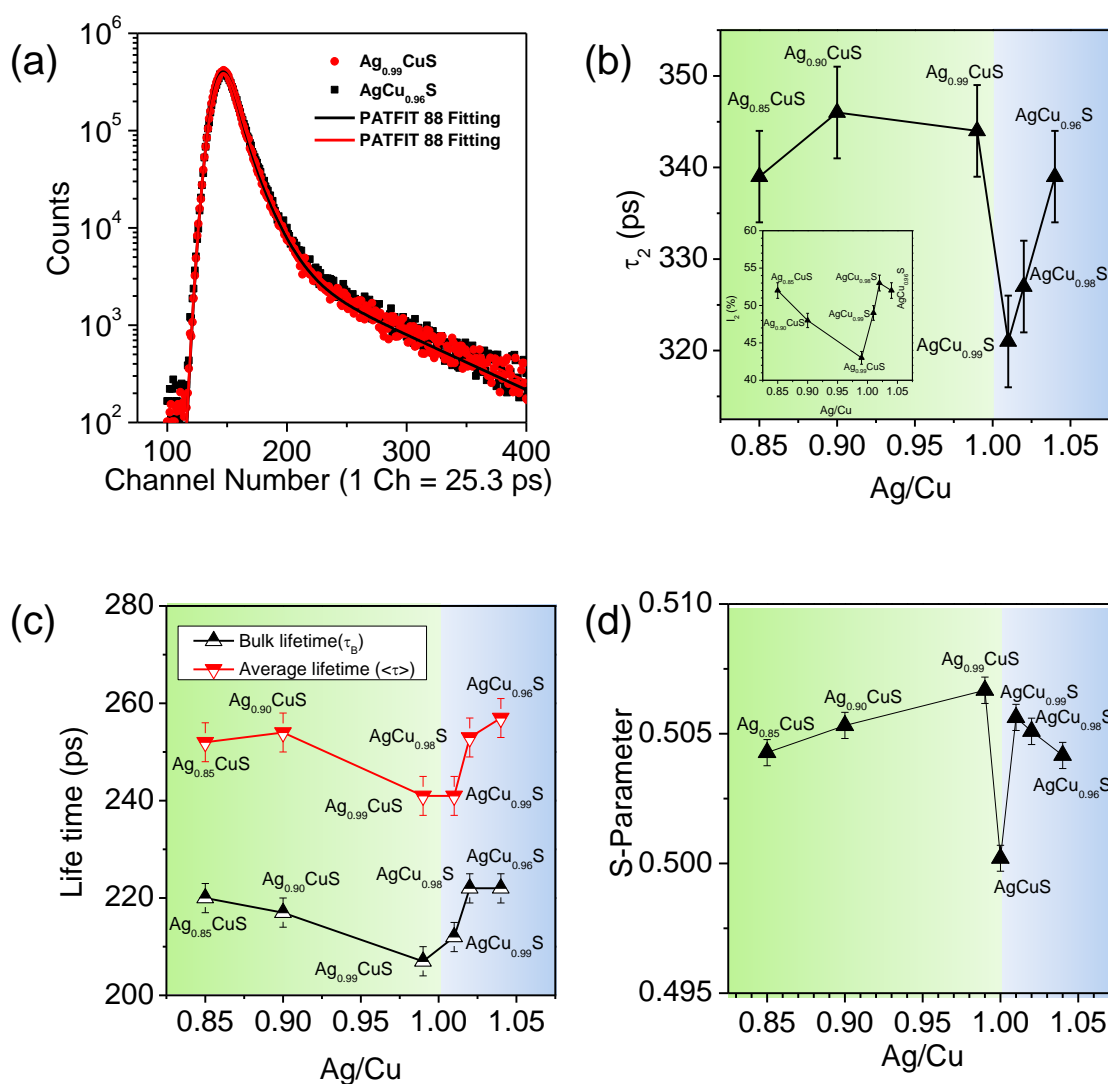


Figure 4.3.7. (a) PAL spectrum for $\text{Ag}_{0.99}\text{CuS}$ (red dots) and $\text{AgCu}_{0.96}\text{S}$ (black dots). The red and black fitting lines are used to obtain different lifetime components for the two samples, respectively. Vacancy-dependent (b) τ_2 values due to the formation of positronium at larger voids. (inset) Plot of I_2 (%) with respect to the cation (Ag^+/Cu^+) vacancies. Vacancy-dependent (c) average lifetime ($\langle\tau\rangle$), and bulk lifetime (τ_B). (d) Variation of the DBPAR line-shape parameter (S parameter in PAS) with the stoichiometric ratio of Ag and Cu (Ag/Cu) in AgCuS.

Doppler broadening of positron annihilation radiation (DBPAR) line shape parameter, S-parameter (defined in experimental section), provides us a quantitative idea about the number of positrons being annihilated with the lower momentum valence electrons. Figure 4.3.7d shows the variation of S parameter of the different samples plotted against their stoichiometry. With the corresponding increase of vacancies (due to the change of stoichiometry, i.e., $\text{Ag}_{1-x}\text{CuS}$ or $\text{AgCu}_{1-x}\text{S}$) the S-parameter value increases drastically compared to that of the pristine AgCuS and then it varies only slightly with increase in vacancy concentration in nonstoichiometric samples. The initial drastic increase in S-parameter in nonstoichiometric sample is due to the formation of vacancies, which is expected.²⁷ The consequent slight change in S-parameter in cation vacant samples can be ascribed to saturation trapping of positrons which can be activated with even a few atomic percent of vacancies. The lifetime (τ_2) of the cation (Ag/Cu) vacant samples is in the range of 320 to 345 ps, which can mainly be attributed to the formation of vacancy clusters, unlike the lifetime of pristine AgCuS (~ 272 ps), which is mainly due to the innate Ag vacancies. The $I_2\%$ plot against cation (Ag^+/Cu^+) vacancies (inset of Figure 4.3.7b) shows the increase in cation defect concentration with increase in vacancy. The slight decrease in S-parameter for nonstoichiometric samples can thus be a combination of certain factors along with cation vacancy like formation of vacancy clusters, saturation trapping and diffusion of positrons to grain boundaries.

4.3.4. Conclusion

Cation (Ag and Cu) vacancies in AgCuS tune the temperature dependent *p-n-p* type conduction switching and the samples remain *p*-type, which indeed improve the thermoelectric performance. Cu non-stoichiometry proved to be more detrimental to the *p-n-p* conduction switching than Ag vacancies. Cu non-stoichiometry disrupts the hybridized Cu-S orbitals which are pivotal for the formation of intermediate *n*-type semi-metallic state and subsequent electronic band overlap, which is the key for the *p-n-p* conduction switching in AgCuS. Thus, the vacancy induced disappearance of *p-n-p* conduction switching can be due to a combination of a couple of contributing factors: (a) Excess Ag vacancies impart *p*-type conduction to the material, and (b) perturbation of

Cu-S *n*-type semi-metallic state by formation of Cu non-stoichiometry, which enables the compounds to remain *p*-type throughout the measured temperature range. Ag⁺/Cu⁺ vacancy increases the *p*-type carrier concentration, which provides a boost to the electrical transport. Further, Ag_{1-x}CuS and AgCu_{1-x}S samples demonstrate ultralow thermal conductivity due low energy soft phonons arises from hopping of cations within the rigid anion sublattice.

4.3.5. References

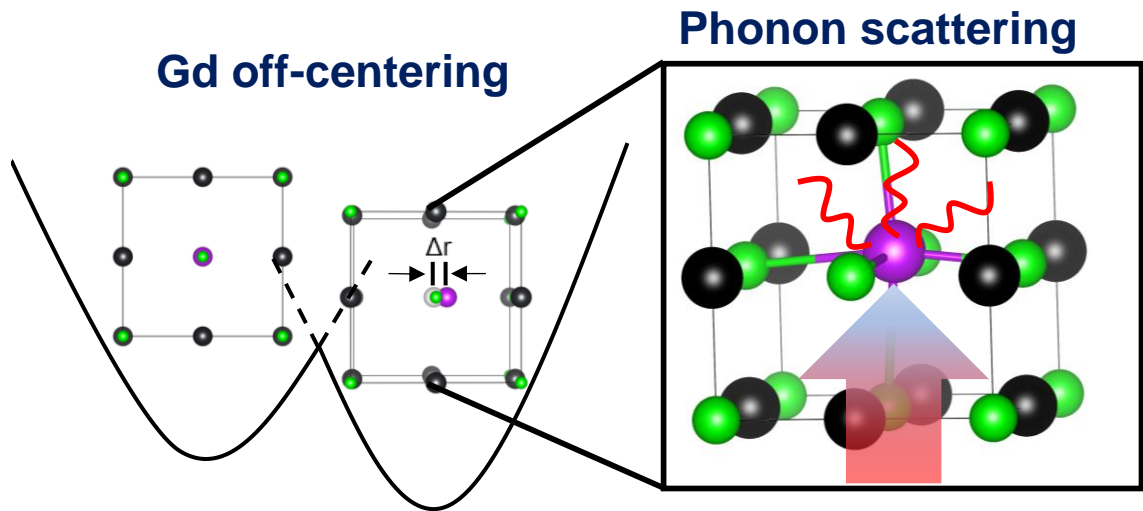
- [1] C. N. R. Rao, *Acc. Chem. Res.*, 1984, **17**, 83-89.
- [2] E. Coronado, C. Martí-Gastaldo, E. Navarro-Moratalla, A. Ribera, S. J. Blundell and P. J. Baker, *Nat. Chem.*, 2010, **2**, 1031-1036.
- [3] S. N. Guin and K. Biswas, *Phys. Chem. Chem. Phys.*, 2015, **17**, 10316-10325.
- [4] D. A. Keen, *J. Phys.: Condens. Matter*, 2002, **14**, R819-R857.
- [5] A. A. Olvera, N. A. Moroz, P. Sahoo, P. Ren, T. P. Bailey, A. A. Page, C. Uher and P. F. P. Poudeu, *Energy Environ. Sci.*, 2017, **10**, 1668-1676.
- [6] H. Liu, X. Shi, F. Xu, L. Zhang, W. Zhang, L. Chen, Q. Li, C. Uher, T. Day and G. J. Snyder, *Nat. Mater.*, 2012, **11**, 422.
- [7] Q. Zhang, Y. Liu, X. Bu, T. Wu and P. Feng, *Angew. Chem. Int. Ed.*, 2008, **47**, 113-116.
- [8] Y. Liu, Q. Lin, Q. Zhang, X. Bu and P. Feng, *Chem. Eur. J.*, 2014, **20**, 8297-8301.
- [9] S.-i. Ohkoshi, Y. Tsunobuchi, T. Matsuda, K. Hashimoto, A. Namai, F. Hakoe and H. Tokoro, *Nat. Chem.*, 2010, **2**, 539-545.
- [10] S. Ishiwata, Y. Shiomi, J. S. Lee, M. S. Bahrany, T. Suzuki, M. Uchida, R. Arita, Y. Taguchi and Y. Tokura, *Nat. Mater.*, 2013, **12**, 512.
- [11] T. Nilges, S. Lange, M. Bawohl, J. M. Deckwart, M. Janssen, H.-D. Wiemhöfer, R. Decourt, B. Chevalier, J. Vannahme, H. Eckert and R. Wehrich, *Nat. Mater.*, 2009, **8**, 101-108.
- [12] C. Xiao, X. Qin, J. Zhang, R. An, J. Xu, K. Li, B. Cao, J. Yang, B. Ye and Y. Xie, *J. Am. Chem. Soc.*, 2012, **134**, 18460-18466.
- [13] S. N. Guin, J. Pan, A. Bhowmik, D. Sanyal, U. V. Waghmare and K. Biswas, *J. Am. Chem. Soc.*, 2014, **136**, 12712-12720.
- [14] Y. Shi, A. Assoud, C. R. Sankar and H. Kleinke, *Chem. Mater.*, 2017, **29**, 9565-9571.
- [15] C. Han, Q. Sun, Z. X. Cheng, J. L. Wang, Z. Li, G. Q. Lu and S. X. Dou, *J. Am. Chem. Soc.*, 2014, **136**, 17626-17633.

- [16] L.-D. Zhao, S.-H. Lo, Y. Zhang, H. Sun, G. Tan, C. Uher, C. Wolverton, V. P. Dravid and M. G. Kanatzidis, *Nature*, 2014, **508**, 373.
- [17] L. Pan, D. Bérardan and N. Dragoe, *J. Am. Chem. Soc.*, 2013, **135**, 4914-4917.
- [18] S. N. Guin and K. Biswas, *Chem. Mater.*, 2013, **25**, 3225-3231.
- [19] S. N. Guin, V. Srihari and K. Biswas, *J. Mater. Chem. A*, 2015, **3**, 648-655.
- [20] S. N. Guin, S. Banerjee, D. Sanyal, S. K. Pati and K. Biswas, *Inorg. Chem.*, 2016, **55**, 6323-6331.
- [21] J. Janek, *Nat. Mater.*, 2009, **8**, 88-89.
- [22] S. Lange and T. Nilges, *Chem. Mater.*, 2006, **18**, 2538-2544.
- [23] D. M. Trots, A. Senyshyn, D. A. Mikhailova, M. Knapp, C. Baetz, M. Hoelzel and H. Fuess, *J. Phys.: Condens. Matter*, 2007, **19**, 136204.
- [24] D. Santamaria-Perez, A. Morales-Garcia, D. Martinez-Garcia, B. Garcia-Domene, C. Mühle and M. Jansen, *Inorg. Chem.*, 2013, **52**, 355-361.
- [25] S. N. Guin, D. Sanyal and K. Biswas, *Chem. Sci.*, 2016, **7**, 534-543.
- [26] O. Osters, M. Bawohl, J.-L. Bobet, B. Chevalier, R. Decourt and T. Nilges, *Solid State Sci.*, 2011, **13**, 944-947.
- [27] P. Hautojärvi and C. Corbel, in *Positron spectroscopy of solids*, IOS press, 1995, pp. 491-532.
- [28] R. Krause-Rehberg and H. S. Leipner, 1999.
- [29] A. Sarkar, M. Chakrabarti, S. K. Ray, D. Bhowmick and D. Sanyal, *J. Phys.: Condens. Matter*, 2011, **23**, 155801.
- [30] J. Dhar, S. Sil, A. Dey, P. P. Ray and D. Sanyal, *J. Phys. Chem. Lett.*, 2017, **8**, 1745-1751.

PART 5

**High Performance Thermoelectrics
of IV-VI Chalcogenides Driven by
Low Lattice Thermal Conductivity**

Chapter 5.1



**Discordant Gd and Electronic Band
Flattening Synergistically Induce High
Thermoelectric Performance in n-type
PbTe**

Discordant Gd and Electronic Band Flattening Synergistically Induce High Thermoelectric Performance in n-type PbTe[†]

Summary

p-type PbTe is the most sought-after material in thermoelectrics due to its ultrahigh thermoelectric figure of merit (zT), but the performance of *n*-type PbTe is lacking behind due to the simplicity of its conduction band compared to rich valence bands. In this chapter, we have synergistically enhanced the Seebeck coefficient and lowered the lattice thermal conductivity of *n*-type PbTe by Gd doping, which resulted in high thermoelectric performance. Gd doping in PbTe enhances the electron effective mass via flattening of conduction band which significantly improves the Seebeck coefficient. Gd is found to remain in an off-centered position inside the rock-salt PbTe lattice, which increased the lattice anharmonicity. Density functional perturbation theory (DFPT) calculations indicate that Gd induces a low energy nearly flat optical phonon mode which drastically increases the phonon scattering rate and lowers lattice thermal conductivity to 0.78 W/mK. As a result, we achieved a high zT of 1.65 at 678 K for $\text{Pb}_{1-x}\text{Gd}_x\text{Te}_{1-y}\text{I}_y$ ($x = 0.33\%$, $y = 1\%$).

[†]M. Dutta, R. K. Biswas, S. K. Pati and K. Biswas. *ACS Energy Lett.*, 2021, **6**, 1625–1632.

5.1.1. Introduction

The current technological advancement allows us to convert only a fraction of resources into efficient energy (like electricity) and a major part (~65%) is lost as heat during the conversion. Thermoelectric materials which can directly and reversibly convert waste heat to electricity, are thus seen as a potential candidate in energy management.¹⁻⁵ The performance of the thermoelectric materials is given by its dimensionless figure of merit, zT , which is expressed as $zT = \frac{\sigma S^2}{\kappa} T$; σ , S and κ being electrical conductivity, Seebeck coefficient and total thermal conductivity respectively. While σ is governed by charge carriers in a material, the thermal conductivity propagates due to both charge carriers (κ_{el}) and lattice vibrations (κ_{lat}). The complicated inter-relationship of the thermoelectric parameters (σ , S and κ_{el}) lends a major bottleneck in improving zT . Hitherto, most of the improvements in thermoelectric materials have primarily focused on balancing these interdependent parameters.¹ Several state of the art strategies like electronic band flattening,^{6, 7} band convergence,^{8, 9} charge carrier optimization,¹⁰⁻¹² resonant states,^{13, 14} band alignment,^{15, 16} mobility enhancement,^{17, 18} effective mass engineering,^{6, 19, 20} slight symmetry reduction^{21, 22} etc. have been effectively carried out to improve the power factor (σS^2) of a material.²³ Similarly, lowering the κ_{lat} of a material also garnered several novel approaches, e.g. phonon scattering by point defects,^{6, 24, 25} nano precipitates,^{15, 26-28} all scale hierarchical phonon scattering,²⁹⁻³¹ and intrinsic phonon prohibiting pathways,³² which have been successfully implemented till date.

PbTe adopts a rock salt structure, which is known for its unprecedented p-type thermoelectric performance in temperature range of 700 – 950 K. High performance in p-type PbTe originates due to its intrinsic low thermal conductivity arising from significant lattice anharmonicity and presence of unique electronic band structure.³³ The valence band (VB) of PbTe comprises of two neighboring bands L and Σ which have very little energy off-set ($\Delta E_{L-\Sigma} = 0.15 - 0.20$ eV)³³ and thus effective valence band convergence has been realized in p-type PbTe to improve upon its thermoelectric performance.^{8, 9, 30, 34} On the other hand, conduction band (CB) of PbTe comprises of only a single L band and thus it is lagging to match the performance of its p-type counterpart.^{33.}

³⁵ The presence of lower degenerate valleys in CB as compared to VB generates intrinsically low n-type Seebeck coefficient values and thus poses a greater challenge to improve its n-type thermoelectric performance.^{33, 35}

Recent progress on n-type PbTe primarily focusses on optimizing charge carrier concentration and mobility^{6, 17, 18, 36, 37}, simultaneously modulating the electronic and thermal properties in PbTe-Cu₂Te¹⁷, PbTe-AgSbSe₂³⁸, enhancing band effective mass as in case of Pb_{0.988}Sb_{0.012}Te-GeTe,¹⁹ Pb_{0.98}Ga_{0.02}Te-GeTe²⁰ and PbTe-MnTe⁶. Similarly, nano-structuring to reduce κ_{lat} and simultaneously improve electronic properties is also observed in In and Sb co-doped PbTe,²⁶ PbTe-PbS⁷ etc.^{39, 40} However, simplicity of the conduction band and a large band offset between two neighboring conduction band ($\Delta E_{L-\Sigma} \sim 0.45$ eV) prohibited n-type PbTe to be as efficient as its p-type counterpart.^{33, 35}

Herein, we demonstrate superior n-type thermoelectric performance for Gd doped PbTe in the temperature range of 295 – 823 K. Pb_{1-x}Gd_xTe (x = 0.33%) exhibits an zT of ~ 1.2 at 783 K and subsequent n-type electrical transport optimization with iodine (I) doping, the maximum zT reaches to a high value of ~ 1.65 at 678 K for Pb_{1-x}Gd_xTe_{1-y}I_y (x = 0.33%, y = 1%), which is among the highest value reported for n-type PbTe. Gd is an n-type dopant and even 0.25 mol% Gd doping on PbTe increases the n-type carrier concentration to $1.46 \times 10^{19} \text{ cm}^{-3}$. Electronic structure analysis through Density Functional Theory (DFT) shows that on Gd doping the principal band gap at L point opens up along with formation of a non-interacting nearly flat conduction band which increases the band effective mass (m^*). Atom projected electronic density of states (pDOS) reveals that the non-interacting band is contributed from the hybridized state of Gd which enhances the Seebeck coefficient in Gd doped PbTe. Furthermore, Gd is seen to remain in an off-centered position in the PbTe lattice due to discordant nature of Gd in the octahedral coordination, which creates significant lattice anharmonicity. Phonon dispersion revealed the presence of low frequency nearly flat optical localized phonon mode. Both these effects, *i.e.*, the presence of locally off-centered Gd in PbTe and the formation of low energy localized phonon mode synergistically aid in enhancing the scattering of acoustic phonons. This significantly lowers the κ_{lat} of Pb_{1-x}Gd_xTe (x = 0.33%) to 0.79 W/mK at 735 K. Low κ_{lat} in n-type Gd and I co-doped PbTe coupled with the electronic structure modification results in superior thermoelectric performance and

importantly an impressive average zT (zT_{ave}) of 1.15 is obtained in the temperature range of 423 – 823 K.

5.1.2. Methods

Synthesis. High quality crystalline PbTe and Gd and I co-doped PbTe were prepared by vacuum sealed melting followed by spark plasma sintering (SPS) method. Used stoichiometric quantities of high-purity Pb (99.999%, Alfa Aesar), Te (99.999%, Sigma Aldrich), Gd chips (99.99%, Sigma Aldrich) and PbI₂ (99.9%, Sigma Aldrich) (total weight of 8 g) in a quartz ampoule, sealed during high vacuum of 10^{-5} torr. The contents were heated up to 1323 K in 12 hr, soaked at this temperature for 12 hours, and cooled to room temperature in 12 hr. The obtained product was then finely ground and SPS was performed to solidify. The sample was taken in a graphite die of 10 mm diameter. The die was then heated to 600 °C in 12 mins; kept at that temperature for 5 mins and then cooled to room temperature in 12 mins. The pressure was maintained at 45 MPa throughout the sintering process.

Powder X-ray diffraction (PXRD). Room temperature PXRD measurements were recorded on Rigaku SmartLab SE diffractometer using Cu K α ($\lambda = 1.5406 \text{ \AA}$) radiation.

Thermal conductivity. The thermal diffusivity, D , was measured between 290 K and 823 K using laser flash diffusivity technique in Netzsch LFA-457 instrument. Disc-shaped pellets with ca. 10 mm x 2 mm dimensions were used for thermal transport measurement. Lattice thermal conductivity (κ_{lat}) is extracted by subtracting electronic thermal conductivity (κ_{el}) from total thermal conductivity. Electrical and thermal transport properties were measured in same direction.

Electronic properties. Electrical conductivity (σ) and Seebeck coefficient (S) were simultaneously measured under He-atmosphere from 290 K up to 823 K using ULVAC-RIKO ZEM-3 instrument. Rectangular bar shaped samples (ca. $2 \times 2 \times 9 \text{ mm}^3$) cut from cylindrical samples were used for the electrical measurements. The best sample is further

measured in Linseis LSR-3 instrument for reproducibility in the same temperature range. Electrical and thermal transport properties were measured in same direction.

Band gap. Finely ground sample was used to obtain the optical band gap at room temperature. The optical band gap was estimated in a FT-IR Bruker IFS 66V/S spectrometer within the range of $6000 - 400 \text{ cm}^{-1}$. Absorption (α/S) data were derived using Kubelka-Munk equation: $\alpha/S = (1-R)^2/(2R)$, where R is the reflectance, α and S corresponds to absorption and scattering coefficient, respectively. The energy band gaps were deduced from α/S vs E_g (eV) plot.

Field emission scanning electron microscopy (FESEM). FESEM images in back scattered electron (BSE) mode and normal mode were taken using ZEISS Gemini SEM – Field Emission Scanning Electron Microscope.

Transmission electron microscopy. The transmission electron microscopy (TEM) image of the sample were taken using a JEOL (JEM3010) instrument (300 kV accelerating voltage) and the high resolution TEM (HRTEM) images was taken using JEOL (JEM2100PLUS) instrument (200 kV accelerating voltage).

Theoretical Methods. First principle based density function theory (DFT) has been performed to study structural relaxation and electronic structure property calculations using the Quantum Espresso package.⁴¹ The Kohn-Sham equations are solved using a 70 Ry plane wave basis states with the projector augmented wave (PAW) method⁴² and the generalized gradient approximation⁴³ is employed. The total energy and ionic forces are converged to within 10^{-8} eV and $0.025 \text{ eV}/\text{\AA}$, respectively. A uniform grid of k-mesh in the Brillouin zone of 4000 k-points has been considered for electronic structure calculations. The sharp discontinuity of the electronic states near the Fermi level are smeared out with the Fermi-Dirac distribution function with broadening of 0.003 Ry. We consider $3 \times 3 \times 3$ supercell of PbTe containing 54 atoms ($\text{Pb}_{27}\text{Te}_{27}$) and one Pb substituted with Gd atom ($\text{Pb}_{26}\text{Gd}_1\text{Te}_{27}$) for electronic structure calculation. In order to incorporate relativistic effects because of the presence of heavy metals in the supercell, we include

spin-orbit coupling (SOC) in the band structure. Our calculated electronic band dispersion obtained using PBE-SOC functional matches well consistently with previous DFT results on controlled PbTe.⁶ To access the bond strength and bonding interaction, we execute crystal orbital Hamiltonian population (COHP) analysis between the pairwise orbitals corresponding to Te-Gd atoms in the crystal structure of Gd doped PbTe. The phonon dispersion calculation of PbTe and Gd-doped PbTe unit cells have been carried out using density functional perturbation theory (DFPT) formalism implemented in Quantum Espresso. A strict energy convergence of 10^{-10} eV has been used to obtain phonon frequencies accurately. We calculate phonon group velocity (v_{iq}) using the equation, $v_{iq} = \nabla (E_{iq})/h$. For phonon calculations, we have considered a 2x2x1 supercell (primitive cell of PbTe contains 2 atoms). Therefore, we have obtained the phonon dispersion curve for 8 atoms in the constructed 2x2x1 supercell. It contains 24 phonon modes at each q-point: out of the 24 phonon modes, there are 3 acoustic phonon modes and 21 optical phonon modes present.

For determining the scattering rates, we have used ShengBTE⁴⁴ code which solves for the scattering rates considering the three phonon scattering processes. The calculation of scattering process required information of the third-order interatomic force constant (IFC) matrix along with second-order IFCs. First, we considered an initial 2x2x1 supercell (primitive cell of PbTe contains 2 atoms) containing 8 atoms for second-order IFC calculations. Then, to calculate the third-order IFC matrix, we have generated a 4x4x1 supercell containing 32 atoms with displaced configurations, using `thirdorder.py` utility.⁴⁵ This third-order IFC matrix in conjunction with the second-order IFC matrix are incorporated in ShengBTE code which solves for the scattering rates using a dense sampling of q-points spanning over the BZ. Theoretical calculations are done in collaboration with Prof. Swapan K. Pati of JNCASR, Bangalore.

5.1.3. Results and Discussion

High quality polycrystalline $\text{Pb}_{1-x}\text{Gd}_x\text{Te}$ ($x = 0.25 - 0.75\%$) samples were synthesized using vacuum sealed tube melting reaction followed by spark plasma sintering (SPS). Like its parent sample all the doped samples crystallized in rock-salt structure (Figure 5.1.1a). Powder X-ray diffraction (PXRD) of all the samples show no secondary phases

within the detection limit of the instrument indicating complete solubility of Gd into PbTe lattice (Figure 5.1.1b). On Gd doping we observe a slightly shift in the PXRD peaks towards higher 2θ , indicating decrease in the lattice parameter (Figure 5.1.1c), which is due to the smaller ionic radius of Gd^{3+} (1.07 Å) as compared to Pb^{2+} (1.33 Å). Field emission scanning electron microscopy (FESEM) done in back scattering electron (BSE) mode and transmission electron microscopy (TEM) on $\text{Pb}_{1-x}\text{Gd}_x\text{Te}$ ($x = 0.33\%$) further confirms the absence of second phase precipitates and it is consistent with our PXRD data (Figure 5.1.2a and 5.1.3). Elemental colour mapping during Energy dispersive X-ray (EDAX) of the FESEM imaging shows that all the three atoms i.e., Pb, Te and Gd are distributed homogeneously over the observed area (Figure 5.1.2c). The d-spacing obtained from Figure 5.1.3c is found to be 0.33 nm which corresponds to (200) plane in the rocksalt structure.

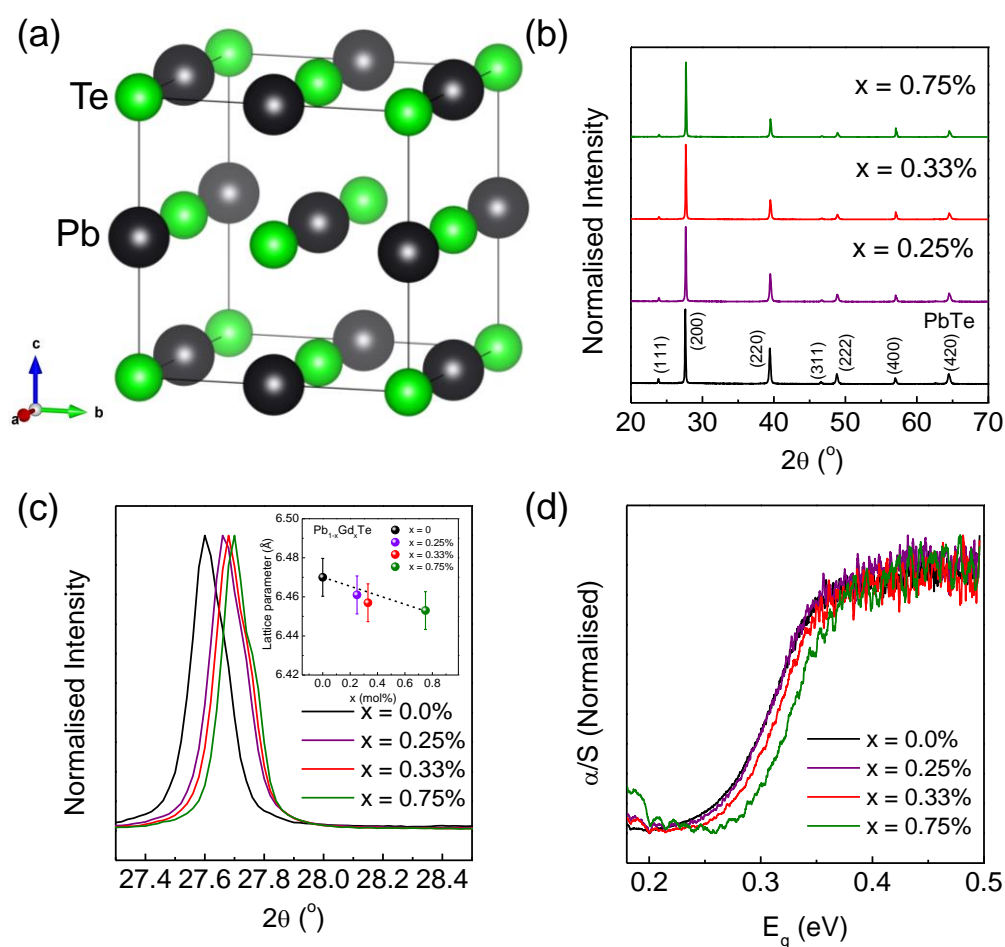


Figure 5.1.1. (a) Rock-salt structure of PbTe. (b) Room temperature powder XRD pattern for pristine PbTe and Gd doped PbTe. (c) Zoomed (200) peak of PbTe and Gd doped

samples. Gd doped samples show clear red shift in the 2θ value with increasing dopant concentration. (inset) Variation of lattice parameter of PbTe with Gd doping. (d) Band gap of PbTe and Gd doped PbTe. The band gap increases on increasing doping concentration.

Table 5.1.1. Room temperature n-type carrier concentration and mobility of the $Pb_{1-x}Gd_xTe_{1-y}I_y$ samples.

Sample Name	Carrier concentration ($\text{cm}^{-3} \times 10^{19}$)	Mobility ($\text{cm}^2 \text{V}^{-1} \text{s}^{-1}$)
x = 0.25%, y = 0%	1.46	436
x = 0.33%, y = 0%	2.97	522
x = 0.75%, y = 0%	4.30	396
x = 0.33%, y = 1%	3.32	263
x = 0.33%, y = 2%	3.60	203
x = 0.33%, y = 3%	2.63	197

Gd is a n-type donor with a common oxidation state of +3, and on substituting Pb^{2+} it will impart an additional electron into the lattice. Previous low temperature electronic transport measurement on Gd doped PbTe showed similar n-type behavior.⁴⁶ Increase in the dopant concentration will thus lead to an increase in the n-type carrier concentration and hence subsequent enhancement in the electrical conductivity (σ). On Gd doping the n-type carrier concentration of PbTe increases from $1.46 \times 10^{19} \text{ cm}^{-3}$ for $\text{Pb}_{1-x}\text{Gd}_x\text{Te}$ (x = 0.25%) to $4.30 \times 10^{19} \text{ cm}^{-3}$ for $\text{Pb}_{1-x}\text{Gd}_x\text{Te}$ (x = 0.75%) at room temperature (Table 5.1.1). Such increase in carrier concentration is also observed in σ as it increases from 1020 S/cm for $\text{Pb}_{1-x}\text{Gd}_x\text{Te}$ (x = 0.25%) to 2484 S/cm for $\text{Pb}_{1-x}\text{Gd}_x\text{Te}$ (x = 0.33%) and finally to 2731 S/cm for $\text{Pb}_{1-x}\text{Gd}_x\text{Te}$ (x = 0.75%) at ~300 K (Figure 5.1.4a). With increasing temperature, we observe that σ decreases for all the samples as it is expected for degenerate semiconductors. Similarly, the Seebeck coefficient (S) for Gd doped PbTe at ~ 300 K decreases systematically from -111 $\mu\text{V/K}$ for $\text{Pb}_{1-x}\text{Gd}_x\text{Te}$ (x = 0.25%) to -72 $\mu\text{V/K}$ for $\text{Pb}_{1-x}\text{Gd}_x\text{Te}$ (x = 0.75%) (Figure 5.1.4b). The negative sign indicates its n-type conduction and agrees with the negative Hall coefficients.

Temperature dependent S increases with increase in temperature with highest S value of $-261 \mu\text{V/K}$ is obtained for $\text{Pb}_{1-x}\text{Gd}_x\text{Te}$ ($x = 0.25\%$) at 817 K. As a result, we obtained a high power factor of $\sim 24.7 \mu\text{W/cmK}^2$ at 483 K for $\text{Pb}_{1-x}\text{Gd}_x\text{Te}$ ($x = 0.33\%$) (Figure 5.1.4c).

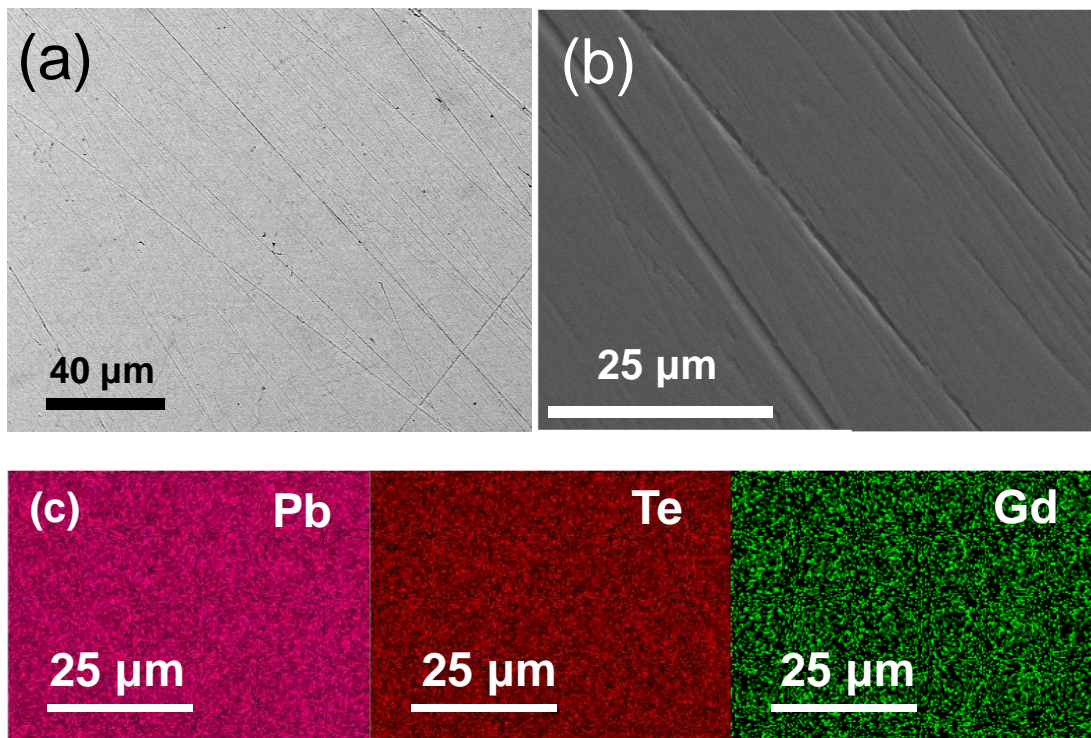


Figure 5.1.2. (a) FESEM image in BSE mode obtained for $\text{Pb}_{1-x}\text{Gd}_x\text{Te}$ ($x = 0.33\%$). (b) FESEM image of $\text{Pb}_{1-x}\text{Gd}_x\text{Te}$ ($x = 0.33\%$). (c) Representative colour mapping showing homogeneous distribution of the atoms.

To investigate the cause for such enhanced power factor for Gd doped PbTe, we plot the room temperature Seebeck coefficient as a function of carrier concentration (n). The resultant relationship when plotted against theoretical single band Pisarenko plot with varying effective mass (m^*) ($m^* = 0.30, 0.35, 0.42 m_e$), indicated an increase in effective mass with increase in Gd incorporation (Figure 5.1.4d). The effective mass for $\text{Pb}_{1-x}\text{Gd}_x\text{Te}$ ($x = 0.25\%$) is $\sim 0.35m_e$, which increase to $\sim 0.45m_e$ for $\text{Pb}_{1-x}\text{Gd}_x\text{Te}$ ($x = 0.75\%$) and is comparable to PbTe-MnTe,⁶ but higher than PbTe-PbS ($\sim 0.32 m_e$),⁷ PbTe:I ($\sim 0.25 m_e$),⁴⁸ La doped PbTe ($\sim 0.33 m_e$),³⁹ PbTe-Cu₂Te,¹⁷ GeTe alloyed $\text{Pb}_{0.988}\text{Sb}_{0.012}\text{Te}$ (~ 0.40

m_e)¹⁹ etc. This enhanced m^* dictates the high Seebeck coefficient for Gd doped PbTe and influences the n-type thermoelectric performance in PbTe.

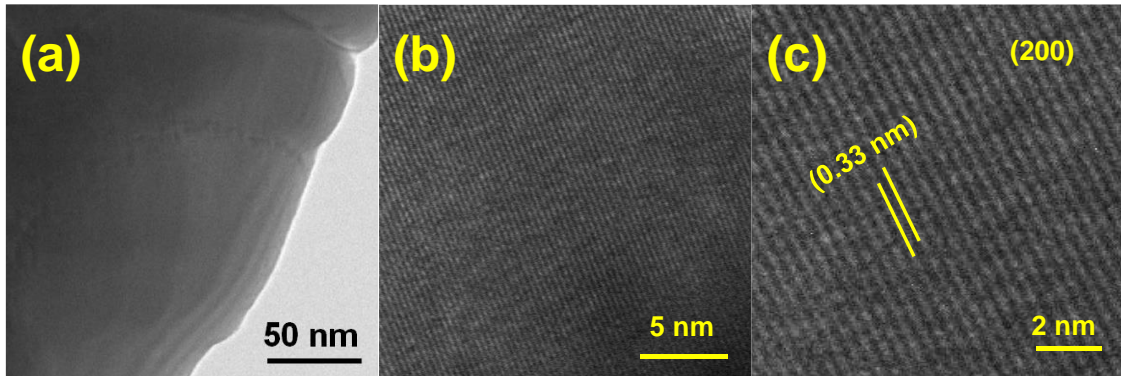


Figure 5.1.3. (a) TEM and (b, c) HRTEM images of $Pb_{1-x}Gd_xTe$ ($x = 0.33\%$) showing absence of any nano precipitates.

To understand how Gd doping influences the electronic transport properties of PbTe, we have performed DFT analysis of electronic structure. Figure 5.1.5a represents the electronic band structures of PbTe and Gd-doped PbTe plotted together for comparison. It is evident that on Gd incorporation the band gap at L point opens up from 0.15 eV to 0.25 eV and is in line with the experimentally observed band gap opening upon Gd doping in PbTe (Figure 5.1.1d). Experimentally pristine PbTe has a band gap of ~ 0.27 eV which increases to 0.29 eV for $Pb_{1-x}Gd_xTe$ ($x = 0.75\%$). Furthermore, doping with Gd atoms introduces new features in the electronic band structure which is beneficial for thermoelectric power factor. We observe non-interacting single band just above the Fermi level in the conduction band which is nearly dispersionless around Γ point and relatively dispersive along the $L \rightarrow \Gamma$ direction (red lines, Figure 5.1.5a). In fact, the flat nature is further verified through the sharp peak observed in the electronic DOS plot which is shown by the purple arrow in Figure 5.1.5b and resembles to that of Sb and I co-doped PbTe.²⁴ Here, this non-dispersive band leads to higher Seebeck coefficient.^{49, 50} This band flattening is accompanied with an increase in the effective mass (m^*) of the conduction band. Pristine PbTe has an effective mass of $\sim 0.3m_e$ which increases to $\sim 0.42m_e$ for Gd doped PbTe and correlates closely with our modelled S vs. n Pisarenko relationships (Figure 5.1.4d).

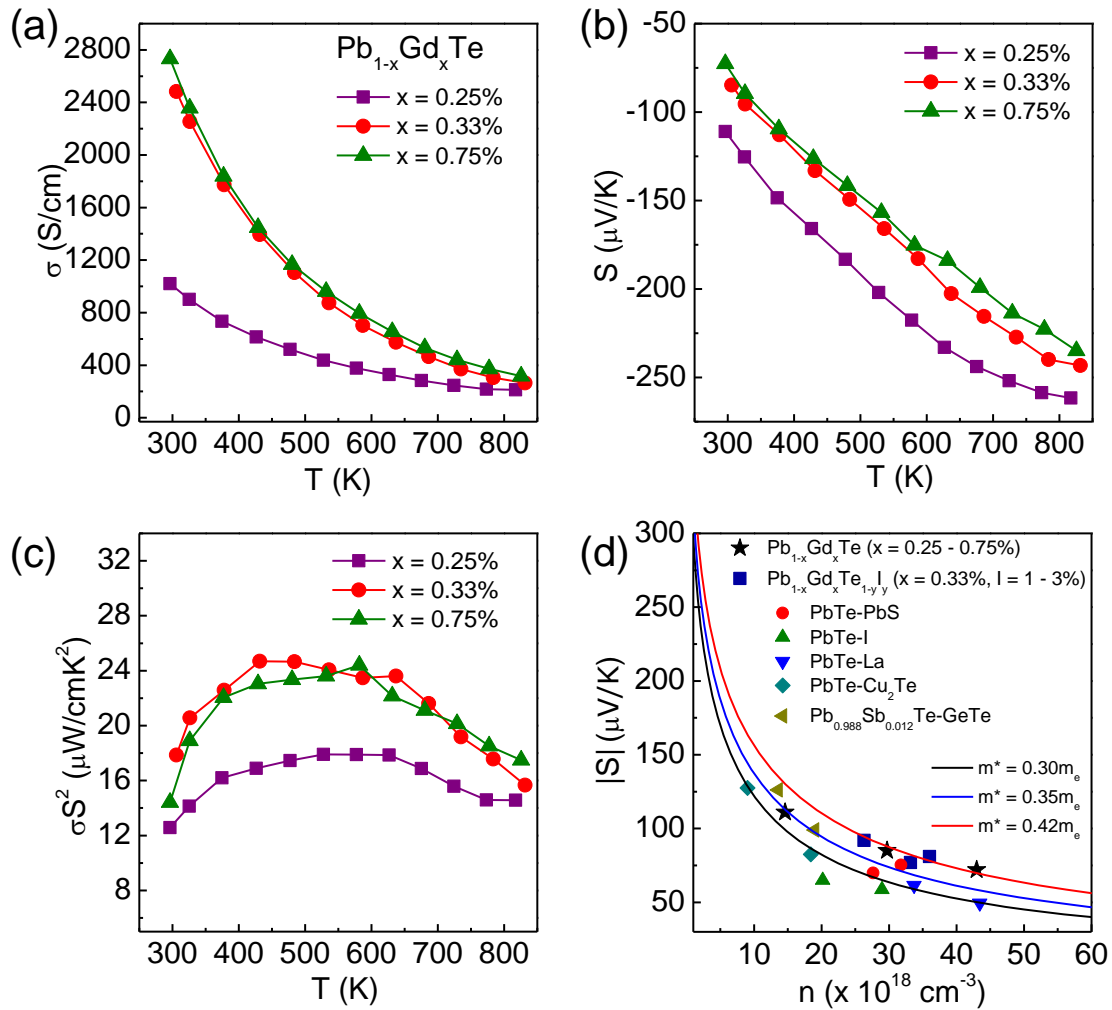


Figure 5.1.4. Temperature dependent (a) electrical conductivity (σ), (b) Seebeck coefficient (S), (c) power factor (σS^2) for Gd doped PbTe samples. (d) $|S|$ vs. n plot for $\text{Pb}_{1-x}\text{Gd}_x\text{Te}$ ($x = 0.25 - 0.75\%$) and $\text{Pb}_{1-x}\text{Gd}_x\text{Te}_{1-y}\text{I}_y$ ($x = 0.33\%$, $y = 1 - 3\%$) and plotted against the theoretical Pisarenko plot (solid lines) using single band model with varying effective masses (m^*) of 0.30 , 0.35 and $0.42 m_e$ and compared with previous results- PbTe-PbS ⁷, PbTe:I ⁴⁸, PbTe:La ³⁹, $\text{PbTe-Cu}_2\text{Te}$ ¹⁷, $\text{Pb}_{0.988}\text{Sb}_{0.012}\text{Te-GeTe}$ ¹⁹.

Atom projected electronic density of states (pDOS) for Gd-doped PbTe, revealed that the conduction bands are contributed by hybridized states of Te-Gd and Te-Pb bonding, with Pb showing the maximum contribution (Figure 5.1.5c). The electronic structures are calculated based on energetically most favourable configuration where Gd atoms are displaced along the crystallographic direction [111] from their ideal octahedral positions (Figure 5.1.6a). The off-centering of the Gd atom from regular octahedral site

is around 0.21 Å. This tendency of Gd to off-center from the parent Pb position might arise due to the discordant nature of Gd, which prefers to attain a higher coordination number (CN) (CN > 6) than possible for rock-salt PbTe (CN = 6).⁵¹ Through the off-center configuration in Gd doped PbTe, the structure further reduces their total energy significantly by 13 meV which is shown in Figure 5.1.6b.

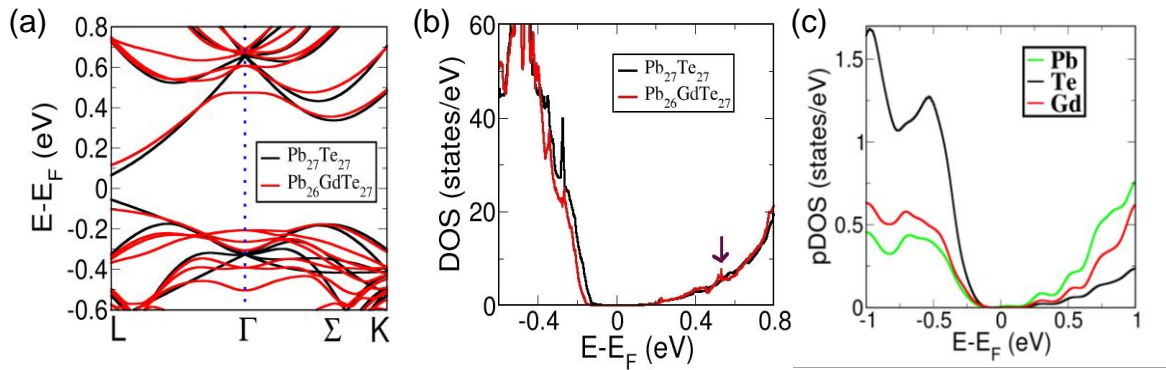


Figure 5.1.5. (a) Electronic band structure of PbTe (black) and Gd doped PbTe (red), containing 54 atoms in the 3x3x3 supercell. (b) Electronic DOS of PbTe and Gd doped PbTe. The relatively flat nature in the conduction band is further confirmed by a sharp peak in DOS, marked by a purple arrow. (c) Atom projected electronic density of states (pDOS).

To further understand the chemical aspect of such Gd off-centering, we perform Crystal Orbital Hamiltonian Population (COHP) analysis between the orbitals of Te and Gd. COHP is calculated considering the DOS multiplied by the Hamiltonian matrix element and it indicates degree of covalency and nature of bonding interactions. The negative value of COHP signifies bonding nature while positive value implies antibonding nature. Figures 5.1.6c, d represent the COHP between the orbital of Te and Gd for both the undistorted (at regular octahedral site) and off-centered site of Gd atom in the PbTe lattice, respectively. Interestingly, interaction between Te and Gd orbital is antibonding in nature above the Fermi level when Gd atoms are placed at their undistorted octahedral site. However, through the off-centering, Gd-Te interaction becomes bonding in nature which is energetically favorable than the undistorted case. This locally off-centered Gd atoms increases the lattice anharmonicity and subsequently plays an important role in reducing lattice thermal conductivity of n-type PbTe significantly (discussed later).^{20, 52, 53}

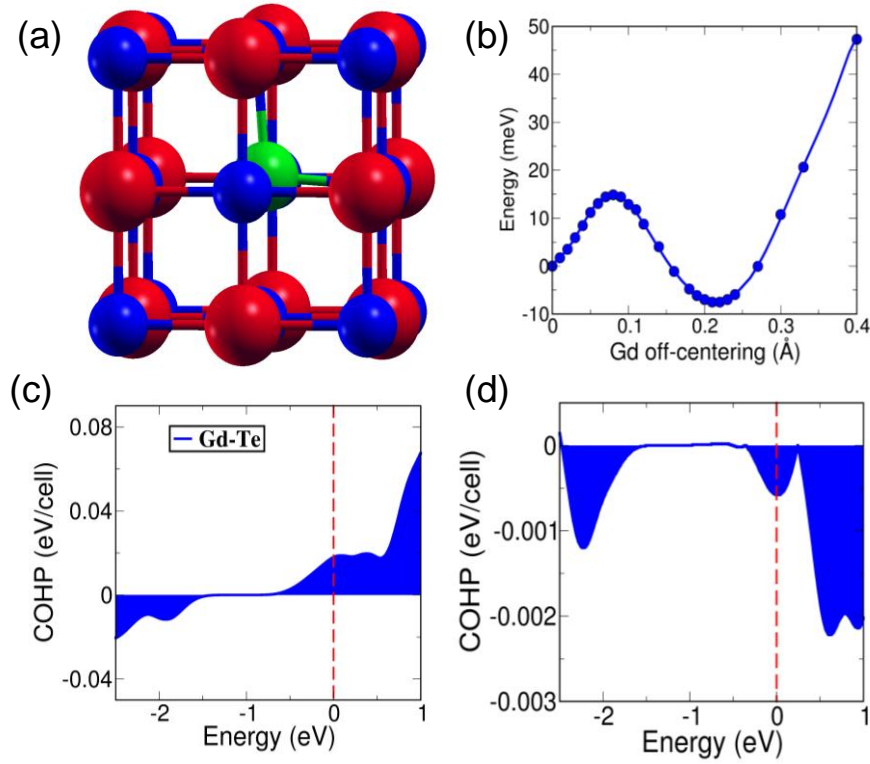


Figure 5.1.6. (a) Off-centered Gd atom at the distorted octahedral position in PbTe. Color codes are represented as follows: Pb - Red; Te - Blue; Gd - Green. (b) Energy vs. Gd off-centering plot showing a minimum energy is obtained when Gd is off-centered by ~ 0.21 Å along [111] direction. Crystal orbital Hamiltonian population (COHP) is plotted for Gd doped PbTe with (c) undistorted and (d) off-centered Gd atom from the equilibrium octahedral position.

Table 5.1.2. List of some irreducible q -points and corresponding degenerate vibrational Eigen values. The q -points are in the unit of $\frac{2\pi}{l}$; where l is lattice constant.

q_x	q_y	q_z	$\omega_1(\text{cm}^{-1})$	$\omega_2(\text{cm}^{-1})$
0.00	-0.57	0.20	38	38
0.00	-0.57	-1.02	41	41

To comprehend the nature of thermal transport in these materials, we have calculated the phonon dispersion of pristine PbTe and Gd doped PbTe (Figure 5.1.7a, b). We have observed that Gd atom introduces nearly flat band around frequency ~ 38 cm^{-1} along $\Gamma \rightarrow Z \rightarrow R \rightarrow X$ directions over the Brillouin zone of phonon dispersion (Figure

5.1.7b). The low energy nearly dispersionless optical mode reflects weak interatomic force constant (IFC) and thereby reflects weak bonding between the associated atoms. These disentangled nondispersive optical phonons mode behave similar to the Kondo-like phonon mode as seen for type-I Clathrates with Ce and La as guests previously and are doubly degenerate in nature (Figure 5.1.8).⁵⁴ These non-dispersive degenerate phonon modes strongly scatter acoustic phonon modes, and is evident from the phonon-phonon anharmonic scattering rates, which increases by a few folds ($\sim 10^5$ 1/ps) at the frequency ~ 38 cm^{-1} (Figure 5.1.7c). Here, the localized phonon mode shows larger scattering rates than that of other highly anharmonic compounds.^{55, 56} Moreover, we observe avoided crossing between longitudinal acoustic (LA) mode and low energetic optical mode at 40 cm^{-1} near high symmetry S point in the phonon dispersion curve (Figure 5.1.7b). Such avoided crossing is a signature for strong scattering of heat carrying acoustic phonons. Figures 5.1.9a, b represent phonon DOS for PbTe and Gd doped PbTe. A sharp peak in density of states near 38 cm^{-1} (black arrow, Figure 5.1.9b) is evidenced due to the appearance of non-dispersive flat optical phonon mode.

For microscopic understanding of this nearly flat optical phonon band, we carefully analyse phonon dispersion over the full Brillouin zone. In this regard, the vibrational frequencies have been accurately calculated using density functional perturbation theory (DFPT)⁵⁷ as implemented in Quantum Espresso (QE).⁴¹ In fact, we compute vibrational eigenvalues at the particular irreducible q -points depending upon crystal symmetry. Some of the important vibrational modes for particular q -points are tabulated in Table 5.1.2. While doping with Gd atom in place of Pb, we encounter two sets of possible degenerate Einstein modes (ω_1 and ω_2) at the non-zero q - points. Interestingly, the Gd atom at the 4a crystallographic site constitutes a non-interacting hybridized state with Te and Pb atoms and constructs phonon mode which is flat in nature over the Brillouin zone along $\Gamma \rightarrow Z \rightarrow R \rightarrow X$ directions. These non-dispersive vibrational modes are degenerate in energy due to specific crystal symmetry for some particular irreducible q -points. These degenerate vibrational modes are identified as pseudospins in the Kondo model.⁵⁸ In the context of the spin Kondo model,⁵⁹ pseudospins represent spin up and spin down states. Similar to the spin systems, the vibrational eigenvectors associated to the degenerate eigenvalues have orthogonal to each other.

These nearly non-dispersive Kondo-like degenerate optical phonon modes strongly scatter extended acoustics modes, similar to the spin kondo system where localized spin scatters free electrons and in turn reduces the carrier conductivity.

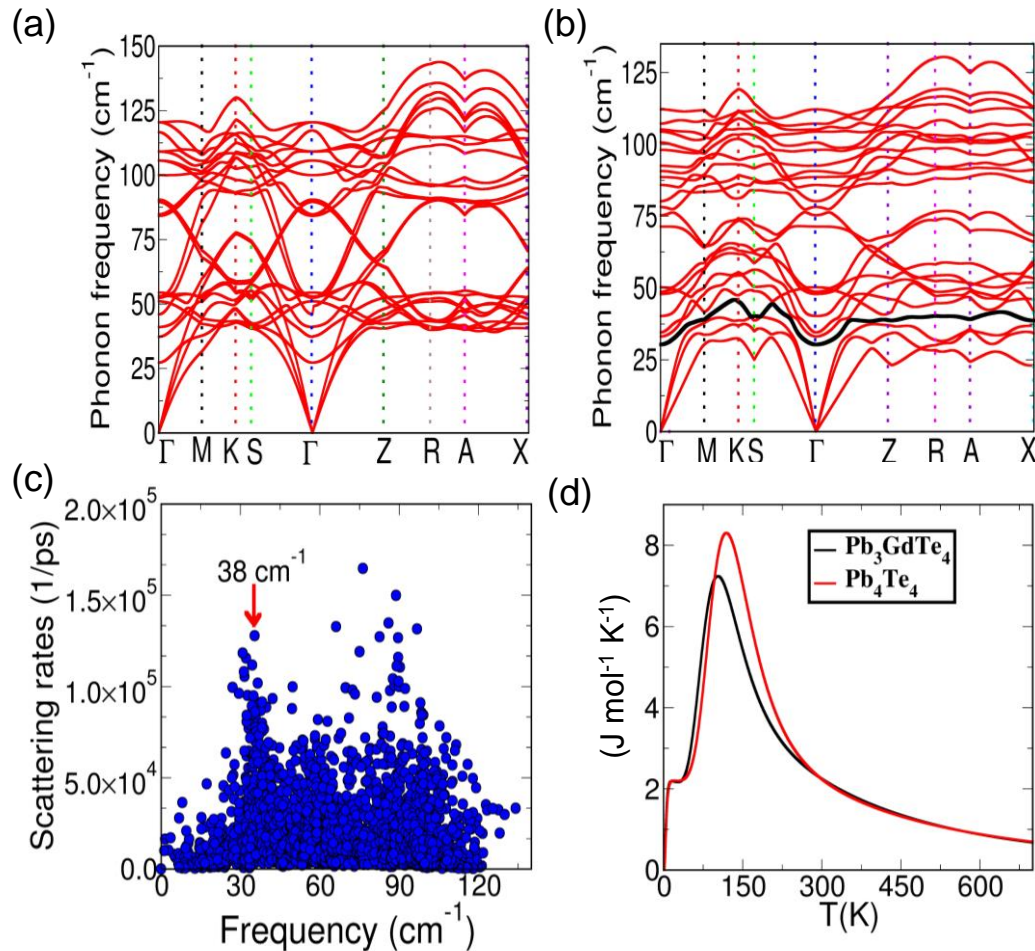


Figure 5.1.7. Phonon dispersion for (a) PbTe and (b) Gd doped PbTe . Appearance of a special band which is represented by black color, reveals nearly non-dispersive nature along $\Gamma \rightarrow \text{Z} \rightarrow \text{R} \rightarrow \text{X}$ directions due to Gd doping. (c) Anharmonic scattering rates as a function of frequency at $T=700 \text{ K}$ has been shown. Very high values of scattering rates have been observed at frequency $\sim 38 \text{ cm}^{-1}$. (d) Phonon contribution to the specific heat as a function of temperature for pristine and Gd doped PbTe .

The signature of the appearance of the Kondo like non-dispersive mode has also been verified from the phonon contribution to the theoretical specific heat (Figure 5.1.7d). In fact, a broad maximum of specific heat curve appears around 121 K which is actually near to the Debye temperature of PbTe system.^{60, 61} Interestingly, it is observed that the

broad maximum of the specific heat sharpened and shifted towards the lower temperatures as a result of Gd doping. Such behaviours can be explained in terms of temperature scales where these effects are controlled not by Debye temperature, rather governed by reduced energy scale⁵⁴. Thus, reduced temperature scale strongly enhances Umklapp scattering that results in limiting the lattice thermal conductivity.

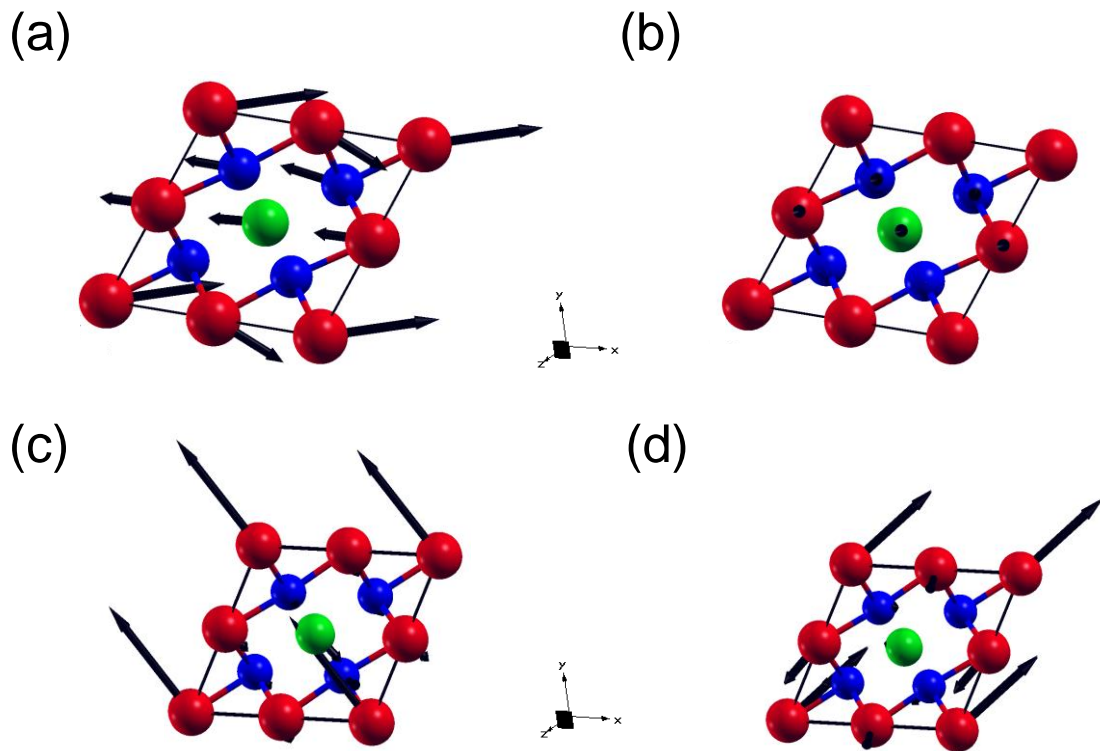


Figure 5.1.8. Eigen vector visualization for degenerate energy modes at 38 cm^{-1} (a and b) and 40 cm^{-1} (c and d). Color codes are represented as follows: Pb - Red; Te - Blue; Gd - Green.

To uncover how this localized optical phonon mode affects the thermal transport, we have calculated the atom projected phonon DOS (Figure 5.1.9c). Atom projected phonon DOS of Gd overlaps significantly with Pb atoms and hybridizes less with Te atoms at $\sim 38 \text{ cm}^{-1}$. Furthermore, the eigen mode visualization of this flat phonon mode, shows significant contribution of the Gd atoms indicating that the chemical origin of this flat phonon mode arises due to the doping of Gd atom in PbTe (Figure 5.1.8). These hybridized modes effectively scatter acoustic phonons and reduce lattice thermal

conductivity significantly. Moreover, this localized optical mode reveals very low group velocity ~ 230 m/s along $\Gamma \rightarrow Z \rightarrow R \rightarrow X$ directions (Figure 5.1.9d). The large scattering rates in combination with low group velocity driven by the low energy localized optical mode is the primary reason to achieve low lattice thermal conductivity in Gd doped PbTe. Gd doping further decreases the speed of sound along one of the transverse directions (v_{t2}) from 1690 m/s to 1160 m/s (Table 5.1.3). This reduction in v_{t2} decreases the overall mean speed of sound of the acoustic phonons from 1570 m/s for Gd doped PbTe compared to 2035 m/s for pristine PbTe. This reduction in the mean speed of sound along with the presence of low energy flat optical phonon mode and lattice anharmonicity induced via Gd off-centering plays a pivotal role in lowering the κ_{lat} of Gd doped PbTe.

Table 5.1.3. Speed of sound of the acoustic phonons

Compound	v_l (m/s)	v_{l1} (m/s)	v_{t2} (m/s)	v_{mean} (m/s)
PbTe	2680	2180	1690	2035
PbGdTe	2700	2290	1160	1570

The thermal diffusivity (D) of these Gd doped PbTe samples are shown in figure 5.1.10a. Total thermal conductivity (κ) was estimated using the relation, $\kappa = D \times C_p \times \rho$, where ρ is the density ($> 97\%$) of the sample and C_p is the heat capacity (C_p) of PbTe estimated from the relation C_p/k_B per atom = $3.07 + (4.7 \times 10^{-4} \times (T - 300))^{8, 62, 63}$ and are shown in Figure 5.1.10b. The total thermal conductivity value at ~ 300 K for $\text{Pb}_{1-x}\text{Gd}_x\text{Te}$ ($x = 0.25\%$) is 3.3 W/mK, while for $\text{Pb}_{1-x}\text{Gd}_x\text{Te}$ ($x = 0.33\%$) and $\text{Pb}_{1-x}\text{Gd}_x\text{Te}$ ($x = 0.75\%$) the values are 3.5 W/mK and 3.8 W/mK respectively at the same temperature. The increase is mainly attributed to the increase in the electrical conductivity of the material with Gd doping, which increases the electrical thermal conductivity (κ_{el}). κ_{el} is calculated using the Wiedemann Franz law, $\kappa_{\text{el}} = L\sigma T$, where σ is the electrical conductivity and L is the temperature dependent Lorenz number obtained by fitting the Seebeck coefficient to the reduced chemical potential.⁶³ The temperature dependent Lorenz number and κ_{el} are given in Figure 5.1.10c, d. The lattice thermal conductivity (κ_{lat}) however, is seen to decrease initially when Gd doping is changed from 0.25 mol% to 0.33 mol% but increases for 0.75 mol% doping. κ_{lat} for $\text{Pb}_{1-x}\text{Gd}_x\text{Te}$ ($x = 0.25\%$) decreases from ~ 2.76 W/mK to

2.02 W/mK for $\text{Pb}_{1-x}\text{Gd}_x\text{Te}$ ($x = 0.33\%$) at room temperature (Figure 5.1.10e). κ_{lat} for all the samples is found to decrease with increase in temperature. Low κ_{lat} of 0.78 W/mK is obtained at 735 K for $\text{Pb}_{1-x}\text{Gd}_x\text{Te}$ ($x = 0.33\%$), which is due to a synergistic effect of off-centered Gd atom and phonon scattering due to the presence of low energy localized optical phonon mode.

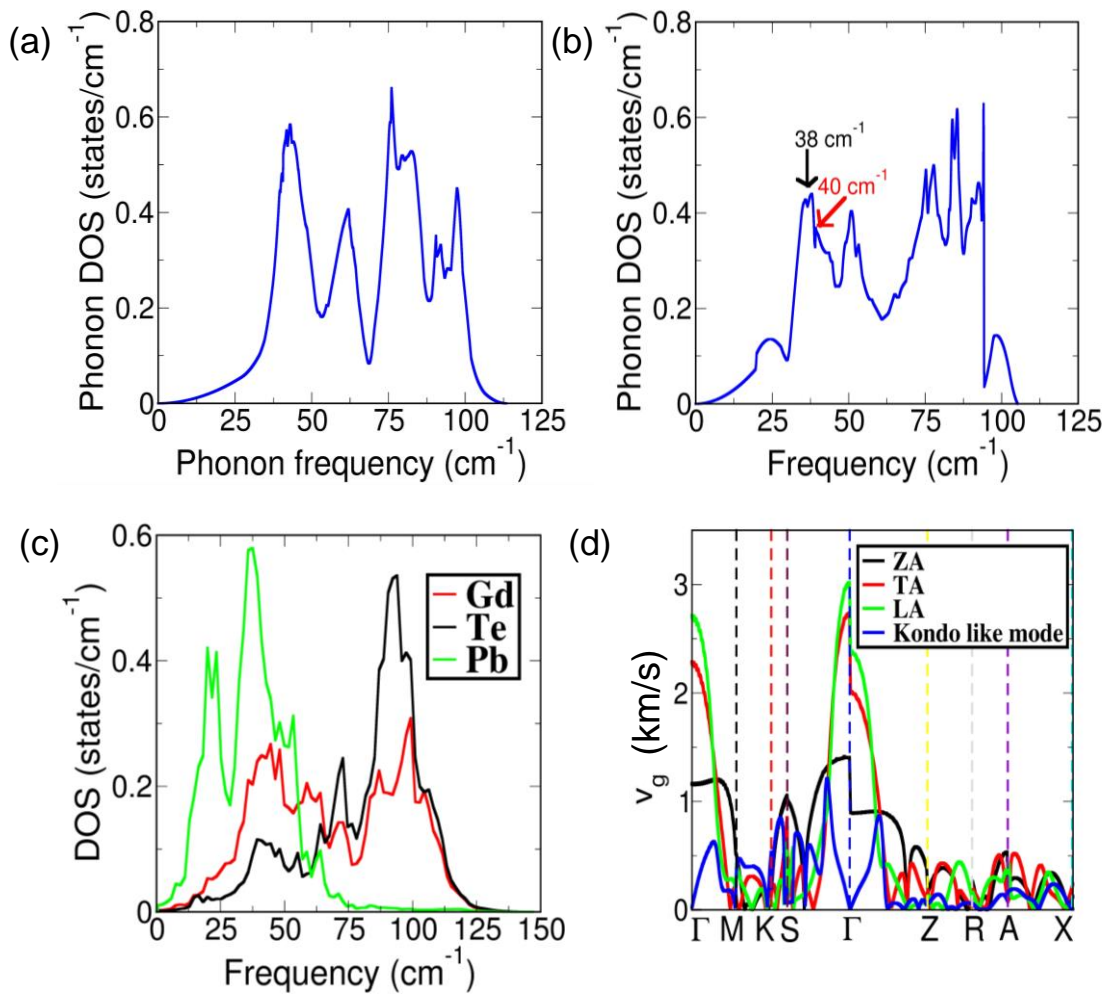


Figure 5.1.9. Phonon DOS for (a) PbTe and (b) Gd doped PbTe. Here, a sudden enhancement in DOS at 38 cm^{-1} which is indicated by a black arrow, appears because of Gd doping in PbTe. This increment in DOS originated because of a low energy nearly flat band (shown in black color in Figure 5.1.7b) in the Gd-doped PbTe. (c) Atom projected phonon DOS. (d) Phonon group velocity vs. q -points. The avoided crossing is further verified from the phonon group velocity plot where sharp changes in phonon group velocity is observed in S point. Please note the group velocity is low for flat low energy Kondo-like optical phonon band (shown in blue color).

The peak thermoelectric figure of merit (zT) of ~ 1.2 at 783 K is observed for $\text{Pb}_{1-x}\text{Gd}_x\text{Te}$ ($x = 0.33\%$) which is a resultant of superior power factor and low κ_{lat} (Figure 5.1.10f). Further optimization is done on $\text{Pb}_{1-x}\text{Gd}_x\text{Te}$ ($x = 0.33\%$) with I co-doping. All the I co-doped samples are found to crystallize in NaCl type structure with no observable impurities within the instrument detection limit (Figure 5.1.11a, b). With subsequent Gd and I co-doping, the band gap is found to increase from ~ 0.28 eV for $\text{Pb}_{1-x}\text{Gd}_x\text{Te}_{1-y}\text{I}_y$ ($x = 0.33\%$, $y = 0\%$) to ~ 0.33 eV for $\text{Pb}_{1-x}\text{Gd}_x\text{Te}_{1-y}\text{I}_y$ ($x = 0.33\%$, $y = 3\%$) at room temperature (Figure 5.1.11b). I co-doping found to decrease the electrical conductivity but increases the S . Even 1 mol% I doped $\text{Pb}_{1-x}\text{Gd}_x\text{Te}$ ($x = 0.33\%$) reduces the room temperature σ value to 1400 S/cm compared to ~ 2484 S/cm for $\text{Pb}_{1-x}\text{Gd}_x\text{Te}$ ($x = 0.33\%$) (Figure 5.1.12a). Additional incorporation of aliovalent I in Te position results in further degradation of σ . 2 mol% and 3 mol% I doped $\text{Pb}_{1-x}\text{Gd}_x\text{Te}$ ($x = 0.33\%$) shows σ value of ~ 1172 S/cm and 832 S/cm at room temperature respectively (Figure 5.1.12a). This decrease in σ value might arise due to enhanced charge carrier scattering (Table 5.1.1). The σ of these I doped $\text{Pb}_{1-x}\text{Gd}_x\text{Te}$ ($x = 0.33\%$) however decreases with increasing temperature, hence retaining the degenerate semiconductor properties of PbTe.

The Seebeck coefficient for $\text{Pb}_{1-x}\text{Gd}_x\text{Te}_{1-y}\text{I}_y$ ($x = 0.33\%$, $y = 1 - 3\%$) increases with increase in y and is in line with the electrical conductivity trend. The room temperature S value for $\text{Pb}_{1-x}\text{Gd}_x\text{Te}_{1-y}\text{I}_y$ ($x = 0.33\%$, $y = 1\%$) is -77 $\mu\text{V}/\text{K}$ which increases to -81 $\mu\text{V}/\text{K}$ for $\text{Pb}_{1-x}\text{Gd}_x\text{Te}_{1-y}\text{I}_y$ ($x = 0.33\%$, $y = 2\%$) and finally up to -92 $\mu\text{V}/\text{K}$ for $\text{Pb}_{1-x}\text{Gd}_x\text{Te}_{1-y}\text{I}_y$ ($x = 0.33\%$, $y = 3\%$) (Figure 5.1.12b). $|S|$ vs. n Pisarenko plot (Figure 5.1.4d) shows that I doping do not perturb the conduction band effective m^* and it is only essential for optimizing the n-type carrier concentration (Table 5.1.1), thereby the S and σ values. S is found to increase almost linearly with increase in temperature for all the samples. High power factor of ~ 20.3 $\mu\text{W}/\text{cmK}^2$ is found for $\text{Pb}_{1-x}\text{Gd}_x\text{Te}_{1-y}\text{I}_y$ ($x = 0.33\%$, $y = 1\%$) at 579 K and remains almost flat up to the measured maximum temperature (Figure 5.1.12c).

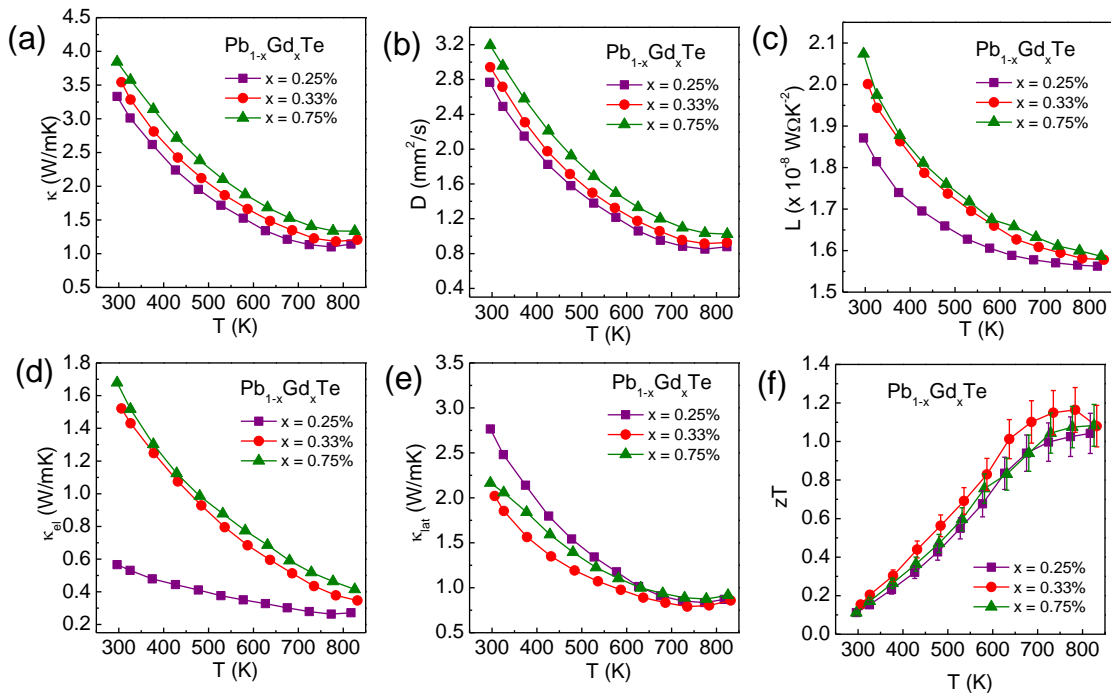


Figure 5.1.10. Temperature dependent (a) total thermal conductivity (κ), (b) thermal diffusivity (D), (c) Lorenz number (L), (d) electrical thermal conductivity (κ_{el}), (e) lattice thermal conductivity (κ_{lat}) and (f) thermoelectric figure of merit (zT) of Gd doped PbTe samples.

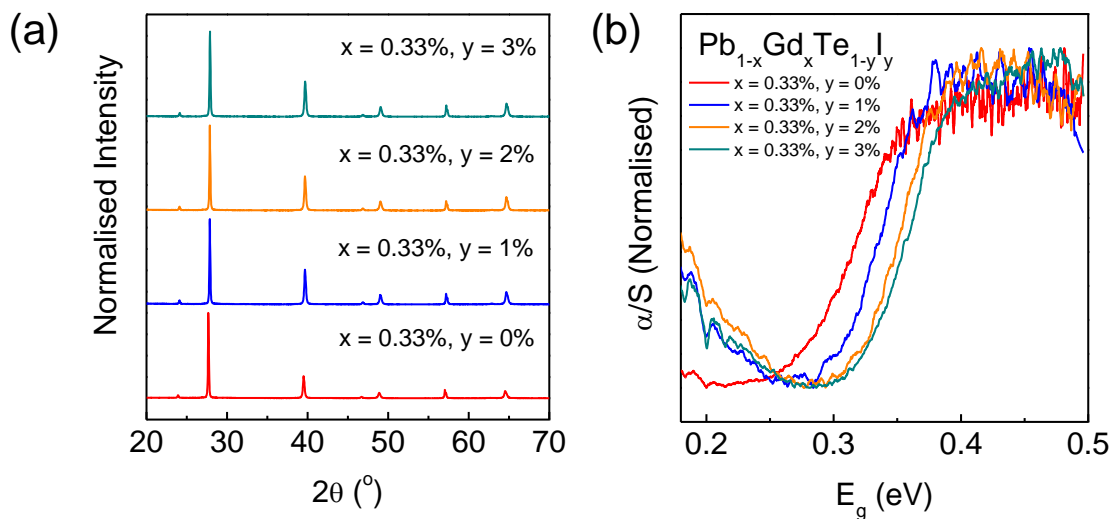


Figure 5.1.11. (a) Room temperature powder XRD pattern of $Pb_{1-x}Gd_xTe_{1-y}I_y$ samples. (b) Room temperature band gap of $Pb_{1-x}Gd_xTe_{1-y}I_y$ samples. The band gap increases on increasing doping concentration.

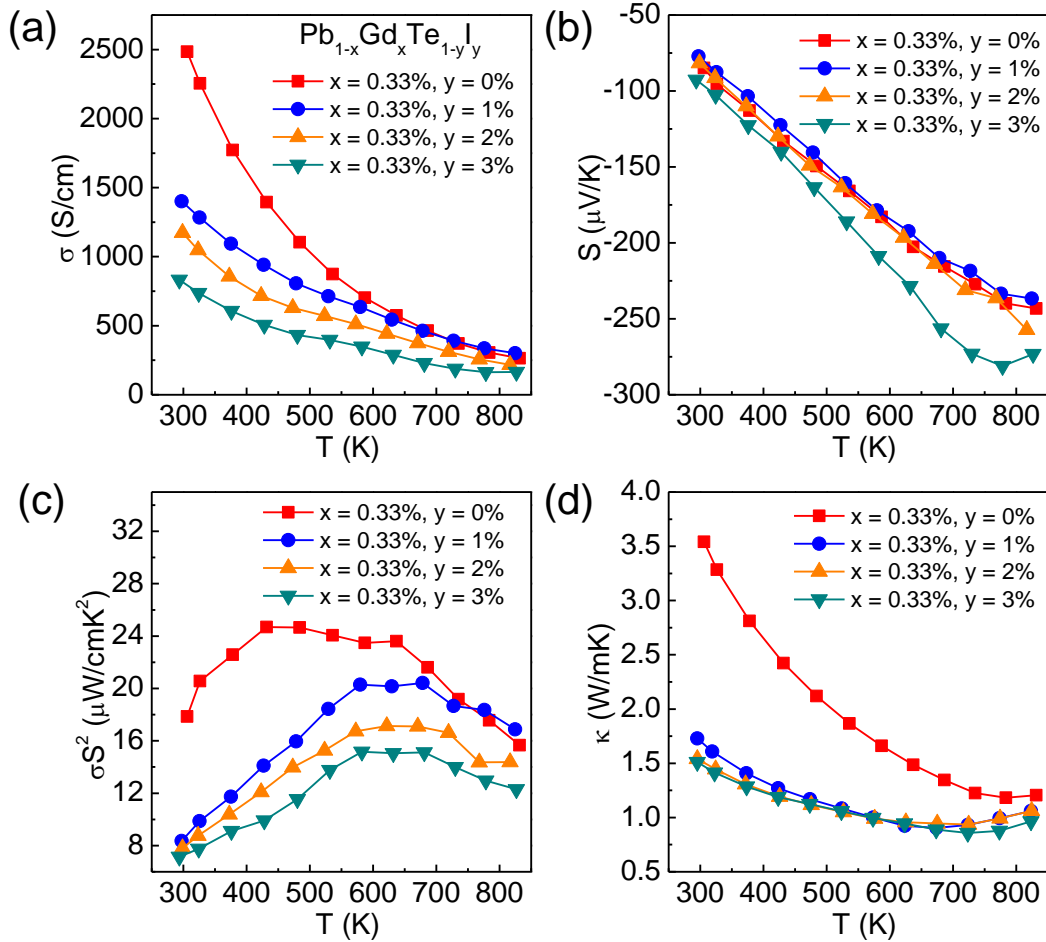


Figure 5.1.12. Temperature dependent (a) Electrical conductivity (σ), (b) Seebeck coefficient (S), (c) power factor (σS^2) and (d) total thermal conductivity (κ) for $\text{Pb}_{1-x}\text{Gd}_x\text{Te}_{1-y}\text{I}_y$ samples.

The room temperature thermal conductivity of $\text{Pb}_{1-x}\text{Gd}_x\text{Te}_{1-y}\text{I}_y$ ($x = 0.33\%$, $y = 1 - 3\%$) decreases dramatically from 3.54 W/mK to 1.51 W/mK for $y = 0\%$ and $y = 3\%$ respectively (Figure 5.1.12d). Such decrease in total thermal conductivity is due to the combination of two effects: first one being significant reduction in the κ_{el} and the other being phonon scattering due to additional point defect scattering from I doping. The temperature dependent thermal diffusivity, Lorenz number and κ_{el} are given in Figure 5.1.13a-c. The κ_{lat} decreases from ~ 2.02 W/mK for $\text{Pb}_{1-x}\text{Gd}_x\text{Te}_{1-y}\text{I}_y$ ($x = 0.33\%$, $y = 0\%$) to ~ 0.78 W/mK for $\text{Pb}_{1-x}\text{Gd}_x\text{Te}_{1-y}\text{I}_y$ ($x = 0.33\%$, $y = 2\%$) at room temperature (Figure 5.1.13d). The κ_{lat} reaches an ultralow value of 0.36 W/mK at ~ 630 K for $\text{Pb}_{1-x}\text{Gd}_x\text{Te}_{1-y}\text{I}_y$

($x = 0.33\%$, $y = 1\%$), lying above the predicted lower limit κ_{diff} value of 0.157 W/mK (Figure 5.1.13d).⁶⁴

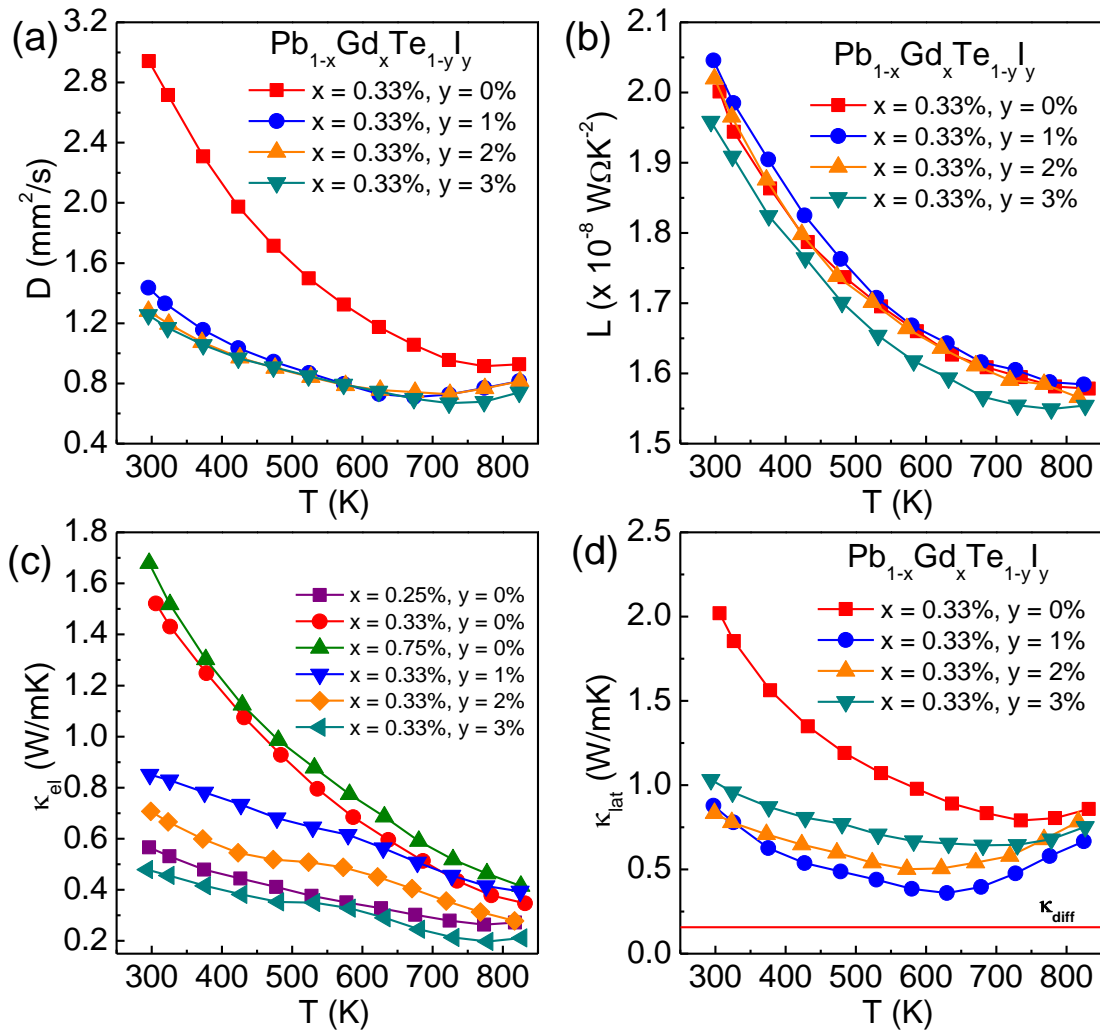


Figure 5.1.13. Temperature dependent (a) Thermal diffusivity (D), (b) Lorenz number (L), (c) electrical thermal conductivity (κ_{el}), and (d) lattice thermal conductivity (κ_{lat}) for $\text{Pb}_{1-x}\text{Gd}_x\text{Te}_{1-y}\text{I}_y$ samples.

The maximum zT of 1.54 at 678 K for $\text{Pb}_{1-x}\text{Gd}_x\text{Te}_{1-y}\text{I}_y$ ($x = 0.33\%$, $y = 1\%$) (Figure 5.1.14) was found. This high zT is a resultant of the synergistic effect of Gd and I co-doping, and this effect is found to increase the thermoelectric performance of the n-type PbTe as compared to their individual contributions as shown in Figure 5.1.14b. The thermoelectric performance was further verified through repeated cycles and the electrical

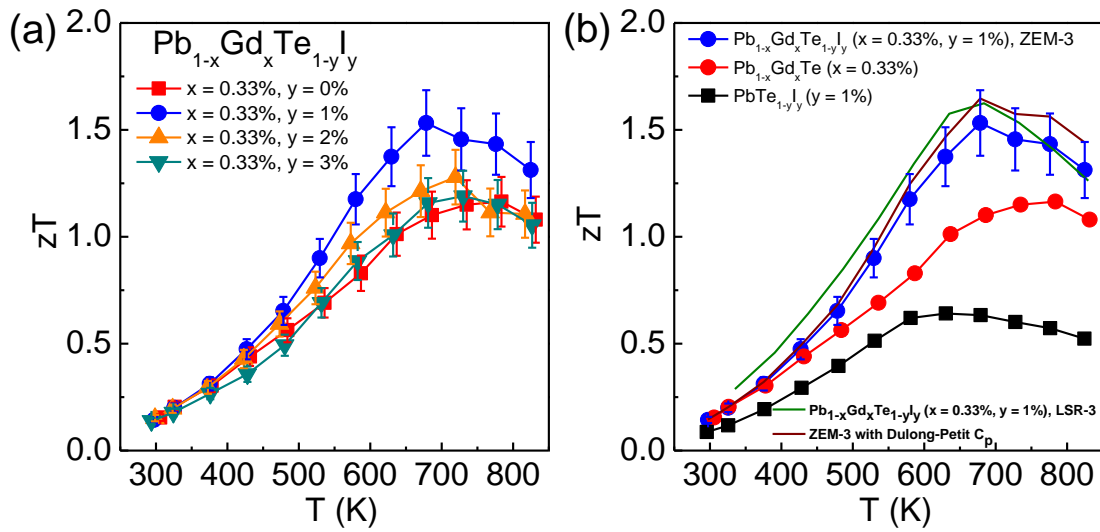


Figure 5.1.14. Temperature dependent (a) thermoelectric figure of merit (zT) for $Pb_{1-x}Gd_xTe_{1-y}I_y$ samples. (b) zT vs T of $Pb_{1-x}Gd_xTe_{1-y}I_y$ compared with controlled individual doping in PbTe. High zT is validated by measuring the properties in different instruments.

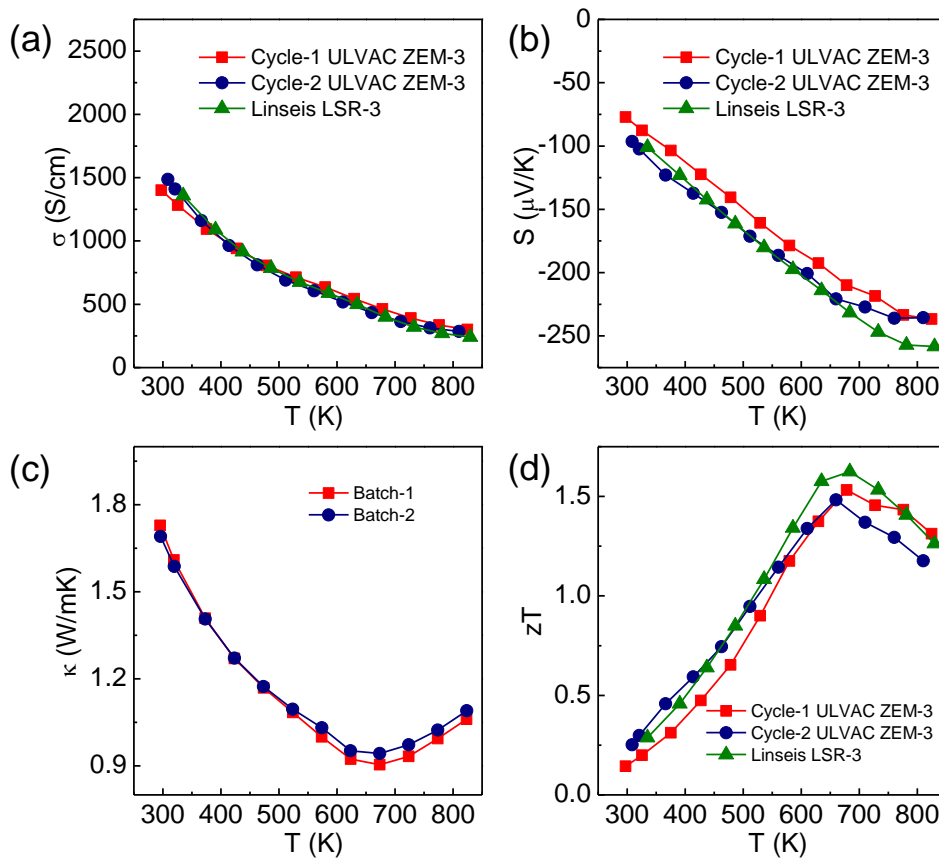


Figure 5.1.15. Reproducibility of the data using multiple cycles and in multiple instruments.

properties were verified using two different instruments (Figure 5.1.15). The peak zT using Ulvac Riko ZEM-3 and Linseis LSR-3 are found to be 1.54 at 678 K and 1.62 at 683 K respectively (Figure 5.1.14b). Peak zT further improves to ~ 1.65 at 678 K (Figure 5.1.14b) if the thermal conductivity is estimated using heat capacity from Dulong-Petit limit of 0.15 J/gK like determined in other previous n-type PbTe based reports^{6, 17, 24, 26}. The high zT in the present system is comparable and even higher to other state of the art n-type PbTe materials. We have achieved a high zT_{ave} of 1.15 in the temperature range of 423 – 823 K for $Pb_{1-x}Gd_xTe_{1-y}I_y$ ($x = 0.33\%$, $y = 1\%$).

5.1.4. Conclusion

In conclusion, Gd doping introduces a non-interacting flat conduction band in n-type PbTe which increases its band effective mass (m^*). The presence of this nearly flat conduction band distorts the electronic DOS which is beneficial for enhancing the Seebeck coefficient of n-type PbTe. $|S|$ vs. n Pisarenko plot reveals that the m^* increases from $0.35 m_e$ to $\sim 0.45 m_e$ with increase in Gd doping (from 0.25 mol% to 0.75 mol%) for n-type PbTe. Gd found to be favorable when it is locally off-centered from its parent position by $\sim 0.21 \text{ \AA}$ along [111] crystallographic direction in the PbTe lattice, which creates significant lattice anharmonicity. Phonon dispersion revealed the presence of low frequency nearly flat optical phonon mode and plays a pivotal role in scattering the heat carrying acoustic phonons, thus lowering its κ_{lat} to a low value. The high thermoelectric performance of Gd doped PbTe is resultant of high power factor arising due to distortion of electronic DOS and simultaneous low thermal conductivity due to Gd off-centering and enhanced scattering due to formation of low energy localized phonon modes. Further improvement in the zT is obtained via I incorporation in $Pb_{1-x}Gd_xTe$ ($x = 0.33\%$), with 1 mol% I co-doping shows a high peak zT of 1.65 at 678 K and an impressive zT_{ave} of 1.15 is obtained in a broad temperature range of 423 – 823 K.

5.1.5. References

- [1] G. Tan, L.-D. Zhao and M. G. Kanatzidis, *Chem. Rev.*, 2016, **116**, 12123-12149.
- [2] X.-L. Shi, J. Zou and Z.-G. Chen, *Chem. Rev.*, 2020, **120**, 7399-7515.
- [3] Y. Xiao and L.-D. Zhao, *Science*, 2020, **367**, 1196.
- [4] S. Roychowdhury, T. Ghosh, R. Arora, M. Samanta, L. Xie, N. K. Singh, A. Soni, J. He, U. V. Waghmare and K. Biswas, *Science*, 2021, **371**, 722.
- [5] B. Jiang, Y. Yu, J. Cui, X. Liu, L. Xie, J. Liao, Q. Zhang, Y. Huang, S. Ning, B. Jia, B. Zhu, S. Bai, L. Chen, S. J. Pennycook and J. He, *Science*, 2021, **371**, 830.
- [6] Y. Xiao, H. Wu, J. Cui, D. Wang, L. Fu, Y. Zhang, Y. Chen, J. He, S. J. Pennycook and L.-D. Zhao, *Energy Environ. Sci.*, 2018, **11**, 2486-2495.
- [7] G. Tan, C. C. Stoumpos, S. Wang, T. P. Bailey, L.-D. Zhao, C. Uher and M. G. Kanatzidis, *Adv. Energy Mater.*, 2017, **7**, 1700099.
- [8] Y. Pei, X. Shi, A. LaLonde, H. Wang, L. Chen and G. J. Snyder, *Nature*, 2011, **473**, 66-69.
- [9] P. Jood, J. P. Male, S. Anand, Y. Matsushita, Y. Takagiwa, M. G. Kanatzidis, G. J. Snyder and M. Ohta, *J. Am. Chem. Soc.*, 2020, **142**, 15464-15475.
- [10] D. Sarkar, T. Ghosh, A. Banik, S. Roychowdhury, D. Sanyal and K. Biswas, *Angew. Chem. Int. Ed.*, 2020, **59**, 11115-11122.
- [11] L. You, J. Zhang, S. Pan, Y. Jiang, K. Wang, J. Yang, Y. Pei, Q. Zhu, M. T. Agne, G. J. Snyder, Z. Ren, W. Zhang and J. Luo, *Energy Environ. Sci.*, 2019, **12**, 3089-3098.
- [12] C. Qin, L. Cheng, Y. Xiao, C. Wen, B. Ge, W. Li and Y. Pei, *Mater. Today Phys.*, 2021, **17**, 100355.
- [13] J. P. Heremans, V. Jovovic, E. S. Toberer, A. Saramat, K. Kurosaki, A. Charoenphakdee, S. Yamanaka and G. J. Snyder, *Science*, 2008, **321**, 554.
- [14] A. Banik, U. S. Shenoy, S. Saha, U. V. Waghmare and K. Biswas, *J. Am. Chem. Soc.*, 2016, **138**, 13068-13075.
- [15] J. He, S. N. Girard, M. G. Kanatzidis and V. P. Dravid, *Adv. Funct. Mater.*, 2010, **20**, 764-772.

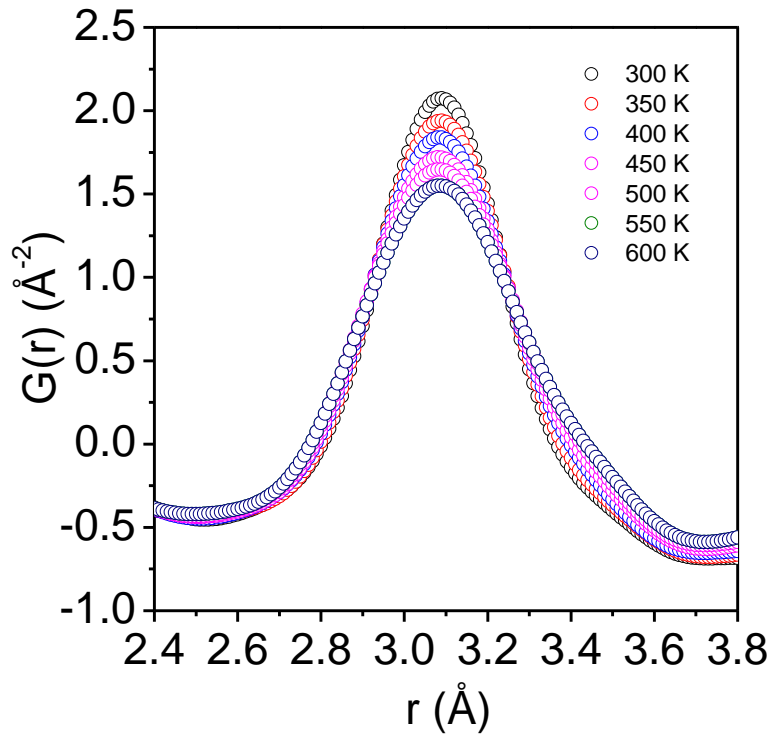
- [16] L.-D. Zhao, S. Hao, S.-H. Lo, C.-I. Wu, X. Zhou, Y. Lee, H. Li, K. Biswas, T. P. Hogan, C. Uher, C. Wolverton, V. P. Dravid and M. G. Kanatzidis, *J. Am. Chem. Soc.*, 2013, **135**, 7364-7370.
- [17] Y. Xiao, H. Wu, W. Li, M. Yin, Y. Pei, Y. Zhang, L. Fu, Y. Chen, S. J. Pennycook, L. Huang, J. He and L.-D. Zhao, *J. Am. Chem. Soc.*, 2017, **139**, 18732-18738.
- [18] S. Wang, Y. Xiao, Y. Chen, S. Peng, D. Wang, T. Hong, Z. Yang, Y. Sun, X. Gao and L.-D. Zhao, *Energy Environ. Sci.*, 2021, **14**, 451-461.
- [19] Z.-Z. Luo, X. Zhang, X. Hua, G. Tan, T. P. Bailey, J. Xu, C. Uher, C. Wolverton, V. P. Dravid, Q. Yan and M. G. Kanatzidis, *Adv. Funct. Mater.*, 2018, **28**, 1801617.
- [20] Z.-Z. Luo, S. Cai, S. Hao, T. P. Bailey, X. Su, I. Spanopoulos, I. Hadar, G. Tan, Y. Luo, J. Xu, C. Uher, C. Wolverton, V. P. Dravid, Q. Yan and M. G. Kanatzidis, *J. Am. Chem. Soc.*, 2019, **141**, 16169-16177.
- [21] J. Li, X. Zhang, Z. Chen, S. Lin, W. Li, J. Shen, I. T. Witting, A. Faghaninia, Y. Chen, A. Jain, L. Chen, G. J. Snyder and Y. Pei, *Joule*, 2018, **2**, 976-987.
- [22] S. Roychowdhury and K. Biswas, *Chem*, 2018, **4**, 939-942.
- [23] M. Dutta, T. Ghosh and K. Biswas, *APL Mater.*, 2020, **8**, 040910.
- [24] L. Fu, M. Yin, D. Wu, W. Li, D. Feng, L. Huang and J. He, *Energy Environ. Sci.*, 2017, **10**, 2030-2040.
- [25] S. Roychowdhury, R. K. Biswas, M. Dutta, S. K. Pati and K. Biswas, *ACS Energy Lett.*, 2019, **4**, 1658-1662.
- [26] J. Zhang, D. Wu, D. He, D. Feng, M. Yin, X. Qin and J. He, *Adv. Mater.*, 2017, **29**, 1703148.
- [27] S. Liu, Y. Yu, D. Wu, X. Xu, L. Xie, X. Chao, M. Bosman, S. J. Pennycook, Z. Yang and J. He, *Adv. Funct. Mater.*, 2021, **31**, 2007340.
- [28] M. H. Lee, J. H. Yun, G. Kim, J. E. Lee, S.-D. Park, H. Reith, G. Schierning, K. Nielsch, W. Ko, A.-P. Li and J.-S. Rhyee, *ACS Nano*, 2019, **13**, 3806-3815.
- [29] K. Biswas, J. He, I. D. Blum, C. I. Wu, T. P. Hogan, D. N. Seidman, V. P. Dravid and M. G. Kanatzidis, *Nature*, 2012, **489**, 414-418.

-
- [30] L. D. Zhao, H. J. Wu, S. Q. Hao, C. I. Wu, X. Y. Zhou, K. Biswas, J. Q. He, T. P. Hogan, C. Uher, C. Wolverton, V. P. Dravid and M. G. Kanatzidis, *Energy Environ. Sci.*, 2013, **6**, 3346-3355.
- [31] H. Liu, Z. Chen, J. Tang, Y. Zhong, X. Guo, F. Zhang and R. Ang, *ACS Appl. Mater. Interfaces*, 2020, **12**, 52952-52958.
- [32] M. K. Jana and K. Biswas, *ACS Energy Lett.*, 2018, **3**, 1315-1324.
- [33] Y. Xiao and L.-D. Zhao, *npj Quantum Mater.*, 2018, **3**, 55.
- [34] G. Tan, F. Shi, S. Hao, L.-D. Zhao, H. Chi, X. Zhang, C. Uher, C. Wolverton, V. P. Dravid and M. G. Kanatzidis, *Nat. Commun.*, 2016, **7**, 12167.
- [35] Y. Zhong, J. Tang, H. Liu, Z. Chen, L. Lin, D. Ren, B. Liu and R. Ang, *ACS Appl. Mater. Interfaces*, 2020, **12**, 49323-49334.
- [36] Y. Qin, Y. Xiao and L.-D. Zhao, *APL Mater.*, 2020, **8**, 010901.
- [37] A. D. LaLonde, Y. Pei and G. J. Snyder, *Energy Environ. Sci.*, 2011, **4**, 2090-2096.
- [38] Z. Yang, S. Wang, Y. Sun, Y. Xiao and L.-D. Zhao, *J. Alloys Compd.*, 2020, **828**, 154377.
- [39] Y. Pei, J. Lensch-Falk, E. S. Toberer, D. L. Medlin and G. J. Snyder, *Adv. Funct. Mater.*, 2011, **21**, 241-249.
- [40] K. F. Hsu, S. Loo, F. Guo, W. Chen, J. S. Dyck, C. Uher, T. Hogan, E. K. Polychroniadis and M. G. Kanatzidis, *Science*, 2004, **303**, 818.
- [41] P. Giannozzi, S. Baroni, N. Bonini, M. Calandra, R. Car, C. Cavazzoni, D. Ceresoli, G. L. Chiarotti, M. Cococcioni, I. Dabo, A. Dal Corso, S. de Gironcoli, S. Fabris, G. Fratesi, R. Gebauer, U. Gerstmann, C. Gougoussis, A. Kokalj, M. Lazzeri, L. Martin-Samos, N. Marzari, F. Mauri, R. Mazzarello, S. Paolini, A. Pasquarello, L. Paulatto, C. Sbraccia, S. Scandolo, G. Sclauzero, A. P. Seitsonen, A. Smogunov, P. Umari and R. M. Wentzcovitch, *J. Phys.: Condens. Matter*, 2009, **21**, 395502.
- [42] P. E. Blöchl, *Phys. Rev. B*, 1994, **50**, 17953-17979.
- [43] J. P. Perdew, K. Burke and M. Ernzerhof, *Phys. Rev. Lett.*, 1996, **77**, 3865.
- [44] W. Li, J. Carrete, N. A. Katcho and N. Mingo, *Comput. Phys. Commun.*, 2014, **185**, 1747-1758.

- [45] W. Li, L. Lindsay, D. A. Broido, D. A. Stewart and N. Mingo, *Phys. Rev. B*, 2012, **86**, 174307.
- [46] D. M. Zayachuk, D. D. Ivanchuk, R. D. Ivanchuk, S. S. Maslyanchuk and V. I. Mikityuk, *phys. stat. sol. (a)*, 1990, **119**, 215-219.
- [47] K. Nouneh, K. Plucinski, M. Bakasse and I. Kityk, *J. Mater. Sci.*, 2007, **42**, 6847-6853.
- [48] Y. Pei, A. D. LaLonde, H. Wang and G. J. Snyder, *Energy Environ. Sci.*, 2012, **5**, 7963-7969.
- [49] E. B. Isaacs and C. Wolverton, *Phys. Rev. Mater.*, 2019, **3**, 015403.
- [50] K. Mori, H. Sakakibara, H. Usui and K. Kuroki, *Phys. Rev. B*, 2013, **88**, 075141.
- [51] V. S. Sastri, J.-C. Bünzli, V. R. Rao, G. V. S. Rayudu and J. R. Perumareddi, in *Modern Aspects of Rare Earths and Their Complexes*, Elsevier, Amsterdam, 2003, DOI: 10.1016/B978-044451010-5/50019-5, pp. 375-422.
- [52] Z.-Z. Luo, S. Hao, X. Zhang, X. Hua, S. Cai, G. Tan, T. P. Bailey, R. Ma, C. Uher, C. Wolverton, V. P. Dravid, Q. Yan and M. G. Kanatzidis, *Energy Environ. Sci.*, 2018, **11**, 3220-3230.
- [53] S. Sarkar, X. Hua, S. Hao, X. Zhang, T. P. Bailey, T. J. Slade, P. Yasaei, R. J. Korkosz, G. Tan, C. Uher, V. P. Dravid, C. Wolverton and M. G. Kanatzidis, *Chem. Mater.*, 2021, **33**, 1842-1851.
- [54] M. S. Ikeda, H. Euchner, X. Yan, P. Tomeš, A. Prokofiev, L. Prochaska, G. Lientschnig, R. Svagera, S. Hartmann, E. Gati, M. Lang and S. Paschen, *Nat. Commun.*, 2019, **10**, 887.
- [55] W. Li and N. Mingo, *Phys. Rev. B*, 2015, **91**, 144304.
- [56] K. Pal, Y. Xia, J. He and C. Wolverton, *Chem. Mater.*, 2019, **31**, 8734-8741.
- [57] S. Baroni, S. de Gironcoli, A. Dal Corso and P. Giannozzi, *Rev. Mod. Phys.*, 2001, **73**, 515-562.
- [58] J. R. Schrieffer and P. A. Wolff, *Phys. Rev.*, 1966, **149**, 491-492.
- [59] P. Nozières and A. Blandin, *J. Phys. France*, 1980, **41**, 193-211.
- [60] Y. Zhang, *J. Materiomics*, 2016, **2**, 237-247.

-
- [61] Y. Zhang, X. Ke, C. Chen, J. Yang and P. R. C. Kent, *Phys. Rev. B*, 2009, **80**, 024304.
- [62] B. Roger and I. Rudolf, *Z. Naturforsch. B*, 1974, **29**, 625-629.
- [63] K. Biswas, J. He, I. D. Blum, C.-I. Wu, T. P. Hogan, D. N. Seidman, V. P. Dravid and M. G. Kanatzidis, *Nature*, 2012, **489**, 414.
- [64] M. T. Agne, R. Hanus and G. J. Snyder, *Energy Environ. Sci.*, 2018, **11**, 609-616.

Chapter 5.2



**Local Ge Off-centering in $\text{Sn}_{0.7}\text{Ge}_{0.3}\text{Te}$
Induces Ferroelectric Instability and
Softens Polar Phonons: Pair
Distribution Function (PDF) Analysis**

Local Ge Off-centering in $\text{Sn}_{0.7}\text{Ge}_{0.3}\text{Te}$ Induces Ferroelectric Instability and Softens Polar Phonons: Pair Distribution Function (PDF) Analysis[†]

Summary

Lowering of optical phonon modes are pivotal for a system to attain low thermal conductivity as they scatter the heat carrying acoustic phonons. In this chapter, we have investigated the structure – property relationship of $\text{Sn}_{0.7}\text{Ge}_{0.3}\text{Te}$ near and above its ferroelectric transition temperature. $\text{Sn}_{0.7}\text{Ge}_{0.3}\text{Te}$ which shows a ferroelectric transition at ~ 290 K, is found to be locally distorted below 290 K by a greater degree which decreases after the ferroelectric transition temperature, but nevertheless retains the local distortion till the measured temperature. Through Synchrotron X-ray Pair Distribution Function (PDF), we have observed that both the cations remain off-centered along the rhombohedral [111] direction, which Ge showing a much greater degree of off-centering in the lattice. We have shown that the local rhombohedral distortions are predominantly associated with correlated local Ge off-centering which forms a short-range chain-like structures and scatter acoustic phonons, resulting in an ultralow lattice thermal conductivity of ~ 0.67 W/mK.

[†]A. Banik, T. Ghosh, R. Arora, **M. Dutta**, J. Pandey, S. Acharya, A. Soni, U. V. Waghmare and K. Biswas. *Energy Environ. Sci.*, 2019, **12**, 589–595. and A. Vasdev,¹ **M. Dutta**,¹ S. Mishra, V. Kaur, H. Kaur, K. Biswas and G. Sheet. *Manuscript under review* (¹Equal first author).

5.2.1. Introduction

Innovative design of solid state structures and compositions with low thermal conductivity is the way forward to high performance thermoelectric (TE) materials, which offer an environment friendly solution for recovery of waste heat in the form of electricity.^{1, 2} The crux of improving a material's thermoelectric performance involves essentially the optimization of three interdependent material properties: electrical conductivity (σ), Seebeck coefficient (S) and thermal conductivity (κ_{tot} = electronic (κ_{el}) + lattice (κ_{lat}) thermal conductivity) which govern the dimensionless thermoelectric figure of merit, $zT = \sigma S^2 T / (\kappa_{\text{lat}} + \kappa_{\text{el}})$.³ The reduction in κ_{lat} by devising an efficient mechanism of scattering heat carrying acoustic phonons is one of the most effective and widely used avenues for high performance thermoelectrics.⁴⁻⁶ Innovative material design like broadband phonon scatterings based on extrinsic all-scale hierarchical nano/meso-architectures^{5, 7} or intrinsic material properties,⁸ e.g., complex crystal structures,⁹ part-crystalline part-liquid state,¹⁰ bonding asymmetry,^{11, 12} superionic substructure with liquid-like cation disordering,¹³⁻¹⁵ lone-pair induced bond anharmonicity¹⁶ and anisotropic layered crystal structure^{17, 18} have been employed in the past to achieve low κ_{lat} . However, in many of these approaches like the introduction of nano/meso-architectures, the reduction in κ_{lat} comes with a cost of reduced charge carrier mobility (μ) and electrical conductivity.

In this chapter, we provide experimental evidence for local structural distortion which induces ferroelectric instability in $\text{Sn}_{0.7}\text{Ge}_{0.3}\text{Te}$ near the room temperature. SnTe resides in global centrosymmetric rocksalt structure at room temperature but has a lattice instability originating from resonant bonding¹⁹⁻²⁴ and undergoes a temperature dependent paraelectric to ferroelectric transition with rhombohedral ($R-3m$) structure below 100 K.²⁵ Ferroelectricity in its rhombohedral phase originates from relative displacements of the Sn and Te sublattices along [111] direction.²⁵⁻²⁹ In the close proximity of the ferroelectric transition ($> T_C$), SnTe exhibits softening of the zone centre (Γ -point) TO phonon modes^{20, 30} and the frequencies of these TO phonons are in fact lower in the cubic phase compared to that of the rhombohedral phase.²⁹ This ferroelectric instability originated from local rhombohedral distortion in cubic SnTe , can be employed to further improve its thermoelectric performance by reducing the κ_{lat} . However, the ferroelectric phase

transition in SnTe occurs in a temperature regime of ~ 100 K, making it impractical to use the associated ferroelectric instability for thermoelectric power generation at high temperatures.

In this chapter, we have alloyed Ge (30 mol%) in SnTe to strengthen its ferroelectric instability near room temperatures and achieve soft phonon modes in a wide range of momenta around ferroelectric instability. $\text{Sn}_{1-x}\text{Ge}_x\text{Te}$ exhibits unstable phonon branches not only at the Brillouin zone center (characteristic of displacive phase transition), but also wave-vectors in a large domain in Brillouin zone. In real space, this results in chain like local off-centering of Ge in the cubic SnTe lattice. The analysis of temperature dependent synchrotron X-ray Pair Distribution Function (PDF) reveals that although the global structure is cubic, local rhombohedral distortion, primarily created by Ge off-centering, persists even at the highest temperature studies here. Analysis of the local structure revealed that the cations are off-centered from their mean position along the rhombohedral [111] direction. The off-centering of Ge is found to be ~ 0.25 Å below the ferroelectric transition temperature which decreases to 0.10 Å after the transition. Sn however are off-centered by a much lesser degree by ~ 0.07 Å below the ferroelectric transition temperature which reduces after the transition. This local off-centering and the ensuing ferroelectric instability in $\text{Sn}_{0.7}\text{Ge}_{0.3}\text{Te}$ scatter heat carrying acoustic phonons, and thereby reduce the κ_{lat} to ~ 0.67 W/mK at 300 K in $\text{Sn}_{0.7}\text{Ge}_{0.3}\text{Te}$. The ultra-low κ_{lat} , aids in enhancing the thermoelectric figure of merit and we achieved highest thermoelectric figure of merit, zT , of ~ 1.6 at 721 K with carrier optimized Sb-doped $\text{Sn}_{0.7}\text{Ge}_{0.3}\text{Te}$ ($\text{Sn}_{0.57}\text{Sb}_{0.13}\text{Ge}_{0.3}\text{Te}$).

5.2.2. Methods

Reagents. Tin (Alfa Aesar 99.99+ %), germanium (Aldrich 99.999%), tellurium (Alfa Aesar 99.999+ %) and antimony (Alfa Aesar 99.999+ %) were used for synthesis without further purification.

Synthesis. High quality polycrystalline ingots of $\text{Sn}_{0.7}\text{Ge}_{0.3}\text{Te}$ have been synthesized by melting the stoichiometric amount of Sn, Ge and Te in vacuum sealed (10^{-5} Torr) quartz

tube. The tubes were kept vertically in a box furnace and slowly heated to 900 °C over 12 hrs, then kept for 10 hrs, and cooled slowly to room temperature.

Pair Distribution Function (PDF): For performing X-ray PDF, the samples were finely ground using agate mortar pestle and the powder crystals were then filled in a capillary having diameter of 0.6 mm and is sealed on ends using adhesive. The capillaries then mounted on an instrument holder which is placed right in between the beam source and the image plate. Cryostream (250 – 300 K) and hot air blower (300 – 600 K) was used for the temperature dependent measurement. The Perkin Elmer detector was placed at ~230 mm from the sample. A dark measurement was performed prior to every data set, and to obtain the background data sets from empty capillary was taken after each sample. Lanthanum Hexaboride (LaB_6) was used as a standard for calibration purposes in our experiment. The beam spot size had a dimension of $0.5 \times 0.5 \text{ mm}^2$ and a fixed energy of ~60 keV was used.

Processing and normalization of data provided us with $G(r)$, which gives the probability of finding nearest neighbor atoms at a distance r in the material. $G(r)$ is obtained via Fourier Transformation of scattering structure function $F(Q)$, using the formula³¹

$$G(r) = \frac{2}{\pi} \int_{Q_{min}}^{\infty} F(Q) \sin Qr dQ$$

Where Q is the momentum transfer of the scattering particle. $F(Q)$ is related to structure function $S(Q)$ which is attained from proper correction of scattering data via the relation $F(Q) = Q[S(Q)-1]$. The data was taken from the beamline P02.1, PETRA III, DESY, Germany.³²

Modelling of the PDF data was performed using PDFgui³³ software. All the datasets from 250 K – 600 K were initially modeled using a rock-salt cubic model. The refinement parameters were the lattice parameter, peak shape parameter, scale and the thermal parameter values.

5.2.3. Results and Discussion

$\text{Sn}_{0.7}\text{Ge}_{0.3}\text{Te}$ is prepared by the high vacuum melting reaction and are found to crystallize globally in rocksalt cubic $Fm\bar{3}m$ structure. The cations occupy the 4a Wyckoff site in a positional disorder whereas the anion position is taken up by Te. Differential Scanning Calorimetry (DSC) measurements revealed an exothermic peak at ~ 291 K, signifying the ferroelectric transition temperature in this material. PFM studies confirmed the presence of local ferroelectric domains in $\text{Sn}_{0.7}\text{Ge}_{0.3}\text{Te}$ which are suppressed at ~ 300 K. Moreover, DFT calculations strongly suggest the presence of off-centered Ge atoms which induces ferroelectric instability. This demands investigation to the overall structure of the compound. Synchrotron generated X-ray pair distribution function (PDF) is a powerful tool to extract structural information of a compound in both local as well as global scale. Here to ascertain local ferroelectric domain, we have analyzed the structure of $\text{Sn}_{0.7}\text{Ge}_{0.3}\text{Te}$ using PDF analysis.

PDF analysis revealed that $\text{Sn}_{0.7}\text{Ge}_{0.3}\text{Te}$ resides globally in rock-salt cubic lattice throughout the measured temperature range. When fitted with $Fm\bar{3}m$ model with partial occupancy of Sn/Ge in the cation site and Te in the anion site, the total PDF (2.5 – 20 Å) near the room temperature (~ 290 K) agrees reasonably well with the simulated curve (Figure 5.2.1a). An excellent R_w value of $\sim 6.6\%$ at 250 K obtained for the whole range fitting indicates that the global structure remains unperturbed with Ge alloying in SnTe (Figure 5.2.1b). With increase in temperature, the R_w value further decreases to $\sim 6.4\%$ at 300 K (Figure 5.2.1c). The temperature evolution (250 - 300 K) of PDF over a range of 2.5 - 20 Å at 10 K intervals is shown in Figure 5.2.2a. As the temperature increases, the thermal vibrations of atoms inside the lattice increases, which is observed in the decrease of peak intensities and increase in the peak width. The lattice parameter of $\text{Sn}_{0.7}\text{Ge}_{0.3}\text{Te}$ also increases from ~ 6.165 Å at 250 K to ~ 6.171 Å at 300 K (Figure 5.2.2b). The isotropic atomic displacement parameter (U_{iso}) ranges from 0.030 Å² to 0.033 Å² for cations (Sn/Ge) whereas for Te it ranges from 0.019 Å² to 0.022 Å² for 250 - 300 K region (Figure 5.2.2c). The thermal parameter provides a quantitative description of the vibrations of the atoms inside the lattice and its increase with temperature concurs with the increase (decrease) in peak width (intensities) with temperature (Figure 5.2.2a).

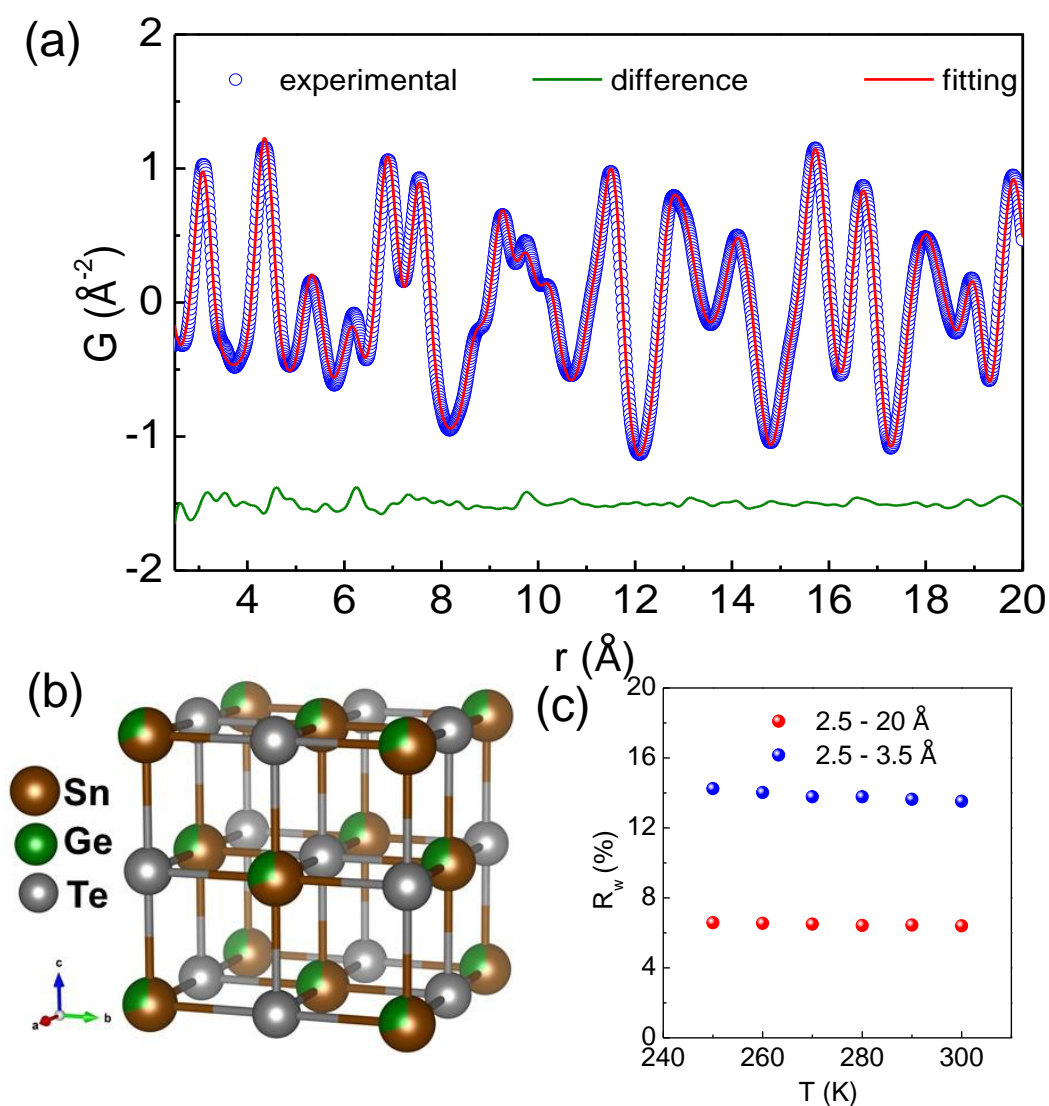


Figure 5.2.1. (a) X-ray Pair Distribution Function (PDF) plot of $\text{Sn}_{0.7}\text{Ge}_{0.3}\text{Te}$ measured at 290 K and is fitted using cubic $Fm\bar{3}m$ model. (b) Cubic $Fm\bar{3}m$ structure of $\text{Sn}_{0.7}\text{Ge}_{0.3}\text{Te}$. (c) Temperature dependent Goodness of fit (R_w %) value for the total structure (2.5 – 20 Å) and local structure (2.5 – 3.5 Å) of $\text{Sn}_{0.7}\text{Ge}_{0.3}\text{Te}$ fitted with $Fm\bar{3}m$ model.

To unravel the nearest neighbour correlation in $\text{Sn}_{0.7}\text{Ge}_{0.3}\text{Te}$, that is the local bonding between cations ($\text{Sn}^{2+}/\text{Ge}^{2+}$) and anion (Te^{2-}), we have examined the bonding characteristics of the first peak ($2.5 \text{ \AA} < r < 3.5 \text{ \AA}$). When fitted using cubic model with parameters obtained from the total PDF fitting, the simulated fit does not correctly describe the local structural features (Figure 5.2.3a). As shown in Figure 5.2.1c, the R_w

value for the first peak (2.5 - 3.5 Å) of $\text{Sn}_{0.7}\text{Ge}_{0.3}\text{Te}$, using an undistorted cubic model is as high as ~14.2% at 250 K and decreases slightly to 13.5 % at 300 K. Such poor description of the first peak is most likely attributed to local distortion in $\text{Sn}_{0.7}\text{Ge}_{0.3}\text{Te}$. On off-centering Sn and Ge from their parent position, the fit for the nearest neighbour drastically improves (Figure 5.2.3b). The R_w for first peak fitting at 250 K drops to ~6.2% (from 14.2%), when Sn and Ge are allowed to off-center from their mean position.

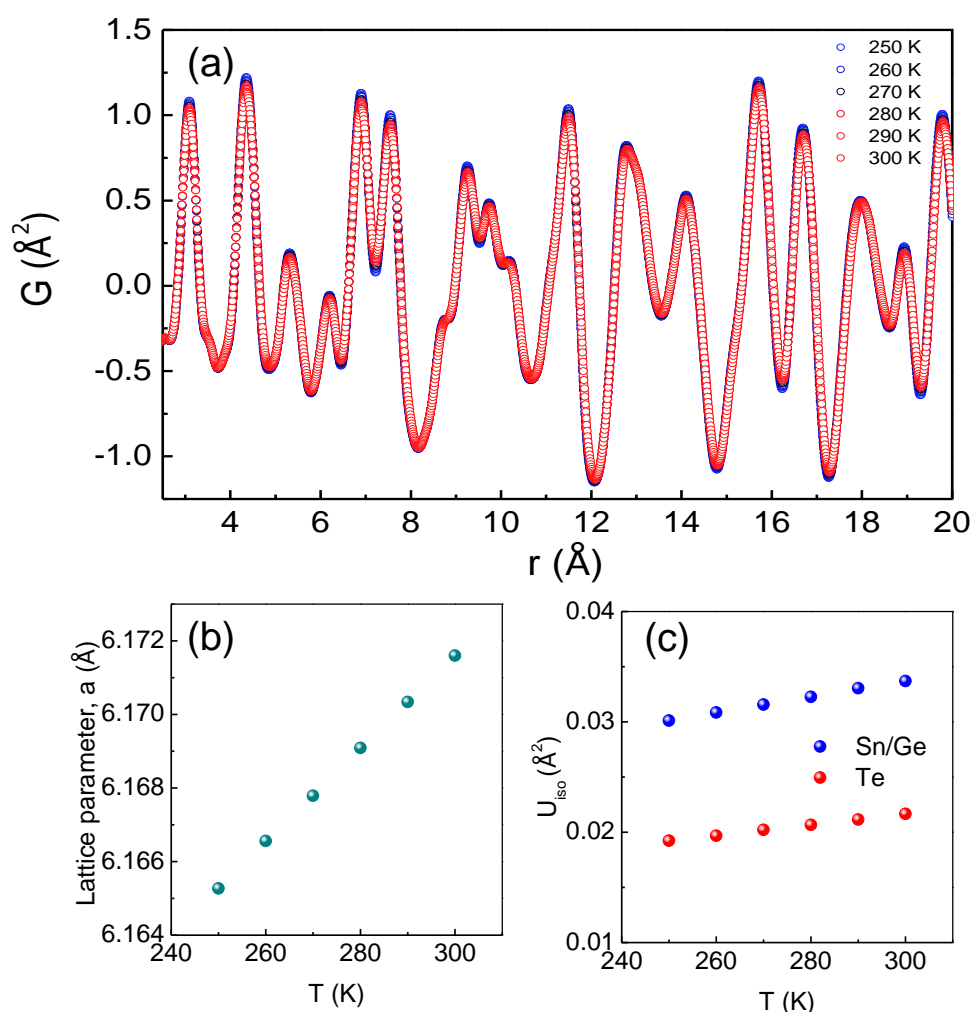


Figure 5.2.2. (a) Temperature variation of PDF plot showing a decrease in intensity with warming. (b) Temperature dependent lattice parameter. (c) Temperature dependent ADP values.

Interestingly, we observed that while Sn remains slightly off-centered (~0.07 Å) from its mean position at 250 K, Ge is found to be off-centered by a much greater extent

(~ 0.24 Å) along the rhombohedral [111] direction in the global cubic SnTe. Such off-centering of Ge is a resultant of strong stereochemical activity of $4s^2$ lone pair on Ge^{2+} which exerts a significant repulsion on the neighbouring bond-pairs. Mention must be made that the lone pair of Ge^{2+} in pure GeTe resides in a global rhombohedral structure (ferroelectric phase) up to 623 K.^{34, 35} Hence, in a symmetrical rock-salt type octahedral environment (in SnTe present case), the Ge will tend to off-center along the rhombohedral direction by expressing its $4s^2$ lone pair which we observe in the present PDF experiments and predicted by DFT calculation. Such locally off-centered Ge cations will induce charge polarization that can give rise to local ferroelectric instability as seen from PFM measurements.

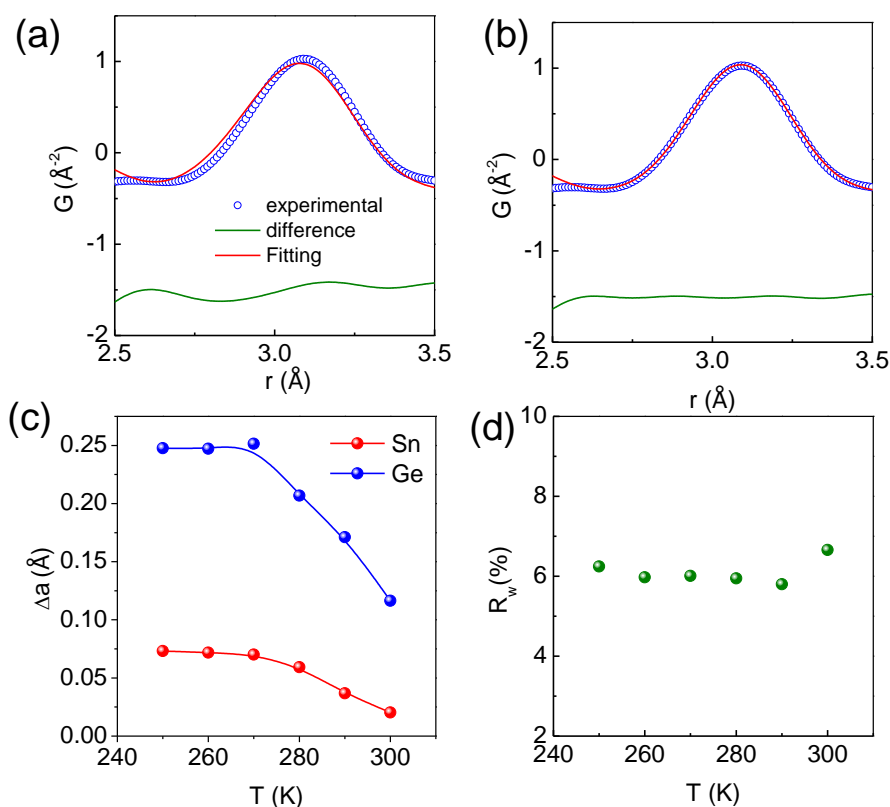


Figure 5.2.3. 300 K PDF first peak fitted using (a) cubic $Fm\bar{3}m$ model and (b) Distorted model. (c) Magnitude of locally distortion for Sn and Ge atoms. (d) Temperature dependent Goodness of fit (R_w %) value for local structure (2.5 – 3.5 Å) of $\text{Sn}_{0.7}\text{Ge}_{0.3}\text{Te}$ fitted with distorted model.

Temperature evolution of the local structure shows dynamic off-centering of cations. Ge remains off-centered by ~ 0.25 Å at 270 K and then starts to decrease the off-

centering near the ferroelectric T_c (Figure 5.2.3c), T_c is the ferroelectric transition temperature) in $\text{Sn}_{0.7}\text{Ge}_{0.3}\text{Te}$, whereas Sn distorts only by $\sim 0.07 \text{ \AA}$ along rhombohedral direction at 250 K. At 300 K Ge and Sn shows local displacement of about 0.11 \AA and 0.02 \AA respectively. Low R_w values for locally off-centered Sn/Ge (Figure 5.2.3d) compared to undistorted Sn/Ge (Figure 5.2.1c) indicates that the structure does reside as a low symmetric entity locally, although globally it averages out as a symmetrical rock-salt lattice. Such temperature dependent local distortion corroborates the PFM observations of local polarization and subsequent ferroelectric instability.

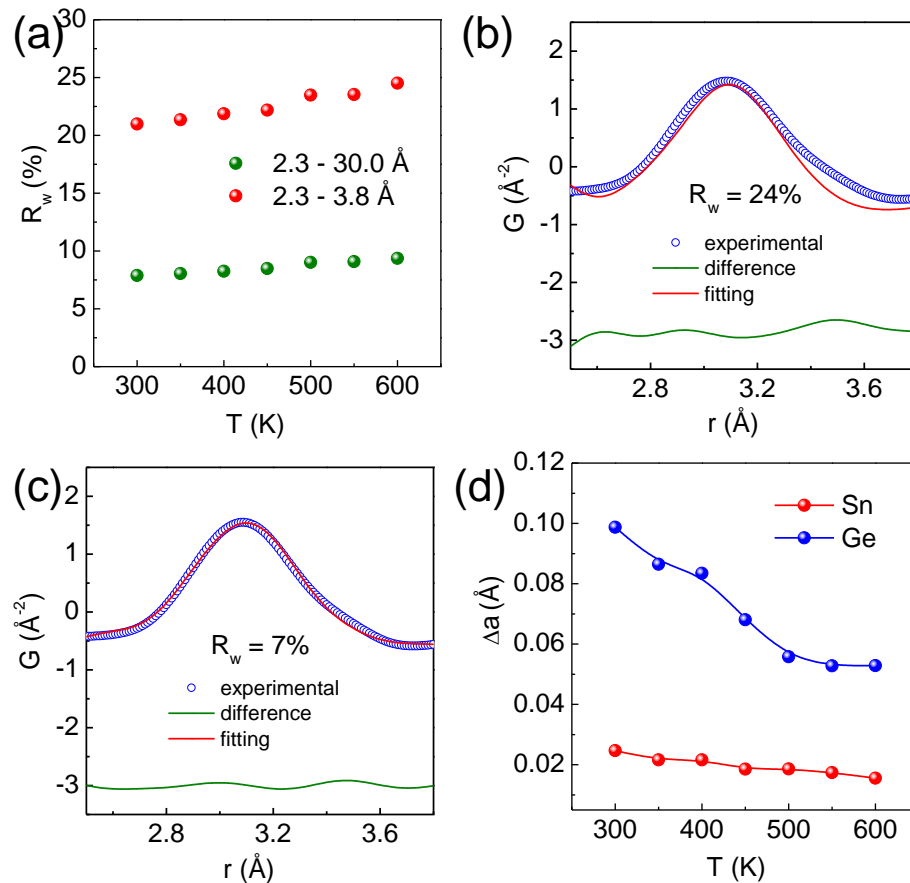


Figure 5.2.4. (a) Temperature dependent Goodness of fit (R_w %) value for local structure (2.3 – 3.8 Å) and total (2.3 – 30.0 Å) of $\text{Sn}_{0.7}\text{Ge}_{0.3}\text{Te}$ fitted with cubic $Fm\bar{3}m$ model. 600 K PDF first peak fitted using (b) cubic $Fm\bar{3}m$ model and (c) Distorted rhombohedral model. (d) Magnitude of locally distortion for Sn and Ge atoms.

To further understand the local structure of $\text{Sn}_{0.7}\text{Ge}_{0.3}\text{Te}$ at above the ferroelectric transition temperature, we have performed PDF analysis from 300 – 600 K for this

compound. The fit of total structure ($2.3 - 30 \text{ \AA}$) supports the global cubic symmetry of the structure as observed from their R_w values (Figure 5.2.4a). However, when we looked into the PDF for the nearest neighbour correlation, we find that the cubic undistorted model does not describe the experimentally observed data satisfactorily, as evident from the high R_w values (Figure 5.2.4a). The PDF data fits better when the cations are distorted along $[111]$ direction, as apparent from the local structural modelling at 600 K (Figure 5.2.4b, c) as well as from their corresponding R_w values. This local rhombohedral distortion is predominantly created through Ge off-centering along the $[111]$ direction within the global cubic model, as seen in Figure 5.2.4d. At room temperature, Ge atoms are off-centered by $\sim 0.10 \text{ \AA}$, significantly higher than that of Sn atoms ($\sim 0.02 \text{ \AA}$). The analysis of the temperature evolution of the nearest neighbour correlation exhibits that the amplitude of Ge off-centering decreases with increasing temperature (Figure 5.2.4d). This local distortion, however, is sustained much above the ferroelectric transition temperature ($\sim 2T_c$), as predicted from the phonon dispersion of $\text{Sn}_{0.75}\text{Ge}_{0.25}\text{Te}$. This persistent local structural distortion and the associated ferroelectric instability strongly affect the high temperature thermal conductivity, and thus its overall thermoelectric properties. The lowering of thermal conductivity due to the presence of off-centered Ge and Hg dopants has been observed recently in the PbSe system as well.^{36, 37}

5.2.4. Conclusion

In conclusion, we have demonstrated local ferroelectric polarization in $\text{Sn}_{0.7}\text{Ge}_{0.3}\text{Te}$ is caused due to the local local off-centering of Ge^{2+} along the rhombohedral direction ($[111]$) in the global rock-salt SnTe lattice, which is confirmed by synchrotron X-ray PDF investigations. The off-centering of Ge^{2+} is due to its stereochemically active $4s^2$ lone pair of electrons which distorts the local octahedral coordination and forms local chain type off-centered region in global cubic lattice. We observe that below room temperature this local off-centering is significant and decreases after the transition but persist till $2T_c$. This local off-centering is the primary driving cause for low κ_{lat} in $\text{Sn}_{0.7}\text{Ge}_{0.3}\text{Te}$

5.2.5. References

- [1] G. Tan, L.-D. Zhao and M. G. Kanatzidis, *Chem. Rev.*, 2016, **116**, 12123-12149.
- [2] Z.-H. Ge, L.-D. Zhao, D. Wu, X. Liu, B.-P. Zhang, J.-F. Li and J. He, *Mater. Today*, 2016, **19**, 227-239.
- [3] L.-D. Zhao, V. P. Dravid and M. G. Kanatzidis, *Energy Environ. Sci.*, 2014, **7**, 251-268.
- [4] Y. Xiao, H. Wu, W. Li, M. Yin, Y. Pei, Y. Zhang, L. Fu, Y. Chen, S. J. Pennycook, L. Huang, J. He and L.-D. Zhao, *J. Am. Chem. Soc.*, 2017, **139**, 18732-18738.
- [5] K. Biswas, J. He, I. D. Blum, C.-I. Wu, T. P. Hogan, D. N. Seidman, V. P. Dravid and M. G. Kanatzidis, *Nature*, 2012, **489**, 414-418.
- [6] M. Samanta and K. Biswas, *J. Am. Chem. Soc.*, 2017, **139**, 9382-9391.
- [7] G. Tan, F. Shi, S. Hao, L.-D. Zhao, H. Chi, X. Zhang, C. Uher, C. Wolverton, V. P. Dravid and M. G. Kanatzidis, *Nat. Commun.*, 2016, **7**, 12167.
- [8] M. K. Jana and K. Biswas, *ACS Energy Lett.*, 2018, **3**, 1315-1324.
- [9] G. J. Snyder and E. S. Toberer, *Nat. Mater.*, 2008, **7**, 105-114.
- [10] B. Li, H. Wang, Y. Kawakita, Q. Zhang, M. Feygenson, H. L. Yu, D. Wu, K. Ohara, T. Kikuchi, K. Shibata, T. Yamada, X. K. Ning, Y. Chen, J. Q. He, D. Vaknin, R. Q. Wu, K. Nakajima and M. G. Kanatzidis, *Nat. Mater.*, 2018, **17**, 226-230.
- [11] M. K. Jana, K. Pal, A. Warankar, P. Mandal, U. V. Waghmare and K. Biswas, *J. Am. Chem. Soc.*, 2017, **139**, 4350-4353.
- [12] M. K. Jana, K. Pal, U. V. Waghmare and K. Biswas, *Angew. Chem., Int. Ed.*, 2016, **55**, 7792-7796.
- [13] H. Liu, X. Shi, F. Xu, L. Zhang, W. Zhang, L. Chen, Q. Li, C. Uher, T. Day and G. J. Snyder, *Nat. Mater.*, 2012, **11**, 422-425.
- [14] S. Roychowdhury, M. K. Jana, J. Pan, S. N. Guin, D. Sanyal, U. V. Waghmare and K. Biswas, *Angew. Chem., Int. Ed.*, 2018, **57**, 4043-4047.
- [15] A. A. Olvera, N. A. Moroz, P. Sahoo, P. Ren, T. P. Bailey, A. A. Page, C. Uher and P. F. P. Poudeu, *Energy Environ. Sci.*, 2017, **10**, 1668-1676.

-
- [16] D. Morelli, V. Jovovic and J. Heremans, *Phys. Rev. Lett.*, 2008, **101**, 035901.
- [17] L.-D. Zhao, S.-H. Lo, Y. Zhang, H. Sun, G. Tan, C. Uher, C. Wolverton, V. P. Dravid and M. G. Kanatzidis, *Nature*, 2014, **508**, 373-377.
- [18] M. Samanta, K. Pal, P. Pal, U. V. Waghmare and K. Biswas, *J. Am. Chem. Soc.*, 2018, **140**, 5866-5872.
- [19] U. V. Waghmare, N. A. Spaldin, H. C. Kandpal and R. Seshadri, *Phys. Rev. B*, 2003, **67**, 125111.
- [20] S. Katayama and H. Kawamura, *Solid State Commun.*, 1977, **21**, 521-524.
- [21] K. R. Knox, E. S. Bozin, C. D. Malliakas, M. G. Kanatzidis and S. J. L. Billinge, *Phys. Rev. B*, 2014, **89**, 014102.
- [22] K. V. Mitrofanov, A. V. Kolobov, P. Fons, M. Krbal, T. Shintani, J. Tominaga and T. Uruga, *Phys. Rev. B*, 2014, **90**, 134101.
- [23] L. Aggarwal, A. Banik, S. Anand, U. V. Waghmare, K. Biswas and G. Sheet, *J. Materiomics*, 2016, **2**, 196-202.
- [24] S. Lee, K. Esfarjani, T. Luo, J. Zhou, Z. Tian and G. Chen, *Nat. Commun.*, 2014, **5**, 3525.
- [25] M. Sist, E. M. Jensen Hedegaard, S. Christensen, N. Bindzus, K. F. F. Fischer, H. Kasai, K. Sugimoto and B. Brummerstedt Iversen, *IUCrJ*, 2016, **3**, 377-388.
- [26] G. S. Pawley, W. Cochran, R. A. Cowley and G. Dolling, *Phys. Rev. Letters*, 1966, **17**, 753-755.
- [27] M. Iizumi, Y. Hamaguchi, K. F. Komatsubara and Y. Kato, *J. Phys. Soc. Jpn.*, 1975, **38**, 443-449.
- [28] K. Murase and S. Sugai, *Solid State Comm.*, 1979, **32**, 89-93.
- [29] C. D. O'Neill, D. A. Sokolov, A. Hermann, A. Bossak, C. Stock and A. D. Huxley, *Phys. Rev. B*, 2017, **95**, 144101.
- [30] S. Sugai, K. Murase and H. Kawamura, *Solid State Commun.*, 1977, **23**, 127-129.
- [31] T. Proffen, S. J. L. Billinge, T. Egami and D. Louca, *Z. Kristallogr. Cryst. Mater.*, 2003, **218**, 132.

-
- [32] A.-C. Dippel, H.-P. Liermann, J. T. Delitz, P. Walter, H. Schulte-Schrepping, O. H. Seeck and H. Franz, *J. Synchrotron Rad.*, 2015, **22**, 675-687.
- [33] C. L. Farrow, P. Juhas, J. W. Liu, D. Bryndin, E. S. Božin, J. Bloch, P. Th and S. J. L. Billinge, *J. Phys: Condens. Matter*, 2007, **19**, 335219.
- [34] S. Roychowdhury, M. Samanta, S. Perumal and K. Biswas, *Chem. Mater.*, 2018, **30**, 5799-5813.
- [35] M. Samanta, T. Ghosh, R. Arora, U. V. Waghmare and K. Biswas, *J. Am. Chem. Soc.*, 2019, **141**, 19505-19512.
- [36] Z.-Z. Luo, S. Hao, X. Zhang, X. Hua, S. Cai, G. Tan, T. P. Bailey, R. Ma, C. Uher, C. Wolverton, V. P. Dravid, Q. Yan and M. G. Kanatzidis, *Energy Environ. Sci.*, 2018, **11**, 3220-3230.
- [37] J. M. Hodges, S. Hao, J. A. Grovogui, X. Zhang, T. P. Bailey, X. Li, Z. Gan, Y.-Y. Hu, C. Uher, V. P. Dravid, C. Wolverton and M. G. Kanatzidis, *J. Am. Chem. Soc.*, 2018, **140**, 18115-18123.

Part 6



Summary and Future outlook

Summary and Future Outlook[†]

6.1 Summary

This part summarizes the thesis. The work done in this thesis provides a systematic pathway to achieve high thermoelectric performance in metal chalcogenides through manipulating the lattice thermal conductivity (κ_{lat}). Since κ_{lat} originates due to periodic lattice vibrations in a crystal, its properties are directly related to the chemical bonding of a material. Therefore, a detailed knowledge of the solid-state chemistry and keen chemical intuition is necessary to achieve desirable κ_{lat} , which can be used in applications ranging from thermoelectrics to thermal barrier coatings.

Part 1 of the thesis provides salient structural features that can be manipulated to achieve low κ_{lat} . Our compound of interest revolves around several metal chalcogenides, chosen primarily because of their vast compositional and structural varieties. In this part we provide a glimpse into the structural versatilities of metal chalcogenides and their role in impeding phonon transport. This part provides the nature of phonon transport in a multitude of different materials with varying bonding characteristics ranging from anharmonic rattling of atoms, bonding heterogeneity to local off-centering. We further discuss about the applicability of crystalline materials with low κ_{lat} in thermoelectrics and provide glimpse into additional parameters to optimize to maximise the thermoelectric figure of merit (zT) value. We finally discuss about the various measurements that has been performed in order to unearth the origin behind low κ_{lat} materials.

In Part 2, we delve into understanding the nature of κ_{lat} in simple binary compounds TlSe and InSe. Tl and In both being in the same group (IIIA), exhibits different bonding characteristics with Se and hence, TlSe and InSe crystallizes in different Bravais lattices at ambient conditions. TlSe for instance, crystallises in tetragonal I4/mcm and is a Zintl type compound, with two different subunits (Tl^+ and $(\text{Tl}^{3+}\text{Se}_2)^-$). The Tl^+ are loosely bound and resides in a cavity formed by the 1-D chains of $(\text{TlSe}_2)_n^-$. This Tl^+

[†]A part of this chapter is published in M. Dutta, D. Sarkar and K. Biswas. *Chem. Commun.*, 2021, **57**, 4751-4767 (Perspective).

is weakly bonded to the 1D chains and thus exhibit independent rattling behavior. This rattling induced low energy optical modes scatters the heat carrying acoustic modes and thereby lowers the κ_{lat} to 0.43 W/mK at 523 K.¹ On the other hand, InSe is a layered material having space group $P6_3/mmc$. The layers are stacked along the crystallographic *c*-direction wherein each layer is separated from each other through van der Waals (vdW) gap. The thermal conductivity of InSe is found to be highly anisotropic with phonon transport getting truncated while traversing the vdW gap along the *c*-axis, while in the in-plane direction, the phonon transport is much facile due to strong covalent bonding. This results in a high anisotropic κ_{lat} ratio of ~ 8.25 along the different direction at room temperature in InSe.

In part 3 we have demonstrated how understanding the total structure (a combination of average and local structure) gives a superior understanding to the origin of intrinsically low κ_{lat} in metal chalcogenides. Herein, aided by the state-of-the-art synchrotron X-ray pair distribution function (PDF) technique and inelastic neutron scattering (INS) measurements, we have explained the cause behind low κ_{lat} in TlInTe_2 (Chapter 3.1) and AgSbSe_2 (Chapter 3.2). TlInTe_2 , a TlSe type Zintl compound having intrinsically ultralow κ_{lat} (~ 0.5 W/mK at 300 K). Using temperature dependent PDF, we directly evidenced bonding heterogeneity with In-Te forms a strong covalent bonding while Tl-Te is weakly bonded. We have revealed the rattling vibration of Tl^+ from its high atomic displacement parameter (*U*) value, which has significant impact on the phonon transport. Furthermore, the rattling is found to be highly anharmonic as observed from INS measurements and induces low energy phonon density of states (< 100 cm^{-1}). These low energy optical phonon density of states have very low lifetimes, indicating their interaction with the heat carrying acoustic phonons results in enhanced phonon scattering, resulting in low κ_{lat} .² Chapter 3.2 demonstrates the glass like thermal conductivity in AgSbSe_2 having κ_{lat} close to minimum thermal conductivity (κ_{min}). Through PDF they have unearthed that Sb remains in a locally off-centered position in a global cubic rock-salt lattice along the crystallographic [111] direction by a factor of ~ 0.2 Å. This is due to the $5s^2$ lone pair of electrons on Sb which stereochemically express themselves and thereby distorts the lattice. This local distortion enhances the phonon scattering and thereby lowers the κ_{lat} to glassy limit in AgSbSe_2 .

Part 4 of the thesis couples total structural understanding with theoretical outputs to unearth the origin behind low κ_{lat} in metal chalcogenides. Here we went a step further to demonstrate the applicability of low κ_{lat} in thermoelectrics. Chapter 4.1 demonstrates the investigation of low κ_{lat} in highly disordered rock-salt structure AgPbBiSe_3 . The theoretical investigation indicated the presence of bonding heterogeneity with Ag atoms being weakly bonded to the lattice as compared to the other atoms and $6s^2$ lone pairs of electrons around Pb and Bi. From PDF analysis, significant local distortion around Pb and Bi octahedra has been observed attributed to the stereochemical activity of the $6s^2$ lone pairs of electrons on them. From atomic displacement parameter (U) analysis, we observe a greater U value for Ag, indicating its weak bonding to the lattice. Both these factors enhance the phonon scattering and lower the thermal conductivity in AgPbBiSe_3 and as a result we obtained a high *n*-type $zT \sim 0.8$ at 814 K for $\text{AgPbBiSe}_{2.97}\text{I}_{0.03}$.³ In chapter 4.2, *emphanisis* has been observed through PDF, which indicates the formation of low symmetric structure from high symmetric structure on warming. Similar to AgPbBiSe_3 , our compound of interest here $(\text{SnSe})_{0.5}(\text{AgSbSe}_2)_{0.5}$ is found to remain in a rock-salt crystal lattice with three cations sharing the same position. Theoretical phonon dispersion indicated the presence of damped phonon modes primarily of Se vibrations. Through local structural analysis we observed first peak asymmetry in PDF, indicative of local distortion and this peak asymmetry is found to increase with temperature. Further analysis revealed that Se resides an off-centered position locally along crystallographic [111] direction. The magnitude of local off-centering is found to increase with temperature from 0.21 – 0.26 Å in the 100 – 400 K range, thus confirming *emphanisis*. This local off-centering enhances the phonon scattering and thereby low κ_{lat} is observed in this compound. Furthermore, Ge doping to modulate the electronic properties have resulted in an impressive *p*-type $zT > 1$ in this material.⁴ In chapter 4.3, we have investigated the modulation of electronic properties, primarily related to tuning of *p-n-p* conduction via externally manipulating the vacancy of Ag and Cu in AgCuS . We observed that Cu is highly effective in arresting this *p-n* transition, while the same transition is found to be robust in respect to Ag vacancy.⁵

In Part 5, we demonstrated high thermoelectric performance arising due to low κ_{lat} . In chapter 5.1, we discussed about the role of discordant Gd in PbTe . Introducing an

atomic species to a coordination environment different from its preferred choice could become a discordant atom in the lattice and consequently, could lead to local structural distortion. When Gd atoms are incorporated in PbTe, they are found to remain in an off-centered position by ~ 0.21 Å along the crystallographic [111] direction.⁶ This is because Gd prefers a higher co-ordination number than the existing 6-atom coordination environment of PbTe with rocksalt structure. DFT based theoretical analysis reveals that the interaction between Gd and surrounding Te atoms become bonding in nature when it is off-centered as opposed to the anti-bonding nature when Gd is in the undistorted position. This discordant nature of Gd results in low κ_{lat} (~ 0.78 W/mK at 735 K) and high n-type $zT \sim 1.65$ at 678 K in Gd doped PbTe.⁶ In chapter 5.2, the role of Ge in engineering ferroelectric instability has been investigated. Ge is found to remain locally off-centered rhombohedrally in $\text{Sn}_{0.7}\text{Ge}_{0.3}\text{Te}$ which although decreases after the ferroelectric transition but still persists up to the measured temperature. As a result, ultralow κ_{lat} is observed throughout the temperature range which drives its high thermoelectric performance of 1.6 at 721 K.^{7,8}

This thesis can be summarized in three categories:

- (1) Designing new materials with potentially low κ_{lat} , from our knowledge of chemical bonding and solid state chemistry.
- (2) Investigating the origin of low κ_{lat} in metal chalcogenides via obtaining a complete structural information combined with theoretical insights.
- (3) Implementing this low κ_{lat} materials in thermoelectrics for energy management and harvesting.

6.2. Future Outlook

Crystalline solids possessing low κ_{lat} is advantageous for achieving high thermoelectric performance.⁹ Manipulation of thermal conductivity using extrinsic route like introduction of nanoprecipitates,¹⁰ or grain boundaries¹¹ are the most acceptable and successful strategies to lower the κ_{lat} . Similarly, tuning the chemical interaction between atoms through material design like synthesizing compounds having van der Waals layers,¹² liquid-like sublattice,¹³ intrinsic rattlers² or stereochemically active lone pair of electrons¹⁴ also exhibited impressive phonon blocking attributes. All these factors mainly

affect the specific heat, the phonon group velocity or the mean phonon free path of a compound, resulting in lowering of the κ_{lat} .⁹

However, new strategies like introduction of ferroelectric instability,⁷ metavalent bonding,¹⁵ locally distorted structure⁴ also show immense promise in the lowering of κ_{lat} through a material. However, they are in the nascent stages and is in need of further investigations to clearly establish their role in diminishing phonon propagation. This requires investigating their nature of chemical bonding among the atoms, their atomic displacement parameter (ADP) and structural uniformity. Analysis of these parameters in both local and global length scales using advanced techniques like Pair Distribution Function (PDF), Transmission Electron Microscopy (TEM), Solid state NMR etc. will advance our understanding and will aid in predicting suitable materials with low thermal conductivity. Similarly, visualizing the momentum resolved phonon spectra through Inelastic Neutron/X-ray Scattering (INS/IXS) will also provide crucial information regarding the behavior of heat flow in a material. Furthermore, integrating of these techniques with theoretical predictions will be the step forward.

The end goal for attaining intrinsically low κ_{lat} is to use it for achieving high thermoelectric performance.¹⁶ Although the above strategies mentioned in this chapter in retrospect should help to accomplish low κ_{lat} , but for high thermoelectric performance, we need a synergy of both low κ_{lat} and high power factor (σS^2). In this regard, low κ_{lat} materials must have favorable electronic band structure for a facile charge carrier transport. Understanding of electronic transport is another important piece to decipher the puzzle of obtaining high thermoelectric performance. Furthermore, the material should be durable and stable unlike superionic Ag based compounds which suffers from Ag^+ ion leaching out, must be environmentally benign materials and should be economically feasible with high material supply. Nonetheless, development of 2D material like SnSe having record thermoelectric performance ($zT \sim 2.6$)¹² provides an important step forward in fabricating cost-effective, environment benign, efficient thermoelectrics for potential commercialization. The strategies outlined in this thesis should serve as an indicator to rationally design and predict materials with low κ_{lat} . This in conjunction with the powerful computational techniques, the next step will be to build up a machine learning based

materials project to catalogue low κ_{lat} materials which can potentially show high thermoelectric performance.

6.3. References

- [1] M. Dutta, S. Matteppanavar, M. V. D. Prasad, J. Pandey, A. Warankar, P. Mandal, A. Soni, U. V. Waghmare and K. Biswas, *J. Am. Chem. Soc.*, 2019, **141**, 20293-20299.
- [2] M. Dutta, M. Samanta, T. Ghosh, D. J. Voneshen and K. Biswas, *Angew. Chem. Int. Ed.*, 2021, **60**, 4259-4265.
- [3] M. Dutta, K. Pal, U. V. Waghmare and K. Biswas, *Chem. Sci.*, 2019, **10**, 4905-4913.
- [4] M. Dutta, K. Pal, M. Etter, U. V. Waghmare and K. Biswas, *J. Am. Chem. Soc.*, 2021, **143**, 16839–16848.
- [5] M. Dutta, D. Sanyal and K. Biswas, *Inorg. Chem.*, 2018, **57**, 7481-7489.
- [6] M. Dutta, R. K. Biswas, S. K. Pati and K. Biswas, *ACS Energy Lett.*, 2021, **6**, 1625-1632.
- [7] A. Banik, T. Ghosh, R. Arora, M. Dutta, J. Pandey, S. Acharya, A. Soni, U. V. Waghmare and K. Biswas, *Energy Environ. Sci.*, 2019, **12**, 589-595.
- [8] A. Vasdev, M. Dutta, S. Mishra, V. Kaur, H. Kaur, K. Biswas and G. Sheet, *Sci. Rep.*, 2021, **11**, 17190.
- [9] M. Dutta, D. Sarkar and K. Biswas, *Chem. Commun.*, 2021, **57**, 4751-4767.
- [10] C. J. Vineis, A. Shakouri, A. Majumdar and M. G. Kanatzidis, *Adv. Mater.*, 2010, **22**, 3970-3980.
- [11] S. I. Kim, K. H. Lee, H. A. Mun, H. S. Kim, S. W. Hwang, J. W. Roh, D. J. Yang, W. H. Shin, X. S. Li, Y. H. Lee, G. J. Snyder and S. W. Kim, *Science*, 2015, **348**, 109.
- [12] L.-D. Zhao, S.-H. Lo, Y. Zhang, H. Sun, G. Tan, C. Uher, C. Wolverton, V. P. Dravid and M. G. Kanatzidis, *Nature*, 2014, **508**, 373.
- [13] S. Roychowdhury, M. K. Jana, J. Pan, S. N. Guin, D. Sanyal, U. V. Waghmare and K. Biswas, *Angew. Chem. Int. Ed.*, 2018, **57**, 4043-4047.
- [14] M. D. Nielsen, V. Ozolins and J. P. Heremans, *Energy Environ. Sci.*, 2013, **6**, 570-578.

-
- [15] D. Sarkar, S. Roychowdhury, R. Arora, T. Ghosh, A. Vasdev, B. Joseph, G. Sheet, U. V. Waghmare and K. Biswas, *Angew. Chem. Int. Ed.*, 2021, **60**, 10350-10358.
- [16] G. J. Snyder and E. S. Toberer, *Nat. Mater.*, 2008, **7**, 105.

List of Publications

• Included in this Thesis

1. **M. Dutta**, K. Pal, M. Etter, U. V. Waghmare and K. Biswas. *J. Am. Chem. Soc.*, 2021, *143*, 16839-16848.
2. **M. Dutta**, R. K. Biswas, S. K. Pati and K. Biswas. *ACS Energy Lett.*, 2021, *6*, 1625-1632.
3. **M. Dutta**, M. Samanta, T. Ghosh, D. J. Voneshen and K. Biswas. *Angew. Chem. Int. Ed.*, 2021, *60*, 4259-4265. (Hot Paper)
4. **M. Dutta**, S. Matteppanavar, M. V. D. Prasad, J. Pandey, A. Warankar, P. Mandal, A. Soni, U. V. Waghmare and K. Biswas. *J. Am. Chem. Soc.*, 2019, *141*, 20293-20299.
5. **M. Dutta**, K. Pal, U. V. Waghmare and K. Biswas. *Chem. Sci.*, 2019, *10*, 4905-4913.
6. **M. Dutta**, D. Sanyal and K. Biswas. *Inorg. Chem.*, 2018, *57*, 7481-7489.
7. A. Banik, T. Ghosh, R. Arora, **M. Dutta**, J. Pandey, S. Acharya, A. Soni, U. V. Waghmare and K. Biswas. *Energy Environ. Sci.*, 2019, *12*, 589-595.
8. **M. Dutta**, D. Sarkar and K. Biswas. *Chem. Commun.*, 2021, *57*, 4751-4767.
9. **M. Dutta**, K. Pal, S. Matteppanavar, A. Warankar, P. Mandal, U. V. Waghmare and K. Biswas. *Manuscript under preparation*.
10. **M. Dutta**, M. V. D. Prasad, J. Pandey, A. Soni, U. V. Waghmare, and K. Biswas. *Manuscript under preparation*.
11. **M. Dutta**,¹ A. Vasdev,¹ S. Mishra, V. Kaur, H. Kaur, K. Biswas and G. Sheet. *Manuscript under review* (¹Equal first author).

- **Not Included in the Thesis**

12. T. Ghosh, S. Roychowdhury, **M. Dutta** and K. Biswas. *ACS Energy Lett.*, 2021, 6, 2825-2837.
13. A. Bhui, **M. Dutta**, M. Mukherjee, K. S. Rana, A. K. Singh, A. Soni and K. Biswas. *Chem. Mater.*, 2021, 33, 2993-3001.
14. **M. Dutta**, T. Ghosh and K. Biswas. *APL Mater.*, 2020, 8, 040910.
15. E. Rathore,¹ **M. Dutta**¹ and K. Biswas. *J. Chem. Sci.*, 2019, 131, 116. (¹Equal first author)
16. S. Roychowdhury, R. K. Biswas, **M. Dutta**, S. K. Pati and K Biswas. *ACS Energy Lett.*, 2019, 4, 1658-1662
17. T. Bernges, J. Peilstöcker, **M. Dutta**, S. Ohno, S. P. Culver, K. Biswas and W. G. Zeier. *Inorg. Chem.*, 2019, 58, 9236-9245.
18. S. Roychowdhury, **M. Dutta** and K. Biswas. *J. Mater. Chem. A*, 2018, 6, 24216-24223.
19. T. Ghosh, **M. Dutta** and K. Biswas. “*High-performance thermoelectrics based on metal selenides.*” Elsevier. (Book chapter)
20. M. Samanta,¹ **M. Dutta**¹ and K. Biswas. “*Thermoelectric energy conversion.*” World Scientific. (Book chapter, ¹Equal first author)

Biography



Moinak Dutta obtained his B.Sc. (2014) degree in Chemistry from University of Calcutta, India and M.Sc. (2016) degree in Chemistry from University of Hyderabad, India. He is currently pursuing his Ph. D. under the guidance of Prof. Kanishka Biswas at New Chemistry Unit, Jawaharlal Nehru Centre for

Advanced Scientific Research (JNCASR), Bangalore, India. His research areas focus on the origin of low lattice thermal conductivity of metal chalcogenides and its implications in thermoelectrics. He is recipient of the best speaker prize at “In-House Symposium (2020), JNCASR, India”, “RSC Roadshow award for oral presentation (2019), JNCASR, India” and best poster award at “In-House Symposium (2019), JNCASR, India”.

